Department of Materials

Imperial College

PhD Thesis

Potential hazards of 2D nanomaterials to the environment

Field of Study: Nanomaterials and Environmental Toxicology

Seigo Masuda, PhD student

Supervisors: Professor Alexandra. E. Porter and Professor Milo. S. P. Shaffer

Date of submission: 24/05/2022

Abstract

2-Dimensional Nanomaterials (2DNMs) have recently gained much momentum in research and industry. Graphene Family Nanomaterials (GFNs) and Transitional Metal Dichalcogenides (TMDs) are two classes of 2DNMs of particular interest due to their potentially wide application such as electronics, sensors, and even biomedical applications. Of the two classes of 2DNMs, graphene oxide (GO) and molybdenum disulfide (MoS_2) were selected as materials of interest due to their volume of research interest and production capacity. Although some environmental assessment has been carried out for GO, the literature has mainly focused on the toxicity and biological mechanisms of model pathogenic bacteria and not soil bacteria. Reports have highlighted that the physiochemical property of lateral size of 2DNMs may impact the inhibitory effect and the mechanism of interaction based on computational and *in-vitro* experiments with GO and pathogenic bacteria. However, findings are not yet conclusive and have not been explored widely beyond the antibacterial application of GO and have not been studied in the context of environmental conditions such as using model environmental media and environmentally relevant bacteria. For MoS_2, reports on their toxicity and interaction with bacteria are even scarcer which emphasises the need to assess their toxicity. A series of toxicity tests modified from a standard ISO protocol (10712) was used, for the first time, to study the effect GO and MoS_2 on the viability of soil bacteria. *Arthrobacter globiformis* and *Pseudomonas putida*, gram-positive and gram-negative bacteria respectively, were exposed to GO under different exposure conditions (chapter 2.4), to different lateral sizes of GO (chapter 3), and to pristine and aged/oxidised MoS_2 (chapter 4) under ISO protocol testing conditions for water/soil contamination. The 2DNMS were extensively characterised using techniques, such as Raman Spectroscopy and X-ray photoelectron spectroscopy (XPS) for chemical properties, and Atomic Force Microscopy (AFM) and Dynamic Light Scattering (DLS) for size and colloidal properties, to understand how the physiochemical

properties related to toxicity. The literature review highlighted that one of the major inconsistencies in reports was a lack of materials' characterisation and understanding of these bacteria-materials' interactions in different experimental conditions. The bioassays revealed that the choice of media and ageing of the material greatly affected the interaction of 2DNMs with bacteria and also the ability of the bacteria to respond to 2DNMs. Pristine MoS_2 showed the greatest inhibitory effects on the soil bacteria which decayed as the nanomaterial oxidised. XPS results showed conversion of Mo (IV) species as MoS_2 to Mo (VI) as soluble molybdate ions. For GO 2DNMs, various media conditions of nutrient-rich media (Luria Bertani Broth), model environmental media (ISO 10712 test media), and minimal salt media (Milli-Q water) showed that different exposure conditions affected their colloidal stability and inhibitory effects. DLS and zeta potential measurements showed increasing stability in the order of Luria-Bertani (LB) broth< ISO 10712< Milli-Q water with increasing agglomerate size of GO in the order of LB broth> ISO 10172> Milli-Q water. The toxicity assay showed that different media varied the GO's inhibitory effect and growth enhancement depending on the media composition which was attributed to the level of salts and organic substrates. TEM images revealed a "gap" between the GO and the bacteria under media conditions with nutrients. It was hypothesised that soil bacteria could display a protective mechanism under nutrient-rich conditions in which they could defend themselves against GO. Comparison between all critical determinants of toxicity showed that they can be ranked using their effect on inhibition as follows: level of salt, organic substrate, and other substances in the media > ageing of 2DNMs >> species of bacteria > lateral size. The thesis uncouples which system parameters influence outcomes of toxicity assays surveying the interaction between 2DNMS and bacteria and provide guidance for future more standardised toxicity testing of this class of nanomaterial.

Acknowledgements

I would like to first of all thank my supervisors, Alex, and Milo, who have provided excellent support throughout my journey during my PhD. They have aspired me to conduct thorough research with their attitude and commitment to scientific excellence. It was truly an honour to have been guided by both of them and I have cherished all of the advice they have given me. I do hope that I was able to reciprocate their dedication through hard work and respect.

I would also like to show appreciation to the respective research groups of which I was part of: Porter's group and NanoHAC group with Milo. All members and also ex-members have been very inclusive and created a cohesive environment in which I enjoyed every moment to be part of.

I also would like to mention the cohort of CDT-ACM and the staff, especially Hafiza. The cohort members have been great to hang out with and I appreciated the diversity of project which we could all take interest in. Many thanks to Hafiza for all of the administrative work she had done for me especially through some difficult time with the pandemic.

I also cannot go without mentioning all the people from the squash community within and outside of Imperial. IC squash club Men's 1st Team, "The Curry Club", "The Squad", Bath Cup teams, they have all been a great team and we had been through some memorable victories.

Last but not least, I would like to thank my parents, my girlfriend, Jess, whom I met during my PhD journey, and Pugsy, the most wonderful companion to a journey anyone can ask for. This PhD is dedicated to my mother whose dream was to obtain a PhD, Jess who has supported me throughout the journey, and Pugsy who has shown resilience and brought me happiness during the toughest of times.

Statement of Originality

With this statement I hereby declare that the submitted PhD thesis is solely of my own work unless otherwise mentioned and acknowledged through references.

Copyright Declaration

The copyright of this thesis rests with the author. Unless otherwise indicated, its contents are licensed under a Creative Commons Attribution-Non Commercial 4.0 International Licence (CC BY-NC). Under this licence, you may copy and redistribute the material in any medium or format. You may also create and distribute modified versions of the work. This is on the condition that: you credit the author and do not use it, or any derivative works, for a commercial purpose. When reusing or sharing this work, ensure you make the licence terms clear to others by naming the licence and linking to the licence text. Where a work has been adapted, you should indicate that the work has been changed and describe those changes. Please seek permission from the copyright holder for uses of this work that are not included in this licence or permitted under UK Copyright Law

List of Abbreviations

Abbreviation	Definition
1DNM	1-Dimensional Nanomaterial
2D	2-Dimensional
2DNM	2-Dimensional Nanomaterial
AAS	Atomic Absorption Spectrometry
AFM	Atomic Force Microscopy
AR	As-Received
CEH	Centre for Ecology and Hydrology
CFU	Colony Forming Unit
CNT	Carbon Nanotube
CVD	Chemical Vapour Deposition
DCFDA	2, 7 dichlorofluorescein diacetate
DCFH-DA	2,7-dichlorofluorescin diacetate
DNA	Deoxyribose Nucleic Acid
ENM	Engineered Nanomaterial
FA	Fulvic acid
FTIR	Fourier-Transform Infrared Spectroscopy
GaAs	Galium Arsenide
GFN	Graphene Family Nanomaterial
GO	Graphene Oxide

GSH	glutathione
LDH	Lactate Dehydrogenase
LPS	Lipopolysaccharides
MoS2	Molybdenum Disulphide
MRSA	Methicillin-resistant Staphylococcus aureus
MTT	Methylthiazolyldiphenyl-tetrazolium bromide
NBT	Nitro blue tetrazolium
NOM	Natural Organic Matter
OD	Optical Density
PBS	Phosphate Buffer Solution
PCR	Polymerase Chain Reaction
PDI	Polydispersity Index
PES	Photoelectron Spectroscopy
RBC	Red Blood Cells
ROS	Reactive Oxygen Species
RTP	Room Temperature and Pressure
SD	Standard deviation
SEM	Scanning Electron Microscopy
Si	Silicon
SPM	Scanning Probe Microscopy
STEM	Scanning Transmission Electron Microscopy
TEM	Transmission Electron Microscopy
TMD	Transitional Metal Dichalcogenide

tpa	Tonne per Annum
TSB	Tryptic Soy Broth
TSBY	Tryptic Soy Broth with Yeast
UHV	Ultra High Vacuum
WST-8	water-soluble tetrazolium salt
WWTP	Wastewater Treatment Plan
XPS	X-ray Photoelectron Spectroscopy
XTT	2,3-bis-(2-methoxy-4-nitro-5-sulfophenyl)-2H-tetrazolium-5-carboxanilide

List of Figures

Figure 1. 2. 1 Schematic diagram of the structure of the thesis 40

Figure 1.3.1.1 The number of publications of research literature in Web of Science with the specified words of common 2DNMs shown in each key. Web of science data taken on February 2022. 45

Figure 1.3.2.1 Global mass flow of 10 ENMs during full cycle analysis with the assumption of high production and release estimates as of 2010. Taken from ref (*21*).....46

Figure 1.3.2.2 Predicted mass flow of CNTs as of 2010 in tonnes per annum assuming maximum production and release. Taken from ref (*22*) 48

Figure 1.4.1.1 A depiction of a typical AFM set-up.....51

Figure 1.4.4.1 Iterative XPS measurements of GO from ACS material taken at the C1s peak (278-298 eV) over 130 measurements on the same spot.....59

Figure 2.1.1.1 The principal synthesis routes used to produce graphene 67

Figure 2.1.1.2 Schematic of typical synthesis, Modified Hummer's method, to produce GO.....68

Figure 2.1.1.3 Typical reduction of GO to produce rGO. 70

Figure 2.1.2.1 Schematic representation of the differences in the structure of the cell wall between gram-negative and gram-positive bacteria.....82

Figure 2.1.2.2 Proposed physical mechanism of interaction between a bacteria membrane and GO sheets. GO is represented by graphene here without the oxygen functional group for simplicity. The

phospholipid bilayer consists of hydrophilic head and hydrophilic tail. 4 mechanisms are proposed: a.) A slicing mechanism, in which GO acts as a "nano-knife" that spears through the membrane. b.) An extraction mechanism where hydrophobic tails travel up through the surface of GO and the integrity of the membrane is not retained. c.) A wrapping mechanism where the GO does not enter the phospholipid bilayer, but instead wraps around the bacteria. d.) An embedding mechanism where the GO embeds itself in the membrane.86

Figure 2.2.2.1 Optical image of monolayer ARGO dispersion in Milli-Q water. Concentrations from left to right: 1000 mg L^{-1}, 100 mg L^{-1}, 10 mg L^{-1}, 1 mg L^{-1}. 108

Figure 2.2.2.2 Size measurement obtained by AFM a.) Showing the representative image of as-received GO (ARGO) dispersion in water that has been drop cast on to a freshly cleaved mica sheet at 1 mg L^{-1} b.) Showing the distribution plot of the lateral diameter (measured using the Feret diameter) with a sample size of N = 161 and bin size of 20 (Mean = 0.96 μm, S.D. = 0.80 μm).....109

Figure 2.2.2.3 Further example of AFM images obtained.....110

Figure 2.2.2.4 TEM image of ARGO dispersion in water on a lacey carbon copper grid a.) Bright Field low magnification image of monolayer GO dispersion from ACS material b.) Bright Field high magnification image with Cs aberration correction of a GO monolayer with a visible i.) Graphitic region, ii.) Functionalised/defect region, and iii.) holes as pointed by each arrows associated. 111

Figure 2.2.2.5 Representative Raman spectra of one of multiple measurements. The peak around 1300 cm^{-1} represents the D peak and the peak around 1600 cm^{-1} represents the G peak.....112

Figure 2.2.2.6 D/G ratio distribution plot of as-received GO (ARGO) from ACS material deposited on silica wafer (5 mg mL-1). Mean = 0.74, S.D. = 0.03, Sample size N = 1227. 113

Figure 2.2.2.7 XPS survey spectra of ACS material ARGO drop-casted on silica wafer with the main chemical transition peaks labelled. 114

Figure 2.2.2.8 High resolution XPS spectra of the C1s transition peak of ACS material ARGO sample on a silica wafer. The spectra had been deconvoluted and fitted to show the different chemical environments of C1s. ……..115

Figure 2.2.2.9 High resolution XPS spectra of the O1s transition peak of ACS material ARGO sample on a silica wafer. The spectra had been deconvoluted and fitted to show the different chemical environments of O1s. ……..……116

Figure 2.2.2.10 Zeta potential measurement of as-received GO (ARGO) dispersion from ACS material in different pHs (50 mg L^{-1}). The pH was adjusted using 0.1M NaOH and HCl at 25 °C.....120

Figure 2.2.2.11 DLS hydrodynamic diameter plot by intensity of GO dispersion in Milli-Q water and ISO 10712 test media at 0 hour, 4 hours, and 24 hours. Each plot was average of three repeated measurements at concentration of 50 mg L^{-1}.....122

Figure 2.2.2.12 OD change of *A. globiformis* with increasing dose of ARGO dispersion in the concentration range between 0-200 mg L^{-1}. The OD change was calculated at T0h and T24h (same sample left for 24-hours' exposure) and each data point is an average of 5 independent samples. The error bars represent the standard error. 123

Figure 2.2.2.13 OD change of *P. putida* with increasing dose of ARGO from ACS material dispersion in the concentration range between 0-200 mg L^{-1}. The OD change was calculated from OD reading at T0h and T24h sample (same sample left for 24-hour exposure) and each data point is an average of 5 independent samples. The error bars represent standard error. 124

Figure 2.2.2.14 Optical images of bacteria with ARGO from ACS material with concentrations of 0, 10, 21.15, 44.72, 94.57, and 200 mg L^{-1} (from left to right) at 24-hours. e a.) *A. globiformis* and b.) *P. putida*. ……125

Figure 2.3.3.1 Proliferation of *A. globiformis* after exposure to ARGO from ACS material based on OD changes. The toxicity test results of all ISO 10712 runs against *A. globiformis*. This proliferation plot was based on the OD change data with 5 replicates for each of the data points with each error bar representing the standard error. Each of the samples were run independently from the other. Each shade of colour represents the location and the time frame in which the experiment was carried out. The shade of pink represents experiments carried out at Location 1 in 2019. The shade of green represented experiments carried out at Location 2 in 2020. The shade of blue represented experiments carried out at Location 3 in 2021 and 2022. ……..131

Figure 2.3.3.2 Proliferation of *P. putida* with ARGO from ACS material based on OD changes. Toxicity test results of all ISO 10712 runs against *P. putida*. This proliferation plot was based on the OD change data with 5 replicates for each of the data points with each error bar representing standard error. Each of the samples were run independently. Each shade of colour represents the location and the time frame in experiment was carried out. Pink shades represent experiments carried out at Location 1 in 2019. Green shades represent experiments carried out at Location 2 in 2020. Blue shades represented experiments carried out at Location 3 in 2021 and 2022. 132

Figure 2.3.3.3 Proliferation plot of *A. globiformis* with ARGO from ACS material based on CFU results. Toxicity test results of all ISO 10712 runs against *A. globiformis*. This proliferation plot was based on the CFU data with 5 replicates for each of the data points with each error bar representing the standard error. Each of the samples were run independently from the other. Each shade of colour represents the

location and the time frame in which the experiment was carried out. Pink shades represent experiments carried out at Location 1 in 2019. Green shades represent experiments carried out at Location 2 in 2020. Blue shades represent experiments carried out at Location 3 in 2021 and 2022.....133

Figure 2.3.3.4 Proliferation of *P. putida* with ARGO from ACS material based on CFU results. Toxicity test results of all ISO 10712 runs against *P. putida*. This proliferation plot was based on the CFU data with 5 replicates for each of the data points with each error bar representing standard error. Each of the samples were run independently from the other. Each shade of colour represents the location and the time frame in which the experiment was carried out. Pink shades represent experiments carried out at Location 1 in 2019. Green shades represent experiments carried out at Location 2 in 2020. Blue shades represent experiments carried out at Location 3 in 2021 and 2022. 134

Figure 2.3.3.5 OD change of pristine ARGO from ACS material of concentration range between 0-200 mg L^{-1} in ISO 10712 test media. The OD change was calculated from OD reading at T0h and T24h sample (same sample left for 24-hour exposure) and each data point are average of 3 independent samples. Each line represents the OD change under abiotic condition result that were carried out at the same time as the results shown in figure 2.3.3.1, 2.3.3.2 and 2.3.3.6. The error bars represent the standard error. 139

Figure 2.3.3.6 The raw data of the result shown in figure 2.3.3.1 and 2.3.3.2. Each plot represents the OD change of ARGO from ACS material of concentration range between 0-200 mg L^{-1} in ISO 10712 test media against *A. globiformis* and *P. putida*. The OD change was calculated from OD reading at T0h and T24h sample (same sample left for 24-hour exposure) and each data point are average of 3 independent samples. The error bars represent the standard error. 140

Figure 2.4.3.1 Schematic diagram depicting the experimental procedure for the toxicity test with three different end-point assays: OD change results, 24h CFU results, and 3h CFU results. 149

Figure 2.4.3.2 Proliferation of a.) *A. globiformis* exposed to GO in three different media: water, ISO 10712 test media, and LB broth based on OD change results b.) *A. globiformis* exposed to GO in three different media: water, ISO 10712 test media, and LB broth based on 24h CFU results c.) *P. putida* exposed to GO in three different media: water, ISO 10712 test media, and LB broth based on OD change results d.) *P. putida* exposed to GO in three different media: water, ISO 10712 test media, and LB broth based on 24h CFU results. Each data point was an average of 5 measurements with error bars representing the standard errors (S.E.)…….....150

Figure 2.4.3.3 Proliferation of both *A. globiformis* and *P. putida* from the 3h CFU results after the pre-exposure step (3 hours of contact time in water without being re-introduced to the test media). Each data point is from 3 repeated measurements. 151

Figure 2.4.3.4 ARGO in suspension with bacteria in the three different exposure environments after the 24 hours of incubation. Suspension photo of GO with a.) *A. globiformis* in water (Left to Right: Water control, ISO 10712 test media control, 0 mg L^{-1} of GO with bacteria, 50 mg L^{-1} of GO with bacteria, 100 mg L^{-1} of GO with bacteria, 150 mg L^{-1} of GO with bacteria, 200 mg L^{-1} of GO with bacteria), b.) *P. putida* in water (Left to Right: Water control, ISO 10712 test media control, 0 mg L^{-1} of GO with bacteria, 50 mg L^{-1}, 100 mg $L^{-1,}$ 150 mg L^{-1} and 200 mg L^{-1} of GO with bacteria), c.) Exposure in ISO 10712 test media with (Left to Right: 0 mg L^{-1} , 50 mg L^{-1}, 100 mg L^{-1}, 150 mg L^{-1}, 200 mg L^{-1} of GO with *A. globiformis*, 0 mg L^{-1}, 50 mg L^{-1}, 100 mg L^{-1}, 150 mg L^{-1} and 200 mg L^{-1} of GO with *P. putida),* d.) Exposure in an LB broth with (Left to Right: 0 mg L^{-1}, 50 mg L^{-1}, 100 mg L^{-1}, 150 mg L^{-1} and 200 mg L^{-1} of GO with *A. globiformis*, 0 mg L^{-1}, 50 mg L^{-1} , 100 mg L^{-1} of GO, 150 mg L^{-1} and, 200 mg L^{-1} of GO with *P. putida)*…….....153

Figure 2.4.3.5 Optical microscope image of both bacteria with 50 mg L^{-1} of GO after 3 hours. a.) GO with *A. globiformis* in water, b.) GO with *A. globiformis* in ISO 10712 test media, c.) GO with *A. globiformis* in LB broth, d.) GO with *P. putida* in water, e.) GO with *P. putida* in ISO 10712 test media, f.) GO with *P. putida* in LB broth. Arrows indicate the following: Green arrows indicate bacteria on their own, brown arrows indicate aggregated GO with bacteria, black arrows indicate aggregated GO on its own. 154

Figure 2.4.3.6 TEM images the different interactions of bacteria with GO from ACS material in Milli-Q water, ISO 10712 test media, and LB broth. Images for LB broth samples could not be obtained due to the stronger interaction displayed by the GO-bacteria mixture, which did not allow the infiltration of fixative and resin. The red arrow shows the GO penetration mechanism. The black arrow shows a direct contact of GO onto the bacteria. The yellow double headed arrow shows a gap between the bacteria and the GO (~200 nm). The white arrow shows the GO.....157

Figure 2.4.3.7 Lower magnification TEM images the different interactions of bacteria with GO from ACS material in Milli-Q water, ISO 10712 test media, and LB broth. Images for LB broth samples could not be obtained due to the stronger interaction displayed by the GO-bacteria mixture, which did not allow the infiltration of fixative and resin. The red arrow shows the GO penetration mechanism. The black arrow shows a direct contact of GO onto the bacteria. The yellow double headed arrow shows a gap between the bacteria and the GO (~200 nm). The white arrow shows the GO. 158

Figure 2.4.4.1 Illustration of GO interactions with soil bacteria with GO dispersed in Milli-Q water, ISO 10712 test media, and LB broth. 161

Figure 3.5.1.1 Plot of sonication time versus lateral size of the GO flakes given by lateral area measured using AFM of the results but also compared to two other data sets from the literature. (*113, 120*) 180

Figure 3.5.2.1 AFM image of SGO drop-casted on to freshly cleaved mica sheet at 1 mg L^{-1}. 182

Figure 3.5.2.2 Distribution plot of lateral diameter of SGO (measured using Feret diameter) with sample size N = 495 with bin size of 14 (mean = 0.28, S.D. = 0.14). 183

Figure 3.5.2.3 D/G ratio distribution plot of SGO deposited on silica wafer (5 mg mL^{-1}). Mean = 0.75, S.D. = 0.03, Sample size N = 318.....184

Figure 3.5.2.4 Comparative D/G ratios of LGO (As-Received GO) and SGO on the same graph. ...184

Figure 3.5.2.5 XPS survey spectra of SGO drop-cast onto a silica wafer with the main chemical transition peaks labelled. 185

Figure 3.5.2.6 High resolution XPS spectra of C1s transition peak of SGO on silica wafer. The spectra had been deconvoluted and fitted to show the different chemical environment of C1s. 186

Figure 3.5.2.7 High resolution XPS spectra of O1s transition peak of SGO on silica wafer. The spectra had been deconvoluted and fitted to show the different chemical environment of O1s.....187

Figure 3.5.2.7 DLS hydrodynamic diameter plot by intensity of SGO dispersion in Milli-Q water and ISO 10712 test media at different time points of 0 hour, 4 hours, and 24 hours. Each plot was average of three repeated measurements at concentration of 50 mg L^{-1}. 188

Figure 3.5.3.1 Proliferation plot of *A. globiformis* with SGO based on OD change results. Toxicity test results of all ISO 10712 runs against *A. globiformis*. This proliferation plot was based on the OD change data with 5 replicates for each of the data points with each error bar representing standard error. Each of the samples were run independently from the other. Each shade of colour represents the location and the time frame in which the experiment was carried out. Shade of pink represents experiments carried out at

Location 1 in 2019. Shade of green represents experiments carried out at Location 2 in 2020. Shade of blue represents experiments carried out at Location 3 in 2021 and 2022. 190

Figure 3.5.3.2 Proliferation plots of *P. putida* with SGO based on OD change results. Toxicity test results of all ISO 10712 runs against *P. putida*. This proliferation plot was based on the OD change data with 5 replicates for each of the data points with each error bar representing standard error. Each of the samples were run independently from the other. Each shade of colour represents the location and the time frame in which the experiment was carried out. Shade of pink represented experiments carried out at Location 1 in 2019. Shade of green represents experiments carried out at Location 2 in 2020. Shade of blue represents experiments carried out at Location 3 in 2021 and 2022. 191

Figure 3.5.3.3 Proliferation plot of *A. globiformis* with SGO based on CFU results. Toxicity test results of all ISO 10712 runs against *A. globiformis*. This proliferation plot was based on the CFU data with 5 replicates for each of the data points with each error bar representing standard error. Each of the samples were run independently from the other. Each shade of colour represents the location and the time frame in which the experiment was carried out. Shade of pink represents experiments carried out at Location 1 in 2019. Shade of green represents experiments carried out at Location 2 in 2020. Shade of blue represents experiments carried out at Location 3 in 2021 and 2022.....192

Figure 3.5.3.4 Proliferation plot of *P. putida* with SGO based on CFU results. Toxicity test results of all ISO 10712 runs against *P. putida*. This proliferation plot was based on the CFU data with 5 replicates for each of the data points with each error bar representing the standard error. Each of the samples were run independently from each other. Each shade of colour represents the location and the time frame in which the experiment was carried out. Shade of pink represented experiments carried out at Location 1 in 2019.

Shade of green represents experiments carried out at Location 2 in 2020. Shade of blue represents experiments carried out at Location 3 in 2021 and 2022.....193

Figure 3.5.3.5 OD change of pristine SGO of concentration range between 0-200 mg L^{-1} in ISO 10712 test media. The OD change was calculated from OD reading at T0h and T24h sample (same sample left for 24-hour exposure) and each data point are average of 3 independent samples. The error bar represents the standard error…… 194

Figure 3.5.4.1 Proliferation plot of bacteria from a.) OD change results of A. globiformis exposed to LGO and SGO in Milli-Q water b.) 24h CFU results of A. globiformis exposed to LGO and SGO in Milli-Q water c.) 3h CFU results of A. globiformis exposed to LGO and SGO in Milli-Q d.) OD change results of P. putida exposed to LGO and SGO in Milli-Q water e.) 24h CFU results of P. putida exposed to LGO and SGO in Milli-Q water f.) 3h CFU results of P. putida exposed to LGO and SGO in Milli-Q water. Each data was an average of 3 measurements with error bars representing the S.E.. ANOVA statistical results were also plotted with "ns" = not statistically significant and "**" = statistically significant ($p<0.01$)...196

Figure 3.5.5.1 TEM images showing the different interaction of *A. globiformis* and *P. putida* bacteria with LGO and SGO. Images taken were of the samples after the 3h at 150 mg/L of GOs. White arrows show LGOs. Green arrows show SGOs. Black arrows show direct contact of GO with bacteria membrane. Red arrows show perpendicular contact of GO with bacteria membrane. 200

Figure 3.5.5.2 Lower magnification TEM images showing the different interaction of *A. globiformis* and *P. putida* bacteria with LGO and SGO. Images taken were of the samples after the 3h at 150 mg/L of GOs. White arrows show LGOs. Green arrows show SGOs. Black arrows show direct contact of GO with the bacterial membrane. Red arrows show perpendicular contact of GO with the bacterial membrane...201

Figure 4.2.1.1 3D model of monolayer MoS_2. Mo in black and S in green. 209

Figure 4.5.1.1 DLS hydrodynamic diameter by intensity of MoS_2 dispersion in water at three different concentrations (10, 50 and 200 mgL^{-1}), together with a photo of as-received dispersion of MoS_2 in DI water. Each plot was an average of three repeated measurements. 236

Figure 4.5.1.2 AFM image of as-received MoS_2 from ACS material drop-casted on freshly cleaved mica with the height profile taken from the MoS_2 flakes to show the monolayer nature of the material for 6 different profiles across the MoS_2. 239

Figure 4.5.1.3 Lateral size distribution of monolayer MoS_2 flakes represented by Feret diameter measurements taken from 32 AFM images. (Mean = 2.00, S.D. = 0.72, N = 32) 240

Figure 4.5.1.4 XPS survey spectra of as-received exfoliated MoS_2 drop-cast on silica wafer with the main transition peaks labelled 241

Figure 4.5.1.5 High resolution XPS spectra of the Mo3d peak of as-received exfoliated MoS_2 sample on silica wafer. The spectra have been deconvoluted and fitted to show the different chemical environment of Mo3d, as well as S2s where the B.E. overlap.. 242

Figure 4.5.1.6 DLS hydrodynamic diameter by intensity of MoS_2 dispersion in ISO 10712 test media at two different concentrations (50 and 200 mgL^{-1}). Each plot was an average of three repeated measurements. 245

Figure 4.5.2.1 Toxicity test result in ISO 10712 of a.) OD change of *A. globiformis* with increasing dose of as-received exfoliated MoS_2 dispersion in the concentration range between 0-200 mg L^{-1} b.) CFU of *A. globiformis* with increasing dose of as-received exfoliated MoS_2 dispersion in the concentration range between 0-200 mg L^{-1} c.) OD change of *P. putida* with as-received exfoliated MoS_2 dispersion of

concentration range between 0-200 mg L^{-1} d.) CFU of *P. putida* with increasing dose of as-received exfoliated MoS_2 dispersion in the concentration range between 0-200 mg L^{-1}. The OD change was calculated from OD reading at T0h and T24h sample with the same sample left for 24 hour exposure. Each data point is an average of 5 independent samples. CFU was calculated from the plate reading method and each data point are average of 5 independent samples. The error bars represent the standard error. The annotations indicate the following for p-value of comparison of means: ns = $p>0.05$, * = $p<0.05$, ** = $p<0.01$ as shown in table 4.4.2.3. 248

Figure 4.5.2.2 OD change of as-received exfoliated MoS_2 dispersion of concentration range between 0-200 mg L^{-1} in ISO 10712 test media. The OD change was calculated from OD reading at T0h and T24h sample (same sample left for 24-hours' exposure) and each data point are average of 3 independent samples. The error bars represent the standard error. 249

Figure 4.5.2.3 Optical images of soil bacteria with MoS_2 dispersion after 24-hour exposure taken directly in the 96 well plate used to measure the OD changes. a.) *A. globiformis* with 50 mg L^{-1} of MoS_2. b.) *A. globiformis* with 200 mg L^{-1} of MoS_2. c.) *P. putida* with 50 mg L^{-1} of MoS_2. d.) *P. putida* with 200 mg L^{-1} of MoS_2. Green arrows indicate bacteria. Black arrows indicate MoS_2 agglomeration. 252

Figure 4.5.3.1 Toxicity test results of all samples of MoS_2 (As-received, 1 month old, 2 months old, 3 months old, and 3 years old) against a.) *A. globiformis* based on OD change results b.) *A. globiformis* based on CFU results c.) *P. putida* based on OD change results d.) *P. putida* based on CFU results. All proliferation plot was based on 5 replicates for each of the data points with each error bar representing the standard error. Each of the samples were run independently from the other. 254

Figure 4.5.3.2 High resolution XPS of As-received, 3 months old, and 3 years old MoS_2 on silica wafer. a.) High resolution XPS spectra of Mo3d peak with deconvolutions as well as S2s peak of pristine

MoS_2. Inset image shows the pristine MoS_2 dispersion in water at 1 mg mL^{-1} b.) High resolution XPS spectra of S2p peak with deconvolutions of pristine MoS_2 c.) High resolution XPS spectra of Mo3d peak with deconvolutions as well as S2s peak of 3 months old MoS_2. Inset image shows the 3 months old MoS_2 dispersion in water 1 mg mL^{-1} d.) High resolution XPS spectra of S2p peak with deconvolutions of 3 months old MoS_2 e.) High resolution XPS spectra of Mo3d peak with deconvolutions as well as S2s peak of 3 years old MoS_2. Inset image shows the 3 years old MoS_2 dispersion in water 1 mg mL^{-1} f.) High resolution XPS spectra of S2p peak with deconvolutions of 3 years old MoS_2 258

Figure 5. 1 Proliferation plot of 2DNMs (pristine and aged MoS_2 and GO of different lateral size) against a.) *A. globiformis* given by the OD change results; b.) *A. globiformis* given by 24h CFU results; c.) *P. putida* given by the OD change results; d.) *P. putida* given by 24h CFU results, under different media conditions (Milli-Q water, ISO 10712, and LB broth).....269

Figure 6. 1 Diagram showing the change in toxicity of GO over time. i.) with little to no salt content on the basal plane of GO, GO can actively extract salt content from the bacteria causing osmotic pressure and bactericidal effect on bacteria ii.) GO basal plane gradually saturated with salt and the extraction process and the toxicity decreasing iii.) Little to no extraction of salt due to GO basal plane being fully saturated and GO no longer has bactericidal effect. 275

List of Tables

Table 1.3.1.1 Global Graphene Family Nanomaterials production capacity by companies. Total of 141 Companies which are listed on graphene-info.com (accessed throughout November 2017) were investigated for any production claims. 44

Table 1.3.2.1 Summary of the estimated magnitudes of CNTs released to different environmental compartments, from ref (*23*). 49

Table 1.4.1.1 Table showing the three types of AFM imaging mode and what they can measure. 52

Table 1.4.1.2 Summary of advantages and limitations of AFM, in comparison to other imaging techniques…… 53

Table 2.1.2.1 Summary of literature results on the interactions between gram-negative and gram-positive bacteria and GO. 83

Table 2.2.1.1 Composition for Solution I-IV used to make the pre-culture and test media used in ISO 10712…….. 101

Table 2.2.1.2 Composition for pre-culture media and test media used in ISO 10712 102

Table 2.2.1.3 Statistical denotation used in the toxicity test results in OD and CFU. 103

Table 2.2.2.1 Characterisation of ARGO, Single Layer Graphene Oxide Dispersions, in DI Water, 5 mg mL^{-1} using the Modified Hummer's Method, GNODAW01 as specified the manufacturer. 106

Table 2.2.2.2 Elements detected in the survey XPS spectra of GO from ACS material on silica wafer……. 116

Table 2.2.2.3 The Peak B.E. of different deconvoluted chemical environments of GO from ACS material on a silica wafer together with the relative amount of each transition from the high-resolution C1s XPS spectra……. 117

Table 2.2.2.4 The Peak B.E. of different deconvoluted chemical environments of GO from ACS material on a silica wafer together with the relative amount of each transition from the high-resolution O1s XPS spectra……. 117

Table 2.2.2.5 DLS measurement of Z-average (hydrodynamic diameter), Polydispersity Index (PDI) and Zeta potential measurement of ARGO dispersion in Milli-Q water and ISO 10712 test media (pH 7) at 50 mg L^{-1}.There were 3 independent measurements with each measurement consisting of +10 measurements. The values presented are average values ±the standard deviation. 118

Table 2.2.2.6 pH of GO dispersion (5000 mg L^{-1}) diluted in Milli-Q water and ISO 10712 test media at the concentrations tested in the toxicity test in chapter 2.2.2. pH was measured in triplicate ±S.D. 119

Table 2.2.2.7 DLS results of hydrodynamic diameter (Z-average) and PDI as well as Zeta potential measurement of ARGO dispersion in Milli-Q water and ISO 10712 test media (50 mg L^{-1}) at 0h, 4h, and 24h time points. 121

Table 2.3.3.1 A colour table of proliferation values with respect to each experimental runs of ISO 10712 carried out with a range of concentrations of ARGO from the ACS material from OD change results. Each value was associated with the ANOVA test results to determine the difference in their mean values at 95%

confidence level ($p<0.05$) as well as 99% confidence level ($p<0.01$). The colours on the proliferation values represent the range of values of proliferation, as well as the description status. 135

Table 2.3.3.2 A colour table of proliferation values with respect to each experimental runs of ISO 10712 carried out with a range of concentrations of ARGO from the ACS material from CFU results. Each value was associated with the ANOVA test results to determine the difference in their mean values at 95% confidence level ($p<0.05$) as well as 99% confidence level ($p<0.01$). The colours on the proliferation values represent the range of values of proliferation, as well as the description status. 136

Table 2.3.4.1 The composition of typical PBS. 142

Table 2.4.3.1 pH of GO in water, ISO 10712, and LB broth with different concentrations of GO including without GO. 3 repeated measurements ± S.D. 155

Table 2.4.3.2 DLS and zeta potential results of GO in water, ISO 10712, and LB broth. All measurements shown are an average of 3 measurements ± S.D. 155

Table 2.4.4.1 Composition of ISO 10712 and LB broth. 160

Table 2.4.4.2 Composition of the Simulated Urban Wastewater (SUW) and the Simulated Industrial Wastewater (SIW) used by Combarros *et al*. (*143*) 162

Table 3.5.2.1 Mean and S.D. of both LGO and SGO from AFM measurements taken from figure 2.2.2.2 and 3.5.2.2 183

Table 3.5.2.2 C/O ratio and O/C ratio calculated from survey and C1s spectra of XPS obtained from SGO in comparison to LGO (As-Received GO). 187

Table 3.5.2.3 DLS hydrodynamic diameter given by Z-average and PDI as well as Zeta potential measurements of SGO dispersion in Milli-Q water and ISO 10712 test media (50 mg L^{-1}) at 0h, 4h, and 24h……. 189

Table 3.5.4.1 EC50 calculated from each condition. Logistic regression function was used to best fit the plot using Origin 2022. 197

Table 3.5.4.2 Z-test statistical test result showing the statistical significance of differences between each of the EC50 values. Red indicates no statistical significance where p>0.1. Green indicates statistical significance where p<0.01 The left bottom hand side of the table are results from OD change and 24h CFU result. The right top hand side of the table are results from 3h CFU result.....197

Table 3.5.4.3 Statistical test (Z-test) of comparison of EC50 values between the results with the different end point assay. 3hCFU results are from direct exposure in Milli-Q water whereas 24hCFU and OD change results are from Milli-Q water exposure followed by media exposure (figure 2.4.3.1) 198

Table 4.4.2.1 Composition of Solution I-IV 229

Table 4.4.2.2 Composition of the pre-culture media and test media. 230

Table 4.4.2.3 Statistical denotation used in the toxicity test results in OD and CFU. 232

Table 4.5.1.1 Material properties specified by the manufacturer 235

Table 4.5.1.2 Z-average, Polydispersity Index (PDI), and Zeta-potential measurement of MoS_2 dispersion in water at three different concentrations. The values for all measurements were average of three measurements with the information taken from intensity reading. 237

Table 4.5.1.3 The Peak B.E. of different deconvoluted chemical environments of Mo in Mo3d transition together with the S2s peak positions showing S environments. 244

Table 4.5.1.4 Z-average, Polydispersity Index (PDI), and Zeta-potential measurement of MoS_2 dispersion in ISO 10712 test media (pH 7.01) at two different concentrations between time points of 0 hour and 24 hours. The samples were incubated at 25 °C under shaking in the dark to replicate exposure conditions in the toxicity tests. The values for all measurements are an average of three measurements……. 246

Table 4.5.3.1 EC50 values from individual logistic regression fit of all samples of MoS_2 (As-received exfoliated, 1 month, 2 months, 3 months, and 3 years old). Both OD and CFU results were used to deduce the EC50 for each toxicity assessment technique. *Note the 2 months old MoS_2 with *P. putida* result from CFU method did not yield a good fit. 256

Table 4.5.3.2 % of each main chemical species deduced from the area under the graph of deconvoluted high resolution XPS spectra of Mo3d and S2s peaks. The environments and the amount were deduced using protocols described in Zhang *et al*. (*36*). Sulfide and oxysulfide were from the S2s peak while the Mo (IV), Mo (V), Mo (VI) were from the Mo3d peak. 259

Table 4.5.3.3 % of each main chemical species deduced from the area under the graph of the deconvoluted high resolution XPS spectra of S2s peaks. The species and the amount was deduced using protocols described by Zhang *et al*. (*36*). 259

Table 4.5.3.4 % of each phase calculated from Mo3d peak based on Domi *et al*. (*27*) and the ratio of 2H/1T phase present. 259

Table 4.5.3.5 pH of MoS_2 dispersion in water at 1 mg L^{-1}. Each result consist of at least 3 repeated measurements at 25 °C. 262

Table 4.5.3.6 Concentration of Mo ions present in each of the MoS_2 dispersion leachate from as-received, 3 months aged, and 3 years aged. For conversion to mM, 1 ppm of Mo roughly eauls to 0.01 mM of Mo. All measurements were at least 5 replicates with average and the S.D. shown. 262

Table of Contents

Abstract 2

Acknowledgements 5

Statement of Originality 6

Copyright Declaration 7

List of Abbreviations 8

List of Figures 11

List of Tables 24

1 Preface 39

1.1 Introduction: Potential hazards of 2-Dimensional nanomaterials (2DNMs) to the environment 39

1.2 Outline of thesis structure 40

1.3 Identification of 2DNMs of interest and its potential release point 41

1.3.1 Identification of 2DNMS with most threat to the environment 41

1.3.2 Potential routes of release of 2DNMs to the environment 45

1.4 Characterisation techniques used 50

1.4.1 AFM – Atomic Force Microscopy 51

1.4.2 DLS – Dynamic Light Scattering 54

1.4.3 Zeta potential 56
1.4.4 XPS – X-ray Photoelectron Spectroscopy 57
1.4.5 Raman Spectroscopy 59
1.4.6 TEM – Transmission Electron Microscopy 61
1.5 Bacteria of interest – Arthrobacter globiformis and Pseudomonas putida 64
2 Environmental impact of Graphene Oxides 66
2.1 Literature Review of GFNs and GOs toxicity 66
2.1.1 Graphene Family Nanomaterials (GFNs) 66
2.1.2 Biological interaction of GOs 71
2.1.3 Summary 98
2.2 Initial ISO 10712 toxicity test 100
2.2.1 Methods and Materials – GO (GO dispersion in water, ACS material, US) 100
2.2.2 Results 106
2.2.3 Discussion 126
2.3 Repeats of ISO 10712 with modifications 128
2.3.1 Introduction 128
2.3.2 Methods 128

2.3.3 Results....129
2.3.4 Discussion....140
2.3.5 Conclusions....145
2.4 Toxicity testing and imaging with different media and Milli-Q water....145
2.4.1 Introduction....145
2.4.2 Materials and Methods....146
2.4.3 Results....148
2.4.4 Discussion....159
2.4.5 Conclusions....165
3 Effect of lateral size of GOs on toxicity....166
3.1 Introduction....166
3.2 Literature review on the biological interactions of GO with varied lateral diameters....167
3.2.1 Lateral size dependency of GO towards model pathogenic mammalian cells....167
3.2.2 Lateral size dependency of GO towards model pathogenic bacteria....169
3.3 Preparation of different lateral sized GO....176
3.4 Method and Materials....178
3.4.1 Preparation of SGO....178

3.4.2 Characterisation of SGO 179
3.4.3 Toxicity test for SGO 179
3.4.4 Statistical test 179
3.4.5 TEM image 180
3.5 Results 180
3.5.1 AFM result of probe sonication 180
3.5.2 Characterisation of SGO (120 minutes sonicated GO) 181
3.5.3 Toxicity tests using ISO 10712 189
3.5.4 Toxicity testing – Pre-exposure with Milli-Q water 195
3.5.5 TEM 200
3.6 Discussion 202
3.7 Conclusion 206
4 Environmental toxicity of next emerging 2DNMs: MoS_2 208
4.1 Introduction to TMDs and MoS2 208
4.2 Literature Review of MoS_2 and its biological interaction 208
4.2.1 MoS_2 structure 208
4.2.2 MoS_2 synthesis and associated phases 209

4.2.3 MoS_2 applications 211

4.2.4 Applications of MoS_2 in the environment 212

4.2.5 Environmental Fate of MoS_2 212

4.2.6 MoS_2 in a biological context 214

4.2.7 Impacts of MoS_2 on bacteria in the environment 222

4.2.8 The ageing/oxidation process of MoS_2 223

4.3 Aims 226

4.4 Methods and Materials – MoS_2 228

4.4.1 Materials 228

4.4.2 Methods 229

4.5 Results 234

4.5.1 Material characterisation of AR exfoliated MoS_2 234

4.5.2 As-received exfoliated MoS_2 toxicity test results against soil bacteria 247

4.5.3 Effect of ageing/oxidation on MoS_2 253

4.6 Discussion 262

4.7 Conclusions 266

5 Comparison between GO work and MoS_2 268

6 Overall Conclusions & Future Outlook 272

References 279

7 Appendix 294

Appendix I: Raw data for repeated ARGO (LGO) measurements (Chapter 2.2) 294

Appendix II: Results from silver nitrate (positive control) (Chapter 2.2) 298

Appendix III: Other nanoparticles with ISO 10712 (Chapter 2.2) 302

Appendix IV: ISO 10712 with different GO (Graphenea) (Chapter 2.2) 315

Appendix V: ANOVA statistic results of the effect of different media & abiotic conditions on OD changes (Chapter 2.3) 321

Appendix VI: Complementary results to the MoS_2 toxicity data (Chapter 4) 325

Appendix VII: Ageing of GO (Chapter 5) 326

585

590

595

600

605 “Attitude is everything”

1 Preface

1.1 Introduction: Potential hazards of 2-Dimensional nanomaterials (2DNMs) to the environment

2-Dimensional Nanomaterials (2DNMs), such as graphene family nanomaterials (GFNs) and transition metal dichalcogenides (TMDs), have attracted a lot of attention, due to their wide spectrum of applications, ranging from electronic devices to sensors. (*1-3*) These 2DNMs have a high aspect ratio and form sheet-like structures. Their thickness tends to range from sub-nm to a couple of nm, depending on the chemical structure, but their lateral dimensions can range from few nm to few μm. The sheet-like layers are stacked together by Van der Waals forces to form layered materials and although debated, researchers usually refer to 2DNMs as materials that are not only monolayers, but also bilayers and few-layered materials, ranging between 3-10 layers. (*4*) In recent times, researchers have been developing production methods to potentially produce large volumes of 2DNMs for commercial use, such as Chemical Vapour Deposition (CVD) (*5, 6*), epitaxial growth (*7, 8*), and liquid phase exfoliation (*9, 10*), to meet the increasing number of applications of 2DNMs. However, there is still a lack of understanding about the risks and the safety of 2DNMs in the environment as well as the framework to assess their risks to the environment. With the development in application and mass scale production of 2DNMs, release of 2DNMs into the environment is set to increase in the future.

1.2 Outline of thesis structure

The structure of thesis is split into 2 main bodies with smaller subsections after the initial introduction and identification of 2DNMs of interest. One part focuses on the toxicity of Graphene Oxides (GOs) and the other focuses on the toxicity of Molybdenum disulphides (MoS_2). In each main area of focus, a current landscape of the research field is discussed to present the aims and hypothesis of each sub sections, and then the experimental methods as well as results and discussions are presented. Conclusions are made for each subsection which is eventually brought together to make a final overall conclusion and some recommendations for future work and environmental safety advice on the 2DNMs. Figure 1.2.1 below shows a schematic diagram of the flow of the thesis.

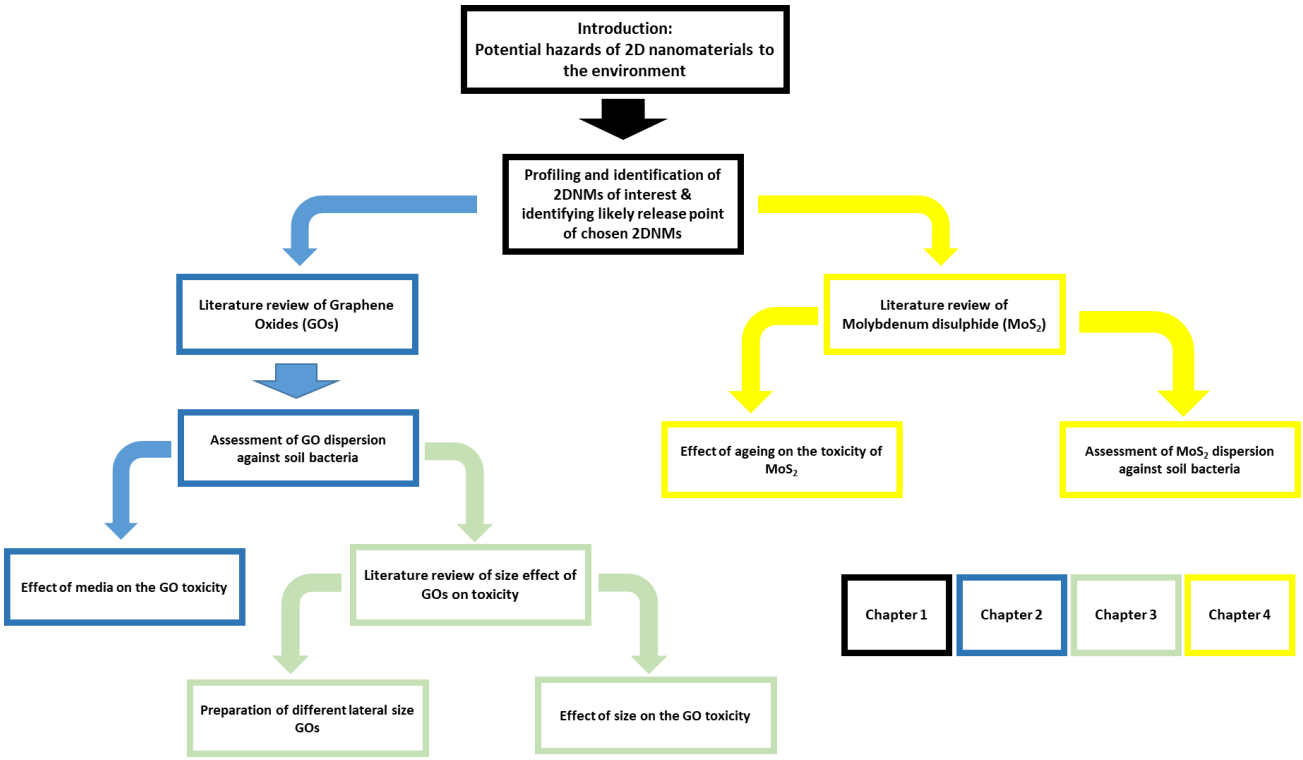


Figure 1. 2. 1 Schematic diagram of the structure of the thesis

1.3 Identification of 2DNMs of interest and its potential release point

1.3.1 Identification of 2DNMS with most threat to the environment

In order to assess the potential hazard of 2DNMs to the environment, firstly, a survey was conducted to evaluate which 2DNMs are more likely to be released to the environment. This was achieved by understanding the scale of 2DNMs being produced currently, and by assessing the research demand for each group of 2DNMs.

Figure 1.3.1.1 shows the number of publications with types of 2DNMs as the topic of the paper (Web of science, accessed in February 2022). Graphene is the most heavily researched within 2DNMs, indicating that Graphene Family Nanomaterials (GFNs) are the leading class of 2DNMs, followed by MoS_2 of the Transitional Metal Dichalcogenides (TMDs). Comprehensive reviews on the study of the environmental impacts of 2DNMs and their potential hazards to living organisms are available.(*11, 12*) Both sets of literature covers a wide area of environmental impacts and discussion about which emerging materials might affect humans and/or environment. Both sets of literature cover 2DNMs including GFNs and TMDs, as these were identified as the two leading classes of 2DNMs. Although there is a lack of data on this topic, even for GFNs, it is highlighted that risk assessment of 2DNMs is complex due to the diversity of physiochemical properties across the 2DNMs. Even though there has been increasing awareness and research into 2DNMs, there were still gaps and inconsistency in the literature. Ultimately, the environmental and safety assessments of GFNs is in its infancy, so further research is required.

To understand the scale of 2DNMs produced, the landscape of current 2DNMs manufacturing methods needs to be appreciated. The findings of the initial study summarised that there are already tonnes of 2DNMs produced world-wide, with little thought given to their environmental hazards. GFNs are one of

the most intensively researched 2DNMs and therefore used to estimate the future production capacity of 2DNMs. It is likely that TMDs and other 2DNMs would follow the development in GFNs and the scale production would quickly increase, since 2DNMs synthesis routes usually involve similar methods. It was estimated that by 2013, the production capacity of graphene globally would exceed 500 tonnes per annum (tpa.). (*13*) Estimates made by existing graphene production and manufacturing companies, predicts that the total global production capacity of GFNs exceeds 10,000 t.pa (Table 1.3.1.1). However, these estimates are far from the actual production of GFNs, as some values given are the maximum production capacity and claims are made by companies with a vested interest to increase shareholders. The actual production is probably much lower. A Nature paper had claimed that in 2009, there was 15 tpa. of graphene produced that was estimated to increase to 200 tpa. within a few years. (*14*) Another estimate by a Nature paper claimed that the estimated production in 2015 was 120 tpa., which was to increase to 1,200 tpa. in 2019. (*15*) 2DNMs, a company that produces graphene, claimed that in 2017 annual production was 370 tpa. (accessed on November 2017). Considering these values, the production of GFNs was between 300-500 tpa as of 2017, with a likely increase in the next 10 years. This value was close to a reported production amount of Carbon Nanotubes (CNT) for 2008. (*16, 17*) Considering CNTs were discovered approximately 10 years before the discovery of graphene, it is reasonable to believe that there are more than hundreds of tonnes of GFNs, produced globally. (*18-20*)

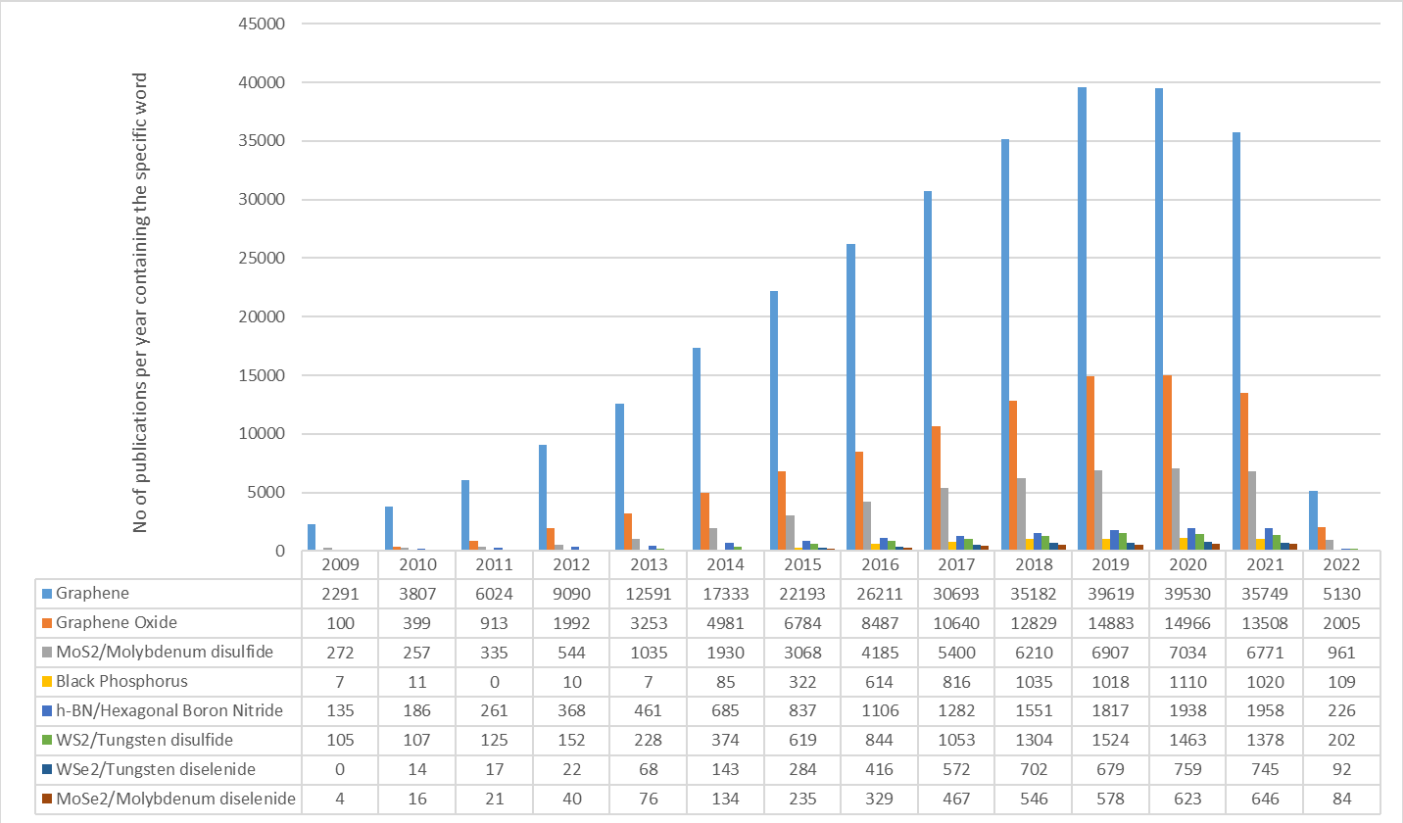
In the next section, the predicted pathway in which GFNs and TMDs are likely to be released to the environment is discussed using an environmental release model for nanomaterials in general, because there are no 2DNMs specific publication available. Particular focus is given to carbon nanotubes (CNTs) since they are very closely related to GFNs. For TMDs, it is assumed that the pathways would be similar to GFNs. The data shown in Table 1.3.1.1 and Figure 1.3.1.1 on the mass scale production of GFNs, and the research demand of 2DNMs, is original and provides important insight into how quickly the 2DNMs market

is growing. GFNs is chosen as the main focus in this project with MoS_2 as the sub-focus because the former is the most intensively researched 2DNMs; the latter the second most researched. TMDs, and MoS_2 are discussed more in depth in later chapter as ideas from GFNs could be applicable to MoS_2 as well. (Table 1.3.1.1 and Figure 1.3.1.1).

685

Company	Capacity for GFN (powder or dispersion)/tpa	Capacity for GFN film/m^2pa
CealTech		3650000.00
Graphenea	1.00	
NanoXplore	70.00	
Graphenemex	1.00	
2D Tech	0.04	
2D Carbon Tech		73000000
Abalonyx	8.00	
Angstron Materials	300.00	
AzTrong	100.00	
Beijing Carbon Century Technology	2.50	
Cambridge Nanosytems	5.00	
Chongqing Moxi		1000000
Deyang Carbonene	300.00	
Directa Plus	30.00	
Fanglin Minerals	200.00	
Felda Global Ventures	9.00	
Garmor	100.00	
Knano	250.00	
LeaderNano (Jiling)	2.00	
Nanesa	3.00	
Ningbo Morsh Technology	300.00	
Perpetuus Carbon	27.00	
Qingdao Haoxin New Energy Technology	500.00	
Standard Graphene	5.50	
Talga Resources	7000.00	
The Sixth Element	1000.00	
Thomas Swan	10.00	
United Nanotech Innovations	360.00	
VNGraphene	3.50	
Vorbeck	40.00	
Wuxi Graphene Films		80000.00
XFNano	50.00	
XG Sciences	80.00	
Total	**10757.54**	**3730000.00**

Table 1.3.1.1 Global Graphene Family Nanomaterials production capacity by companies. Total of 141 Companies which are listed on graphene-info.com (accessed throughout November 2017) were investigated for any production claims.



	2009	2010	2011	2012	2013	2014	2015	2016	2017	2018	2019	2020	2021	2022
Graphene	2291	3807	6024	9090	12591	17333	22193	26211	30693	35182	39619	39530	35749	5130
Graphene Oxide	100	399	913	1992	3253	4981	6784	8487	10640	12829	14883	14966	13508	2005
MoS2/Molybdenum disulfide	272	257	335	544	1035	1930	3068	4185	5400	6210	6907	7034	6771	961
Black Phosphorus	7	11	0	10	7	85	322	614	816	1035	1018	1110	1020	109
h-BN/Hexagonal Boron Nitride	135	186	261	368	461	685	837	1106	1282	1551	1817	1938	1958	226
WS2/Tungsten disulfide	105	107	125	152	228	374	619	844	1053	1304	1524	1463	1378	202
WSe2/Tungsten diselenide	0	14	17	22	68	143	284	416	572	702	679	759	745	92
MoSe2/Molybdenum diselenide	4	16	21	40	76	134	235	329	467	546	578	623	646	84

690 Figure 1.3.1.1 The number of publications of research literature in Web of Science with the specified words of common 2DNMs shown in each key. Web of science data taken on February 2022.

1.3.2 Potential routes of release of 2DNMs to the environment

Applications of GFN are numerous due to the high tunability of the material after synthesis or chemical modification and after production, depending on the desired applications as it will be highlighted in chapter 695 2. This means that there are number of different types of GFNs released to the environment when it comes to commercialising GFN-containing products and upscaling of production. GFNs could be released during production, use, and disposal, and consideration of where the largest potential hazard could lie is important for its risk assessment. Moreover, the exposure route to the environment needs to be considered to

understand the impact of GFNs on different environments including soil, landfill, water, and air. There are no definitive predictions of the release of 2DNMs to the environment. Life cycle assessments of emerging 2DNMs also need further research, in conjunction with the study of how 2DNMs interact with different environmental systems. (*12*)

Keller *et al*. (*21, 22*) predicted the exposure route and the relative mass flow of 10 Engineered Nanomaterials (ENMs), which had a production volume of greater than 100 tonnes per annum at the time of the study. The predicted global mass flow during the full life cycle of 10 ENMs is shown in Figure 1.3.2.1. (*21*) A large part of the ENMs ended up in the landfill, but also significant amount of ENMs, including CNTs, were released into soil and water. Moreover, there was a large amount of discharge from the Wastewater Treatment Plant (WWTP) that was predicted to end up in soil and water.

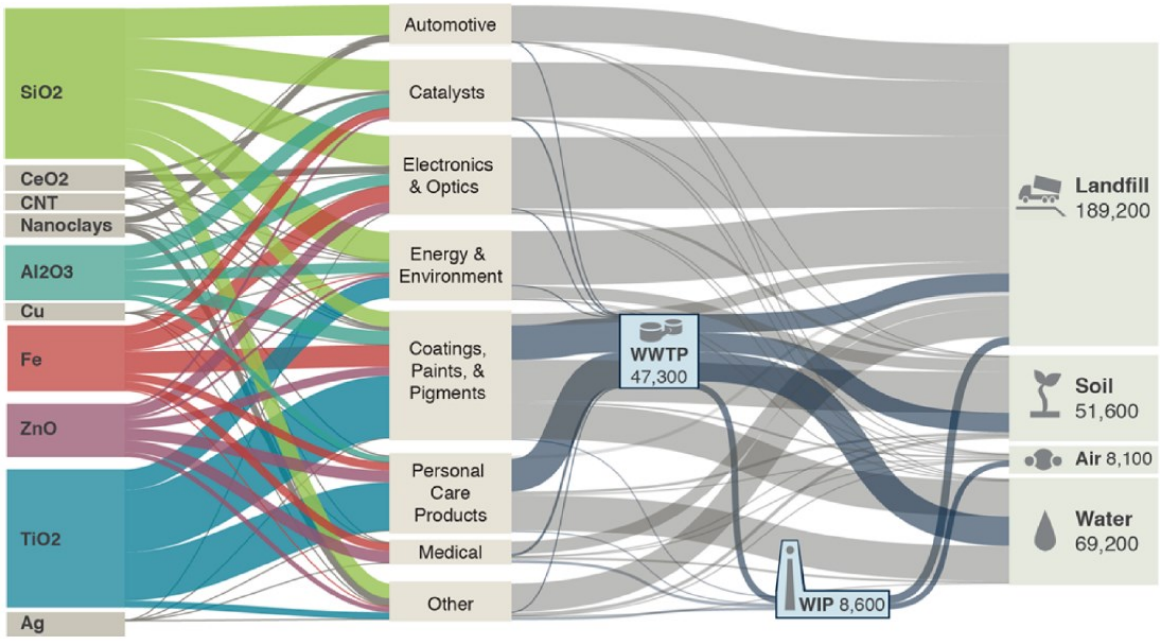


Figure 1.3.2.1 Global mass flow of 10 ENMs during full cycle analysis with the assumption of high production and release estimates as of 2010. Taken from ref (*21*).

Global mass flow of CNTs alone had also been numerically predicted (Figure 1.3.2.2.). (*22*) The production volume of CNTs was estimated to be around 3200 tonnes per annum in 2010 under the assumption of maximum production. (*22*) In reality, the production volume was less, as this was the upper bound estimate for the release model and acknowledged by the authors. Out of the 7 applications listed for CNTs, coatings, paints, and pigments contributed largely to the source of CNTs released into the soil *via* a WWTP or directly. Also, CNTs from composites, energy and environment, electronics and optics devices, and in coatings, paints, and pigments directly ended up in soil, where soil dwelling bacteria plants or other larger organisms could be affected. Only a small fraction was released to the water and air eventually meaning that release into the ocean or persistence in the atmosphere was the least amount predicted. It should be noted that this model did not consider chemical transformations that might occur or the environmental compartment which the CNTs could travel through during release. For example, industrial discharge could travel to the soil system *via* ground or surface water in which only a small fraction stays in the water due to prior environmental transformations. This should not be taken as the accurate prediction of the amount of 2DNMs, especially for GFNs, however, it did serve as an indicator of which environmental system the GFNs are most likely to interact with.

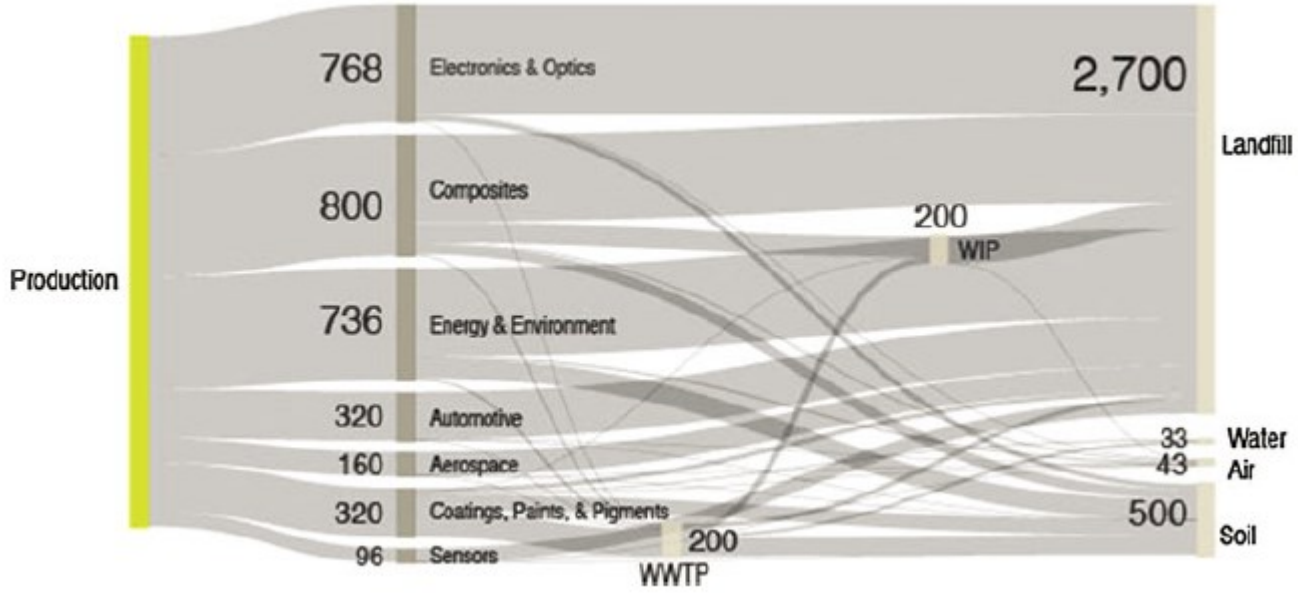


Figure 1.3.2.2 Predicted mass flow of CNTs as of 2010 in tonnes per annum assuming maximum production and release. Taken from ref (*22*)

Another important aspect to consider in the assessment of environmental impact of a material is the estimated concentration of materials released into the different environmental compartments. This was estimated by Gottschalk and Nowack *et al*. in a review which compiled all of the ENMs review paper on the modelling of release thus far. (*23*) The predicted environmental concentration for CNTs only, were extracted and summarised in table 1.3.2.1 below - note that this model did not account for any variance in physiochemical properties, nor did it account for any transformation which may occur during the release. The authors also acknowledged that the largest uncertainty factor lied in the production estimation of the ENMs including types of release such as emission and consumption. To improve the modelling work and the validation of the future prediction work for ENMs release, advancement in analytical techniques for characterisation of environmental samples and modelling for direct comparison of estimated and measured samples are required.

Environmental Compartment	CNT concentration
Surface water	~10^{-4} μg L^{-1}
WWTP effluent water	~10^{-2} μg L^{-1}
Biosolids (Solid waste from WWTP)	~10^{-1} μg g^{-1}
Sediments (In natural water)	~10^{1} μg kg^{-1}
Soils	~10^{-2} μg kg^{-1}
Soils with biosolids	~10^{0} μg kg^{-1}

Table 1.3.2.1 Summary of the estimated magnitudes of CNTs released to different environmental compartments, from ref (*23*).

The values in table 1.3.2.1 are based on production volumes of between 150 tonnes per annum to 500 tonnes per annum, which was close to the value of GFNs production volumes between 2009 to 2015 (*13-15*) and give a good indication of concentration of GFNs that could enter the environment. The current values of GFNs in the environment could be even more and are likely to increase as more GFNs are produced. For other 2DNMs including TMDs, it was very likely that the trend would follow GFNs. TMDs have unique applications separate to GFNs, so even though the current level of release may be low, it is only matter of time before increased production will follow. In fact, many of synthesis method for 2DNMs are shared and therefore, existing companies which specialise in GFNs production are likely to offer other 2DNMs.

Predictions of the global mass flow of GFNs in environmental samples have not yet been modelled, but the CNT studies discussed earlier indicated the following: a.) GFNs are the leading 2DNMs in terms of production and research demand and therefore pose the highest potential risk to the environment of all 2DNMs. b.) MoS_2 pose the second highest risk after GFNs. c.) Of all the environmental compartments, GFNs are most likely to end up in soils, if landfills are considered as a separate entity.

The main types of GFNs are discussed in the next section in more detail. GOs were selected here for a number of reasons. GOs, are synthesised in mass using liquid phase exfoliation and due to their ease of processibility, as well as scalability, they are predicted to be the most abundant and most impactful to the

environment. (*24*) GOs are stable in water and other aqueous phases so it was very likely that they would be even more persistent in the environment in their 2DNMs form. GOs are used in the environmental applications and as antibacterials. Some environmental papers also considered that GOs are the most persistent in the environment. Therefore, the main focus of this project was to assess the environmental impact of 2DNMs, by understanding the interaction of GOs with soil bacteria. This would offer the first point of understanding of their possible impact on the soil compartment as well as developing exiting testing protocols for testing 2DNMs. The testing protocols was then applied to study MoS_2. It is very hard to draw conclusions about whether or not 2DNMs impact the health of bacterial as researchers do not adhere to the same protocols used for testing (i.e. the age of the 2DNMs, cell culture media used, irradiance conditions, pH, sonication prior to testing etc.). The methodological aims of the thesis were to: 1.) Assess the suitability of the ISO 10712 testing protocol, to assess the water quality in soil against soil bacteria with GOs; 2.) To refine the ISO 10712 protocol; 3.) To assess the potential impact of GOs on the soil bacteria; 4.) Using the optimal protocol to assess the impact of MoS_2 on soil bacteria. 5.) Relate the characterisation results with the toxicity test result to understand the possible interaction of 2DNMs with bacteria.

1.4 Characterisation techniques used

In this section, the main characterisation techniques used in this thesis are discussed. The techniques and the theory behind the technique are introduced. Use of these techniques to characterise 2DNMs specifically and the challenges of characterising this class of materials were discussed in more depth. Thorough characterisation of 2DNMs was crucial to begin expanding the volume of literature to draw conclusions about whether 2DNMs are of concern to the health of soil bacteria tested.

1.4.1 AFM – Atomic Force Microscopy

Atomic Force Microscopy (AFM) is a type of Scanning Probe Microscopy (SPM) in which a probe raster scans across a surface. For 2DNMs characterisation, AFM can provide both thickness and lateral size information. In AFM, the probe interacts with the surface in either contact, tapping or non-contact mode depending on the sample and the type of measurements being made. A typical set up of the AFM is shown below in figure 1.4.1.1. The tip or the cantilever scans the surface of the sample at a specified height. As the tip scans across the surface of the sample, any changes in the interaction forces between the tip and the sample are detected by the segmented photodetector from the movement of the laser deflecting off the back of the tip. The photodetector then feeds back the change to the piezo-coupled scanner and this is recorded to reflect the change in height for imaging.

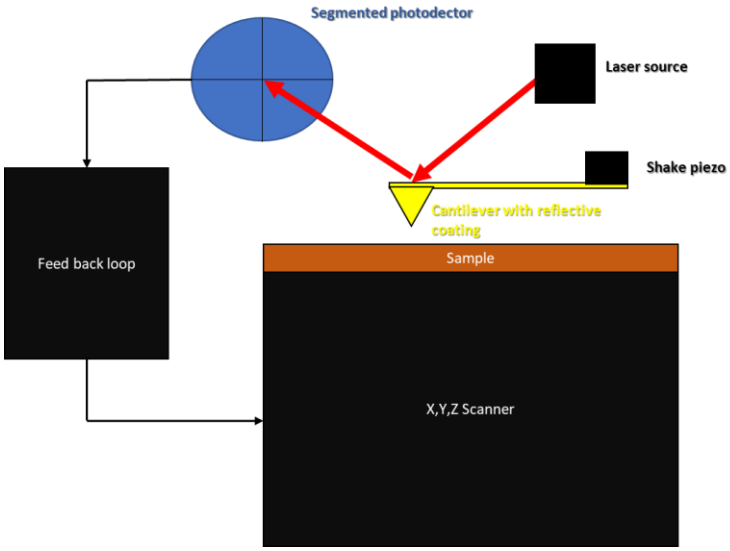


Figure 1.4.1.1 A depiction of a typical AFM set-up.

There are mainly three modes to AFM: contact, non-contact, and tapping mode. There are other modes which the AFM can be coupled with including conductive tips but for this project, these three types of

modes will be introduced with a focus on tapping mode. The differences in three modes of scanning are summarised below in table 1.4.1.1. As the name of each modes suggests, the modes describe the positional relationship between the tip and the sample surface. Depending on the position there are different forces that can influence the cantilever. For contact mode, a short repulsive force dominates the effect on the deflection change in the cantilever, whereas in the non-contact mode, long range forces affect the cantilever greatly. Tapping mode, in essence, captures the best features from both the contact and the non-contact mode and enables topographical imaging without damaging the samples. Therefore, this mode is often used in most imaging set ups.

AFM imaging modes		
Contact	**Non-contact**	**Tapping**
Measures a repulsive force	Measures the attractive force (long range forces, Van der Waals forces)	Intermediatory between contact and non-contact
Accurate topographical imaging	Requires a highly clean environment as it is very sensitive (can be carried out in UHV)	Measures short range forces (topographical images)
Can measure lateral forces	Suitable for fragile or soft samples	Tip oscillates above the sample 'tapping' the surface and the change in tip oscillation is detected
Tip/sample can be damaged quite easily	Tip oscillates above the sample and the change in tip oscillation is detected	Suitable for soft samples
Tip touches the sample and the bending/twisting is detected by the change in deflection		Good height resolution
		Ability to obtain additional information from phase imaging

Table 1.4.1.1 Table showing the three types of AFM imaging mode and what they can measure.

There are several advantages in using AFM over other techniques as well as limitations. These are summarised in the Table 1.4.1.2 below. One of the main advantages of AFM is the ability to obtain

topographical information. The accurate measurement of height is especially important when characterising 2DNMs, as this technique determines whether the sample is truly a monolayer or not. This is unique to characterisation of 2DNMs because for other nanomaterials such nanoparticles, imaging by SEM or TEM is usually enough to describe its dimensions.

Advantages and Limitations of AFM technique	
Advantages	**Limitations**
No diffraction limit	Resolution limited by the quality and the size of the tip
Capable of atomic resolution	Easily affected by artefacts on samples and tips
Ambient conditions (air or liquid)	Slow acquisition rate
3 dimensional data with height	Scan area is often limited
Requires very little sample preparation and can be non-conductive	Sensitive to surrounding environment
Capability for surface analysis	
Can be modified with other surface analysis techniques	

Table 1.4.1.2 Summary of advantages and limitations of AFM, in comparison to other imaging techniques.

AFM is an important technique for characterisation of 2DNMs. However, it is not often reported in literature due to some of the limitations when imaging 2DNMs using AFM. One of the main challenges is the number of images needed to produce a representative sample size. Often when reporting size information about a material, a size distribution plot is used. (*25*) This is often time-intensive and involves taking multiple images, which is time consuming. There are high-speed AFMs which can overcome this limitation but these are not readily available. (*26*) Another limitation is in sample preparation because 2DNMs are often synthesised to overcome the inter-layer forces by exfoliation methods, when the

dispersion is high in concentration, or the layers come into close contact they can aggregate. (*27*) This aggregation can be avoided if the preparation method is optimised to avoid it.

1.4.2 DLS – Dynamic Light Scattering

Another common technique used in characterisation of nanoparticles and 2DNMs is Dynamic Light Scattering (DLS). For characterisation of 2DNMs, DLS provides size information and agglomeration state of the material in dispersion. In detail, DLS measures the speed of particle in suspension using light scattering and deduces the size of the particle based on the Brownian motion and the Stokes-Einstein equation. Different particles sizes in suspension scatter light differently according to the Mie theory, and the change in the light scattering pattern from the sample is monitored over a certain period to provide a correlation function for the sample. For larger particle sizes, the fluctuation in light intensity is slower and for small particle the fluctuation in light intensity is faster. Because this fluctuation in intensity is from Brownian motion of particles, then this can be related to the hydrodynamic diameter of a particle using the Stokes-Einstein equation. Brownian motion describes a particle's movement in a random manner and the velocity of this movement is labelled as a translational diffusion coefficient (D). This is related to the hydrodynamic diameter using the Stokes-Einstein equation where, in DLS, the hydrodynamic diameter is the size of the hard sphere that is diffusing at the same velocity as the particle being measured. Stokes-Einstein equation is shown below in equation 1 where hydrodynamic diameter (d_H) is related to diffusion coefficient (D) by temperature (T) and viscosity (η) with Boltzmann's constant (k).

$$d_H = \frac{kT}{3\pi\eta D}$$

Equation 1

Because the DLS uses the correlation function of the fluctuation of light intensity from the sample dispersion, the measurement not only gives the size information in Z-average diameter (Z_D) but also the polydispersity of the sample given as polydispersity index (PDI). It can also give size distribution information by intensity which is very useful for analysing polydisperse samples (the size distribution by intensity can often be converted to size distribution by number or volume with the relationship of $I \alpha d^6$ and $V \alpha d^3$ but these due to the nature of DLS measurements, intensity measurements are more useful in understanding the data for 2DNMs). The z-average diameter and PDI can provide useful information on the particle behaviour in a medium when coupled with AFM or other characterisation techniques. (*25, 28, 29*) It should be noted that the use of DLS is not common for 2DNMs, since the characterisation assumes that the particles are hard spheres. DLS correlates the fluctuation in intensity of scattered light over a time to a specific size hard sphere. Therefore, when reporting DLS size measurements for non-spherical particles, the measurement taken should be analysed with the consideration of the spherical estimation.

DLS is often used in protein or polypeptide characterisation, but the field is far more established than 2DNMs so the use of DLS for 2DNMs, especially to give hydrodynamic diameter information, is not accurate, and should be used in conjunction with AFM or other techniques, such as electron microscopy. There are developments in the use of DLS for 2DNMs as well as other high aspect ratio nanomaterials to provide accurate size information. However, they are in an early stage and commercialisation of these techniques is in its infancy. (*30, 31*) Nevertheless, the information provided by DLS such as the Z-average, PDI, and size distribution can be useful in providing the relative size information and particle behaviour such as agglomeration in a liquid phase. DLS is also useful for comparing the behaviour of nanomaterials in different media.(*28, 29*)

1.4.3 Zeta potential

Zeta-potential is a characterisation technique often used in conjunction with DLS. To measure the zeta potential of a particle suspension, electrophoresis is used by applying a field across the sample. When the field is applied, the movement of charged particle relative to the liquid is measured, known as the electrophoretic mobility of the particle, and this is correlated to the zeta potential which is indicative of the particle charge by the Henry equation shown below in equation 2. Henry equation relates the electrophoretic mobility (U_E) to zeta potential (z) by dielectric constant (ε), viscosity (η), and Henry's function (F(ka)).

$$U_E = \frac{2\varepsilon z F(ka)}{3\eta}$$ Equation 2

Henry's function in the Henry equation includes a measurement of electrical double layer thickness and the particle radius. Since the zeta potential of a particle relates to the Henry function, factors such as pH and the presence of cations and anions that affect the charges associated with the surface of the particle affects the seta potential values greatly. Therefore, zeta potential measurements can be used to compare the behaviour of particles in different suspension media, relative to each other, as well as giving the charge information of the particle. Zeta potential information is usually used to indicate the stability of a particle in a suspension. (*29*) When the zeta potential value is greater than ±30 mV, it usually means that the particle suspension is stable, and they do not flocculate. If the value is slightly less, but still greater than ±15 mV, then the particle can flocculate but still can form a dispersion. Zeta potential values below ±15 mV often result in rapid agglomeration of the particles. For values greater than ±30 mV, the greater the value, more stable the dispersion is.

For application of zeta potential measurements to characterise non-circular particles such as 2DNMs, the limitation is the same as DLS. Zeta potential values can give relative information about the stability, as well as charge of a material, but it does need to be coupled with other characterisation techniques or have a prior knowledge of the material being characterised. This gives understanding into the behaviour of the material or property change in different liquid media. Similar to DLS, zeta potential measurements can be used to characterise and compare the behaviour of the 2DNMs in different liquid media, relative to in a water dispersion. The zeta potential data can often give insight into the stability of the material in dispersion and explain the colloidal state.

1.4.4 XPS – X-ray Photoelectron Spectroscopy

X-ray photoelectron spectroscopy (XPS) or otherwise known as Photoelectron Spectroscopy (PES) is a spectroscopic technique that measures the photoemission energy from the material as a result of X-ray irradiation. The technique is surface sensitive and can be used to measure elemental composition as well as chemical and electronic states of the material which is important in characterising of 2DNMs since chemical properties can differ across the plane of 2DNMs. (*32*) For each material, the binding energy (B.E.) of an electron can be related to the kinetic energy of the emitted electron (K.E.) as a result of irradiation of photon with sufficient energy (hν) to the material. The B.E. of an electron can simply be worked using the Einstein relationship by subtracting the measured K.E. of the emitted electron from the initial energy of the irradiated photon (hν). The energy of the photon usually greater than 1200 eV and therefore can ionise electrons at the core level. This results in emission of the core electron that can be detected in the XPS. (Note that subsequently, there are several phenomena that occur such as relaxation of the electron to fill the hole in the core level which results in Auger emission and fluorescence which can also be indicative of the material chemical state). The B.E. of the electron is unique to not only different elements but elements in different

environment. Therefore, XPS is a very powerful tool as it can distinguish between materials with the same elemental composition, such as different graphene, and also provides quantitative elemental analysis The detail of the theory here is not mentioned but can be found in the referenced paper. (*32*)

Since XPS is a surface sensitive technique with a field depth of few nm, most research on 2D materials uses this technique for characterisation. (*33-35*) XPS can provide information about the degree of functionalisation or oxidation in graphene to distinguish between different synthesis methods which is an important characterisation step when building a library of materials to test the toxicity against and to understand how toxicity relates to their physiochemical properties. For MoS_2, the XPS measurements can distinguish between pristine and aged material by quantification of Mo (IV) and Mo (VI). (*36*)

As with any other characterisation technique there are few practical measures that should be considered when setting up the measurement. For XPS, because the X-ray source is high in energy, beam damage from prolonged irradiation of the material should be considered. The beam size is typically larger than any functional group so typically a single point collection is enough. However, as with any beam, the focal point of the beam is the most intense and therefore can damage the sample, so a scan across the whole 2DNMs' sample gives the best results: It avoids beam damage and also ensures that the physiochemical information from more of the samples are taken. An example of change in the sample can be seen below in figure 1.4.4.1 showing the result of an iteration experiment using the K-alpha+ XPS spectrometer equipped with a MXR3 Al Kα monochromate X-ray source (hν = 1486.6 eV). The sample is GO from ACS material inc. and this was part of the initial set up optimisation study carried out. As shown in the figure 1.4.4.1, the C peak in GO, which is used to deduce the C/O ration in the characterisation of GO, is affected by the beam over a number of measurements. Therefore, in all XPS data shown in this project, the mapping method was employed to minimise the effect of beam artefacts on the measurement.

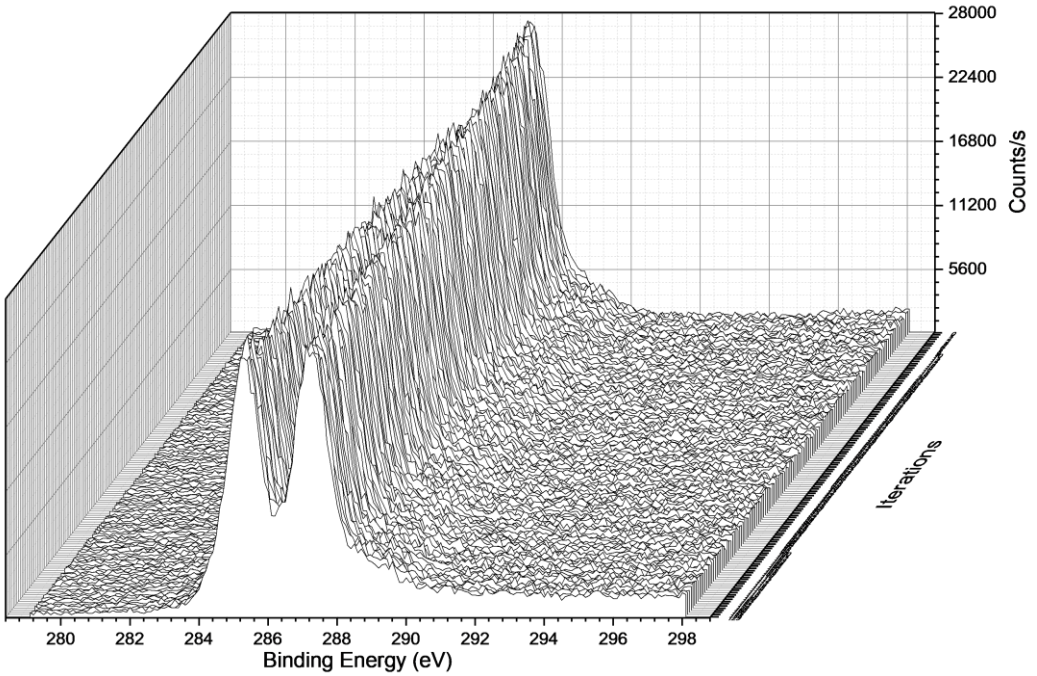


Figure 1.4.4.1 Iterative XPS measurements of GO from ACS material taken at the C1s peak (278-298 eV) over 130 measurements on the same spot.

1.4.5 Raman Spectroscopy

Raman spectroscopy is another spectroscopic technique produces a molecular fingerprint of the material. The energy of the incoming photon is lower than in the XPS (infrared) and this energy excites the material to a higher electronic state from its ground state. Usually, the excited state relaxes back into its ground state which releases the photons with the same energy. This is known as elastic scattering or Rayleigh scattering. However, in some cases at lower probability, Stokes scattering can occur. This is a process where the excited sate of the material loses less energy photon than the process of Rayleigh scattering and return to

its vibrational state, where there is a change in polarizability (ground state -> excited state -> vibrational state). If the incoming energy excites from the vibrational state, then to ground state then this is known as anti-Stokes scattering (vibrational state -> excited state -> ground state) where the released photon has more energy than the initial photon. There are other modes such as rotational and other lower frequency modes present which the transition can happen, but these transitions are unique to each material and produce a structural fingerprint of the material which can be useful when identifying the material.

Raman scattering is frequently used to characterise GFNs. (*37*) One of the main reported values from Raman measurement is the D/G ratio. This value is often quoted to describe the degree of functionalisation or degree of oxidation. (*33, 34*) The value is affected by the graphitic component, sp^2, and the amorphous component, sp^3, and therefore it is used to describe the quality of the graphene sheets and also the degree of functionalisation. The D mode results from the breathing mode of the hexagonal sp^3 network and the G mode is from the relative motion of the sp^2 carbon atoms. Therefore, the overtone bands of these D and G mode can also be useful when quantifying the number of layers in graphitic materials. For MoS_2, Raman spectroscopy has been used to characterise the material but because it is an indirect way to quantify how ageing alters the material, XPS was more widely used for this characterisation. (*27*)

In terms of its limitations, beam damage during acquisition should be considered. Also, the beam size is usually slightly smaller than XPS, between sub micro-metres, to a couple of micrometres, so for obtaining measurements from heterogenous materials like GFNs, mapping methods are used commonly to overcome these problems. (*28, 34, 35*) In fact, Raman results for GFNs often use the intensity of D and G band (~1350 cm^{-1} and ~1580 cm^{-1} respectively) in a ratio (D/G ratio) to represent the defect density of the graphene sheet. This could be as a result of addition of functional groups such as in the formation of GO. The D band refers to scattering from the local defects and the G band arises from the in-plane stretching of the graphitic

carbon. Therefore, using mapping method provides more representative D/G ratio of the entire GFN sheet rather than single point measurement.

1.4.6 TEM – Transmission Electron Microscopy

Transmission Electron Microscopy is one of the most powerful microscopy techniques. Often for nanomaterials, as well as giving size information TEM images can provide structural information about the nanomaterial. TEM uses electron beam which are generated from an electron source (typically tungsten filament or lanthanum hexaboride crystal) and accelerated at voltage between 100 – 400 kV by a series of electrostatic plates. Because electrons have a very small mass and have the wave-particle duality, the accelerated electrons achieve very small wavelength down to the size of picometers. This means that TEM have much higher spatial resolution than a conventional light microscope which the spatial resolution is limited by the wavelength of light in the visible spectrum.

After the electron beam is generated and accelerated through the electron gun, the beam is manipulated to focus, and defocus, and aligned via series of magnetic lenses called the condenser lens, and a doughnut-shaped metal called condenser apertures. The condenser lens are electromagnets and therefore have magnetic and electrostatic fields which can be varied in strength to focus and control the beam size and path. Condenser apertures physically block some of the beams such as poorly focused beam due to lens aberrations. The combinations of the two systems allow greater control of the beam size that is parallel and focused. Compared to a lens in a normal optical microscope, electromagnetic lens in the TEM can be varied extensively through manipulation of electrical current and therefore allows a greater range of control of the beam to focus and defocus onto the sample.

After the beam has passed through the condenser apertures, the beam hits the specimen on the specimen holder. The sample imaged under TEM is usually less than 100 nm in thickness to allow transmission of the electron through the sample. The sample is usually placed on a grid (made out of copper, gold, platinum etc.) which is mounted on the specimen holder to be inserted so that it is placed after the condenser lens and apertures. The electron beam directly hits the region of interest of the sample with the movement of the specimen holder stage. The beam interacts with the material in several ways such as elastic and inelastic scattering. This produces series of different energy electrons, as well as photons of various energy characteristic to the sample material which can be used to image and carry out chemical analysis of the sample. Depending on the position of detectors as well as beam position and subsequent lens and apertures positions (objective lens, objective aperture, intermediate lens), different imaging and chemical information is obtained.

In terms of imaging of the sample, those electrons that are interacting with the sample elastically can scatter to form contrast in two different ways: a.) diffraction b.) mass-thickness. Diffraction contrast mainly arise from Bragg scattering of a crystalline sample whereas mass-thickness contrast is from amorphous samples. Each scattering event produces electron that are diffracted in different angles from the original line of electron beam. This means that by controlling the apertures that are placed after the samples (objective apertures), different images with selected enhanced contrast can be imaged as well as diffraction patterns of interest.

As well as the apertures, there are a series of lenses after the sample (objective lenses, intermediate lenses, projector lenses). These lenses can focus, magnify, and align the beam so that diffracted electrons are projected onto the detector. The ratio of distance of the intermediate lenses determines the magnification and this results in TEM having magnification range of up to 1M x in some cases.

There are also stigmators which correct for the asymmetric distortions of the electron beam and hence in the image. There are also spherical and chromatic aberration corrected TEMs which produce even more aligned and focused beams resulting in high resolution images.

The entire TEM is operated is operated under Ultra High Vacuum (UHV) to minimise gas-collision of electrons. Poor isolation of chambers and poor vacuum can result in deposition of gaseous materials on the sample, as well as damage to the electron gun.

The set-up of a TEM outlined above allows high magnification images with high spatial resolution to be imaged. Due to the high energy electron beam, there are also other inelastically scattered electrons which hold chemical information. Therefore, the images can often be combined with spatially resolved chemical analysis techniques such as Electron Energy Loss Spectroscopy (EELS) and Energy Dispersive X-ray (EDX) analysis.

TEM is commonly used to image the material dimensions of 2DNMs. It is extremely useful for characterising the lattice structure and defects within these materials at high resolution, (*38, 39*) and complements information provided by other imaging techniques such as Scanning Electron Microscopy (SEM) or AFM. Another advantage of using TEM for studying 2DNMs is that it provides complementary nm-scale spatially resolved chemical analysis of the material. TEM combined with EELS can be used to study the functional groups that are generated during modification in GFNs or phase transitions in MoS_2 between 1T (metallic) and 2H (semiconducting) phases. (*34, 40*) Moreover, TEM can be used to image carbonaceous nanomaterials such CNTs in cells and provide information on the interaction and uptake of nanomaterials with cells. (*28, 41, 42*) Therefore, TEM imaging was used to image the 2DNMs studied in this project and to image biological interactions with bacteria to study processes such as cell-wrapping and membrane piercing by GO 2DNMs. It is only in the past decade that nanoparticle interaction with cells

have been reported as there were challenges uniquely associated with sample preparation containing nanoparticles. These include controlling centrifugation speed to minimise nanoparticles penetrating cell membranes to understanding the specific interaction of each nanoparticles with staining and fixing chemicals and artefacts, such as shearing the particles across cells in thin sections, caused by ultramicrotomy. (*43*)

1.5 Bacteria of interest – Arthrobacter globiformis and Pseudomonas putida

In terms of assessing the effect of 2DNMs in the environment, similar to any other toxicity test, first step in most biological exposures usually begins with testing against bacteria. Although uncommon, exposure of materials to environmental bacteria mainly uses soil bacteria and water-borne bacteria as these bacteria often plays an important role in the ecosystem in the environment. Most common materials that are tested are antibiotics which had been around for nearly hundred years but only recently been of concern to the environment due to potential increased pressure for increase in antibiotic resistant strains. (*44*)

One reliable method that has been used over the decade by researchers are ISO protocols (International Organisation for Standardisation). These protocols have been developed by number of technical experts in a committee who are representatives of national governing bodies worldwide. ISO 10712 is one of those protocols specifically been developed to assess the effect of surface, ground, and waste water against a common soil relevant bacteria, *Pseudomonas putida* (*P. putida*). (*45*) This protocol has been used before to assess nanoparticles which are colourless but never for 2DNMs. (*46, 47*) ISO 10712 has been modified previously for variation of environmentally relevant bacteria including *Arthrobacter globiformis* (*A. globiformis*). (*48, 49*)

Both bacteria are common in soil and important in agriculture. *A. globiformis* is known as a coryneform bacteria which is an irregular shaped bacteria usually in rod-shaped form. It is a gram-positive bacterium but can stain negative in gram-staining when young due to the thin peptidoglycan layers initially. (*50*) On the other hand, *P. putida* is a gram-negative bacterium with extra outer cell membrane. It is also shaped like a rod but is flagellated. Both bacteria have the ability to convert substances in soil such as pesticides and organic pollutants in the soil for bioremediation. (*51-53*) Therefore, both bacteria are important in the soil community of the environment and of interest when assessing the interaction of 2DNMs against environment.

2 Environmental impact of Graphene Oxides

2.1 Literature Review of GFNs and GOs toxicity

To understand the potential hazards of GFNs, an understanding of the types of GFN and the main synthesis method as well as applications and scalability is explored.

2.1.1 Graphene Family Nanomaterials (GFNs)

Graphene Family Nanomaterials (GFNs) refers to any 2D nanomaterial that contains the word "graphene" with layer number less than 10. Within this term, there are graphene, graphene oxide, and reduced graphene oxide which are the 3 main types in GFNs. As described by Bianco *et al*., a term such as "monolayer", "bilayer" or "multi-layer" can be used to describe the number of layers. The lateral dimension can also be included in the nomenclature of GFNs as "microsheet" or "nanosheet". However, this naming-method is not widely used, but is aimed to standardise the nomenclature of GFNs. The terminology for describing "graphene materials" has been inconsistent throughout the literature and industries. The use of accurate nomenclature provides a more accurate description of the physicochemical properties of GFNs, as well as accurate product labelling after manufacture. Henceforth, from here on, nomenclature system outlined by Bianco *et al.* is followed. (*54*)

Graphene

Graphene is a network of sp2 carbon forming series of hexagonal patterns that results in honeycomb-like sheet. Graphene is one atomic thick and it can be made by exfoliating from a graphite, which is a 3D structure formed by stacking multiple graphene that results in thickness greater than 100 nm. The

extraordinary material properties of graphene include its electron mobilities of up to $2.5x10^5$ $cm^2 V^{-1} s^{-1}$, a Young's modulus of 1TPa, a thermal conductivity of 3000 W mK^{-1}. (*55*) Furthermore, functionalisation of graphene can control its physical and chemical properties, for example by improving dispersion of the material in aqueous solution (*56*). A schematic diagram showing a typical synthesis method used to produce graphene is shown below in Figure 2.1.1.1

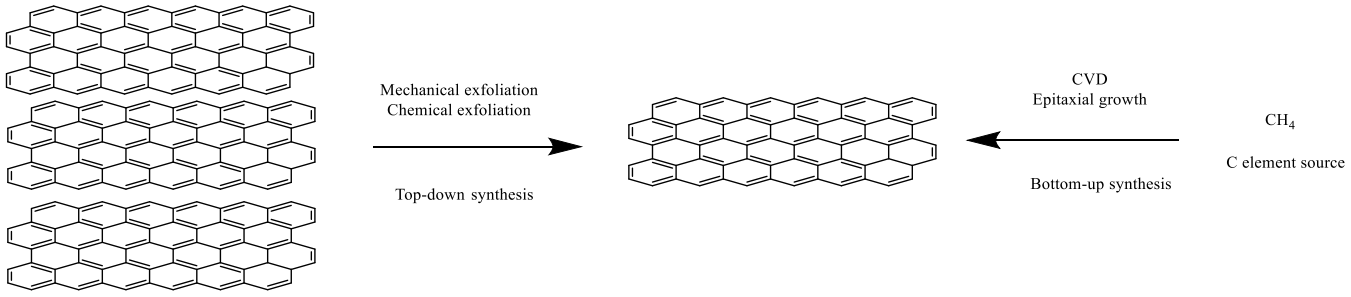


Figure 2.1.1.1 The principal synthesis routes used to produce graphene .

Chemical Vapour Deposition (CVD) and exfoliation methods are the two most focused on methods for synthesising graphene. (*15, 57*) CVD, as well other bottom-up synthesis methods, are mainly used to produce large area graphene films. CVD provides high quality graphene films with high conductivity on metal surfaces, which then needs to be transferred and cleaned for appropriate applications. Roll to roll large area CVD graphene films for touch panels are likely to be made this way in the future. (*6*) Exfoliation methods include mechanical (*18*) and chemical exfoliation. Mechanical exfoliation uses physical forces to peel-off layers of graphene from the bulk graphite, and the repeated process of this eventually ends with monolayer graphene. Liquid phase exfoliation can be done by applying shear or physical forces with or without using surfactants (*10, 58*), or by intercalating ions between layers to enhance exfoliation by weakening the interlayer bonds. (*59*) These methods tend to produce smaller diameter graphene as the lateral diameter size depends on the bulk graphite material, and these routes could be more scalable. Moreover, the quality of graphene used is subject to the application its used in. For example graphene for

batteries and supercapacitors functions better with defects and holes, whereas for electronics, the graphene needs to be defect-free. (*60*) Other applications that could in future exploit the versatility of graphene based materials include touch panels (*6*), sensors (*61*), coatings (*62*), and membranes (*63*).

Graphene Oxide

Graphene oxide (GO) is a functionalised graphene that can be produced by oxidation of graphite and exfoliation. (*64, 65*) GO has oxygen functionalities on the carbon network which breaks some of the sp2 carbon network. This means that GO is an insulator rather than a conductor. However, due to the oxygen functionalities, GO can be easily dispersed in water as a few-layer or monolayer GO, offering more potential for cheaper and easier production of graphene containing materials than using pristine graphene. GO can also be further functionalised for applications in sensors and catalysis (*24*), as well as inks and coatings (*66-68*). Figure 2.1.1.2 below shows typical methods to produce GO. (*65*) The modified Hummer's method is the widely used synthesis methods because of its scalability and the lack of safety issues. (*69*)

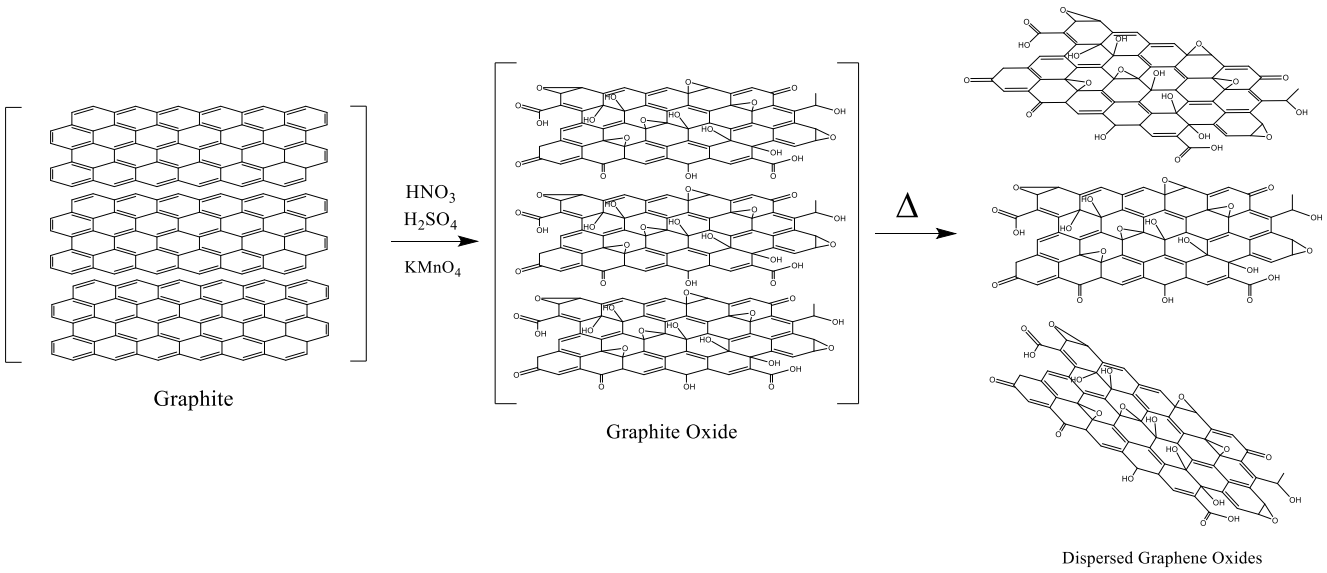


Figure 2.1.1.2 Schematic of typical synthesis, Modified Hummer's method, to produce GO.

The functional groups allow for easier dispersion in water and therefore easier exfoliation of graphite oxide (GO). GO is an important precursor to other GFNs because of the high processability. Moreover, suitable reduction of GO can restore some of sp2 network and offer pristine graphene-like properties again and this is the reason that GO has attracted a lot of attention recently as an important precursor to mass production of GFN. (*69*)

As well as being an important intermediate material for other GFN, GO also has variety of applications such as opto-electronics (*70*), supercapacitors (*71*), memory devices (*72*), composite materials (*73*), photocatalyst (*74*), and medical devices. (*75*) This is due to the unique property of GO that it has a mixture of sp^2 and sp^3 carbon. The oxidation process introduces functional groups, such as carboxyl, carbonyl, epoxy, and hydroxyl groups, and results in formation of islands of sp^2 carbon interrupted by functionalised sp^3 carbon. This results in quantum confinement of the electrons, due to the disrupted conjugated π-system which opens the band gap, broadening the applications of GO as quantum dots for nanophotonic devices. (*76*) As a consequence, there are increasingly a greater number of manufactures producing tonnes scale of GO as part of their products to sell GFNs, listed in Table 1.3.1.1. Note that there are more companies other than the manufactures listed in Table 1.3.1.1, but these were not all listed as a.) there were no estimated production data b.) there were over 140 companies as of 2017 which produced GFNs.

Tuning the degree of oxidation is vital for controlling the electrochemical properties of the GO and therefore developing GFN materials. Krishnamoorthy *et al.* explored the effect of different degrees of oxidation of GO using different amounts of $KMnO_4$ in the modified Hummer's method, to control the ratio of sp^3/sp^2. (*33*) 6g of $KMnO_4$, which was the greatest amount used in the experiment, produced few or monolayer GO with a 51.2 mV zeta potential and the lowest conductivity, indicating that controlling the conditions of

synthesis can greatly affect GO's properties. Like graphene, the properties of GO are greatly affected by the synthesis method, but also the parent graphite material. (*69*)

Reduced Graphene Oxide

Reduced Graphene Oxide (rGO) is as described above as graphene oxide (GO) but with some of the oxygen functional groups reduced to be removed from the GO (Figure 2.1.1.3.1). rGO is synthesised by reduction of GO using chemical (*77*), microwave (*78*), thermal (*79*), photochemical (*80*), and biological (*81*) methods. The reduction restores some sp^2 character which means that rGO is a conductor unlike GO. The conductivity achieved is not as high as pristine graphene due to the presence of defects from the reduction step and some residual functional groups left from GO. However, the conductivity of rGO is sufficiently high enough for some electrical applications, as well as batteries and supercapacitors. (*70, 82*). rGO is one of the GFN materials that shows promise for highly scalable production, but the problem currently lies in the lack of control of the quality of the rGO, as well as its lower conductivity and mechanical properties compared to pristine graphene. (*83*)

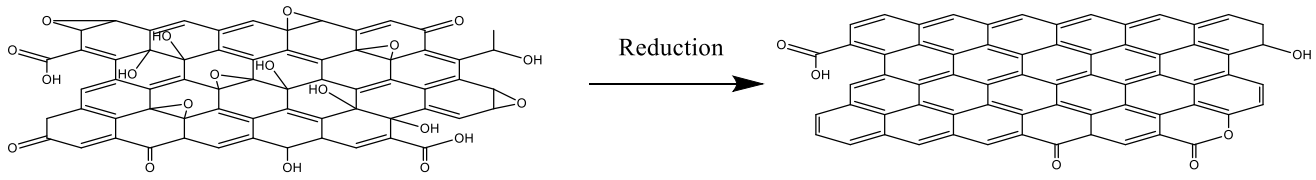


Figure 2.1.1.3 Typical reduction of GO to produce rGO.

.

Environmental application of GOs in the environment

Of all GFNs, GO has the most potential in environmental applications due to its hydrophilic nature. The oxygen functional groups allow GO to be processed easily and used in aqueous media. Due to the versatility of functional groups and defect sites as well as pockets of sp^2, GO has shown to be efficient at removing pollutants and other environmental contaminants in water treatment systems. (*84, 85*) A recent review by Zhao *et al*. (*86*) highlighted that GO is the most likely GFN to be released in aquatic environments and environmental fate as well as environmental interaction and impact have to be assessed.

2.1.2 Biological interaction of GOs

To understand the current knowledge gap in the interaction of GO with biological interaction, studies involving GO using both mammalian cells and bacteria cells have been reviewed, as the literature on interactions of GO with mammalian cells is much more extensive.

In vitro mammalian cells

This section summarises current findings of the interaction between human cells and GO dispersion from *in vitro* studies.

General toxicity

In a review carried out by Rhazouani *et al*. (*87*), the toxicity of GO towards different types of human cells was discussed. The main concern with regards to the current landscape of GO interaction with mammalian cells was that there was no consensus about the toxicity of GO. Ruiz *et al*. (*88*) showed that a GO film preferentially attached to and enhanced the proliferation of adenocarcinoma HT29 cells. This result

contrasted results of other literature, possibly explained by difference in toxic contaminants present in other studies. A further report by Chen *et al*. (*89*) indicated that a mice stem cells preferred to attach and grow on GO films over graphene films and promoted differentiation. The author indicated that functional groups were responsible for the increased adhesion and proliferation, but the mechanism of growth promotion was not established. One possible reason for the different biological responses could be due the different cell types used. Another reason could be the type of exposure environment, where both papers showed cell proliferation on GO membranes on glass slide rather than in suspension.

Numerous studies have demonstrated that GO displays different toxicity to different human cell types. For the studies that did show that GO is toxic to human cells, different levels of toxicity were demonstrated. Chang *et al*. (*90*) studied the effect of GO dispersions on a human A549 lung epithelial cell line using different cell lines. A colorimetric assay, CCK-8 assay, and Trypan blue assay were used to evaluate the cell viability and mortality, respectively, following exposure to GO. The GO dispersion (0.9 nm in thickness, and 3 different lateral diameters: 160 ± 90 nm, 430 ± 300 nm, 780 ± 410 nm, measured by AFM) caused a slight decrease in cell viability with increasing concentration (0-200 mg L^{-1}) for all diameters of GO. There was no clear size dependency except at 200 mg L^{-1} where the smallest GO showed 67% cell viability whereas the other two GOs showed greater than 80% cell viability at the same concentration. The cell mortality test showed no change compared to the control meaning that although cell viability was slightly affected, it did not lead to cell death. The outcome of a Lactate dehydrogenase (LDH) assay (used for assessing membrane damage by measuring the level of LDH released) result indicated that GO in fact, caused restriction of leakage of GO indicating blockage of membrane by GOs, but no effect of lateral diameter size was measured. Finally, the GO did not cause any apoptosis towards A549 cells. TEM imaging showed that GO did not change the cells morphology, damage their intracellular organelles and were not internalised. Interestingly, the GO did increase ROS generation which was concentration dependent but not

size dependent. Taken together, the results of the studies highlighted that GO is most likely to be biocompatible at concentration up to 200 mg L^{-1} and cause oxidative stress.

A more recent study by Mittal *et al*. (*91*) showed that GO and their derivatives were damaging towards A549 cells and another BEAS-2B – a bronchial epithelial cell line. The GO dispersion (0.2-0.6 μm in lateral diameter, 1 nm in thickness, AFM) was exposed to the two lung cells in cell specific culture media for 48 hours and the cell viability was assessed using MTT assay. GO decreased cell viability with increasing dose and time in the concentration range between 1-100 mg L^{-1} and time range between 3-48 hours). Pristine GO was the most toxic when compared to other types of chemically processed GO which was related to their oxygen functional groups. An ROS assay was also carried out to assess the oxidative stress pathway since. The 2, 7 dichlorofluorescein diacetate (DCFDA) assay that measures ROS levels inside cells as well as Ellman's assay (that measures oxidative stress inside the cell) were used for testing. Oxidative stress correlated with cell viability showed that that the reduction in cell viability was caused by oxidative stress and generation of ROS caused by the GO. This oxidative stress led to DNA damage indicating an ability of GO to cause genotoxicity. TEM indicated that GO could impair mitochondria integrity and enter the cytoplasm of the cells. This paper highlighted the potential toxicity of GO towards human cells, but was contradictory to the work of Chang *et al*., highlighting instead a potential use of GO in cancer therapy.

Rhazouani *et al*. (*87*) found contradicting evidence for the activity of GO towards human cells even for the same cell types. The lateral dimension and the thickness of the GO used by Chang *et al*. and Mittal *et al*., was similar and they have both tested against the same cell line A549. Therefore, the contradictory research result indicated there are potentially other reasons that explain the contradictory results highlighting the importance of full reporting of methods and characterisation of research.

It is plausible that the impact of GO on cell health may arise due to the choice of assay used, as assays can measure different endpoints and can also interfere with the results of the cell viability assays generating false positives. Liao *et al*. (*92*) studying the interaction of GO and other GFNs with Red Blood Cells (RBC) and skin fibroblasts, by systematically evaluating the between different physiochemical properties such as lateral diameter, thickness, oxygen content, and particulate state with toxicity. GOs haemolysed RBCs and were toxic towards skin fibroblasts in the concentration range up to 200 mg L^{-1}, but notably GO, and other GFNs, inflated the cell viability measured using an MTT assay. This outcome was previously observed for other carbon nanomaterials that materials partake in electron transfer reaction where MTT assay could react with the material to form insoluble formazan. (*93, 94*) In contrast, the WST-8 assay, which forms soluble formazan product, did not interact with GO or other GFNs and is more reliable. They also showed that GO interfered with the LDH assay by adsorbing it. The WST-8 assay was validated using a Trypan blue dye to assess the cell viability and the two results matched very closely indicating that GO did not significantly decrease the viability of the skin fibroblasts. The restricted production of LDH by GO observed by Chang *et al*. (*90*) indicated that GO could "plug" the membranes by some mechanism.

Mechanism of interaction with mammalian cells

Oxidative stress through generation of ROS has been identified as a main mechanism of GO toxicity towards human and mammalian cells (*95, 96*) and it has been reported that the number defect sites in GOs is proportional to the ability of GO to cause oxidative damage. However, the mechanism of ROS generation is unclear, as it could results from either a direct or indirect interaction with GO.

Another mechanism, which had been suggested from the results of the *in vitro* human cell toxicity assays, was cellular damage resulting from internalisation of GO. (*91, 97-99*) Cellular uptake of GO has been observed in both lung cells A549 and macrophages. The mechanism of internalisation was hypothesised to

be phagocytosis as non-phagocytic cells did not show any uptake of GOs (*97*). The literature was unclear on whether other mechanisms of internalisation, such as endocytosis, was possible for, but suggest that phagocytic cells can internalise the GO and overcome the electrostatic repulsive barrier between negatively charged GO and cell membrane. Interestingly, Mu *et al*. (*100*) showed that protein coating of GO improved the biocompatibility of GO and facilitated uptake of GO by myoblast cell from mice. GO (9.1 ± 7.1 nm) coated in protein entered by phagocytosis whereas smaller GO (1.8 ± 0.9 nm) entered *via* endocytosis. This indicated a size dependency of the mechanism of internalisation, which was discussed in the subsequent chapter in more depth.

Another mechanism of adhesion to cell membrane or "wrapping" had been observed *in vitro* studies with human cells. Ma *et al*.(*99*) showed that lateral diameter size did affect the mechanism of interaction of GO with macrophages (J774.A1). Three different lateral size monolayers GO dispersed in water were prepared by controlling the time of probe sonication: Small-GO (50-350 nm), Intermediate-GO (350-750 nm), and Large-GO (750-1300 nm). These GOs were exposed at 20 mg L^{-1} to macrophages and showed size dependent inflammatory effect on the cells with larger GO showing the highest toxicity. Small-GO were internalised readily whereas the large-GO bounded to the plasma membrane. Xu *et al*. (*101*) also showed GO could interact with cell membrane through cell wrapping around lung and liver cells in mice. They also showed that GO could impair cell membrane integrity. They exposed GO (100-500 nm in lateral diameter, 1 nm in thickness) to the cells and that membrane permeability increased signifying some form of penetration of GO through the cell membrane.

Summary

Current understanding of interaction between GO and mammalian cells is still inconclusive. Certain aspects, such as the ability of GO to generate ROS, as well as internalisation of GO *via* phagocytosis, are

clear, but there has been no consensus about the biocompatibility of GO to human cells or the interaction mechanism of GO with the plasma membrane of the cells. For this reason, GO is being developed to target cancer cells as well as a drug carrier. (*87, 90, 91*) The level of toxicity towards different cell lines still needs to be established unambiguously. Controlled preparation of GO with specific well understood physiochemical properties remains a challenge, as does selecting appropriate assays to assess the biocompatibility or toxicity of GO towards mammalian cells.

Bacteria cell study

General action and toxicity

There have been several toxicological studies that assay GO against environmental bacteria, as well as to assess their toxicity as anti-microbials. Several reviews from Zou *et al*. (*102*), Ngyuen *et al*. (*103*), Fojtu *et al*.(*11*), Seabra *et al*. (*95*), Palmieri *et al*. (*104*), Seifi *et al*. (*105*), and Pulingam *et al*. (*106*) described lateral size, number of layers, shape, surface functionality, and dispersibility as being determinants of the toxicity of GOs towards bacteria. However, the lack of characterisation of the GOs and control over their synthesis led to uncertainty over these properties. Several mechanisms have been proposed for how GO interacts with bacteria both physically and chemically, however it is difficult to draw conclusions about the exact relationship between how the mechanism(s) of interaction relate to the different physicochemical properties of the GO. This led to Palmieri *et al*. (*104*) highlighting the lack of a robust framework for assessing GO toxicity. The variation in mechanism(s) described are most likely explained due to the variability in experimental conditions used for the experiments and poor control over the starting material as well as inadequate characterisation. Therefore, when designing experiments for testing GO in biological systems, it is essential to ensure that measures are taken to control the physicochemical properties from synthesis through to thorough characterisation of the material.

Even though these reviews highlighted existing contradiction in literature about how GO interacts with bacteria, there are still notable results worth discussing in detail. Earlier studies on the effect of GFNs on bacterial health were conducted against *Escherichia coli*, and other pathogens such as *Pseudomonas aeruginosa*, and *Staphylococcus aureus*, but not for environmentally relevant bacteria. (*102*) Most work indicated that GO is the most toxic material out of the GFNs due to its dispersibility. (*107-111*) Therefore, it is understandable that GO has been considered for use in antimicrobial applications. From environmental risk assessment, the choice of GO was reasonable since it can be processed easily, has good dispersibility in water, and synthesis is scalable. These same properties have prompted GO to be considered for use in inks and coatings to prevent corrosion or used as surface modified sensors in clothing or environmental sensors. (*68, 112*) The fact that GO has been the focus for antimicrobial work indicates that GO poses the greatest threat to the environment following its release.

Herein the key literature highlighting each parameter of GO that affects the toxicity, as well different mechanisms of toxicity reported on, are discussed. This review focuses on literature concerning interaction of GO dispersions in solution rather than in other forms such as on a membrane, which would behave differently to GO in dispersion. Size dependency, as well as the toxicity trends within the GFNs, have been reported to be different. (*113, 114*) Therefore, literature on GO dispersion only were discussed here since these conditions are more representative of exposure of GO in environmental conditions.

Contradictory evidence for growth enhancement and antimicrobial effect of GO

A major point of debate in the literature is whether GO is antimicrobial, non-effective, or a growth enhancer. While most literature has reported that GO is antimicrobial, other reports describe GO as being ineffective towards bacteria at high concentrations (400 mg L^{-1}) and that it can even act as a growth enhancer.

Ruiz *et al*. (*88*) reported that exposure of GO dispersion with *E. coli* in Luria-Bertani (LB) broth leads to enhancement of cell proliferation using an OD assay at concentration of 25 mg L^{-1} of GO dispersion. A great amount of dark precipitate formed when GO was exposed to *E. coli,* not only from aggregation and destabilisation of GO in LB broth but also with significant interaction with extracellular polymeric substances (EPS) and bacteria. This growth enhancement was observed for both the GO dispersion and the GO films with cells showing preferential attachment to the GO. This was one of the first reports that indicated that GO could be used to support growth of bacteria.

Chen *et al*. (*115*) showed subsequently that GO dispersion could be used to promote growth in certain probiotic cultures and enhance their antagonistic activity against pathogenic bacteria in the gut. They studied five common bacteria in the gut: *Bifidobacterium adolescentis* (*B. adolescentis*), *Lactobacillus acidophilus* (*L. acidophilus*), *Escherichia coli* (*E. coli*), *Enterococcus faecalis* (*E. faecalis*), and *Staphylococcus aureus* (*S. aureus*). The GO dispersion (monolayer, 0.8-14.4 μm^2, AFM) showed growth enhancement against all five of the tested bacteria with most growth enhancement for anaerobic bacteria, *B. adolescentis*. This was confirmed by OD and CFU measurements, where the exposure was carried out in each respective bacteria media. Notably, the SEM images showed that GO had formed scaffolds around the cells, which the cells adhered to, leading to enhanced proliferation, especially for anaerobes, compared to the control. Subsequent to exposure with GO, the *B. adolescentis* showed greater activity in their antagonistic effect than against other pathogenic bacteria.

Nguyen *et al*. (*116*) identified that GOs could potentially be used in food packaging and so the risk of exposure by ingestion should be assessed. The group exposed intestinal bacteria as well as colon carcinoma to a GO dispersion to assess the safety of GOs. *Escherichia coli* K-12, *Lactobacillus acidophilus* ADH, and *Bifidobacterium animalis* were exposed to a GO dispersion (589.7±90 nm in Milli-Q water, DLS) against

Bif-6 in Tryptic Soy Broth with Yeast (TSBY) in concentration range of up to 400 mg L^{-1}. Cell viability was measured using a Colony Forming Unit (CFU) method. The results showed that there was no difference between the growth of cells in the control condition and the mixture with GO within 24 hours for all of the concentrations tested. SEM confirmed that there were no changes in the structure of the cells exposed to GO. The same results were observed for GO with the intestinal carcinoma, leading to the conclusion that GOs were biocompatible in the intestine.

A group at University of Manchester, Barbolina *et al*. (*117*), proposed that discrepancies in results of the toxicity assays arose from differences in the GO quality. They developed their own protocol to establish that GO has no inhibitory effect, and the discrepancy was due to the difference in pH and contamination with low molecular weight contaminants in the GO dispersions from manufacturing processes. A series of GO dispersions including GO synthesised in-house from graphite, purchased graphite oxide and GO purchased from leading manufacturer (Graphenea included) were exposed to *Escherichia coli* and *Staphylococcus aureus*. They carried out two types of exposure set ups: 1.) Cell viability using OD and CFU assays where GO was exposed to bacteria in an "appropriate double strength growth media" with a concentration range of 0-250 mg L^{-1} and the growth monitored over 24 hours, and 2.) Cell viability using a CFU method for bacteria exposed to GO dispersion (1 mg mL^{-1}) directly for 2 and 4 hours and then recovered in nutrient rich media. The results from these assays led to a number of important findings and highlighted that the inhibitory effect of the GO could be due to the acidic conditions present in the dispersion left over from the synthesis. This could be removed with series of washing steps, even for some manufactured GO dispersions. After washing, the GO dispersion was considered to be non-toxic, and TEM imaging showed that even direct attachment of GO on the membrane of cells did not cause any damage. It was worth noting that testing of the inhibitory effect from different purities of GOs was carried out in water and the rest of cell viability assessing the toxicity of GO, including the effects of lateral dimensions, were

carried out in media. The paper concludes that the pH of the GO dispersion may lead to different toxicological outcomes and points to the fact that the discrepancy between the results on the toxicity of GO to bacteria arises from use of different exposure conditions during testing.

Campos-Delgado *et al*. (*118*) performed series of experiments to elucidate the reason behind the discrepancies reported by exposing GOs prepared in different media. They prepared three types of GO:GO in water (sonicated for 6 hours, 100 nm in lateral size, monolayer), GO in Phosphate Buffer Solution (PBS) (100 nm in lateral size, monolayer), manually ground GO in water (several μm in lateral size, monolayer). They exposed *E. coli* (DH5 α) to this series of GOs in saline solution to allow direct contact of basal planes with cells. They measured the recovery of growth in LB media using OD measurements, following the exposure and showed that only manually ground GO synthesised in water elicited toxicity. They concluded that exposure in PBS, as well as smaller GO in water, did not show any inhibitory effects within the concentration range of up to 200 mg L^{-1}, because of their smaller size and interference from the PBS, respectively. The larger GO showed an inhibitory effect at 200 mg L^{-1} only when the basal planes were available during exposure and without significant nutrient molecules available. This report concluded that GO dispersion under minimum nutrients (in saline) could still be inhibitory.

Chen *et al*. (*107*) demonstrated the effect of GO on phytopathogenic bacteria under different media conditions, systematically. The GO dispersion exposed to *Xanthomonas oryzae pv. oryzae* (*Xoo*) in DI water elicited the highest toxicity compared to when it was dispersed in saline solution (0.9% NaCl) and 0.01 M PBS. In fact, in 0.01 M PBS, GO did not show any inhibitory effect. Other literature indicated similar findings, under DI water exposure conditions, the bacteria showed higher inhibitory effects compared to saline or other nutrient rich media. (*119-121*) These results could be attributed to the availability of active sites on GO, such as the defect sites or functional groups, because the colloidal stability

of GO decreases as the concentration of electrolyte increased. (*122, 123*) Therefore, this set of literature strongly suggest that GO's inhibitory effect was highly dependent on the media and the presence of electrolyte and nutrients that could interact with GO. Nevertheless, some literature still ignores this finding and proposes that it is appropriate to test GO as antibacterial agent under nutrient rich conditions (97).

The literature discussed in the previous section possibly indicates that choice of media was crucial to the outcome of the cell viability tests and such that exposure in nutrient rich media such as LB broth results in no toxicity or growth enhancement. However, Gurunathan *et al*. (*111*) exposed set of GFNs, including GO dispersion in LB media, and showed that GO could still reduce the growth of *P. aeruginosa*. They exposed the GO dispersion in LB media with bacteria and centrifuged down the bacteria to resuspend them in PBS; OD_{600nm} was measured at different time points to obtain growth curves. They also exposed GO dispersions in saline solution and used the conventional CFU counting methods to measure the cell viability. In both cases, GO was toxic towards *P. aeruginosa* even in LB media. However, it is plausible that post exposure centrifugation steps used to separate the bacteria from the media and the GO could have affected the test results, as the cell viability test across both tests did not seem to match.

The above set of literature illustrates the different findings that have been reported and possible reasons for the discrepancies in the different levels of toxicity to GO dispersions. Taken together, this literature suggests that the experimental set up, especially choice of media, as well as physiochemical properties of the GO, such as lateral diameter, play a significant role in the toxicity measured towards pathogenic bacteria but the mechanism of those different interactions is still unclear. The mechanisms proposed, such as wrapping and scaffoldings, that promote bacterial adhesion, seem to contradict each other as these two mechanisms describe contrasting interactions of GO with cells. This literature clearly demonstrates a need

for more in-depth investigations into each of these reported interactions as they form the basis of a number of applications of GO in biotechnology.

Aside from literature on pristine GO dispersions, Luo *et al*. (*124*) studied the effect of PEGylated GOs as well as pure GO with *E. coli* in mixture of LB media and PBS. The MTT and CFU assays indicated that small loaded PEGylated GO promoted growth significantly, whereas no effects were seen for pure GO and other heavily loaded PEGylated GOs.

Efficacy against gram-positive and gram-negative bacteria

There were also indications that GO shows differential toxicity towards gram negative and gram-positive bacteria although no consistent results have been reported. (*114, 125*) The inherent difference in toxicity towards gram negative and gram-positive bacteria is considered to be due to the difference in outer cell surface structure (depicted in figure 2.1.2.1).

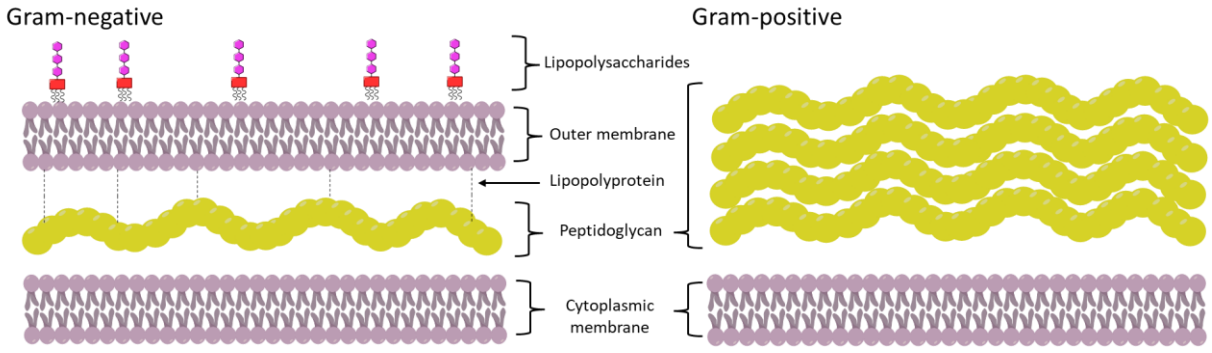


Figure 2.1.2.1 Schematic representation of the differences in the structure of the cell wall between gram-negative and gram-positive bacteria.

As shown in figure 2.1.2.1, there were number of differences between the two types of bacteria that could lead to higher toxicity towards one type of bacteria over the other. In general, for nanomaterials, gram-

negative bacteria are more resistant to nanomaterials damage. (*47, 126*) This is due to the extra outer membrane structure present in gram-negative bacteria, and also the extra complex structure such as lipopolysaccharides that increases surface negative charge of the bacteria surface. The extra layer of membrane as well as further complex structure on the membrane adds both increased structural and chemical integrity to gram negative bacteria than gram positive bacteria which results in less nanomaterials damage observed from nanomaterials.

Graphene oxide is negatively charged in its surface area and therefore expected to have higher effect on gram-positive bacteria than gram-negative bacteria. However, there has been mixture of observation demonstrating that gram-negative bacteria can be more susceptible to GO damage than gram-positive bacteria. The reasons for each side of the observation are summarised in table 2.1.2.1.

Evidence for GOs being more effective towards g-ve	***Evidence for GOs being more effective towards g+ve***
Musico et al. (108) Nanda et al. (127) He et al. (125) Karahan et al. (128) Veerapandian et al. (129) Krishnamoorthy et al. (130) Hu et al. (131)	*Pulingam et al. (132) Akahavan et al. (114) Carpio et al. (133) Krishnamoorthy et al.(134) Bao et al.*
Hydrophobic nature of GOs facilitates partitioning into the external lipid membrane.	Sharp edges of the GOs damaged g+ve more due to less integral outer cell structure in g+ve
Since g+ve has thicker peptidoglycan layer than g-ve (20-80nm vs. 7-8nm thickness) g+ve is more resilient to cell membrane damage and has less disrupted cell structure due to thicker peptidoglycan layers.	G+ve bacteria has peptidoglycan as the outer layer which has adhesive characteristics from teichoic acids and adhesins and this promoted interaction with GOs and the wrapping mechanism.
	G-ve bacteria has an outer membrane with lipopolysaccharides which are negatively charged and result in repelling forces between the GO and the bacteria while G+ve bacteria do not have outer membrane with lipopolysaccharides.

Table 2.1.2.1 Summary of literature results on the interactions between gram-negative and gram-positive bacteria and GO.

One reason which may contribute to the discrepancy in the literature results for effect of GO towards gram-positive and gram-negative bacteria is the size of the bacteria. Since GO is a 2DNM bacteria with lateral size that can span from nm to μm, the lateral size range is comparative to that of bacteria which can range from coupe of μm to tens and hundreds of μm in some dimension. This consideration of relative size of bacteria to GO size is still not yet heavily considered but for the two bacteria used in the study for this project, *Arthrobacter globiformis* and *Pseudomonas putida*, the sizes were both in the range of couple of μm in length. Both bacteria are rod-shaped and therefore shown to be similar in size with *A. globiformis* being slightly larger than *P. putida*. Exact sizes were seens under TEM during the project.

Recent reports by Karahan *et al*. (*128*) studied the effect of GO on different stages of cell growth phase (exponential phase – stationary phase – death phase) and the difference between the GO toxicity against gram positive and gram negative bacteria at each of the three growth phases. They exposed GO dispersion (monolayer, <few hundred nanometres in lateral diameter) to three bacteria: *E. coli*, *P. aeruginosa* (gram negative), and *S. aureus* (gram positive). The exposure experiment was carried out in DI water or in saline using the CFU method to measure the cell viability. The results showed that bacteria were most susceptible in the exponential phase of the growth phase. SEM and AFM imaging also showed that during these exponential phases where the cells were the most vulnerable, the cell membranes did not necessarily show complete destruction. Cells in the exponential phase showed a decrease cell viability, even with incomplete destruction of the membrane, whereas cells in stationary or death phase only showed a decrease in cell viability with a completely compromised cell membrane. The group also showed that over the exponential phase to stationary phase, gram negative bacteria studied showed significant development of their membrane structure. This had led to the gram-negative bacteria studied here being more receptive to GO presence during exponential phase than gram positive bacteria, but less receptive to GO presence during the stationary phase when the ulterior structure have been full formed. This report highlighted the

importance of considering the change in the interaction of bacteria with GO during different stages of their life cycle and highlighted the potential reason for the discrepancies reported in the effectiveness of GO towards gram positive or gram negative. A sweeping statement such as "GO is more effective towards gram positive/negative bacteria" should be used with much more careful consideration, as factors such as maturity of the bacteria, type of bacteria, incubation period as well as GO type may result in different observations.

Mechanism of action

Physical mechanism observed

The above discussions showed that, although there was contradictory evidence available for the toxicity of GO, most evidence suggests that GO could be used as an effective antimicrobial. Several mechanisms were reported for the activity of GO towards bacteria cells, of which many are physical interactions (Figure 2.1.2.2).

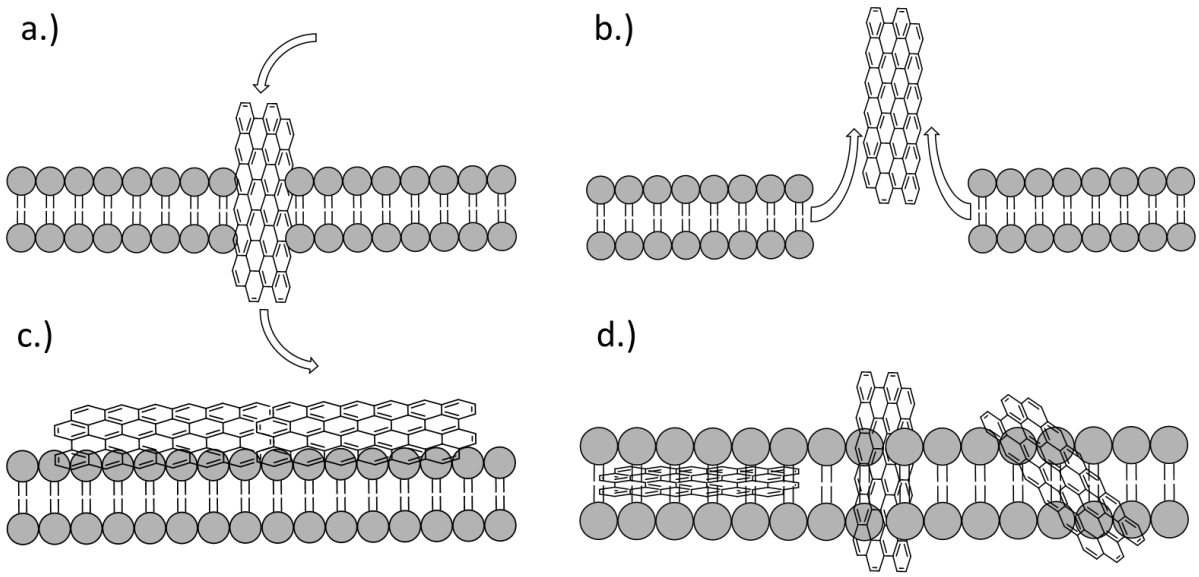


Figure 2.1.2.2 Proposed physical mechanism of interaction between a bacteria membrane and GO sheets. GO is represented by graphene here without the oxygen functional group for simplicity. The phospholipid bilayer consists of hydrophilic head and hydrophilic tail. 4 mechanisms are proposed: a.) A slicing mechanism, in which GO acts as a "nano-knife" that spears through the membrane. b.) An extraction mechanism where hydrophobic tails travel up through the surface of GO and the integrity of the membrane is not retained. c.) A wrapping mechanism where the GO does not enter the phospholipid bilayer, but instead wraps around the bacteria. d.) An embedding mechanism where the GO embeds itself in the membrane.

Wrapping/Entrapment

One of the main mechanisms proposed for GO's toxicity was a process by which the GO sheets entrapped/wrapped around the GO sheets. (*120, 135, 136*) This mechanism has been both modelled computationally and imaged by SEM and AFM. The wrapping mechanism decreases cell viability by trapping the bacteria inside the GO sheets and blocking any transport of nutrients. (*119, 135*) Therefore, the observations of larger lateral-size GO more effectively wrapping bacteria than smaller diameter GO could explain why it's a more effective antimicrobial. Smaller GO would leave gaps around the bacteria where exchanges with the surrounding could still occur. (*120*) There remains controversial evidence,

however, about whether this wrapped GO could be released from the bacteria leading to recovery of the cell's viability. Several reports mentioned that a short period of bath sonication can release the GO from the cell membrane. (*113, 135*) Others have reported that the cells cannot be released, even irrespective of the lateral diameter of the GO used. (*120*) The case when GO wrapping can release the bacteria, categorises it as bacteriostatic, whereas stronger interaction of GO with membrane would categorise it as a bactericidal material.

Another area of ambiguity in the wrapping mechanism reported was whether wrapping mechanism could cause decrease in cell viability. Barbolina *et al*. (*117*) reported that attachment of GO to cells did not damage the cell. Moreover, the similarity in the mechanism of cell proliferation, by availability of GO basal planes for cell attachment, and impairment of cell viability due to GO wrapping its outer membrane is contradictory and yet to be explained.

Insertion/Nano-knife

The insertion mechanism or process by which GO acting as a 'nano-knife' and pierces through the cell membrane had also been widely reported. This had been computationally modelled as well as imaged using AFM and SEM. (*107, 125, 132, 136-138*) The main observations which led to the hypothesis that the GO can act as a nano-knife arises mainly from the leakage of cytoplasmic contents such as nucleic acids and the damage to the cell membrane. In contrast to the wrapping mechanism, the nano-knife mechanism would lead to bactericidal effect with irreversible damage. This process would also damage to intracellular organelles. However, currently, there have been no images taken that describe internalisation of GO nanosheets inside bacteria as bioimaging monolayers of GO inside cells is challenging due to the thickness of the individual layers and with generating contrast between the GO and cells.

Yu *et al*. (*138*) recently reported a simultaneous wrapping and insertion mechanism. They exposed range of sizes of GO dispersion (hydrodynamic size of 1295, 2015, 3074, 4544 nm) with *Streptococcus mutans* (*S. mutans*). The result showed parabolic relationship with size because of the competing effect of insertion and the wrapping mechanism. The medium sized GO (hydrodynamic size of 2015 nm) led to the highest decrease in cell viability (measured in CFU) as this GO could both wrap and insert effectively towards the bacteria. With increasing size, the wrapping mechanism becomes more effective and with decreasing size, the insertion mechanism more effective.

Embedding mechanism and phospholipid extraction

These two mechanisms are less widely reported on. Tu *et al*. (*137*) showed, through computational modelling, that as well as insertion of GO into the membrane through an edge-interaction, phospholipids from the cell membrane could be extracted from the membrane. Both an insertion and extraction mechanism were observed by TEM, although the author does mention that without the prior modelling, the observation of extraction could not be made due to the limited resolution of TEM images and the fact that it is not necessarily a time-resolved technique. Differentiation between the extraction mechanism and the nano-knife mechanism would be hard to differentiate even by imaging and for this reason few reports have been made.

The embedding mechanism where the GO entirely envelopes into the membrane have only been modelled computationally. Dallavalle *et al*. (*136*) and Mao *et al*. (*139*) both modelled different sized GO with different parameters such as degree of oxidation. The embedding mechanism was modelled for very small sized GO (lateral size <10nm) only and also for less oxidised GO, which interact more avidly with hydrophobic parts of the membrane that face inwards. The reason for the lack of experimental observation may be due to the challenges in imaging such a small GO. However, exploitation of these unique properties

of GO where quantum confinements allows them to fluoresce may be exploited in future to image these proposed mechanisms. (*25*)

Non-physical mechanisms

Oxidative stress

Apart from physical interaction of GO with membrane, there have been multiple reports of oxidative stress caused by the presence of GO. (*104, 119, 120, 128, 130, 137, 140, 141*). Krishnamoorthy *et al*. (*130*) showed that GO could induce toxicity towards bacteria *via* lipid peroxidation. This was hypothesised to mediated by reactive oxygen species (ROS) produced as a result of a reaction of GO with water, specifically from hydroxyl radicals. Liu *et al*. (*120*) measured the oxidation capacity of GO using a Glutathione (GSH) measurement in acellular conditions. GSH is a redox mediator in bacteria which has thiol groups that can be converted into disulfide in the presence of oxidising materials. Using Ellman's assay, the levels of GSH were measured following exposure to different lateral-sized GO; Liu *et al*. reported that although GO has an oxidation capacity towards GSH, it was independent of the lateral size. In another paper, the same group considered alternate pathways that cause oxidative stress using 2,3-bis-(2-methoxy-4-nitro-5-sulfophenyl)-2H-tetrazolium-5-carboxanilide (XTT) assay which measures the amount of superoxide anions (*141*). Superoxide anions are one of the main ROS forms along with hydroxyl radicals and singlet oxygen. They concluded that presence of GO resulted in very little production of superoxide anions in acellular conditions and therefore GOs are capable of ROS-independent oxidative stress.

However, under cellular conditions, there has been increasing evidence to suggest that GO could also induce oxidative stress *via* ROS production. Gurunathan *et al*. (*111*) used Nitro blue tetrazolium test (NBT test) to measure the ROS production and showed that exposure of *Pseudomonas aeruginosa* (*P. aeruginosa*)

to GO cause oxidative stress to the cells via ROS production. Perreault *et al*. (*113*) also measured the production of GSH as well as adding α-tocopherol to remove the oxidising effect from ROS on *E. coli*. This showed that GO could cause toxicity via ROS-mediated pathway over two gram-negative pathogenic bacteria. Chen *et al*. (*107*) used oxidation sensitive fluorescent dye 2,7-dichlorofluorescin diacetate (DCFH-DA), as well as Ellman's assay to study the oxidative stress pathway in detail against *Xanthomonas oryzae pv. oryzae* (*Xoo*), a rod-shaped, gram-negative bacteria. They concluded that in the presence of both bacteria and GO, ROS production increased compared to the controls of without bacteria and without GO.

The current set of literature suggested that GO dispersion was capable of inducing oxidative stress *via* both ROS-dependent and independent pathways in the presence of cells. There was still ambiguity around which pathway dominated under certain conditions since the measurements numerous assays were used that measured different aspects of the biological interaction with GO. However, the presence of defects and oxygen functional groups, permitted GO to interact with the surroundings, to cause oxidative stress towards cells, and display the changes in GSH levels reported on. Moreover, wider variety of cell types should be studied for ROS production in the presence of GOs.

Combination of all

There are many hypotheses that can be used explain the various observations of interaction of cells with GO and there is no doubt that experimental design, especially the constituents of the cell culture media, have a considerable impact on the observed GO interaction with cells. There is currently no consensus about the mechanism by which GO causes for toxicity. Recent literature has stated that GO toxicity is most likely to be caused by a combination of all of these mechanisms. (*105*) Sharma *et al*. (*142*) observed both ROS-mediated oxidative stress as well as physical disruption of cell membranes via direct contact of GO. Combination of physical mechanism such as wrapping and insertion with oxidative stress towards cells

could occur simultaneously. However, this hypothesis is still yet to be shown and the steps and order at which these different mechanisms were presented to occur still require investigation.

Bactericidal or bacteriostatic

As mentioned in the above sections, there were evidence to suggest GO could be bactericidal and bacteriostatic. Bactericidal and bacteriostatic materials both inhibit the growth of bacteria cells, but bactericidal materials are able to completely destroy or interrupt important metabolic pathways, so that cells can no longer proliferate under any conditions. However, bacteriostatic materials would only keep the cells at its stationary phase and would not necessarily kill the bacteria. They can disable the cells, but once the materials have been removed then the cells could grow.

The current literature landscape supports both hypotheses. The wrapping mechanism reported by several papers predominantly supported the bacteriostatic effect of GO. Both Perreault *et al*. and Akhavan *et al*. demonstrated that bath sonication could release the GO attached to the cells and recover the growth of bacteria. (*113, 135*) Moreover, higher toxicity of a GO suspension of larger lateral sized can be explained by the wrapping mechanism being more proficient at starving the cells from nutrients in surrounding environments. Considering these two points, the proposed bacteriostatic effect of GO *via* a membrane wrapping mechanism seems plausible.

On the other hand, evidence for bactericidal effect were also discussed in papers. Liu *et al*. (*120*) showed competing results of using bath sonication to release the bacteria from GO. They demonstrated that bath sonication could not recover the growth of bacteria. They tested a similar range of lateral sized GO and concluded that larger GO were more effective in inhibiting growth of bacteria *via* wrapping, but the attachment was a much stronger interaction than the interaction reported by Akhavan *et al*. and Perreault

et al. (*113, 135*) This could be due to the choice of media as Liu *et al*. used DI water for their reported results, whereas Perreault *et al*. and Akhavan *et al*. used saline and LB media respectively as exposure media. It could be hypothesised that media choice not only affected the cell viability results but also the observed attachment level and interaction.

Other evidence, such as oxidative stress and an insertion mechanism, all suggest that GO would be bactericidal rather than bacteriostatic. Oxidative stress *via* ROS dependent or independent pathways would cause permanent damage to the cells and their metabolic pathways *via* lipid peroxidation. (*111, 130, 134*) The proposed insertion mechanism could rupture the membrane and lead to cytoplasm leakage. (*104, 121, 137*)

Reported effective concentration

Minimum Inhibitory Concentration (MIC) or Minimum Bactericidal Concentration (MBC) are terms used evaluate the antibacterial effect of material. Strictly speaking, MIC relates to the bacteriostatic or bactericidal effect where there are no visible growth and MBC relates to bactericidal effect only where there is visible cell death. Most reports have reported MIC or MBC in the range of tens to hundreds mg L^{-1}. The lowest MIC and MBC reported were by Veerapandian *et al*. (*129*) which was below 2 mg L^{-1} for 4 bacteria species (*E. coli*, *S. typhimurium*, *B. subtilis*, and *E. faecalis*). Moreover Combarros *et al*. (*143*) reported that the highest increment in which the concentration increase affected the increased cell inhibition was at a lower concentration. This may be due to the fact that aggregation state is affected by concentration but could also be attributed to the different types of GO used. The MIC and MBC of GO is therefore yet to be determined.

Effect of media

As mentioned in the earlier sections, the effect of media on GO toxicity could arguably the largest factor contributing to the discrepancies in the observed interaction between GO dispersion and cells. Wu *et al*. (*122*) and Zhao *et al*. (*123*) both demonstrated an instability of GO dispersion in the presence of salt ions using colloidal theory. Ionic strength as well as the size of the cations present in the media would affect the aggregation state of the GO with a unique interaction in the presence of Ca^{2+} cations. Hui *et al.* (*119*), Palmieri *et al*. (*121*), Liu *et al*. (*120*), and Chen *et al*. (*107*) all demonstrated that the type of media and the strength of media used affected the outcome of the toxicity results. Liu *et al*. showed decreased toxicity in saline compared to DI water. Chen *et al*. showed that exposure of bacteria to GO in in 0.1 M of PBS resulted in no toxicity compared to exposure in water and saline. Hui *et al*. showed that constituents in LB broth could attach to the GO surface and reduce the availability of the GO basal planes for interaction with membranes - which was proposed to be important in cell interaction mechanism.

Palmieri *et al*. (*121*) conducted an extensive experiment to study the effect of H_2O, PBS, NaCl, $MgCl_2$, and $CaCl_2$ on the toxicity of GO dispersion against *E. coli* and *S. aureus* (GO lateral size: 0.19 μm^2, monolayer. GO zeta potential: -37.8 mV in ddH_2O). They reported that there were three distinct interactions of GO with cells: 1.) A nano-knife mechanism leading to intracellular content leakage; 2.) A wrapping mechanism leading to isolation of cells from surrounding environment and 3.) Scaffolding of GO network enhance bacterial growth. According to the study, which of the three mechanisms occur depends on the aggregation state of the GO. The cutting mechanism occurs under low aggregation condition such as low salt content or low GO concentration. The wrapping mechanism occurs when the GO is highly aggregated, and the GO would completely encapsulate the cells. Growth enhancement occurs in a slightly less aggregated state

where the GO can form support scaffolding for bacteria to grow. The wrapping and scaffolding mechanism was stated to be competing mechanisms worthy of further in-depth study.

There were other reports on aggregation studies that did present contradictory evidence to the findings of Palmieri *et al*. including a lack of toxicity in water and no colloidal destabilisation in cell culture media. (*101, 118, 143*) Therefore, the suggested effects of media were not conclusive, but required significant consideration during the analysis of the results. Environmental conditions often involve different concentrations and types of ions and other constituents which may further complicate the behaviour of GO in dispersion and the subsequent interaction of GO with environmentally relevant bacteria.

GO against soil bacteria

Although there are only few literatures which considers the impact of graphene oxide and other GFNs on the soil community and soil bacteria, the findings already suggests that the interaction of GO with soil bacteria are versatile and may not follow the trend described above with model pathogenic bacteria. Yilihamu *et al*. (*144*) exposed GO to *Azotobacter chroococcum* (*A. chroococcum*) – a known nitrogen-fixing bacteria under *in-vitro* and with soil and reported mixture of results with inhibitory effect as well as growth enhancement. GO was immediately reduced by the bacteria which highlighted the potential for GO to partake in electron transfer reaction with bacteria, and CFU and OD toxicity test result showed that GO at high concentration of 500 mg L^{-1} could induce inhibitory effect but GO at lower concentration could induce growth stimulation. Interestingly, in the presence of soil, the amount of nitrogen in the soil increased which led to the consideration of GO as a potential use in fertiliser.

Another notable research exposed GO to a community of soil bacteria. (*145*) Du *et al*. obtained a sample of soil and measured the change in bacterial community using DNA (Deoxyribose Nucleic Acid) extraction

and PCR Polymerase Chain Reaction) amplification with and without GO. Presence of GO in the soil resulted in change in the bacterial community where the diversity and the richness of the bacteria community increased. Particularly, nitrogen fixing bacteria and other bioremediation bacteria was shown to be enriched by the presence of GO including *Arthrobacter* species while other species of bacteria reduced their gene expression. Analysis of change in the expression by genus level showed that secretive interaction of GO is controlled by the genus and species of bacteria rather than the gram type. They also noted that GO transformed under exposure but instead of reduction of GO, they hypothesised that organic molecules coated the surface of GO.

There is other literature that has reported concentration-dependent toxicity of GO under environmental conditions such as wastewater and agricultural soil. (*143, 146*) Combarros *et al*. exposed GO to *Pseudomonas putida* (*P. putida*), the same bacteria used in ISO 10712, in simulated urban and industrial wastewater and showed, using flow cytometry, that GO has a negative impact on the bacteria under the condition. Notably, at concentration below 50 mg L^{-1}, GO only showed damage to the cells but no loss in the metabolic activity of the cell. Above 100 mg L^{-1}, both membrane damage and reduction in metabolic activity was observed. (*143*) Although the strain of the bacteria as well as set-up of the media was different due to not using ISO protocol, this result could be closely compared to the result reported thereafter.

GO under additional environmental conditions

There are other sets of literature concerned with the effect of GO towards the environment but considered the environmental transformation(s) of the GO and its transformed GO towards model bacteria. These transformation(s) included reduction, fragmentation, and photodegrading under natural sunlight with and without oxygen. (*147, 148*) Depending on the duration and the amount of oxygen present, different transformation took place which increased/decreased its antibacterial activity towards model bacteria.

Additional consideration of chlorination with/without the presence of natural light have also been carried out but all of the transformed GO has only been exposed to model pathogenic bacteria in a similar manner to the earlier set of literature. (*149*)

Another important environmental condition other than light that should be considered is the presence of NOMs (Natural Organic Matters). Chowdhury *et al*. (*150*) investigated the aggregation kinetics of GO under relevant environmental conditions including NOMs. They investigated the effect of changing pH, type of salt, ionic strength, and amount of NOMs on the aggregation kinetics to replicate the aquatic system. The salt types they used were NaCl, $MgCl_2$, and $CaCl_2$, and model NOM used was Suwanee River Humic Acid standard II (SRHA).

Firstly, without the NOMs, the results from the electrokinetic and hydrodynamic measurement indicated that GO suspension remained relatively unaffected between the pH range found in the environment as well as in the presence of monovalent cations. Only in the presence of divalent cations, GO suspension started to show aggregation in the presence of Ca^{2+} ions due to the formation of bridges between the ion and the GO sheets. However, with the addition of NOMs, under all salt conditions, GO formed stable dispersion. The addition of NOMs stabilised the GO by steric repulsion *via* sorption of SRHA on GO. Although they did not carry out bacteria exposure test, it was expected that this would affect the toxicity of GO towards environmentally relevant bacteria.

Other notable observation of consideration

Reduction by bacteria

Several reports have described the ability of bacteria to reduce the GO. (*81, 110, 151*) Gurunathan *et al*. (*110*) demonstrated that *E. coli* could reduce GO in suspension. They grew the *E. coli* in LB broth then washed the culture in PBS to mix with GO dispersion in water (500 mg L^{-1}) to synthesise rGO. It was observed that the presence of *E. coli* in GO dispersion caused a reduction of GO which was characterised by UV-Vis and Raman. The authors noted that the brown dispersion of GO turned darker with visible precipitation of rGO in the suspension. This result indicated that, in some cases, there could be a unique interaction between GO and some bacteria.

Oxidative Debris

One of the possible by-products of GO synthesis are small carboxyl carbonaceous fragments or oxidative debris. Previous work on Carbon Nanotubes (*152*) and GO (*153*) demonstrated that use of strong acids during the oxidation process produces these highly oxidised nm-sized polyaromatic hydrocarbons which can be analogous to polyaromatic hydrocarbons (PAHs) – a known carcinogen. Oxidative debris is hypothesised to be present in GO as well under the debated two-phase structure and interact with the surface of GO *via* π-π interactions. (*154*) These oxidative debris affect the physiochemical properties and the antimicrobial activity of GO as shown by Faria *et al*. (*155*). In this work, Faria *et al*. highlighted that both oxidative debris free GO and oxidative debris contribute to the overall toxicity. The synthesis method of GO does affect the number of oxidative debris, but it is likely that these oxidative debris containing GO are produced and released into the environment, so consideration of oxidative debris is important even though the origin and structure of oxidative debris and graphene oxide is widely debated.

Other contaminants

For carbon nanotubes it is well established that contaminants, such as their heavy metal catalysts, cause acute toxicity. (*156*) For example, modified Hummer's method uses $KMnO_4$ as an oxidising agent which contains manganese that is an environmental hazard (*157*). However, most suppliers claim that their washing methods are sufficient to remove impurities. For this reason, residual toxicity from contaminant synthesis products must be characterised to ensure that the toxicity results are indeed attributed to the GO and not to the impurities.

Yue *et al*. (*97*) showed that the presence of Mn from the $KMnO_4$ used in modified Hummer's method caused enhanced toxicity towards mammalian cells. Barbolina *et al*. (*117*) explored toxicity of different purity grade of GO, including modified Hummer's method, produced GO with different amount washing against *E. coli* and *S. aureus*. They concluded that although Mn and other metals were present in some of the poorly washed GO dispersion, this was not the main contribution to the toxicity observed and pH of the dispersion had a greater contribution to the toxicity measured. Therefore, the presence of metals and contaminants from the synthesis method may not be the most important factor that determines the toxicity of GO towards bacteria.

2.1.3 Summary

The literature review has highlighted that more research is needed to determine whether and which forms of GO are bactericidal and under which testing conditions, and the mechanisms GO interacts with bacteria. The following points are a summary of the most pertinent findings from the literature review.

1. Most GO toxicity tests were typically carried out against *E. coli.*

2. Several methods were used to measure the toxicity of GO against cells such as CFU, OD, MTT, oxidative Stress assays.
3. GO dispersion condition greatly affected the interaction of GO with cells leading to cell death or cell proliferation.
4. Several mechanisms have been reported on under different conditions to explain the mechanism of toxicity but there are no detailed reports about whether, and by which mechanism, GO alters the mechanism of cell growth.
5. The physicochemical properties such as lateral diameter, number of layers, and surface chemistry all influence the toxicity but effect of these properties on the growth has not been established.
6. There is a lack of results that consider all of above factors, such as the effects of media effect lateral size of GO on environmentally relevant bacteria, as well as consideration of different mechanisms, to understand how GO interacts with bacteria.
7. There is also no ISO protocol report for GO against soil bacteria.

Considering the above points, it was considered that GO safety towards the environment should be tested using International Organisation for Standardisation (ISO) protocol. 1SO 10712 specifically tests the water quality and the effect of materials in water in the environment and is often used as the initial test to determine the safety of materials. Therefore, the use of ISO 10712 with GO would identify the suitability of the test against 2DNMs and identify the potential behaviour of GO in environmental matrices.

2.2 Initial ISO 10712 toxicity test

2.2.1 Methods and Materials – GO (GO dispersion in water, ACS material, US)

Materials

Chemicals and Hardware

The GO dispersion in DI water was obtained from ACS materials, US. For the toxicity test of ISO 10712, all chemicals used were purchased from Sigma Aldrich at biological grade suitable for microbial work. A standard Milli Q water was used for any dilution or media preparation. Pipettes, plates, and other materials used in toxicity assay were purchased from VWR, UK. All materials were stored as per the manufacturer instruction where GO dispersion was stored in a fridge. The GO dispersion was referred to as as-received GO (ARGO) in Chapter 2 and Large-GO (LGO) in Chapter 3.

Bacteria

Gram-positive bacteria, *Arthrobacter globiformis* (*A. globiformis*), (DSM 20124) and gram-negative bacteria, *Pseudomonas putida* (*P. putida*) (DSM 50026) were obtained from DSMZ, Germany, in a freeze-dried form and rehydrated for preparation of the assays. Freeze-dried bacteria were rehydrated in Luria-Bertani (LB) broth and half of the culture was plated onto LB Agar plate and incubated at 25° for 48 hours, while the other half remained in the LB broth and mixed with glycerine for long term storage at -80°C. The plated cultures were re-plated again and incubated for another 48 hours and then stored at 4°C until used for the assays. The plated culture was re-plated every 4-6 weeks to obtain fresh cultures. All toxicity tests for GO were run on the same batch of bacteria.

Methods

ISO 10712

Preparation of Media

Media used for ISO 10712 was prepared using an existing method routinely used at Centre for Ecology and Hydrology (CEH, Wallingford, Oxfordshire). There were two media prepared: Pre-culture, and Test media. The compositions of both media are shown in Table 2.2.1.1 and the media were made up with different amounts of solution I-IV. Table 2.2.1.2 shows the composition of each solutions I-IV. All solutions were sterilised using an autoclave (Prestige Medical, Media Autoclave, UK) except for solution III in which a sterile filtration was used as the constituents would decompose high temperature. All solutions and media were stored in a fridge at 4°C until use and a new batch was made up every 6 months.

	Constituent	**Amount**
Solution I (500 mL)	$NaNO_3$	10.0 g
	$K_2HPO_4.3H_2O$	3.14 g
	KH_2PO_4	1.20 g
	Yeast	1.0 g
	Milli /-Q water	500 mL
Solution II (500 mL)	$NaNO_3$	10.0 g
	$K_2HPO_4.3H_2O$	3.14 g
	KH_2PO_4	1.20 g
	Milli-Q water	500 mL
Solution III (500 mL)	D-glucose	36.6 g
	Milli Q water	500 mL
Solution IV (1000 mL)	$MgSO_4.7H_2O$	4.0 g
	Iron (III) citrate	0.01 g
	Milli-Q water	1000 mL

Table 2.2.1.1 Composition for Solution I-IV used to make the pre-culture and test media used in ISO 10712

	Solution	Volume
Pre-culture media (500 mL)	Solution I	13.75 mL
	Solution III	13.75 mL
	Solution IV	27.5 mL
	Milli Q water	445 mL
Test nutrient media (500 mL)	Solution II	15.5 mL
	Solution III	15.5 mL
	Solution IV	31.0 mL
	Milli-Q water	438 mL

Table 2.2.1.2 Composition for pre-culture media and test media used in ISO 10712

Toxicity assays

Bacteria cultures from fridge-stored plates were suspended in pre-culture media and incubated for 16 hours at 25 °C. The bacteria suspensions were then adjusted in concentration so that Optical Density (OD) was 0.5 in the test media as per the protocol. This was to allow OD change measurement from the growth of bacteria. The GO dispersion in water to be tested was then diluted to the desired concentration in the test media. The GO dispersion was sonicated for 30 seconds prior to the dilution. The bacteria suspensions were then added to the GO suspension which was T0h. There were 5 replicates of each concentration, including the negative control without the GO, as well as a blank sample for sterility or cross-contamination checking. All samples were incubated for 24 hours at 25°C in the dark at a shaking speed of 150 rpm (Incu-Shake Maxi Refrigerated Incubating shaker, SciQuip, UK) and at the 24-hour time point, OD and CFU readings were taken.

Optical Density reading

A volume of 200 µL was pipetted out from each replicate of the mixture and onto 96 well plate for the OD readings using a plate reader (Spectramax M2 Microplate reader, Molecular Devices, US). This was performed at T0h and T24h. The difference between OD of T24h and T0h was taken to represent the growth

and change in each mixture. This meant that any change was measured by the OD and the measurements were independent of each other. OD measurements of GO dispersions only were also taken to ensure that the changes were due to the presence of bacteria alone.

Optical imaging

Optical images of bacteria with ARGO were taken using an inverted microscope (Nikon Eclipse TS100, Nikon, Japan) with objective lens at x20 magnification piece. This was used to give a representative image of the interaction of ARGO with the bacteria. Images were taken directly from the well after the 24 hours exposure time period.

Statistical Test

For all toxicity test results with OD and CFU readings, One-way ANOVA statistical test was carried out using OriginPro 2022. The Dunnett test, where the means of control were compared to all other variants, was used to determine whether the presence of GO caused a significant change compared to the control sample. A P-value of 0.05 and 0.01 was used to denote significance which is commonly used in biological test (p-value at 5% and 1%). Table 2.2.1.3 shows the denotation used in the results section with the statistical meaning.

Statistical Denotation	Statistical Meaning
ns	$p>0.05$ (not significant)
*	$p<0.05$ (statistically significant)
**	$p<0.01$ (statistically significant)

Table 2.2.1.3 Statistical denotation used in the toxicity test results in OD and CFU.

Material characterisation

XPS

XPS samples were prepared by drop-cast method onto silica wafer. The samples were dried and measured using a K-alpha+ XPS spectrometer equipped with a MXR3 Al Kα monochromated X-ray source (hν = 1486.6 eV). The X-ray gun power was set to 72 W (6 mA and 12 kV) and charge compensation was achieved using the FG03 flood gun using a combination of low-energy electrons and the ion flood source. Mapping was used to avoid beam damage and the beam spot size was adjusted to 400 µm. All spectra were analysed using Avantage Software and OriginPro 2022. The Mo peak was deconvoluted and analysed for quantification of ageing, as well as comparison with literature. (*27, 36*)

AFM

AFM samples were prepared by diluting the ARGO to 10 mg L^{-1} in Milli-Q water then drop-casting on to freshly cleaved Mica sheets (Agar, UK). The samples were measured using Asylum MFP 3D AFM in AC air topography mode. All images were processed using Gwyddion (Gwyddion, Czech Republic) and Image J software. Size distribution for the lateral diameter was calculated using the same method employed for GOs size distribution. Gwyddion was used to process the images then thresholding was used to create a mask. The masked images were exported to Image J and then using the particle analyser built-in, and the Feret diameter of the particles were calculated. Briefly, the Feret diameter is the distance measured between two parallel planes in which the long and the short distance is averaged to represent the lateral size of an irregular object. It is commonly used in microscopy particle analysis. (*25*)

DLS and Zeta potential

Samples for Dynamic Light Scattering (DLS) were prepared by diluting the dispersion to 50 mg L^{-1}. Measurements were made using a Zetasizer (to take both DLS measurements of the hydrodynamic diameter and zeta potential measurements simultaneously). Because of DLS and zeta potential provides a measurement of behaviour of nanomaterials in different media, these techniques was used to characterise the zeta potential and hydrodynamic diameter of the nanomaterial in test media as well. (*28, 29*) Subsequent data analysis were carried out using OriginPro 2022.

TEM images

ARGO samples were diluted to 10 mg L^{-1} then drop casted onto lacy carbon grids (TAAB Laboratories Equipment Ltd., UK) and dried ambiently. Images were taken in the Harvey Flowers EM suite facility at Imperial College of London. The TEM JEOL 2100F was operated at 200kV to image the samples. Subsequent images processing was carried out using ImageJ.

Raman

Raman samples were prepared by drop-casting the ARGO dispersion at the as-received concentration of 5 mg mL^{-1} on to a silica wafer. Raman measurements were taken using Renishaw inVia micro-Raman (1000–3000 cm−1), using a 50 mW 532 nm laser at 1% laser power. A mapping method was employed to ensure a representative D/G ratio could be obtained from the entire GO sample. The D/G ratio was worked from the normalised intensity of the D and the G band (~1350 cm^{-1} and ~1580 cm^{-1} respectively) from each single measurement. There were over 50 measurement points for each sample of GO taken. All measurements were processed using WiRE 4.1 and OriginPro 2022

2.2.2 Results

Material characterisation of GO dispersion from ACS material

ARGO dispersion in water from ACS material (Single Layer Graphene Oxide Dispersion, DI Water, 5 mg mL^{-1}, Modified Hummer's Method, GNODAW01) was obtained and characterised using AFM, Raman Spectroscopy, XPS, and TEM. The dispersion behaviour of GO was also characterised in water and ISO 10712 test media to understand the behaviour of the GO in the respective solution using Dynamic Light Scattering (DLS) and Zeta potential measurements.

Manufacturer Specification

Although the obtained ARGO dispersion in water was characterised, it was important to note the manufacturer specification of the material for comparison. Table 2.2.2.1 below shows the manufacturer's specification of the ARGO dispersion obtained from ACS material.

ARGO Dispersion in Water	**Manufacturer Specification**
Synthesis method	Modified Hummer's method
Appearance	Dark Brown Dispersion
Solvent	DI water
Lateral size	0.5-2.0 μm
Thickness	0.6-1.2 nm
Single layer ratio	>80%
pH	3-5

Table 2.2.2.1 Characterisation of ARGO, Single Layer Graphene Oxide Dispersions, in DI Water, 5 mg mL^{-1} using the Modified Hummer's Method, GNODAW01 as specified the manufacturer.

The ARGO dispersion in water from ACS material was synthesised using modified Hummer's method. This method is the most commonly used synthesis method. (*60, 69, 86, 87, 105*) Due to the abundant oxygen functional groups on the GOs, the GOs stay exfoliated and form stable dispersion in DI water. The lateral size of the GO flakes was between 0.5-2.0 μm with thickness of the GO flakes in between 0.6-1.2 nm as measured by AFM. Monolayer GOs usually have 1.0 nm thickness measurement on average by AFM and this is comparable to the thickness of graphene sheets which has around 0.4 nm thickness due to the additional functional groups on its graphitic surface. (*60, 69*) The single layer ratio of the GO dispersion was greater than 80% with others mostly bilayers. The pH of the GO dispersion was measured to be between 3-5 indicating that GO in water is acidic. This could be due to the carboxyl groups present on the GO flakes but could also be due to the sulphates from the synthesis method.

Material Characterisation

Although manufacturer have specified their physicochemical properties of ARGO dispersion in water, it is always sensible to characterise the material received to check the quality of the product as well as further characterise the GO to understand the materials' properties. Because 2D nanomaterials are hard to synthesise consistently and to characterise thoroughly, there were instances where the physiochemical properties were different between manufacturer specification and characterisation results. (*27*)

Optical image

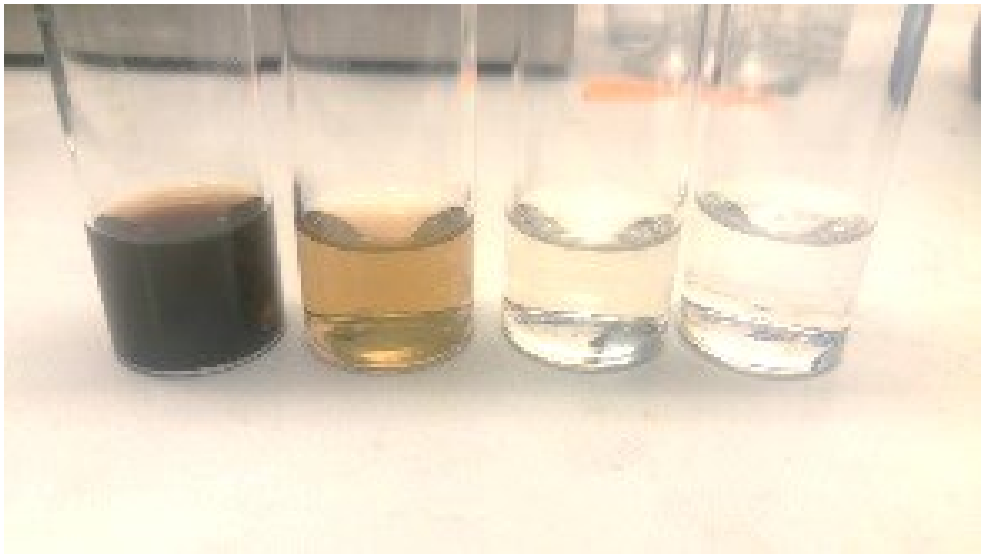


Figure 2.2.2.1 Optical image of monolayer ARGO dispersion in Milli-Q water. Concentrations from left to right: 1000 mg L^{-1}, 100 mg L^{-1}, 10 mg L^{-1}, 1 mg L^{-1}.

The optical image (figure 2.2.2.1) shows the ARGO dispersion in various concentrations between 1 mg L^{-1} and 1000 mg L^{-1}. The image shows a good stable dispersion of the monolayer GO in water with the colour of the GO being dark brown at higher concentrations. As the GO dispersion is serially diluted, the brown colour is diluted. This was indicative of the concentration but also important to consider during sample preparation for characterisation. Diluted samples in the range of 1-10 mg L^{-1} were used to image the dimensions of the GO sheets using AFM and TEM while higher concentration samples were used for chemical characterisation such as XPS and Raman.

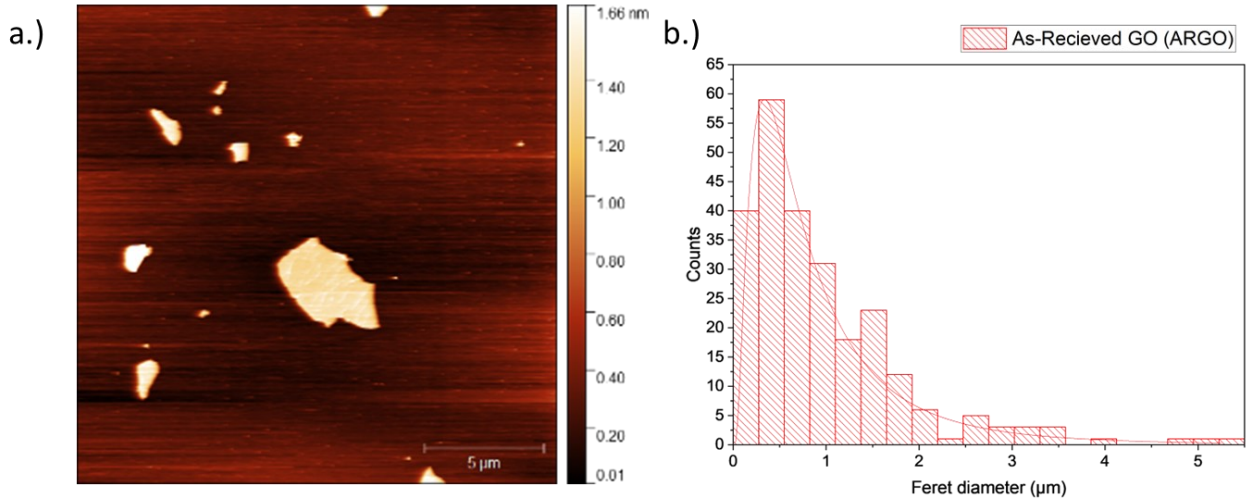


Figure 2.2.2.2 Size measurement obtained by AFM a.) Showing the representative image of as-received GO (ARGO) dispersion in water that has been drop cast on to a freshly cleaved mica sheet at 1 mg L^{-1} b.) Showing the distribution plot of the lateral diameter (measured using the Feret diameter) with a sample size of N = 161 and bin size of 20 (Mean = 0.96 µm, S.D. = 0.80 µm).

AFM measurements of 2DNMs give both lateral and thickness size which are important in the physiochemical characterisation of 2DNMs. As shown in the representative image in figure 2.2.2.2 a.), the AFM images indicated that the GO dispersion was monolayer and as shown in the size distribution plot in figure 2.2.2.2 b.), the average lateral diameter taken from the average Feret diameter is 0.96 ± 0.80 µm. The size distribution plot was plotted with Feret diameter measurements of 161 monolayer GOs from several images. All images taken were similar to that of the AFM images shown in that all GOs were monolayers. The images were processed using Gwyddion (Czech Metrology Institute) and analysed ImageJ (Wayne Rasband). The image backgrounds were flattened and then masked at a threshold of 1 nm in height. The resulting masked images were then converted into binary image and the Feret diameter as well lateral dimension by area was calculated. Most literature reported measuring lateral size using similar method and

therefore the lateral size was represented as a diameter. (*25*) The size distribution showed that, although there are large flakes of size greater than 1 µm with some ranging up to over 5 µm, most flakes had lateral diameter of less than 1 µm. The manufacturer specification only stated that the range of lateral sizes were between 0.5 – 2.0 µm and not the distribution but these results showed that ACS material GO mostly consists of monolayer GO with lateral size less than 1 µm. Further additional AFM images are shown below.

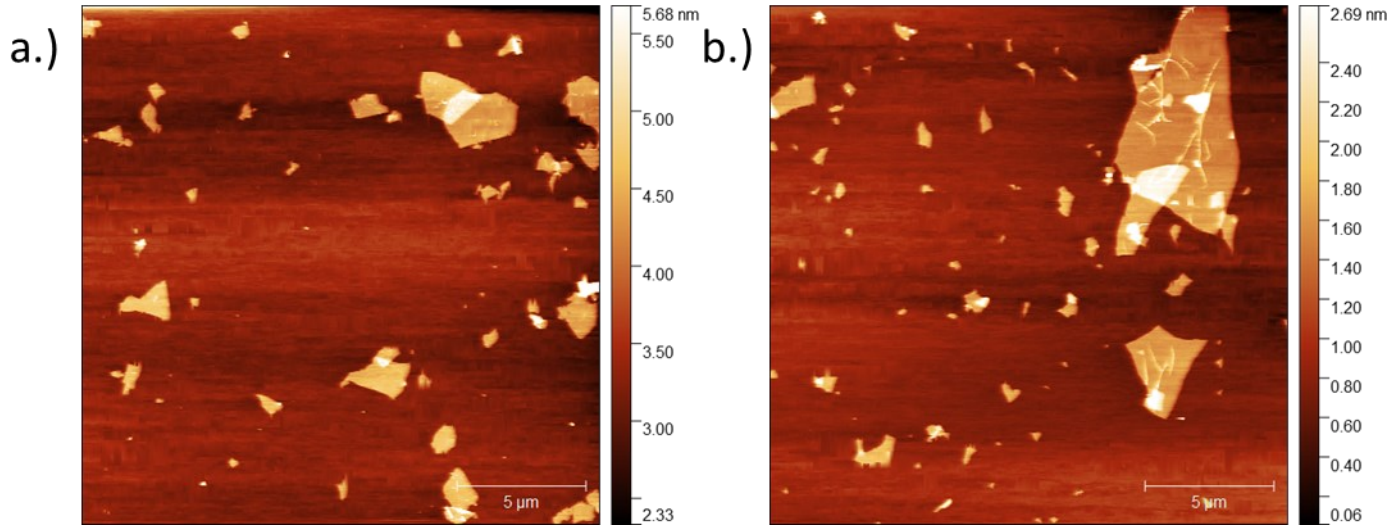


Figure 2.2.2.3 Further example of AFM images obtained

TEM

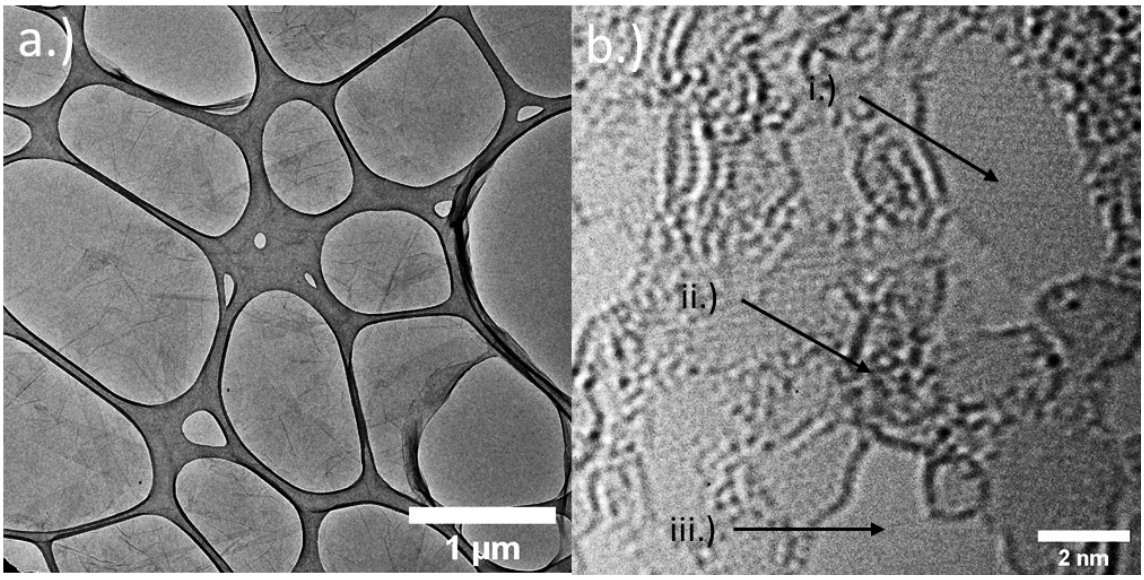


Figure 2.2.2.4 TEM image of ARGO dispersion in water on a lacey carbon copper grid a.) Bright Field low magnification image of monolayer GO dispersion from ACS material b.) Bright Field high magnification image with Cs aberration correction of a GO monolayer with a visible i.) Graphitic region, ii.) Functionalised/defect region, and iii.) holes as pointed by each arrows associated.

The TEM images of ARGO from ACS material (figure 2.2.2.4) showed the heterogenous nature of GO, also reported on in other high resolution TEM studies. (*39*) Figure 2.2.2.4 a.) shows the low magnification TEM image shows monolayers of GO laying over the holes of lacey carbon films. Figure 2.2.2.4 b.) The high magnification image was taken from one of the areas of monolayer GO in the holes of lacey carbon film. The high magnification image shows examples of: i.) graphitic regions, ii.) defected / functionalised regions, and iii.) holes on the monolayer GO. This was typical of high resolution image of GO where the GO structure matches the model structure based on Lerf-Klinowski model. (*69, 158*) Typical GO has regions of graphitic sp^2 carbon with functionalised sp^3 carbon. During the oxidation process of graphite in the Modified Hummers method, part of the graphitic region is oxidised to form the functionalised region

seen which consists of carbonyl, hydroxyl, carboxyl groups. The harsh condition can often also cause holes and breaks in the graphitic network during synthesis which again can be observed in the image. Therefore, the TEM result demonstrated that the ARGO from ACS material is of a typical monolayer GO synthesised using modified Hummer's method.

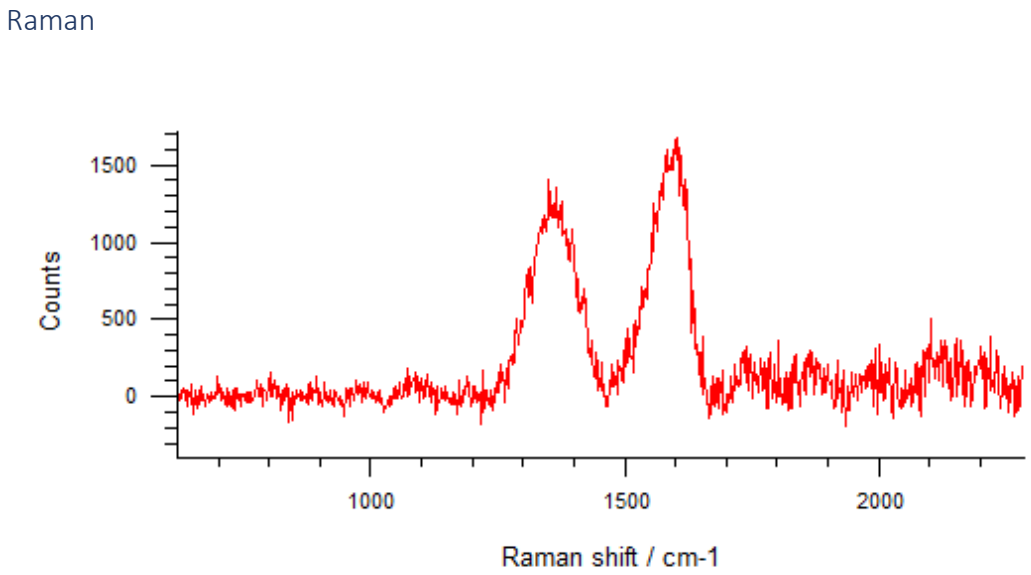


Figure 2.2.2.5 Representative Raman spectra of one of multiple measurements. The peak around 1300 cm^{-1} represents the D peak and the peak around 1600 cm^{-1} represents the G peak

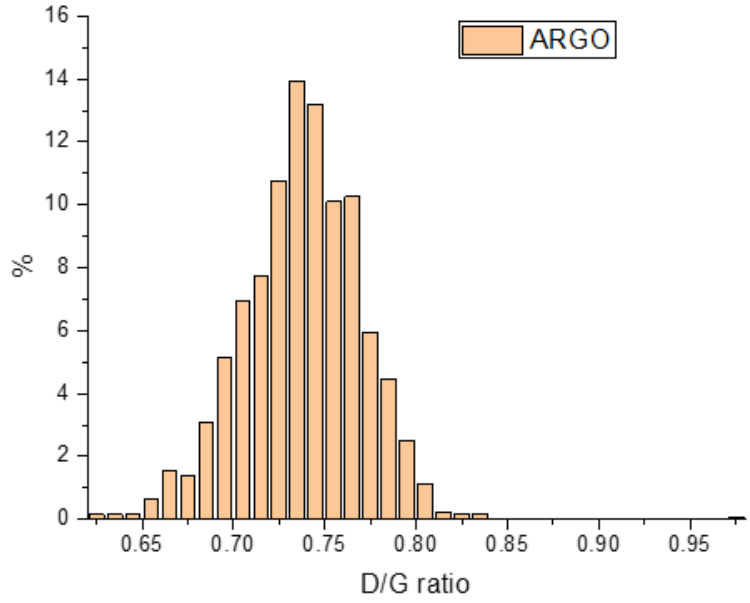


Figure 2.2.2.6 D/G ratio distribution plot of as-received GO (ARGO) from ACS material deposited on silica wafer (5 mg mL-1). Mean = 0.74, S.D. = 0.03, Sample size N = 1227.

Raman measurements are often used in the characterisation of graphitic carbon nanomaterials such as GFNs and CNTs. The D/G ratio value gives a good indication of the amount of defects or quality of the graphitic material as the intensity of D band and G band relates to the amount of sp^3 and sp^2 carbon respectively. Figure 2.2.2.5 shows a typical Raman spectrum of GO with D and G band at position 1300 cm^{-1} and 1600 cm^{-1}. Typical high quality graphene sheets only have in-plane vibrations due to high amount sp^2 carbon and therefore have low D/G ratio. On the other hand, as the amount of defects increases, the amount of out-of-plane vibration increases due to an increase in sp^3 carbon leading to an increase in D/G ratio. Figure 2.2.2.6 shows the distribution of D/G ratio from the mapping measurement of GO on silica wafer. The D/G ratio of 0.74 does not indicate particularly high amount of defect as D/G ratio of GO could be as high as 3. (*159, 160*) However, a D/G ratio of this value is still typical of GOs reported in the literature and the distribution

plot of D/G ratio shows that most GO flakes had the D/G ratio of 0.74 with no significant deviation from the mean value.

XPS

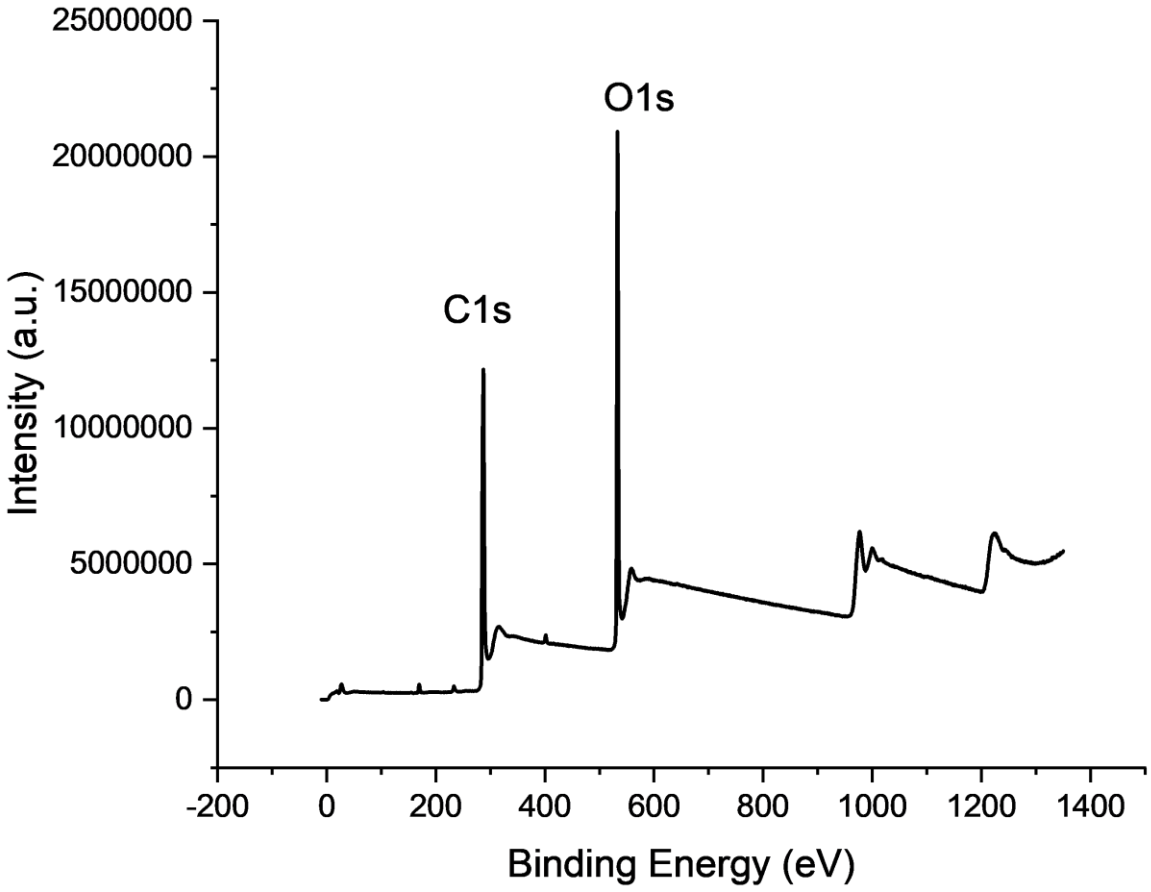
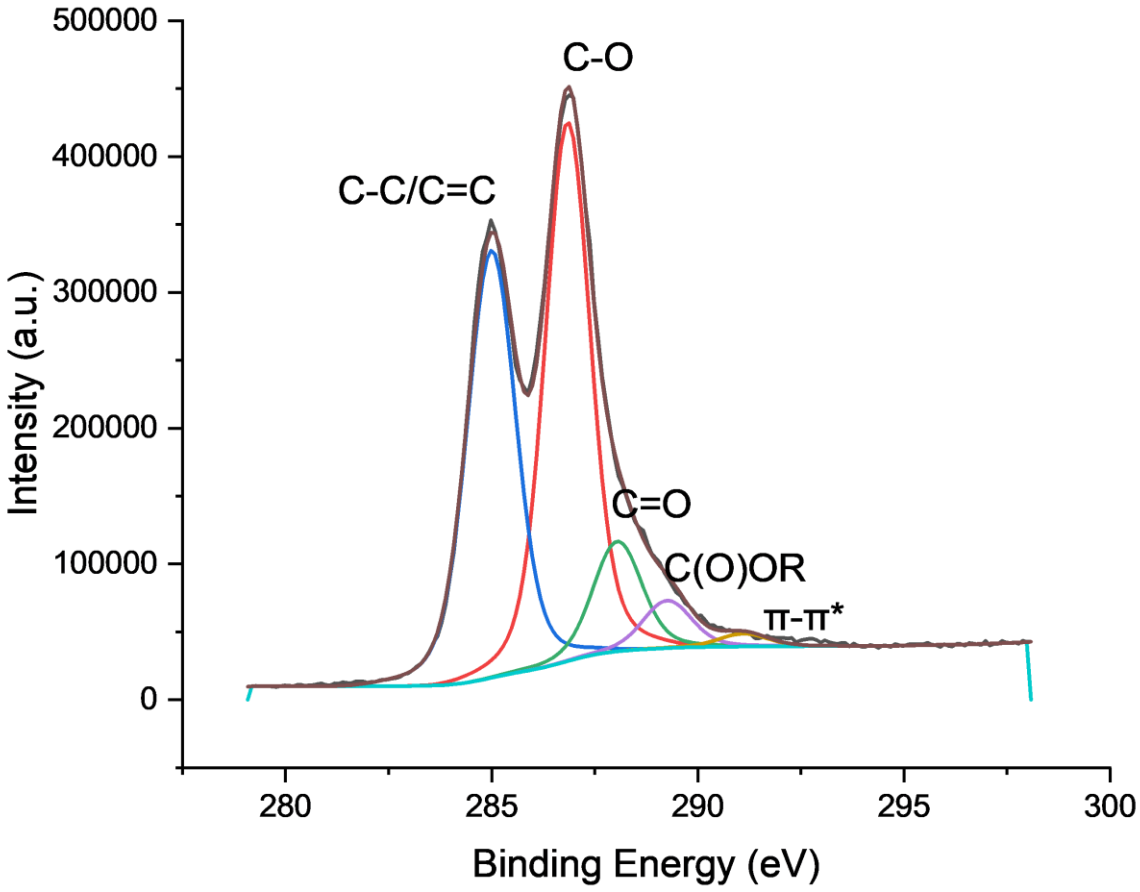


Figure 2.2.2.7 XPS survey spectra of ACS material ARGO drop-casted on silica wafer with the main chemical transition peaks labelled.



1935

Figure 2.2.2.8 High resolution XPS spectra of the C1s transition peak of ACS material ARGO sample on a silica wafer. The spectra had been deconvoluted and fitted to show the different chemical environments of C1s.

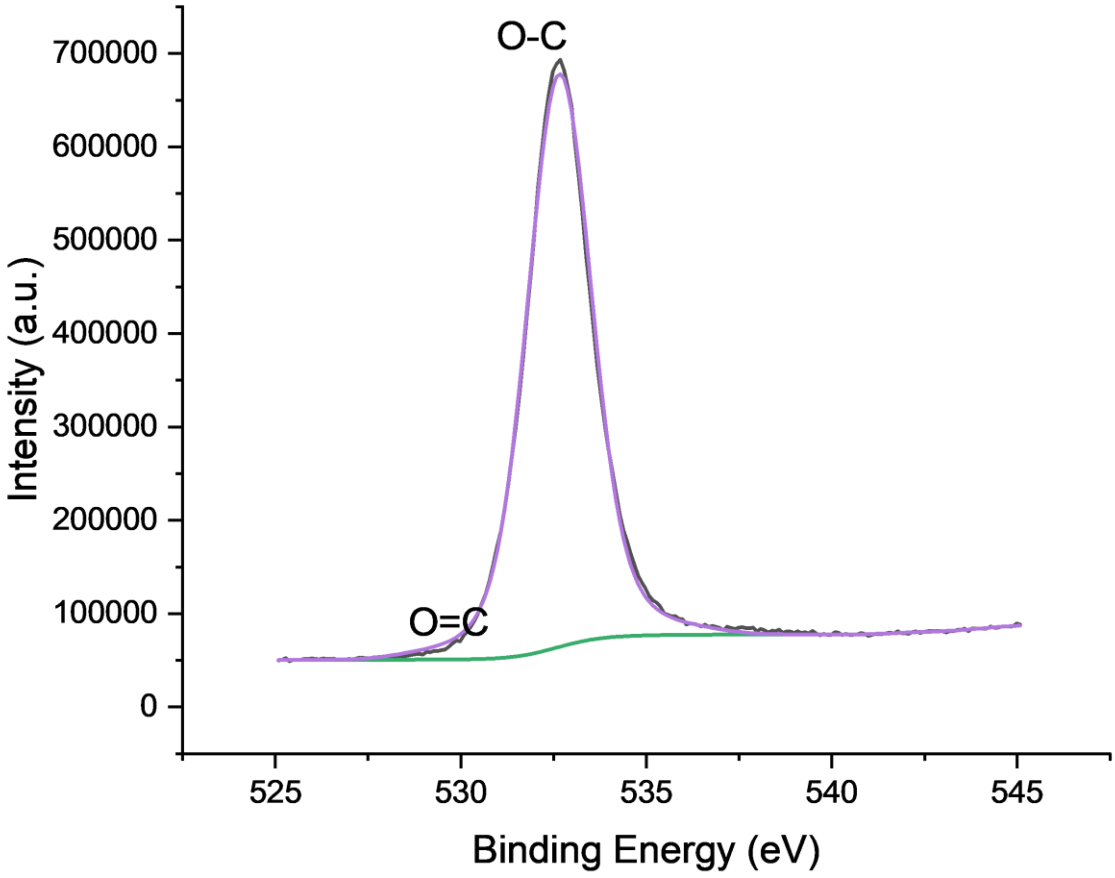


Figure 2.2.2.9 High resolution XPS spectra of the O1s transition peak of ACS material ARGO sample on a silica wafer. The spectra had been deconvoluted and fitted to show the different chemical environments of O1s.

The survey spectra of ACS material ARGO on a silica wafer showed that the GO dispersion mainly consisted of C and O (figure 2.2.2.7). The atomic % of the elements detected is summarised in table 2.2.2.2.

	Atomic %				
	C	**O**	**N**	**S**	**Si**
As-Received GO from ACS Material	66.84	31.75	0.92	0.14	0.35

Table 2.2.2.2 Elements detected in the survey XPS spectra of GO from ACS material on silica wafer.

There were trace amounts of S, N, and Si in the as-received GO sample, but these were less than 1%. It is typical of a GO dispersion to contain traces of S and Mn from the residue of modified Hummer's method but the amount of below 1% was significantly below any reported toxicity level of these elements. (*97, 117*) More importantly, there was no Mn detected, meaning that the GO from ACS material was washed thoroughly of any impurities. The presence of N was from the small adsorption of nitrogen in the atmosphere, and the Si was from the silica wafer.

The high-resolution spectrum of C1s region (figure 2.2.2.8) and O1s region (figure 2.2.2.9) are often used for characterisation and analysis of GO. In the C1s, the measured XPS was deconvoluted into 5 chemical shifts: C-C/C=C (284.99 eV); C-O (286.84 eV); C=O (288.05 eV); C(=O)-(OH) (289.26 eV); and π-π* satellite peak (291.1 eV). In the O1s, the measured XPS was deconvoluted into 2 chemical shifts: O=C (530.76 eV); and O-C (532.66 eV). The deconvolution summary of each chemical environment of C1s and O1 is summarised in table 2.2.2.3 and 2.2.2.4.

C1s chemical environment	**Peak BE (eV)**	**Amount (%)**
C1s C=C/C-C	284.99	38.86
C1s C-O	286.84	45.59
C1s C=O	288.05	10.03
C1s C(O)OR	289.26	4.33
C1s π-π*	291.1	1.18

Table 2.2.2.3 The Peak B.E. of different deconvoluted chemical environments of GO from ACS material on a silica wafer together with the relative amount of each transition from the high-resolution C1s XPS spectra.

O1s chemical environment	**Peak BE (eV)**	**Amount (%)**
O1s O=C	530.76	0
O1s O-C	532.66	100

Table 2.2.2.4 The Peak B.E. of different deconvoluted chemical environments of GO from ACS material on a silica wafer together with the relative amount of each transition from the high-resolution O1s XPS spectra.

The high resolution XPS results (figure 2.2.2.8 and 2.2.2.9) together with the summarised table with relative amount (table 2.2.2.3 and 2.2.2.4) showed that the ARGO were highly oxidised. The values and the analysis were comparable to that of other highly oxidised GO (*161, 162*) with the result showing O/C ratio of 0.5, and most of the oxidised carbon as C-O where the carbon atom is oxidised to hydroxyl carbon instead of carbonyl or carboxyl group.

DLS/Zeta potential and pH

DLS and zeta potential measurements were taken to understand the colloidal behaviour of the GO in water but also in test media used in ISO 10712.

	Z-average (nm)	**PDI**	**Zeta potential (mV)**
50 mg L^{-1} GO in Milli-Q water	398.6±4.8	0.30±0.02	-49.6±0.6
50 mg L^{-1} GO in ISO 10712 Test Media	604.4±29.2	0.36±0.05	-28.7±1.5

Table 2.2.2.5 DLS measurement of Z-average (hydrodynamic diameter), Polydispersity Index (PDI) and Zeta potential measurement of ARGO dispersion in Milli-Q water and ISO 10712 test media (pH 7) at 50 mg L^{-1}.There were 3 independent measurements with each measurement consisting of +10 measurements. The values presented are average values ±the standard deviation.

The DLS and the zeta potential measurements shown in table 2.2.2.5 showed that the GO was better dispersed and more stable in water than the test media used in ISO 10712. Zeta potential measurements, which are often used to indicate the stability of nanoparticles in suspension, indicated that the GO was significantly stable in water (>±40 mV) and less stable in the test media (10-30 mV).(*163*) This was reflected in the PDI which was lower in water than in test media. Decreased stability often leads to

agglomeration of nanoparticles, and this was reflected in the higher value of Z-average of GO in test media than the GO in water.

	pH	
GO concentration	**Milli-Q Water**	**ISO 10712 Test media**
0 mg L^{-1}	7.40±0.41	7.08±0.03
50 mg L^{-1}	4.75±0.14	6.86±0.03
150 mg L^{-1}	3.98±0.07	6.74±0.03

Table 2.2.2.6 pH of GO dispersion (5000 mg L^{-1}) diluted in Milli-Q water and ISO 10712 test media at the concentrations tested in the toxicity test in chapter 2.2.2. pH was measured in triplicate ±S.D.

The pH of GO in water and test media of ISO 10712 was measured at different concentrations relevant to the toxicity test that was carried out and summarised in table 2.2.2.6. The pH results showed that the GO dispersion obtained was inherently acidic and that ISO 10712 test media could act as a buffer to neutralise the pH of GO. There are couple of possible reasons for the measured acidity. One is the presence of the residual sulphate from the synthesis and the other is the inherent acidity of the GO from their oxygen functional groups. (*117, 164*) It was likely that the acidity was mainly from the GO itself rather than the sulphates or impurities as XPS results suggested that the GO dispersion was washed thoroughly to remove the impurities.

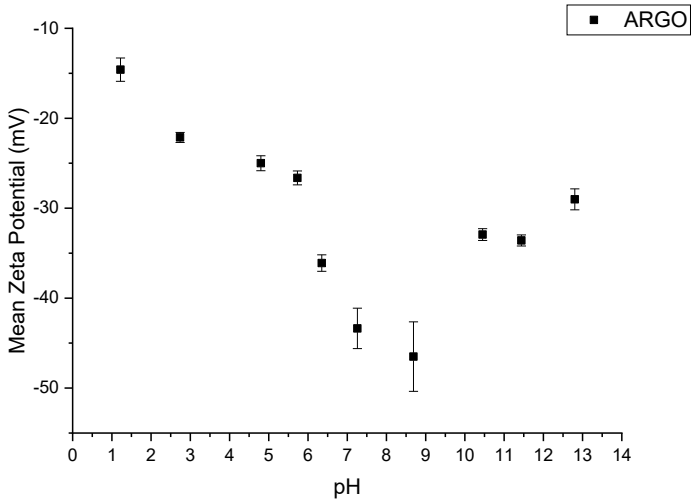


Figure 2.2.2.10 Zeta potential measurement of as-received GO (ARGO) dispersion from ACS material in different pHs (50 mg L^{-1}). The pH was adjusted using 0.1M NaOH and HCl at 25 °C

The range of zeta potentials of ARGO at different pHs shown in figure 2.2.2.10 showed that GO was unstable in extremely acidic conditions. The GO was shown to be most stable around the pH of 8. This was consistent with other colloidal studies reported where the pKa of GO was reported to be 4.3, 6.6, and 9.8. (*165, 166*) This was due to the different carboxyl and carbonyl groups on the GO with different pKa where at acidic pH, the GO became fully protonated and no longer hydrophilic. The result here showed that GO's colloidal behaviour was indeed governed by the range of rich functional groups on the GO nanosheet, where the plot showed inflection points similar to those seen in previous reports by other groups.

	Time (h)	Z-average (nm)	PDI	Zeta potential (mV)
GO in Milli-Q water (50 mg L^{-1})	0	398.64±4.77	0.30±0.02	-49.64±0.64
	4	396.46±4.69	0.30±0.04	-48±0.95
	24	400.46±3.66	0.29±0.03	-47.04±0.89
GO in ISO 10712 Test media (50 mg L^{-1})	0	604.38±29.16	0.36±0.05	-28.72±1.51
	4	696.64±25.39	0.40±0.05	-29.08±1.66
	24	715.76±17.62	0.39±0.05	-27.76±1.45

Table 2.2.2.7 DLS results of hydrodynamic diameter (Z-average) and PDI as well as Zeta potential measurement of ARGO dispersion in Milli-Q water and ISO 10712 test media (50 mg L^{-1}) at 0h, 4h, and 24h time points.

Table 2.2.2.7 showed the different stability of ARGO dispersion in both Milli-Q water and test media at 0h, 4h, and 24h. As stated earlier, GO was more stable in Milli-Q water than ISO 10712 test media and this is shown in the 0h DLS and zeta potential data for GO in Milli-Q water and ISO 10712 test media. The time-dependent measurements of DLS and zeta potential of GO in Milli-Q water and ISO 10712 test media showed that GO in water was stable throughout the 24-hour period. However, in ISO 10712 test media the GO was less stable and showed signs of slight agglomeration throughout the 24-hour period, even under shaking (replicating of toxicity test conditions in chapter 2.2.2). Again, these results supported the incipient instability of GO in ISO 10712 test media and that the GO could agglomerate over time during the course of a biological test with bacteria (in chapter 2.2.2).

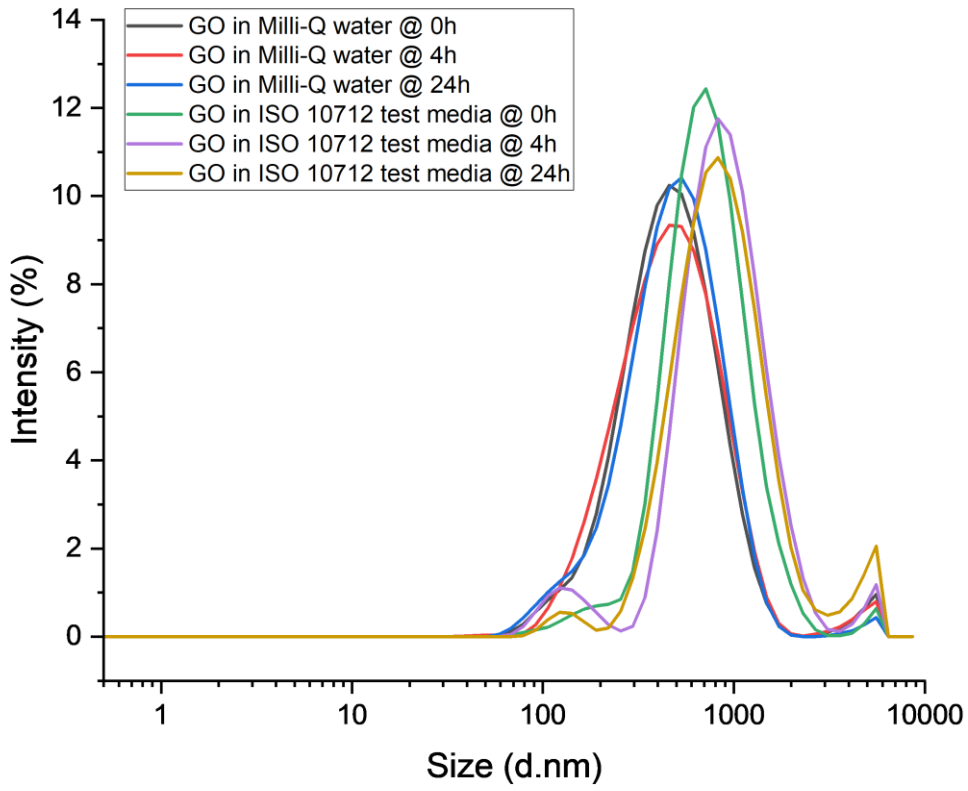


Figure 2.2.2.11 DLS hydrodynamic diameter plot by intensity of GO dispersion in Milli-Q water and ISO 10712 test media at 0 hour, 4 hours, and 24 hours. Each plot was average of three repeated measurements at concentration of 50 mg L^{-1}.

The hydrodynamic diameter plot by intensity, shown in figure 2.2.2.11, showed that ARGO was stable in Milli-Q water at all of the time points. The plot showed main large peak at 459 nm, which is similar to the Z-average value in table 2.2.2.7, suggesting that the GO dispersion in water remained stable and monodisperse. Discrepancy in the Z-average value and main peak position given by size intensity plot indicates polydisperse sample as explained before in chapter 1.4.2. GO in ISO 10712 test media showed a large peak at 712 nm at 0h and then a shift in the peak position to 825 nm at 4h and 24h. This observation of an increase in the hydrodynamic diameter of the GO measured was consistent with the Z-average

increase measured. This again supported the incipient instability of GO in ISO 10712 test media which could lead to agglomeration and effects on the behaviour of GO towards soil bacteria during the toxicity tests.

Toxicity testing: ISO 101712

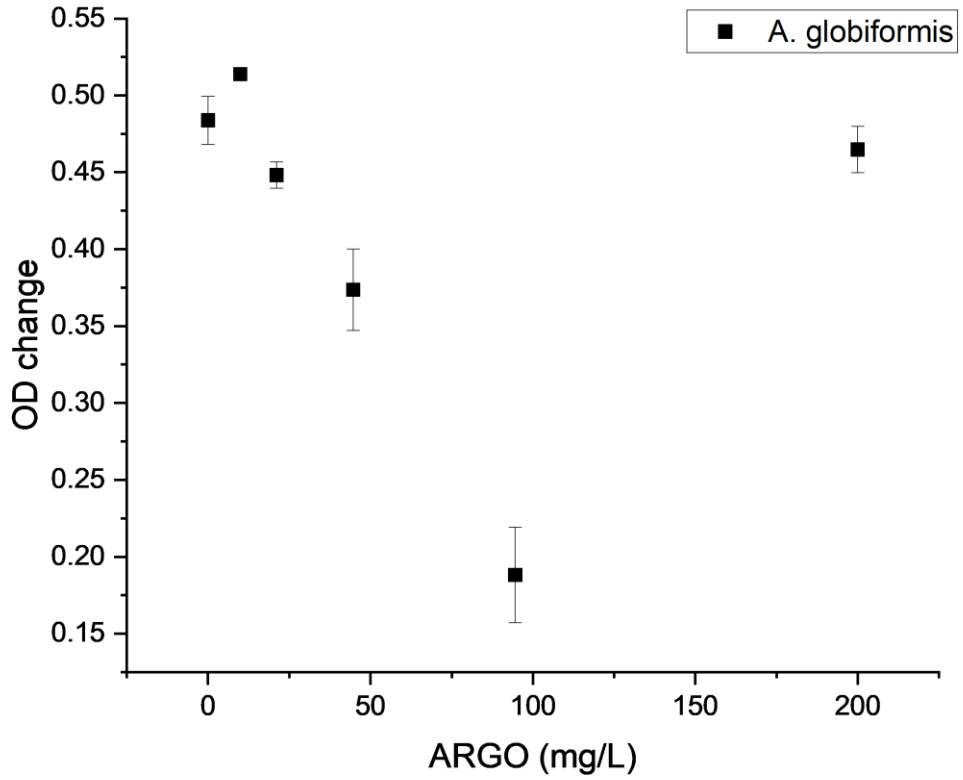


Figure 2.2.2.12 OD change of *A. globiformis* with increasing dose of ARGO dispersion in the concentration range between 0-200 mg L^{-1}. The OD change was calculated at T0h and T24h (same sample left for 24-hours' exposure) and each data point is an average of 5 independent samples. The error bars represent the standard error.

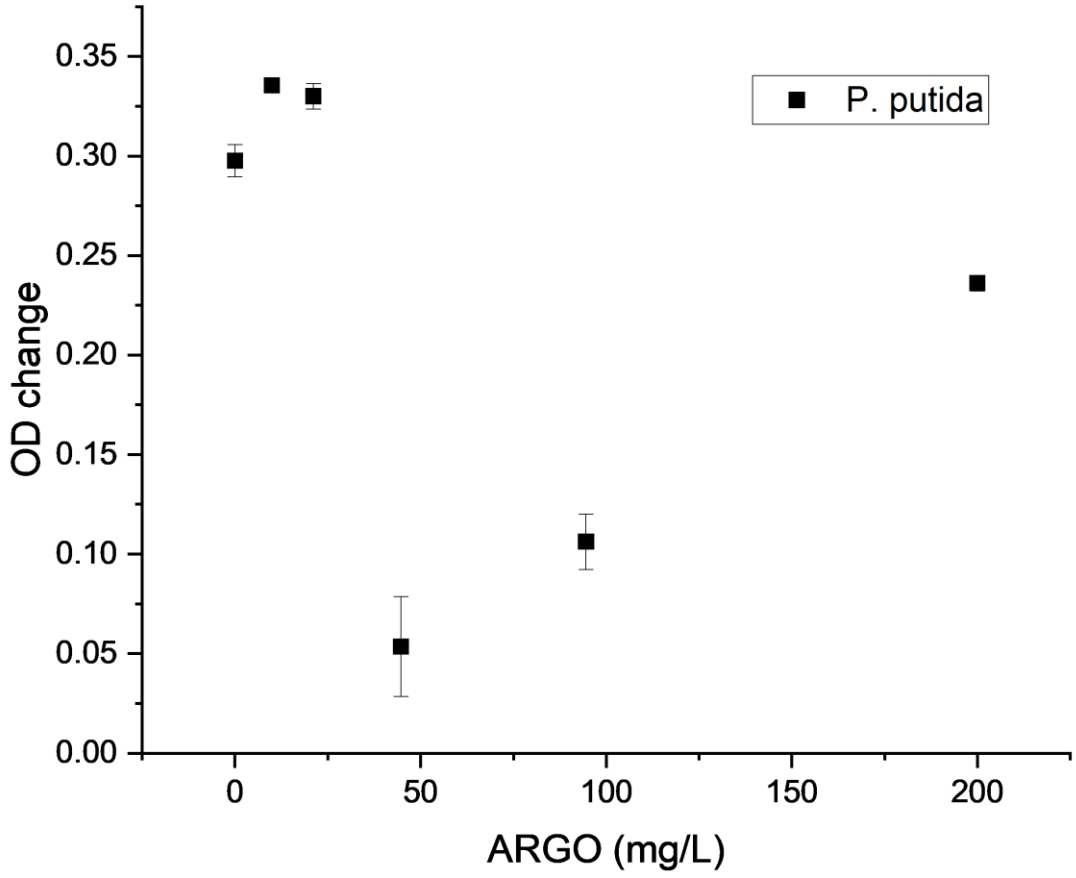


Figure 2.2.2.13 OD change of *P. putida* with increasing dose of ARGO from ACS material dispersion in the concentration range between 0-200 mg L^{-1}. The OD change was calculated from OD reading at T0h and T24h sample (same sample left for 24-hour exposure) and each data point is an average of 5 independent samples. The error bars represent standard error.

The initial toxicity test result from the ISO 10712 method is presented in figure 2.2.2.12 and figure 2.2.2.13. The OD change measures the Optical Density value difference between the T0h and T24h of bacteria with different concentration of material to be tested. In theory, the OD change therefore indicates the growth or proliferation of the bacteria and comparison of the OD change value with the control (0 mg L^{-1}) shows the effect of the material on the growth of the bacteria.

Figure 2.2.2.12 showing toxicity test result of GO with *A. globiformis* showed that presence of GO could potentially inhibit the growth of *A. globiformis* but not completely. *A. globiformis* with up to 100 mg L^{-1} of GO showed decreasing OD change compared to the control. At 100 mg L^{-1} GO caused the highest inhibition to the growth of *A. globiformis*. However, at 200 mg L^{-1} there seemed to be a recovery of growth where the OD change increased from the 100 mg L^{-1} of GO to a OD change value comparable to the control. This pattern of initial decrease in the OD change value indicating inhibition of growth then increase in OD change value indicating recovery growth was observed in the plot of GO with *P. putida* as well. With the GO and *P. putida* OD change plot shown in figure 2.2.2.13, the highest inhibition was observed at 50 mg L^{-1} indicating the possibility of higher sensitivity of *P. putida* towards GO. However, it should be noted that during the experiment there was significant agglomeration at the end of 24-hour period (figure 2.2.2.2.14).

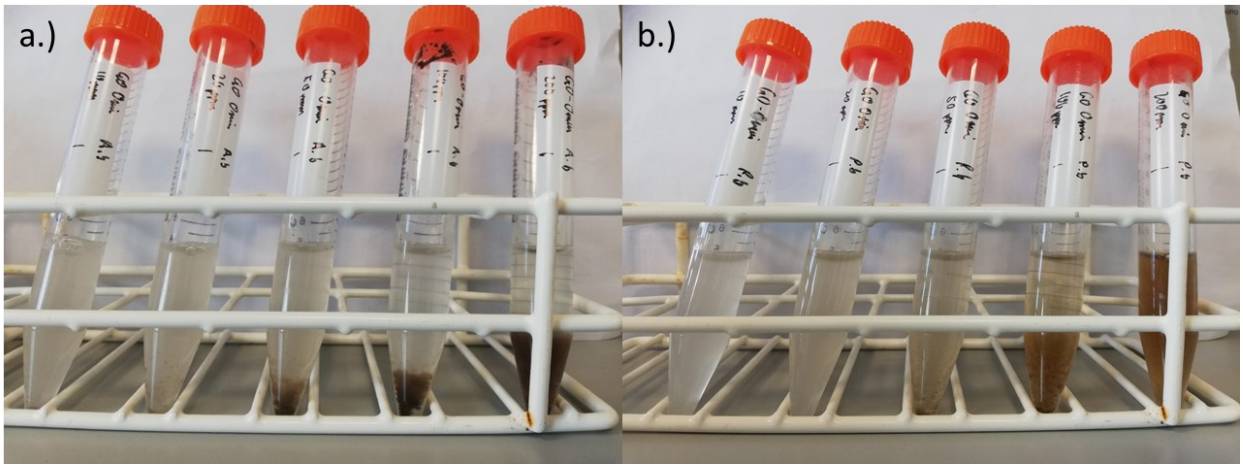


Figure 2.2.2.14 Optical images of bacteria with ARGO from ACS material with concentrations of 0, 10, 21.15, 44.72, 94.57, and 200 mg L^{-1} (from left to right) at 24-hours. e a.) *A. globiformis* and b.) *P. putida*.

The optical images (figure 2.2.2.14) taken after the toxicity test with GO and the bacteria showed that there was significant aggregation especially at higher concentration of GO. The dark aggregates could be re-

suspended but would quickly settle again within few minutes. This suggested that the GO interacted strongly with bacteria in the media and formed aggregates with the bacteria under experimental conditions. In chapter 2.3, and in its subsequent chapter, the interaction between GO and bacteria as well as GO and media will be discussed in more detail with additional results.

In the following discussion section, initial results are discussed with potential problems of the current set up of the ISO 10712 toxicity test method.

2.2.3 Discussion

Material characterisation of GO from ACS material showed that these GOs were predominantly monolayer with a mean lateral diameter of around 1 μm. More significantly, these GOs were well oxidised with plenty of defects, measured by Raman spectroscopy. XPS results showed that these GOs had carboxyl, carbonyl, and hydroxide groups with mostly sp^3 carbon which again represented well oxidised GOs. High-resolution TEM images revealed that, as well as the highly functionalised region and graphitic region, there were holes present from strong acidic conditions used in the oxidation process during modified Hummer's method. (*39*) It was also prevalent from the XPS result that the GO dispersion from ACS material were washed thoroughly with very little impurities. This indicated that the acidity of GO dispersion measured from the pH meter was mainly due to the inherent acidity of GO from the oxygen functional groups present. Although the origin of this acidity is debated since the structure of GO is still to be elucidated, the range of pH and the stability of GO in aqueous dispersion, due to its oxygen functional groups, were consistent with other literature. (*86, 104, 106, 154, 167*) The stability of GO dispersion in water was shown by DLS and zeta potential measurements. Very large negative values of GO in water, as well as the small PDI value and the plot of size intensity and Z-average, showed that the GOs were negatively charged in water with a monodisperse dispersion of GO.

The stability of GO decreased as the GO were dispersed in test media used in ISO 10712. The DLS and zeta potential measurements showed that GOs in test media were starting to become destabilised. The results indicated that the salt ions in the test media decreased the surface negative charge on the GOs and increased agglomeration. The pH measurement of GO dispersed in test media showed that the acidity of GO was buffered in the test media. This was expected as most biological media has a buffer and the ISO 10712 does have monopotassium phosphate, and dipotassium phosphate which act as a buffer. Moreover, as mentioned in the previous colloidal studies presented by Wu *et al*. and Zhao *et al*. presence of salt ions alone could promote aggregation. (*122, 123*) A stronger ionic strength and larger cations or more positively charged cations caused more aggregation of GO. Na^{+}, K^{+}, and Mg^{2+} cations could promote aggregation of GO.

The toxicity test result by OD change showed inhibition but also recovery of growth. This could be interpreted to arise as a lower concentration of GO, GOs existed in monolayer and caused membrane damage by a "nano-knife" mechanism, and at higher concentration of GO, the GO would either wrap, to starve the cells, or enhance the growth of cells by providing a supporting scaffold of GO. However, as the optical image showed, there was significant agglomeration of GO in the mixture of bacteria in the media where the "nano-knife" mechanism is unlikely to occur. (*121*) Moreover, the OD measurement could have been heavily affected by the heavy aggregation of GO. Therefore, the OD change alone could not be used to draw conclusions about the underlining mechanisms suggested by the toxicity testing results. It was perfectly plausible for the slight inhibition and growth recovery to arise from a competing mechanism of wrapping of the bacteria, possibly starving the bacteria of nutrients in the media and the scaffolding mechanism that enhances growth. However future work is needed to confirm this hypothesis.

2.3 Repeats of ISO 10712 with modifications

2.3.1 Introduction

The initial ISO 10712 toxicity test carried out against *A. globiformis* and *P. putida* using GO dispersion from ACS material, revealed that GO dispersion in the given experimental conditions showed both an inhibitory and enhancement of growth. To further explain these observations, to corroborate the findings of the results obtained by OD change method, other toxicity assays had to be added to the protocol to complement the ISO 10712. For this reason, the CFU method (Colony Forming Unit method), was used, where the mixture was spread onto a nutrient-rich agar to measure the active bacteria present after the exposure period was completed. This method selected were both a traditional method used to estimate the number of viable bacteria and an end-point assay used to demonstrate whether inhibition was bactericidal or bacteriostatic, in conjunction with the OD results.

2.3.2 Methods

2.3.2.1 Additional method to ISO 10712

As well as the OD readings, there were additional methods to ensure better understanding of the toxicity results.

Colony Forming Unit reading

After 24 hours incubation performed in the toxicity test and the final optical density reading, the mixtures were serially diluted to the specified concentration. For *A. globiformis*, the mixture was diluted 3-fold, and

for *P. putida*, the mixture was diluted 5 folds. Then 50 µL from the diluted samples were taken out and plated out on to LB agar. All plates were incubated for 48 hours or longer until sufficient colonies formed for counting. The CFU readings were converted back to the original dilution for results.

Abiotic condition test

As well the negative controls without the GO material and the sterile controls without GO and bacteria, a control without bacteria with only GO was added for the OD measurement. This was added to study the extent of interaction of GO with the test media and to compare against the GO-bacteria mixture.

During the toxicity test, samples without bacteria were also measured using a 96 well plate reader at T0h and T24h. Equivalent concentrations matching the range used in the toxicity test were prepared and incubated in the same conditions for 24 hours in the dark (25 °C, 150 rpm)

Further data analysis

In order to compare across all results of toxicity test carried out, the results were normalised against the control from each toxicity test run. Each experiment had 0 mg L^{-1} of GO control that the other concentration range of GO results were normalised to and converted into percentage.

2.3.3 Results

As well as CFU result and abiotic result, additional test results of GO from ACS material were presented since there were other considerations which were external factors that could have influenced the toxicity test results (COVID-19, site movement, equipment changes etc.). All of the proliferation results (figures 2.3.3.1-2.3.3.4 and tables 2.3.3.1-2.3.3.2) consisted of results from 3 different occasions. In figures 2.3.3.1-

2.3.3.4, the pink shades report results from the initial ISO 10712 toxicity test run at Centre for Ecology and Hydrology (CEH) in 2019. The green shades report results from second batch of results from CEH after their equipment and facility was refurbished in 2020. The blue shades reported results from Imperial College of London after the pandemic carried out in 2021 and 2022 (experiments had to be relocated due to limited lab access at CEH during the pandemic). The repeats were numbered in chronological order in which they were performed. The variations in the conditions are detailed in the table below with the different shaking speeds and locations together with the ANOVA statistic test results.

Toxicity of GO measured by OD and CFU method using updated ISO 10712

Figures 2.3.3.1-2.3.3.4 present all of the ISO 10712 test results on GO from ACS material. Both the OD change results and CFU results were presented separately. In some of the toxicity test runs, only results on the OD changes were obtained. The reasons being that the CFU method was only introduced to corroborate the CFU results on the effect of GO on the soil bacteria and to bypass the problem presented with agglomeration during the exposure period. The raw OD and CFU are included in the Appendix.

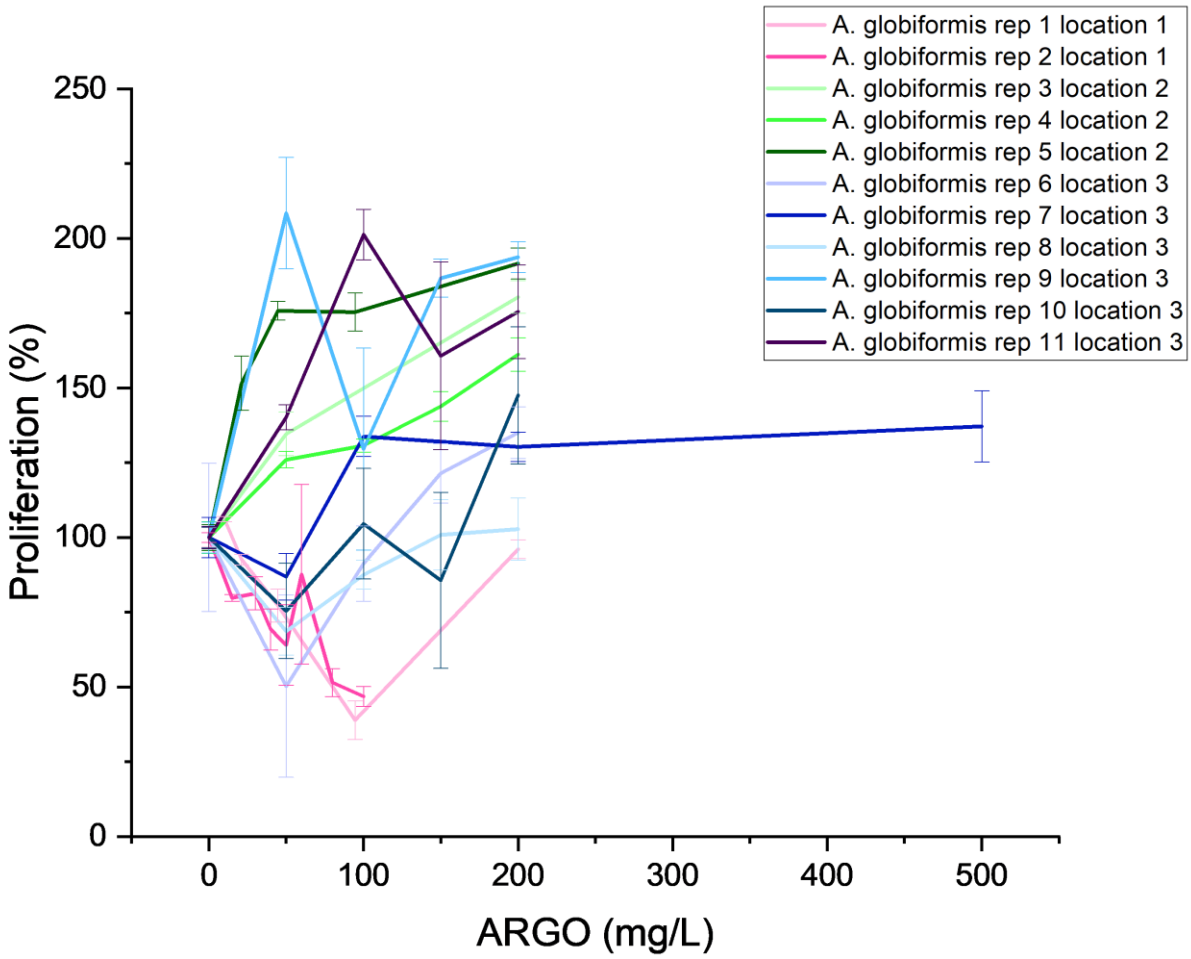


Figure 2.3.3.1 Proliferation of *A. globiformis* after exposure to ARGO from ACS material based on OD changes. The toxicity test results of all ISO 10712 runs against *A. globiformis*. This proliferation plot was based on the OD change data with 5 replicates for each of the data points with each error bar representing the standard error. Each of the samples were run independently from the other. Each shade of colour represents the location and the time frame in which the experiment was carried out. The shade of pink represents experiments carried out at Location 1 in 2019. The shade of green represented experiments carried out at Location 2 in 2020. The shade of blue represented experiments carried out at Location 3 in 2021 and 2022.

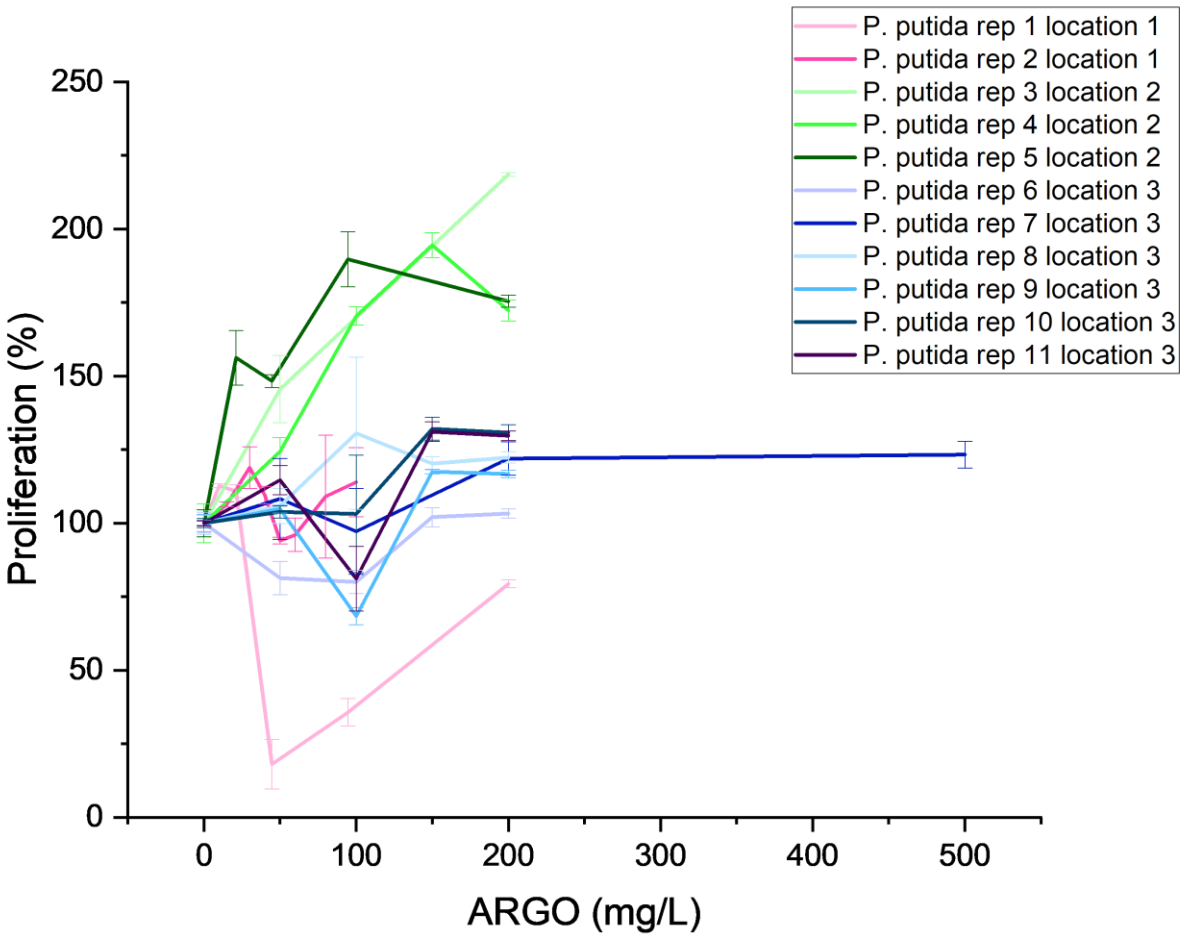


Figure 2.3.3.2 Proliferation of *P. putida* with ARGO from ACS material based on OD changes. Toxicity test results of all ISO 10712 runs against *P. putida*. This proliferation plot was based on the OD change data with 5 replicates for each of the data points with each error bar representing standard error. Each of the samples were run independently. Each shade of colour represents the location and the time frame in experiment was carried out. Pink shades represent experiments carried out at Location 1 in 2019. Green shades represent experiments carried out at Location 2 in 2020. Blue shades represented experiments carried out at Location 3 in 2021 and 2022.

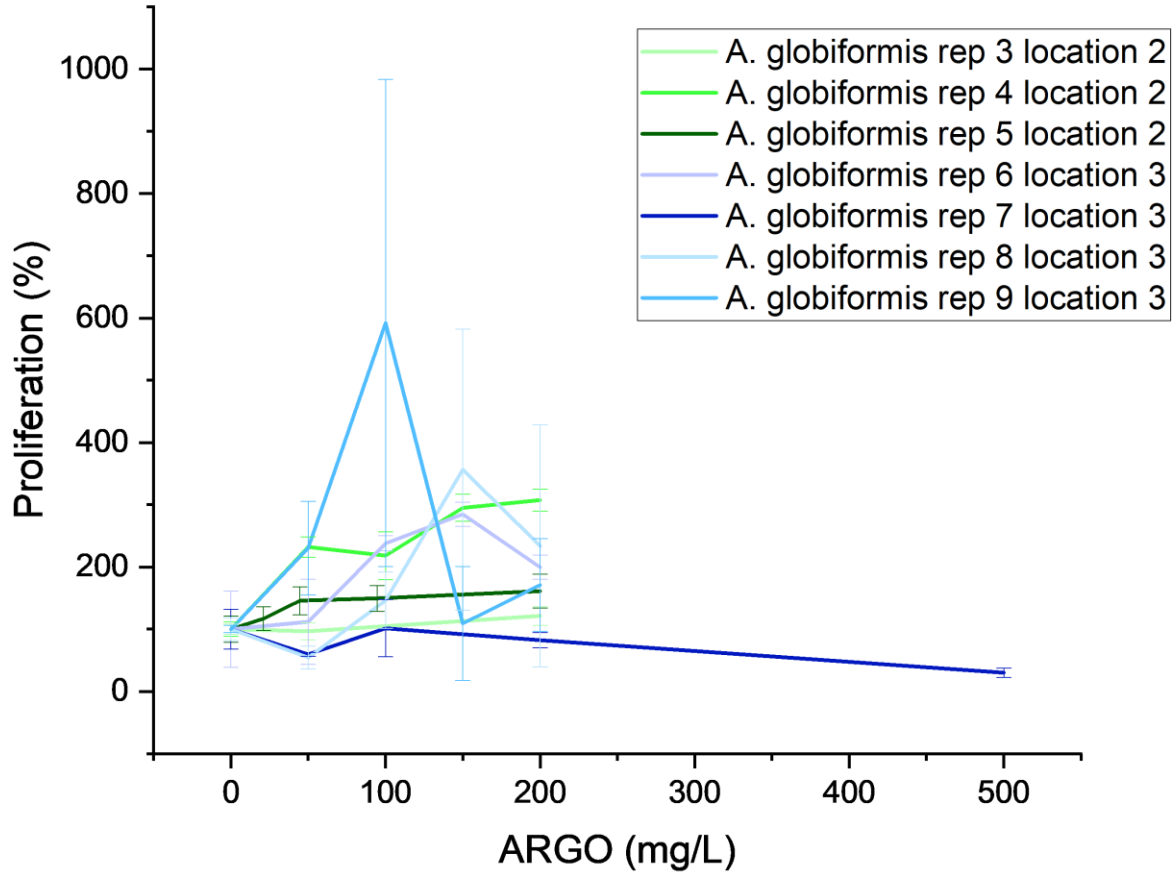


Figure 2.3.3.3 Proliferation plot of *A. globiformis* with ARGO from ACS material based on CFU results. Toxicity test results of all ISO 10712 runs against *A. globiformis*. This proliferation plot was based on the CFU data with 5 replicates for each of the data points with each error bar representing the standard error. Each of the samples were run independently from the other. Each shade of colour represents the location and the time frame in which the experiment was carried out. Pink shades represent experiments carried out at Location 1 in 2019. Green shades represent experiments carried out at Location 2 in 2020. Blue shades represent experiments carried out at Location 3 in 2021 and 2022.

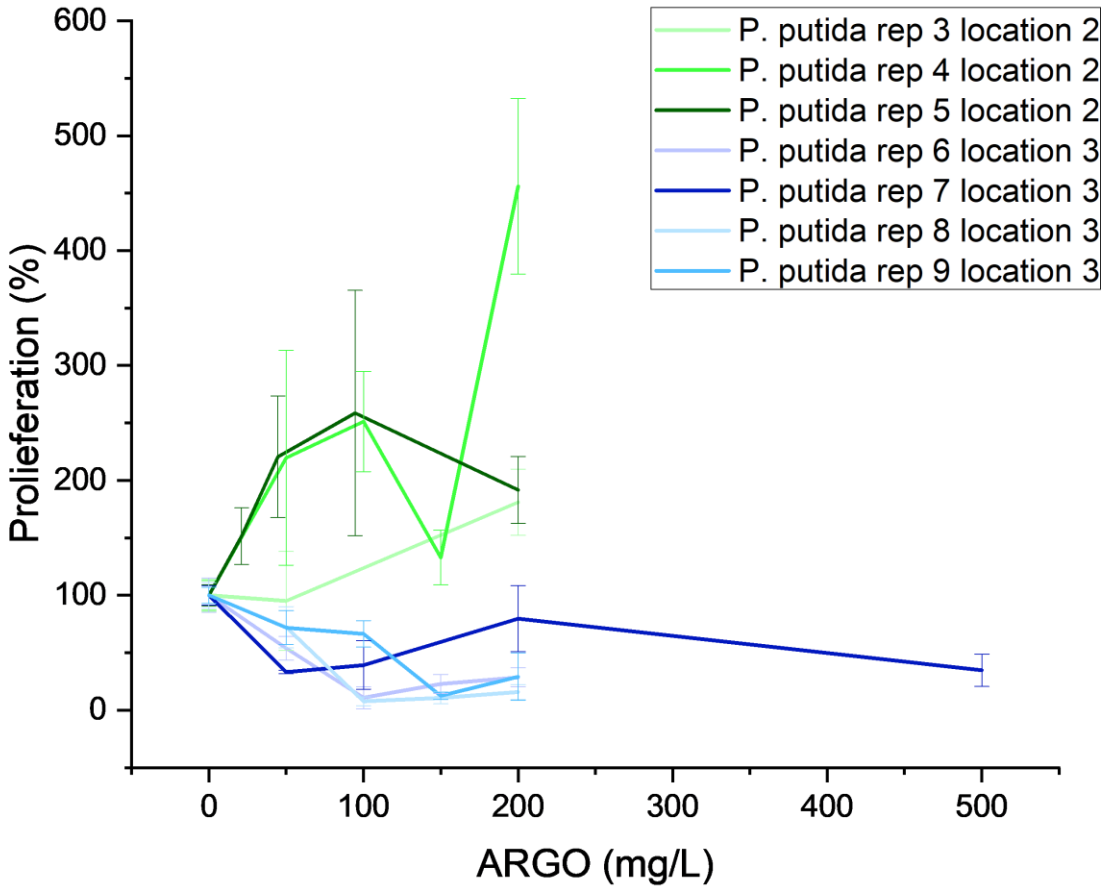


Figure 2.3.3.4 Proliferation of *P. putida* with ARGO from ACS material based on CFU results. Toxicity test results of all ISO 10712 runs against *P. putida*. This proliferation plot was based on the CFU data with 5 replicates for each of the data points with each error bar representing standard error. Each of the samples were run independently from the other. Each shade of colour represents the location and the time frame in which the experiment was carried out. Pink shades represent experiments carried out at Location 1 in 2019. Green shades represent experiments carried out at Location 2 in 2020. Blue shades represent experiments carried out at Location 3 in 2021 and 2022.

A. globiformis

OD result	150rpm		150rpm		150rpm		150rpm		150rpm		150rpm		100rpm		150rpm		250rpm		150rpm		150rpm	
	CEH Before renovation				CEH Post renovation						Imperial											
mg/L	Rep 1	ANOVA	Rep 2	ANOVA	Rep 3	ANOVA	Rep 4	ANOVA	Rep 5	ANOVA	Rep 6	ANOVA	Rep 7	ANOVA	Rep 8	ANOVA	Rep 9	ANOVA	Rep 10	ANOVA	Rep 11	ANOVA
10	106.2009	ns																				
15			79.77174	ns																		
21.1	92.64159	ns							151.6279	**												
30			81.31225	ns																		
40			69.25607	ns																		
44.7	77.22199	**							175.814	**												
50			64.03172	ns	134.6387	*	126.0119	**			50.26134	ns	86.88834	ns	68.60793	ns	208.4822	**	75.43474	ns	140.1934	ns
60			87.67523	ns																		
80			51.50669	ns																		
94.6	38.90037	**							175.3488	**												
100			46.81817	*			130.7143	**			91.27405	ns	133.7982	*	87.53205	ns	129.572	ns	104.5723	ns	201.306	**
150							143.8095	**			121.4447	ns			100.8546	ns	186.7086	*	85.65361	ns	160.7282	ns
200	96.07276	ns			180.3995	**	161.1905	**	191.6279	**	135.0163	ns	130.3295	*	102.7859	ns	193.7348	**	147.5365	ns	175.4848	*
500													137.1742	**								

Colour	Description	Value
	Growth	>110
	no change	90-110
	inhibition	0-25
	inhibition	25-75
	inhibition	75-90
	complete kill	<0

Annotation	ANOVA result
ns	not significant
*	p<0.05
**	p<0.01

P. putida

OD result	150rpm		150rpm		150rpm		150rpm		150rpm		150rpm		100rpm		150rpm		250rpm		150rpm		150rpm	
	CEH Before renovation				CEH Post renovation						Imperial											
	Rep 1	ANOVA	Rep 2	ANOVA	Rep 3	ANOVA	Rep 4	ANOVA	Rep 5	ANOVA	Rep 6	ANOVA	Rep 7	ANOVA	Rep 8	ANOVA	Rep 9	ANOVA	Rep 10	ANOVA	Rep 11	ANOVA
10	112.7016	ns																				
15			106.3712	ns																		
21.1	110.8871	ns							156.2353	**												
30			118.9289	ns																		
40			109.5106	ns																		
44.7	18.01075	**							148.3137	**												
50			94.09049	ns	145.614	*	124.3343	**			81.32193	*	108.2712	ns	105.8947	ns	104.8319	ns	103.8337	ns	114.6654	ns
60			96.02955	ns																		
80			109.0489	ns																		
94.6	35.68548	**							189.7255	**												
100			113.9428	ns			170.4142	**			80.03127	**	97.17379	ns	130.5922	ns	68.43357	**	103.1084	ns	81.10572	ns
150							194.5266	**			102.099	ns			120.2314	ns	117.5328	**	132.1006	ns	131.0921	**
200	79.36828	**			218.5673	**	172.3373	**	175.451	**	103.2999	ns	121.9875	ns	122.315	ns	116.7292	**	130.8134	ns	129.7187	**
500													123.3022	ns								

Table 2.3.3.1 A colour table of proliferation values with respect to each experimental runs of ISO 10712 carried out with a range of concentrations of ARGO from the ACS material from OD change results. Each value was associated with the ANOVA test results to determine the difference in their mean values at 95% confidence level ($p<0.05$) as well as 99% confidence level ($p<0.01$). The colours on the proliferation values represent the range of values of proliferation, as well as the description status.

2185

A. globiformis

CFU	150rpm		150rpm		150rpm		150rpm		150rpm		150rpm		100rpm		150rpm		250rpm		150rpm		150rpm	
	CEH Before renovation				CEH Post renovation						Imperial											
	Rep 1	ANOVA	Rep 2	ANOVA	Rep 3	ANOVA	Rep 4	ANOVA	Rep 5	ANOVA	Rep 6	ANOVA	Rep 7	ANOVA	Rep 8	ANOVA	Rep 9	ANOVA	Rep 10	ANOVA	Rep 11	ANOVA
10																						
15																						
21.1									116.8906	ns												
30																						
40																						
44.7									145.6814	*												
50					96.52174	ns	232.0675	**			111.8551	ns	59.52649	ns	54.54545	ns	230.2326	ns				
60																						
80																						
94.6									149.7121	*												
100							218.1435	**			237.7895	ns	101.4656	ns	146.281	ns	591.8605	ns				
150							294.9367	**			284.6136	*			356.1984	ns	109.3023	ns				
200					121.3044	ns	307.5949	**	161.2284	**	199.5873	ns	82.34498	ns	233.8843	ns	170.9302	ns				
500													29.96618	ns								

Colour	Description	Value
	Growth	>110
	no change	90-110
	inhibition	0-25
	inhibition	25-75
	inhibition	75-90
	complete kill	<0

Annotation	ANOVA result
ns	not significant
*	p<0.05
**	p<0.01

P. putida

CFU	150rpm		150rpm		150rpm		150rpm		150rpm		150rpm		100rpm		150rpm		250rpm		150rpm		150rpm	
	CEH Before renovation				CEH Post renovation						Imperial											
	Rep 1	ANOVA	Rep 2	ANOVA	Rep 3	ANOVA	Rep 4	ANOVA	Rep 5	ANOVA	Rep 6	ANOVA	Rep 7	ANOVA	Rep 8	ANOVA	Rep 9	ANOVA	Rep 10	ANOVA	Rep 11	ANOVA
10																						
15																						
21.1									151.3889	ns												
30																						
40																						
44.7									220.4861	ns												
50					95.03438	ns	219.6581	ns			53.93983	**	33.2218	ns	72.23908	ns	71.85162	ns				
60																						
80																						
94.6									258.6806	ns												
100							251.2821	ns			10.81662	**	39.29254	ns	7.73665	**	66.45885	ns				
150							132.906	ns			22.77937	**			10.67961	**	12.46883	**				
200					180.9779	ns	455.9829	**	191.6667	ns	28.58166	**	79.68451	ns	15.83738	**	29.08354	**				
500													34.75143	ns								

Table 2.3.3.2 A colour table of proliferation values with respect to each experimental runs of ISO 10712 carried out with a range of concentrations of ARGO from the ACS material from CFU results. Each value was associated with the ANOVA test results to determine the difference in their mean values at 95% confidence level ($p<0.05$) as well as 99% confidence level ($p<0.01$). The colours on the proliferation values represent the range of values of proliferation, as well as the description status.

Proliferation results from OD change results of GO against *A. globiformis* showed that in all of the runs, there were no complete inhibitions. There were inhibition and growth enhancements, and no effects observed. The initial set of runs at CEH (shade of pink on the plot and purple headers on the table) showed some inhibitory effect with no growth enhancement observed. The second set of runs at CEH (shade of green on the plot and grey headers on the table) showed all growth enhancements in all of the runs with an increasing growth effect with higher GO concentrations. The third batch of runs at ICL (shade of blue on the plot and blue headers on the table) showed mostly growth enhancement but some inhibition. However, the possible inhibition shown were statistically not significant in some cases as shown in table 2.3.3.1 and table 2.3.3.2 but most growth enhancement effects were statistically significant.

Proliferation results from OD change results of GO against *P. putida* showed that in all of the runs, there were no complete inhibitions. There were inhibitions, growth enhancement, and no effect observed in a similar manner to the results shown against *A. globiformis*. The general observation was similar to the observation made in the results from *A. globiformis*. Growth enhancement was predominantly observed in the second set of runs at CEH with highest inhibitory effect observed in the initial set of runs at CEH.

Proliferation results from CFU results were less marked in proportion to the OD change results. However, in general, they showed that there was no complete inhibitory effect by the GOs. In some cases that the proliferation values and therefore the observations differed greatly with the results shown in the OD change. This was likely to be due to heavy agglomeration observed during the exposure. It was apparent from this comparison that the CFU method which involved serial dilutions, were more heavily affected by agglomeration of the bacteria cells. This reason could also explain the large error values and the large difference in the *P. putida* proliferation measured by the CFU.

The table and the plot also showed different set up used. It was clear from the plot and the results that the set up used at CEH after the refurbishment showed more growth enhancement. The results from the initial set of results from CEH showed the highest inhibition with some proliferation falling under 25 %. The set of results with the greatest number of runs (from ICL) showed mixture of responses from inhibition and growth enhancement. Within the runs from the ICL the only parameter varied were the shaking speed and other factors such as the serial dilution method and mixing order of bacteria, GO and media. Shaking speeds were noted at the headers of the table and Rep 11 had bacteria in the media with direct addition of GO for the required concentration to minimise the possible GO agglomeration in the media. All other runs were prepared with GO dispersed in the media at the desired concentrations and the bacteria added after to control the exposure time more accurately. There were no clear trends observed with regards to the variation of shaking speed or the slight variation in methodology.

Abiotic test result

To understand to the effect of the agglomeration caused by the GO, bacteria, and the media, the changes in the OD measurements from the GO and media only were plotted for comparison.

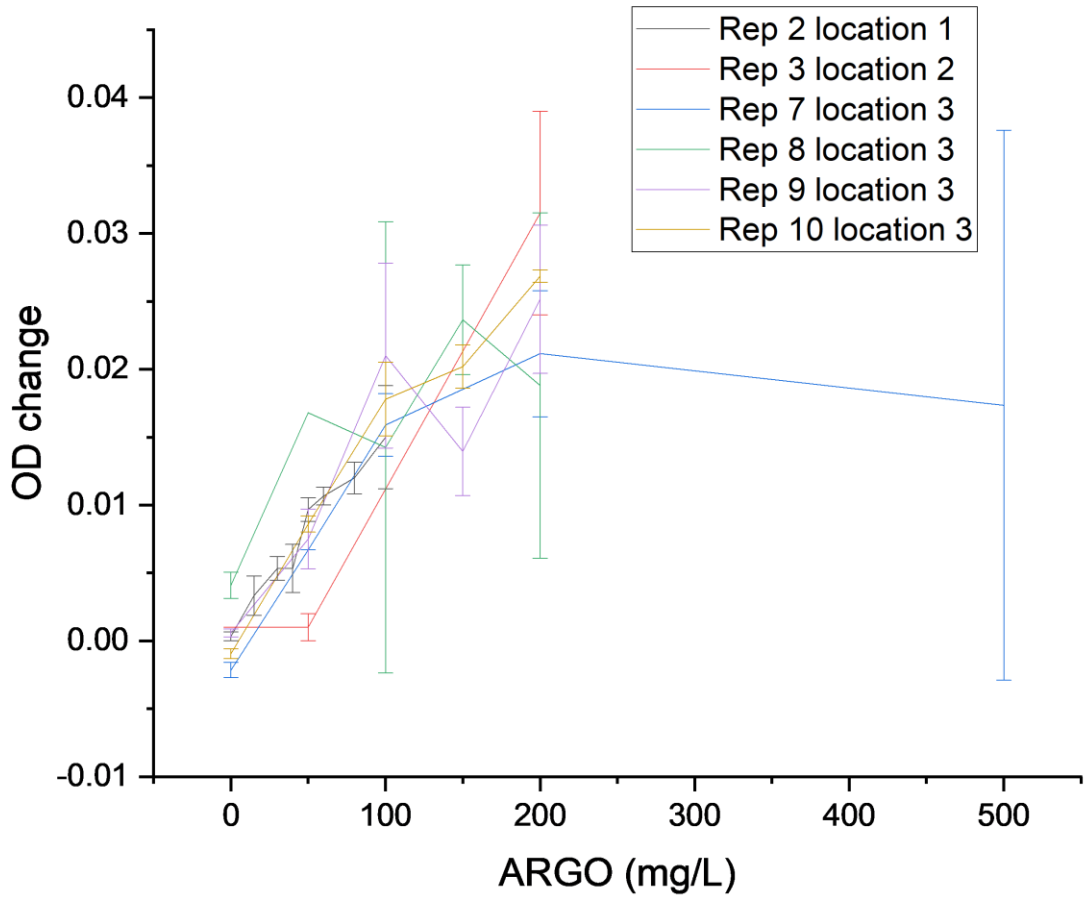


Figure 2.3.3.5 OD change of pristine ARGO from ACS material of concentration range between 0-200 mg L^{-1} in ISO 10712 test media. The OD change was calculated from OD reading at T0h and T24h sample (same sample left for 24-hour exposure) and each data point are average of 3 independent samples. Each line represents the OD change under abiotic condition result that were carried out at the same time as the results shown in figure 2.3.3.1, 2.3.3.2 and 2.3.3.6. The error bars represent the standard error.

Figure 2.3.3.5 shows the OD change measured of the ARGO under abiotic conditions. Each set of data labelling corresponds to the same experiment shown in figure 2.3.3.1 and 2.3.3.2. When compared to the OD change measurement under biotic condition shown in figure 2.3.3.6, the OD changes under abiotic condition was an order of magnitude smaller. Therefore, the heavy agglomeration seen in the biotic

condition was due to an interaction of GO *with bacteria* in media and not just agglomeration of the GO in the media alone.

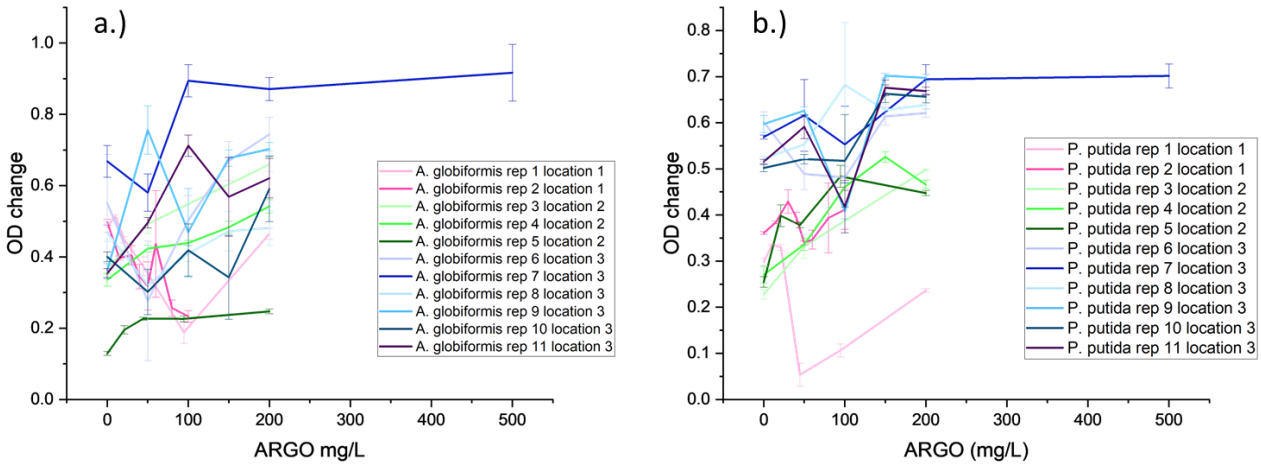


Figure 2.3.3.6 The raw data of the result shown in figure 2.3.3.1 and 2.3.3.2. Each plot represents the OD change of ARGO from ACS material of concentration range between 0-200 mg L^{-1} in ISO 10712 test media against *A. globiformis* and *P. putida*. The OD change was calculated from OD reading at T0h and T24h sample (same sample left for 24-hour exposure) and each data point are average of 3 independent samples. The error bars represent the standard error.

The plot of the OD change in the abiotic condition also showed that the GO agglomerated more with increasing concentration in the ISO 10712 media, as indicated by an increase in the value of OD change. More agglomeration over the 24 hours period would lead to more increase in OD and the heavy agglomeration would lead to greater variation in the repeated measurements and therefore standard error.

2.3.4 Discussion

The repeated runs of ISO 10712 against *A. globiformis* and *P. putida* using GO from ACS material showed that GO could show range of effects from inhibition, no effect on bacteria proliferation, and growth

enhancement. However, over the entire set of experiments, there was no complete inhibition observed when there was no complete kill of the bacteria. This mixture of observations of both enhancement and inhibition, without complete inhibition, indicated that there was a mixture of mechanisms occurring in the toxicity test of ISO 10712.

Palmieri *et al*. (*104, 121*) showed that there were three mechanisms by which GO could interact with bacteria depending on the solution which the GO and the bacteria were dispersed in. In Phosphate Buffer Saline solution (PBS), at a concentration of below 25 mg L^{-1}, resulted in inhibition of growth, and at concentration above 25 mg L^{-1}, suggesting that there was scaffolding mechanism resulting in growth enhancement. This change in the interaction mechanism was attributed to the increased aggregation of GO, as its concentration increased. In water, an increase in GO concentration from 3 mg L^{-1} to 200 mg L^{-1} showed a concentration-dependent inhibition of growth. In NaCl, an example of a monovalent cation, at a low concentration of below 12 mg L^{-1}, there was clear inhibition of growth, which could possibly be explained by the" nano-knife mechanism" being prevalent. Between 12 mg L^{-1} and 100 mg L^{-1}, there was a recovery of growth where the scaffolding mechanism was prevalent. Above 100 mg L^{-1}, there was an inhibition of growth again where the wrapping mechanism was possibly prevalent. In previous work divalent cation solution, $MgCl_2$ and $CaCl_2$, the response by the bacteria was similar to that of monovalent cation except for the less pronounced effect of the scaffolding mechanism. This was attributed to the fact that divalent cations promoted a GO-bacteria interaction more than monovalent cations. $CaCl_2$ promoted more interaction of GO and bacteria to favour the wrapping mechanism over the scaffolding mechanism due to the unique interaction of Ca^{2+} with GO and bacteria. (*121, 123*)

It is worth noting that the ISO 10712 test media contained many components necessary for bacterial growth including Na^+, K^+, Mg^{2+}, and Fe^{3+}. Both K^+ and Na^+ are also present in PBS so it was likely that the GO

interaction in ISO 10712 media could be extrapolated from the interaction in PBS. The composition of PBS is shown below for comparison.

Composition	**Concentration (mg/L)**
NaCl	8000
KCl	200
$Na_2H_2PO_4$	1150
KH_2PO_4	200

Table 2.3.4.1 The composition of typical PBS.

As shown in the table 2.3.4.1, the ISO 10712 test media has more components than PBS and also share a common composition with PBS such as K^+, Na^+, and PO_4^{2-}. However, the amount of these common components was much less in the ISO 10712 test media compared to PBS. Therefore, it may be that the mixture of responses observed was due to the ISO 10712 test media displaying the same interaction observed in salt cations and PBS by Palmieri *et al*. (*121*)

Some results of proliferation by *A. globiformis* (rep 6, rep 7, rep 8, rep 10) showed an inhibition below 100 mg L^{-1} with recovery and growth enhancement above 100 mg L^{-1} up to 500 mg L^{-1} (rep 7). This change in the cell proliferation (Observation (i.)) was the same as the change observed in the PBS by Palmieri *et al*. (*121*), indicating that there could be a competing mechanism between the proposed "nano-knife" and "scaffolding" mechanisms in which an increased concentration of GO increases aggregation and therefore favour the "scaffolding mechanism for growth enhancement . At lower concentration of GO in media, GO could still remain in its monolayer form and cut the cell membrane causing inhibitory effect. However, as the concentration of the GO increases in the media, GO aggregates and loses it monolayer nature and no longer able to cut membranes. Further increase in the GO concentration leads to scaffolding of the GO

which provides a surface for the bacteria to grow and proliferate as suggested by Ruiz *et al*. and Chen *et al*. (*88, 115*)

Other notable trends observed for *A. globiformis* were Observation (ii.) no effect initially then an inhibition effect followed by another recovery of growth for rep 1. Observation (iii.) a consistent inhibitory response for rep 2 and Observation (iv.) growth enhancement at all concentrations for rep 3, rep 4, rep 5, rep 9, and rep 11). The observation of trend 1.) could be explained by initial lag of response by bacteria at the low concentration where the nano-knife mechanism of inhibition did not cause enough inhibition initially, but then followed the trend explained earlier in the similar manner to the GO and bacteria in PBS by Palmieri *et al*. (*121*) Therefore observation (i.) and (ii.) could be grouped together. Observation (iii.) was rare and similar to the response in water by Palmieri *et al*. However, the response was not concentration dependent, and the range of data obtained meant that there was no indication of other competitive mechanisms acting. Observation (iv.) was unique as this was more similar to the observation by Ruiz *et al*. (*88*) using LB media where the bacteria only responded by increasing cell proliferation and in a concentration dependent manner. This was ascribed to the scaffolding mechanism by Chen *et al*. (*115*) It was interesting to note that for rep 11, the highest concentration, led to a tail-off of the growth enhancement which may be an indication that wrapping mechanism was starting to be factor in a similar manner to the observation in salt cations experiment by Palmieri *et al*. (*121*) However, it was difficult to tell with the range of concentrations studied.

It should be noted that the range of concentrations used were similar to the range used in other literature including Palmieri *et al*. Therefore, the discrepancy between repeats must have been due to differences in the experimental set up. Rep 3-5 clearly showed growth enhancement only (in both bacteria) so it may be that there was possible error in the experimental set up or other external factors that affected the results. However, even when results from experiments performed at ICL were compared, there was growth

enhancement only (Observation (iv.)) and observation (i.). Therefore, the ISO 10712 test using GO displayed results similar to those in PBS and LB media.

The response by *P. putida* displayed a similar set of observations where observation (i.) for rep 6, Observation (ii.) for rep 1 and 9, observation (iii.) for none of them, observation (iv.) for rep 3, 4, 5 with another observation (observation (v.)) where there was no effect throughout the range of concentrations or no effect at low concentrations then growth enhancement at a higher concentration. This may be attributed to the scaffolding mechanism where in some cases the scaffolding was not enough to support the growth of *P. putida*. *P. putida* may be less susceptible to the "nano-knife" mechanism due to the tendency of this bacteria to agglomerate under suspension without any materials or stressors.

The heterogeneity of the repeated results may be credited to number of reasons. One reason could be the zeta potential of GO in the ISO 10712 test media of around -30 mV. This value indicates incipient instability, and that agglomeration was starting to occur. The uncontrollable agglomeration state of the GO dispersion in the ISO 10712 test media on a given day may have resulted in heterogeneity in the results.

The CFU results confirmed that the GO could not completely kill the bacteria. However, due to the high agglomeration of the GO-bacteria complex especially in the *P. putida* sample, it was difficult to conclude quantitative results with the CFU results alone. It was especially problematic when the bacteria alone showed agglomerated (*P. putida*). However, the series of ISO 10712 tests carried out using other nanomaterials showed that for Rutile, TiO_2 NPs where there was significant interference from the nanoparticle on the OD measurement, the changes in OD did require that the CFU results were used. This set of data is shown in Appendix III. Similarly, these series of tests using materials showed the effectiveness of ISO 10712 against more known material.

In the next chapter, the behaviour of GO in dispersion was studied in more depth in water and LB media, to understand the response of the bacteria to GO in these media. Then the bacteria and the GOs were imaged to understand the agglomeration state and the potential mechanism occurring with different media conditions.

2.3.5 Conclusions

The ISO 10712 water and soil quality test on GO from ACS material against *A. globiformis* and *P. putida* showed that ARGO did not display complete inhibition under the experimental set up. The ARGO did suppress the proliferation of the bacteria to a degree (up to 20 %) but also enhanced proliferation (over 200 %). It was likely that the heterogeneity in the results arose due to the unique composition of ISO 10712 test media where the GO displayed incipient instability in this media. These differences in media composition could lead to alterations to the mechanism of interaction between the GO and bacteria. In terms of relevancy of the results to the environment, there were inhibitions observed at concentration as low as 50 mg L^{-1}. The predicted concentration of GO based on CNT calculation that could be released to the environment is in the range of 1-1000 μg L^{-1} and therefore the effect of GO could be minimal. However, more detailed studies on effect at lower concentration have not been carried out using environmentally relevant bacteria and therefore require further investigation.

2.4 Toxicity testing and imaging with different media and Milli-Q water

2.4.1 Introduction

A series of ISO 10172 tests with GO revealed that the agglomeration state of the GO under biotic conditions greatly affected the observed toxicity results. One way to control the agglomeration state or the colloidal

stability of the nanoparticles is to change the media which the GO was dispersed. Since ISO 10712 tests against GO had not been carried out before, to understand the various observations reported in Chapter 2.3, a more common media and Milli-Q water was elected as an alternative exposure condition in which GO could interact with bacteria. T this section described a study in which the GO from the ISO 10172 test was exposed to the same bacteria but using Milli-Q water and Luria Bertani (LB) media.

2.4.2 Materials and Methods

Materials

Chemicals and materials used were the same as the ISO 10712 test in the previous section with additional chemicals of Luria-Bertani agar and broth from Sigma-Aldrich at biological grade for microbiological work.

Methods

Toxicity assays – GO suspended in Milli-Q water

Bacteria cultures were suspended in pre-culture media and incubated for 16 hours at 25 °C. The bacteria suspensions were then adjusted in concentration so that the OD was 0.5 in the Milli-Q water. The bacteria suspension was then exposed to the GO dispersion in the concentration range of 0-200 mg L^{-1} for 3 hours (Pre-exposure step). After the pre-exposure step of GO with the bacteria culture, the GO-bacteria mixture was resuspended in ISO 10712 test media. Samples of the mixture was pipetted into a 96 well plate and the OD was read using the OD plate reader in the same way as previously explained to take the OD measurement at T0h. The mixtures were then incubated for 24 hours in the dark at 150 rpm shaking speed at 25 °C (standard ISO protocol step). After 24 hours, another OD measurement was taken by taking

samples and pipetting into 96 well-plates (T24h measurement). CFU readings were taken as well as the OD measurements. CFU readings were taken after the pre-exposure step and after the 24-hour incubation with the standard ISO protocol step. Samples were taken and serially diluted and plated onto LB agar. These plates were incubated for 48-72 hours and the CFU measurements were taken.

Toxicity assays – GO suspended in LB broth

Bacteria cultures were suspended in LB broth and incubated for 16 hours at 25 °C. The rest of the steps were exactly the same as the ISO 10712 protocol, except the ISO 10712 test media was replaced with LB broth. OD and CFU measurements were taken at T0h and T24h.

Imaging – Optical Microscope images

Optical microscope images were taken directly from the 96 well-plates after the OD measurement at T0h and T24h. An inverted bright field microscope (Nikon, Eclipse TS1000) was attached with Nikon camera to obtain images at x20 magnification. Images were then processed using ImageJ.

Imaging – TEM Imaging

. Bacteria cultures were exposed to 50 mg L^{-1} of GO in Milli-Q water, ISO 10712 test media, and LB broth, and after 3 hours of exposure, the samples were centrifuged (1780 g, 3500 rpm) for 10 minutes to form a pellet in each sample. The supernatant was removed, and the pellets were washed with sodium cacodylate buffer solution (0.1M, pH 7.0). The washing step was repeated 3 times. The pellets were then fixed using glutaraldehyde (2.5%) in buffer solution (1 hour, RTP). After the fixation, the pellets were washed again 3 times with the buffer solution. The pellets were stained using osmium tetroxide (1% in sodium cacodylate buffer) for 1 hour at room temperature. The pellets were washed with sodium cacodylate buffer solution 5

times then the buffer solution was exchanged for De-ionised water (DI Water) by washing 3 times. The pellets were dehydrated using serial dehydration method using dried ethanol (50%, 70%, 90%, and 100%) and embedded using Taab Epon 812 (Taab Laboratories) with a medium hardness recipe. The embedded samples were then ultramicrotomed using a 35^{o} diamond knife to form 70 nm thickness sections and mounted on a 300-mesh copper grid for imaging in the JEOL 2100F operated at 200 kV. The TEM images were taken using bright field mode with largest condenser aperture and no objective aperture.

2.4.3 Results

Results of the toxicity assay from OD measurements, 24h CFU results using GO dispersed in Milli Q water and LB broth have been plotted together with the previous result from ISO 10712 for direct comparison in figure 2.4.3.2. Result from 3h CFU have also been plotted on figure 2.4.3.3. The schematic diagram in figure 2.4.3.1. shows the different end point assay and the difference in methods of exposure.

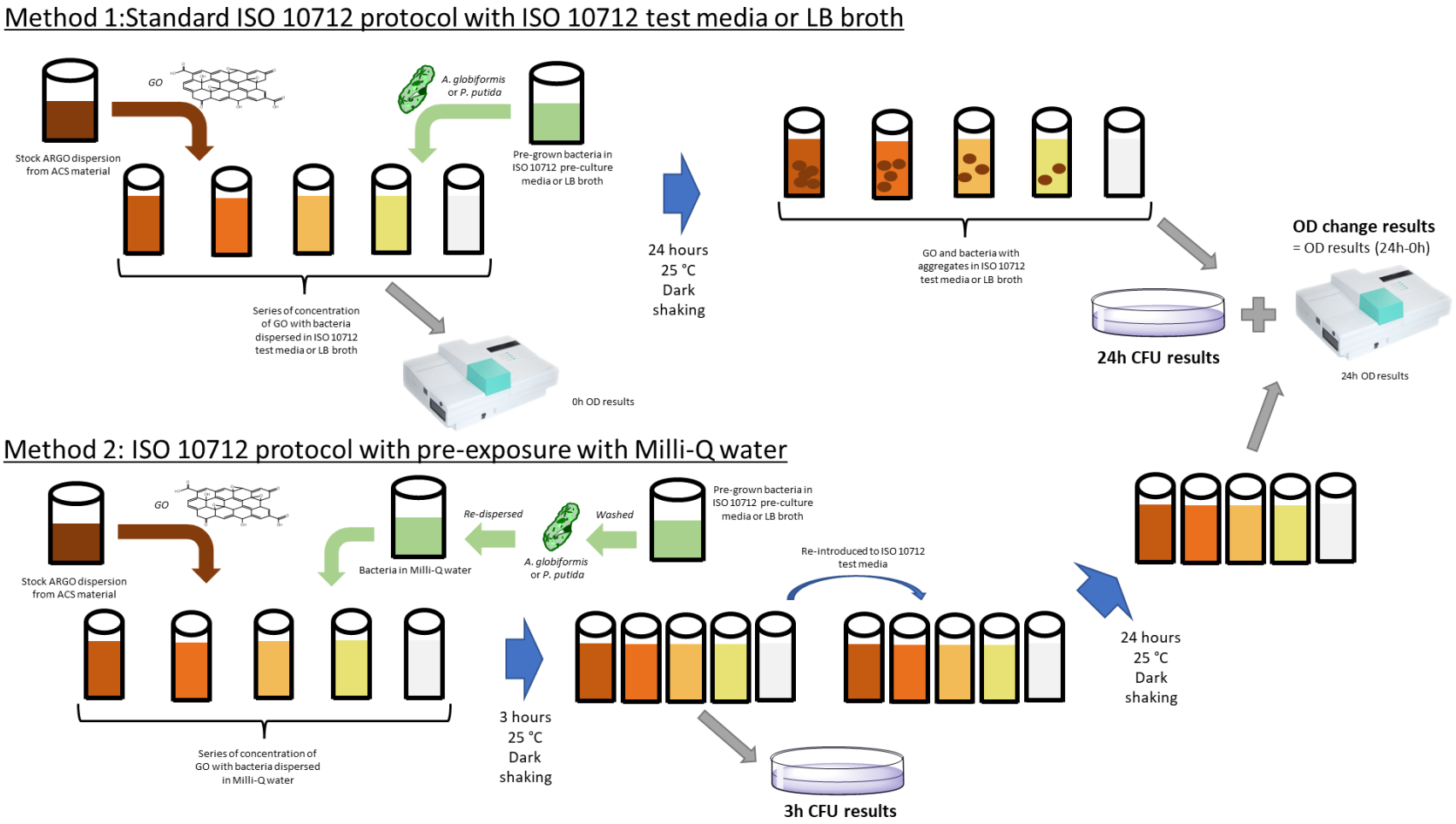


Figure 2.4.3.1 Schematic diagram depicting the experimental procedure for the toxicity test with three different end-point assays: OD change results, 24h CFU results, and 3h CFU results.

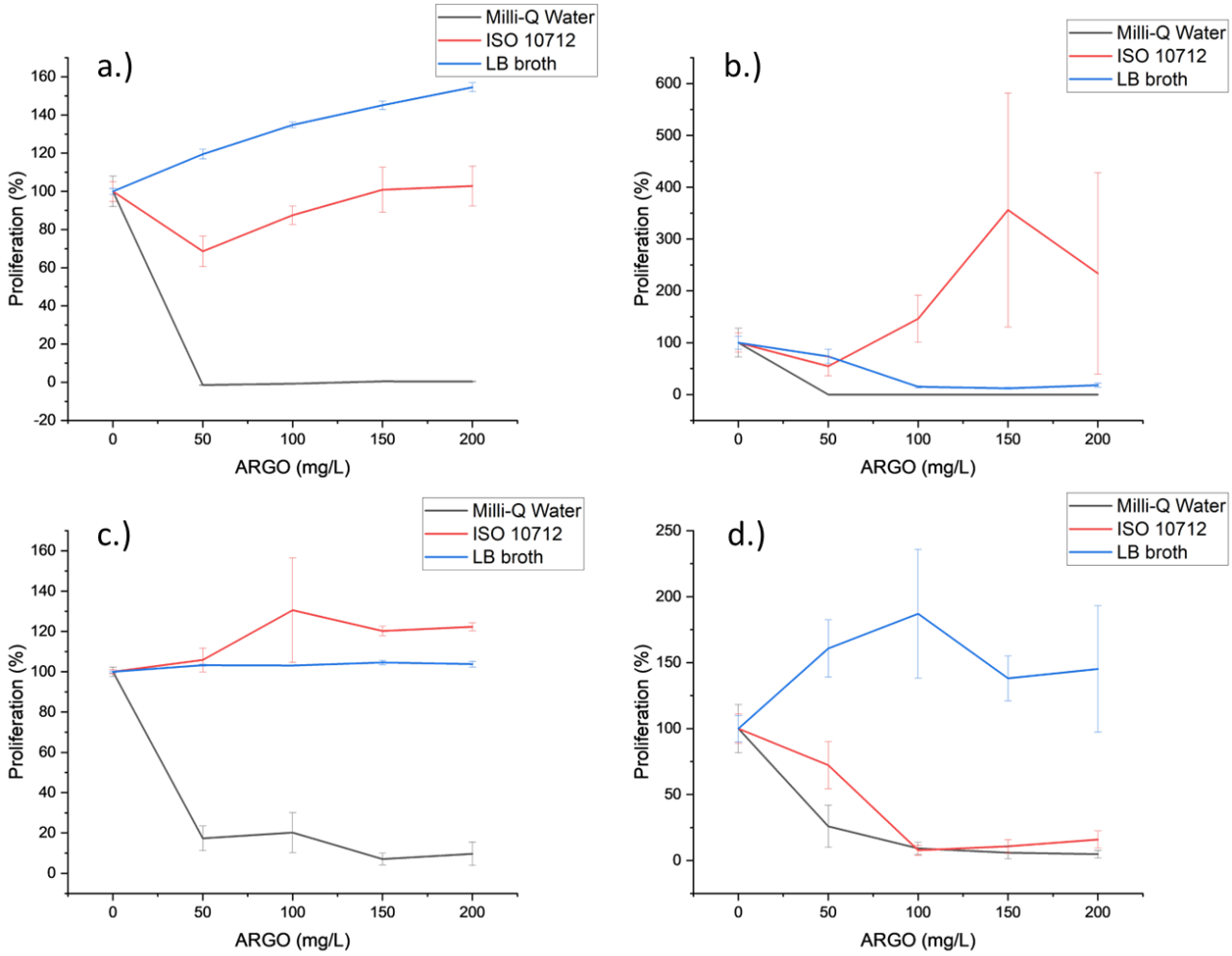


Figure 2.4.3.2 Proliferation of a.) *A. globiformis* exposed to GO in three different media: water, ISO 10712 test media, and LB broth based on OD change results b.) *A. globiformis* exposed to GO in three different media: water, ISO 10712 test media, and LB broth based on 24h CFU results c.) *P. putida* exposed to GO in three different media: water, ISO 10712 test media, and LB broth based on OD change results d.) *P. putida* exposed to GO in three different media: water, ISO 10712 test media, and LB broth based on 24h CFU results. Each data point was an average of 5 measurements with error bars representing the standard errors (S.E.).

The proliferation results comparing the three conditions of GO exposure to *A. globiformis* and *P. putida* in water, ISO 10712 test media, and LB broth showed that GO exhibited different degrees of inhibitory effects

depending on the media used during exposure. It was apparent, especially from the OD measurements, that exposure of GO in water resulted in severe inhibitory effects towards both bacteria with complete inhibition of *A. globiformis* at 50 mg L^{-1}. Inhibitory effect of GO on *P. putida* was observed to be less. A concentration above 50 mg L^{-1} reached more than 70 % inhibition with 90 % inhibition at concentration greater than 150 mg L^{-1}.

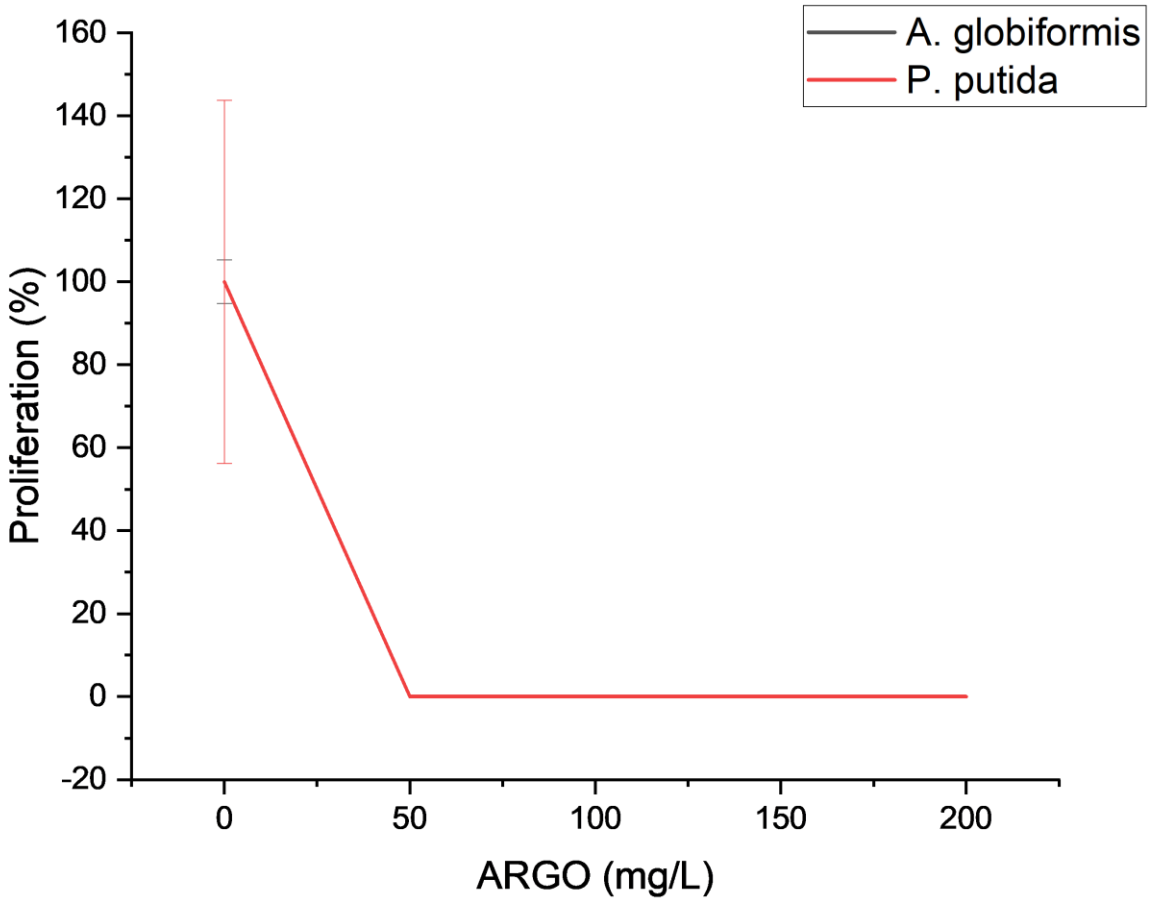


Figure 2.4.3.3 Proliferation of both *A. globiformis* and *P. putida* from the 3h CFU results after the pre-exposure step (3 hours of contact time in water without being re-introduced to the test media). Each data point is from 3 repeated measurements.

The 3h CFU result in which the bacteria's' proliferation was measured directly after a contact time of 3 hours in water showed slightly different results to the 24h CFU results. The 3h CFU result was similar to the results of reported in the literature that demonstrated strong antimicrobial activity of GO. (*104, 107, 111, 113, 120, 121, 130, 131, 134, 137, 141, 168*) They also used similar non-growth supportive media such as water or saline or PBS and showed that GO could completely inhibit the growth of model pathogenic bacteria. The 3h CFU result showed that neither the *A. globiformis* nor *P. putida* bacteria were active bacteria after the exposure to GO in water in the concentration range between 50 – 200 mg L^{-1} of GO. The range was similar to previously reported inhibitory concentration for GO in water, but the 100 % inhibition at 50 mg L^{-1} meant that both bacteria may have been very sensitive to the GO or this particular GO was very effective at inhibiting bacterial growth. (*104*)

When the proliferation data were compared across the three different media (figure 2.4.3.2) and SI table V a-d (Appendix V), they showed that both the LB broth and ISO 10712 reduced GO inhibition towards both bacterium types. The changes to OD showed that both bacteria exposed to GO in LB broth increased proliferation compared to the control. This was more clearly represented in the ANOVA statistical test (in Appendix V). Bacteria exposed to GO in the ISO 10712 test showed no statistically significant change compared to the control.

The 24h CFU results for ISO 10712 and LB broth were less reliable as similar problem as described in the previous section was encountered. LB broth showed much higher agglomeration meaning that the serial dilution step in the CFU method was affected. The optical image of the suspension as well as the optical microscope together with the DLS/Zeta potential data and pH data.

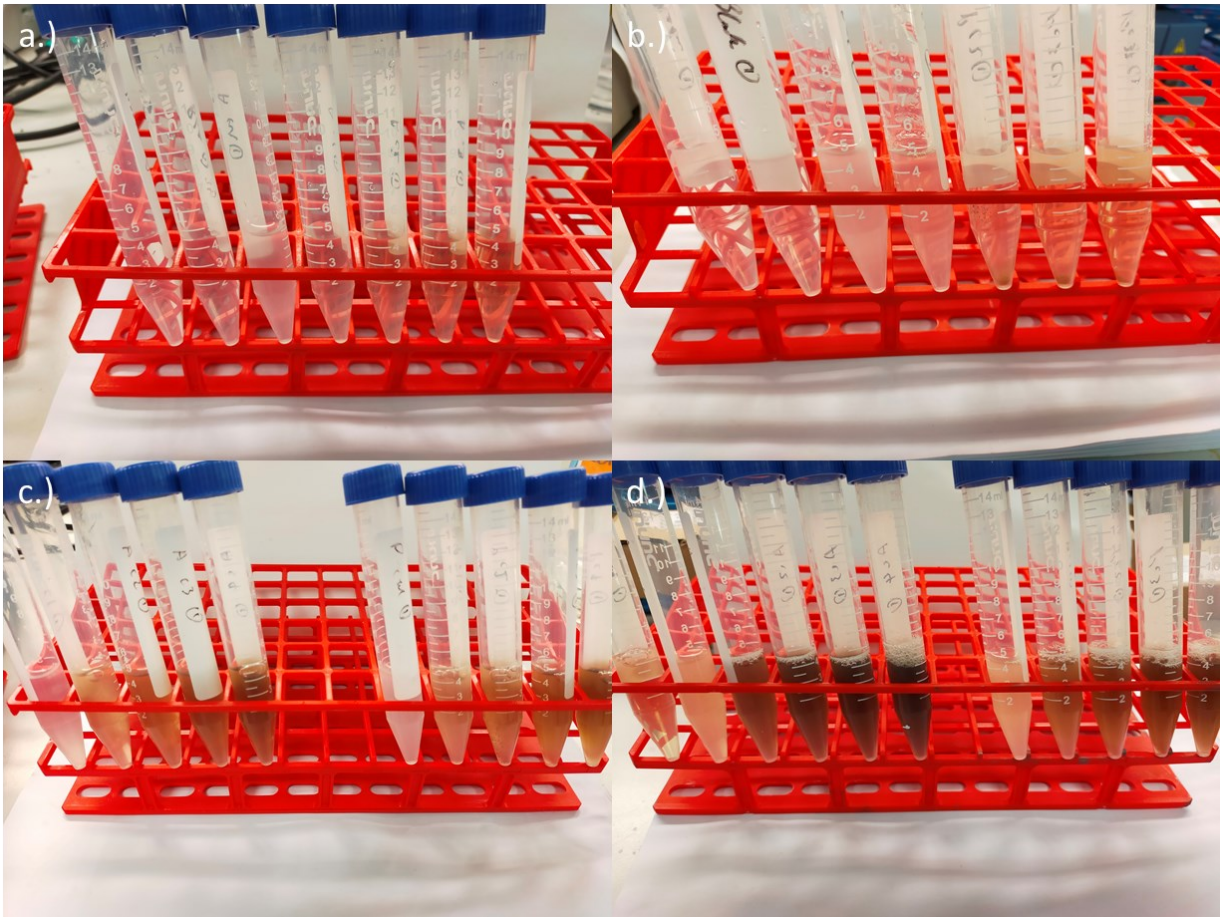


Figure 2.4.3.4 ARGO in suspension with bacteria in the three different exposure environments after the 24 hours of incubation. Suspension photo of GO with a.) *A. globiformis* in water (Left to Right: Water control, ISO 10712 test media control, 0 mg L^{-1} of GO with bacteria, 50 mg L^{-1} of GO with bacteria, 100 mg L^{-1} of GO with bacteria, 150 mg L^{-1} of GO with bacteria, 200 mg L^{-1} of GO with bacteria), b.) *P. putida* in water (Left to Right: Water control, ISO 10712 test media control, 0 mg L^{-1} of GO with bacteria, 50 mg L^{-1}, 100 mg L^{-1}, 150 mg L^{-1} and 200 mg L^{-1} of GO with bacteria), c.) Exposure in ISO 10712 test media with (Left to Right: 0 mg L^{-1} , 50 mg L^{-1}, 100 mg L^{-1}, 150 mg L^{-1}, 200 mg L^{-1} of GO with *A. globiformis*, 0 mg L^{-1}, 50 mg L^{-1}, 100 mg L^{-1}, 150 mg L^{-1} and 200 mg L^{-1} of GO with *P. putida),* d.) Exposure in an LB broth with (Left to Right: 0 mg L^{-1}, 50 mg L^{-1}, 100 mg L^{-1}, 150 mg L^{-1} and 200 mg L^{-1} of GO with *A. globiformis*, 0 mg L^{-1}, 50 mg L^{-1} , 100 mg L^{-1} of GO, 150 mg L^{-1} and, 200 mg L^{-1} of GO with *P. putida)*.

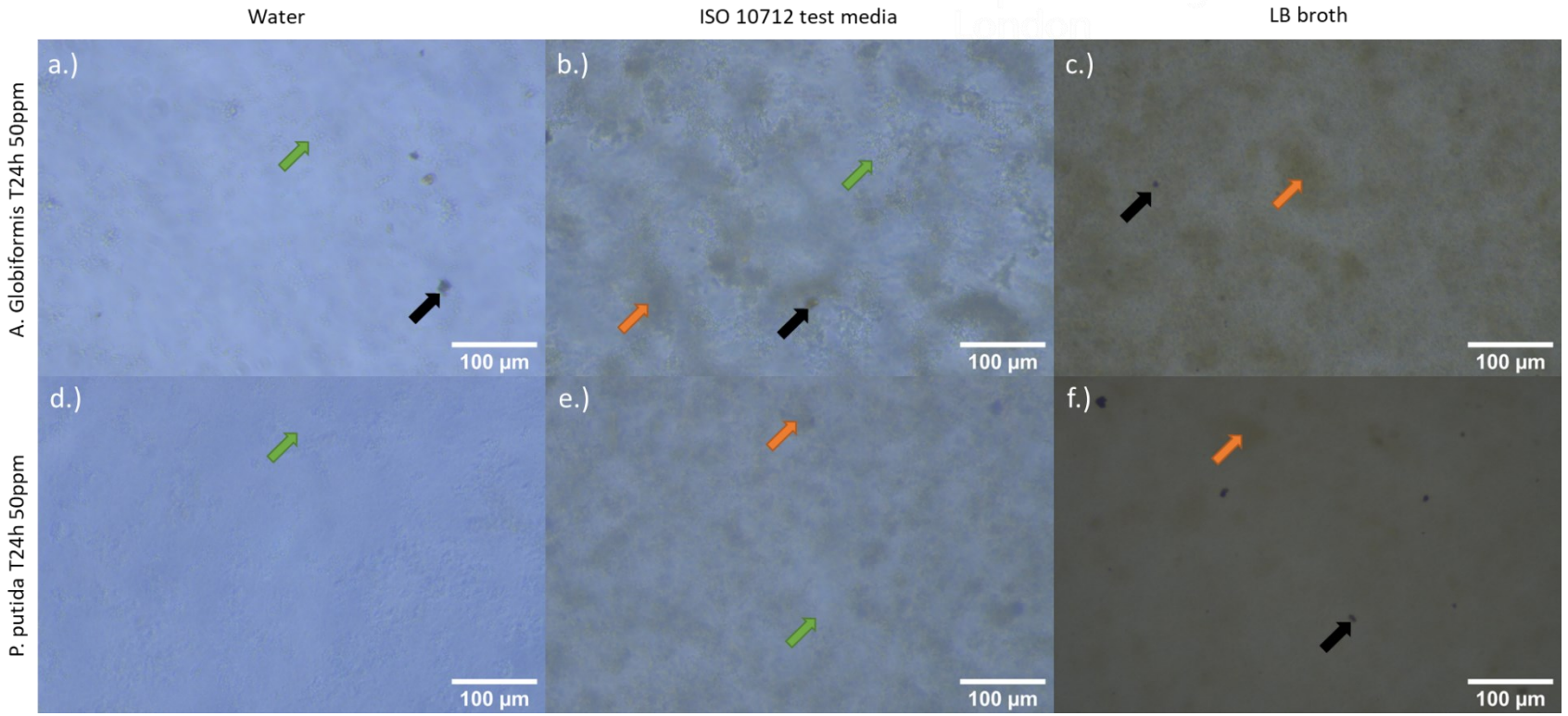


Figure 2.4.3.5 Optical microscope image of both bacteria with 50 mg L^{-1} of GO after 3 hours. a.) GO with *A. globiformis* in water, b.) GO with *A. globiformis* in ISO 10712 test media, c.) GO with *A. globiformis* in LB broth, d.) GO with *P. putida* in water, e.) GO with *P. putida* in ISO 10712 test media, f.) GO with *P. putida* in LB broth. Arrows indicate the following: Green arrows indicate bacteria on their own, brown arrows indicate aggregated GO with bacteria, black arrows indicate aggregated GO on its own.

	pH		
GO concentration	**Milli-Q Water**	**ISO 10712 test media**	**LB broth**
0 mg L^{-1}	7.40±0.41	7.08±0.03	7.15±0.01
50 mg L^{-1}	4.75±0.14	6.86±0.03	7.08±0.02
150 mg L^{-1}	3.98±0.07	6.74±0.03	7.06±0.00

Table 2.4.3.1 pH of GO in water, ISO 10712, and LB broth with different concentrations of GO including without GO. 3 repeated measurements ± S.D.

	Z-average (nm)	PDI	Zeta potential (mV)
GO in Milli-Q water	398.6±4.8	0.30±0.02	-49.6±0.6
GO in ISO 10712 test media	604.4±29.2	0.36±0.05	-28.7±1.5
GO in LB broth	11256.7±1595.9	0.34±0.05	-11.8±0.9

Table 2.4.3.2 DLS and zeta potential results of GO in water, ISO 10712, and LB broth. All measurements shown are an average of 3 measurements ± S.D.

The optical images (figure 2.4.3.5) of the suspension shows the agglomeration state of the GO-bacteria mixture in water, ISO 10712 test media and LB broth. Brown arrows shown in figure 2.4.3.5 indicated the agglomeration of GO-bacteria complex. The images showed more instances of darker GO-bacteria agglomeration in the order of LB broth > ISO 10712 > Milli-Q water. The black arrow showed GO aggregation and this aggregation was more prominent in the order of LB broth > ISO 10712 > Milli-Q water. Green arrows showed bacteria that had not interacted to form GO-bacteria complex, and these instances were more prominent in Milli-Q water> ISO 10712 > LB broth.

The pH data along with DLS and Zeta potential data of GO in Milli-Q water, ISO 10712 test media, and LB broth (table 2.4.3.1 and 2.4.3.2) showed that GO agglomerate under ISO 10712 test media and LB broth condition. GO in LB broth showed the highest agglomeration with largest value of hydrodynamic diameter (given by Z-average) with least negative value (lowest magnitude) of zeta potential value followed by GO

in ISO 10712 test media and then GO in Milli-Q water. The pH data showed that the GO was acidic in Milli-Q water, but the acidity was reduced when the GOs were introduced to ISO 10712 test media and LB broth. LB broth provided better buffer for the acidity of GO and therefore showed the most neutral pH with the least change in the pH with increasing concentration of GO.

The interaction of GO with bacteria in Milli-Q water, ISO 10712 test media, and LB broth were imaged using TEM.

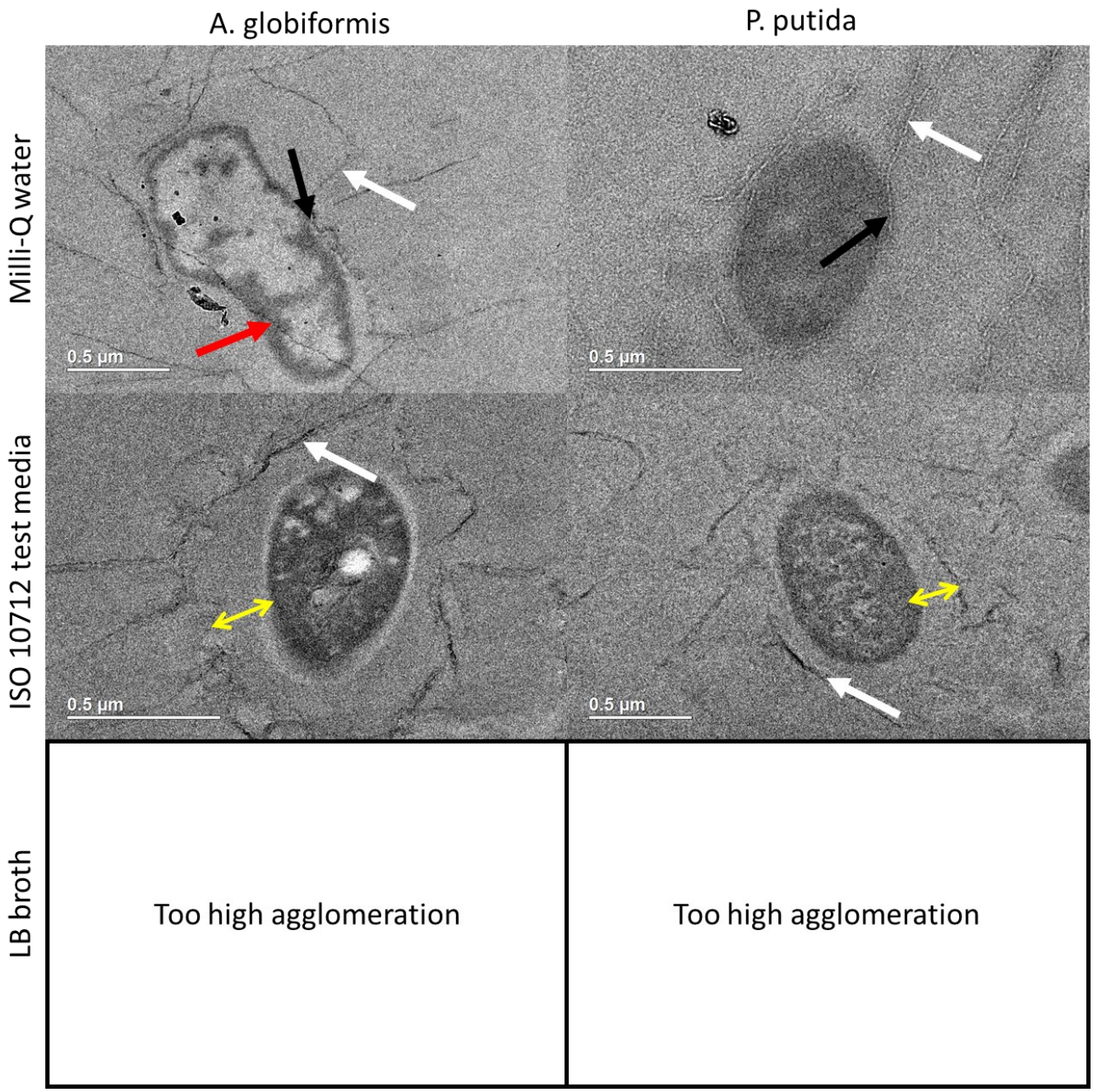


Figure 2.4.3.6 TEM images the different interactions of bacteria with GO from ACS material in Milli-Q water, ISO 10712 test media, and LB broth. Images for LB broth samples could not be obtained due to the stronger interaction displayed by the GO-bacteria mixture, which did not allow the infiltration of fixative and resin. The red arrow shows the GO penetration mechanism. The black arrow shows a direct contact of GO onto the bacteria. The yellow double headed arrow shows a gap between the bacteria and the GO (~200 nm). The white arrow shows the GO.

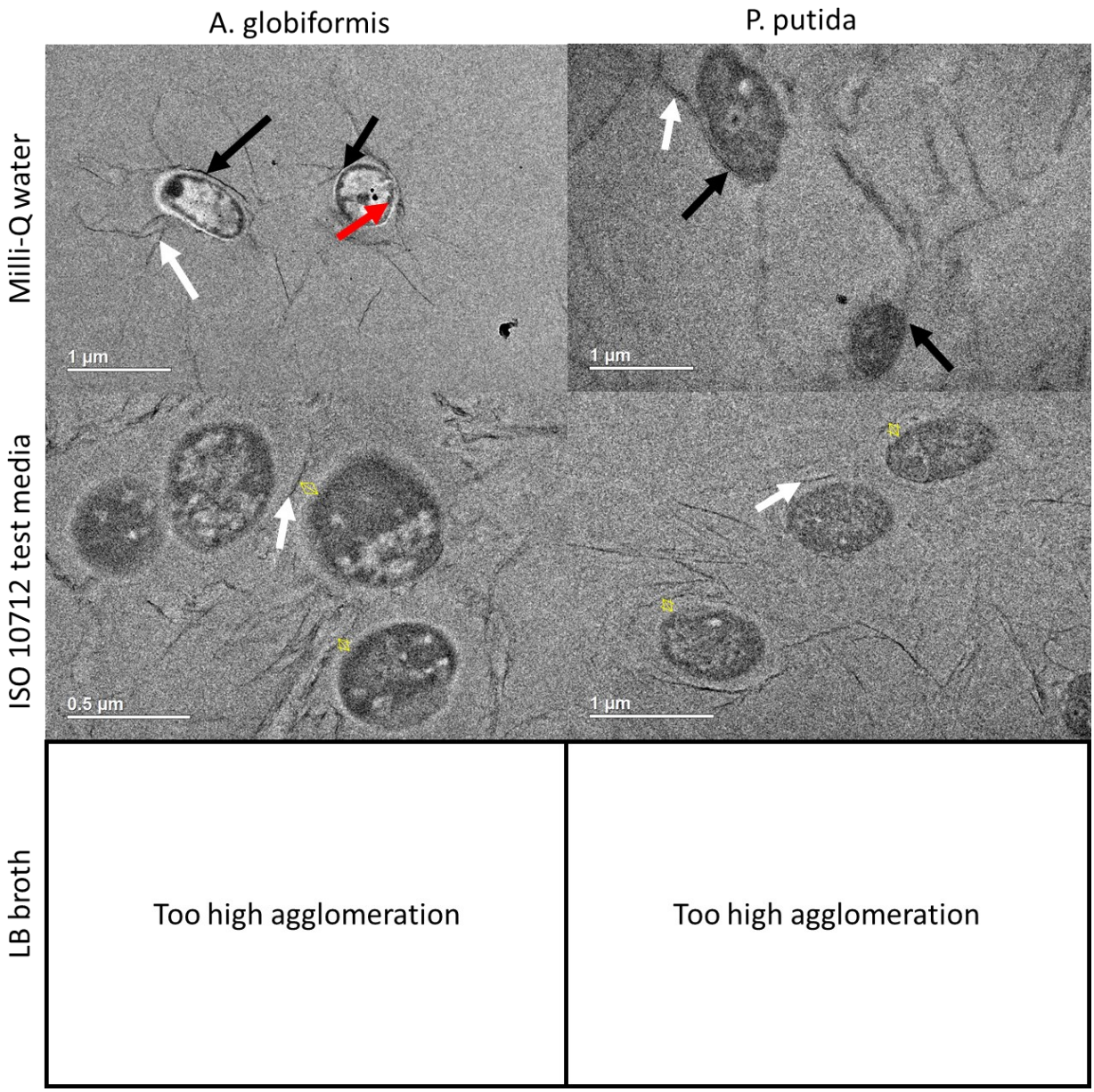


Figure 2.4.3.7 Lower magnification TEM images the different interactions of bacteria with GO from ACS material in Milli-Q water, ISO 10712 test media, and LB broth. Images for LB broth samples could not be obtained due to the stronger interaction displayed by the GO-bacteria mixture, which did not allow the infiltration of fixative and resin. The red arrow shows the GO penetration mechanism. The black arrow shows a direct contact of GO onto the bacteria. The yellow double headed arrow shows a gap between the bacteria and the GO (~200 nm). The white arrow shows the GO.

The TEM images (figure 2.4.3.6.and 2.4.3.7) showed the interaction of both bacteria with GO in Milli-Q water and ISO 10712 test media. The TEM images showed GO actively interacted surrounded and interacted with the bacteria in both Milli-Q water and ISO 10712 test media. There was a larger space in between the GO and the bacteria in ISO 10712 test media condition (yellow arrows), and direct contact of GO with bacteria membrane in Milli-Q water condition (black arrows). This observation can be explained by the absence of salt ions in the Milli-Q water that facilitates direct contact between the GO and the bacteria. The *A. globiformis* was also more susceptible to the presence of GO in Milli-Q water. The abnormal deformity in the membrane structure as well as the lighter internal structure suggested clear damage to the bacteria shown in both figure 2.4.3.6 and 2.4.3.7. The higher magnification images (figure 2.4.3.6) showed that there was no internalisation observed of the GO in the bacteria except in the *A. globiformis* with GO in Milli-Q water where there was a penetration of GO through the bacteria (red arrows). LB broth image was not obtained due to the stronger interaction shown in the GO-bacteria agglomerate that did not allow the infiltration of necessary chemicals for resin embedding.

2.4.4 Discussion

The results showing the different behaviour of GO in Milli-Q water, ISO 10712 test media, and LB broth, with and without bacteria, showed that GOs were dispersed the best in Milli-Q water followed by ISO 10712 test media then the LB broth. This was due to the different composition of each media. For completeness, table 2.4.4.1 shows the composition of both the ISO 10712 test media and LB broth. Milli-Q water was not included, as it did not comprise any salt ions or components.

ISO 10712 test media		LB broth	
Components	**Test-culture (mg/L)**	**Components**	**LB broth (mg/L)**
NaNO3	500	**NaCl**	10000
K2HPO4.3H2O	120	**Tryptone**	10000
KH2PO4	60	**Yeast Extract**	5000
D-glucose anhydrous	2000		
MgSO4.7H2O	200		
Iron citrate (III)	0.5		

Table 2.4.4.1 Composition of ISO 10712 and LB broth.

Table 2.4.4.1 showed that the LB broth had higher salt content but also more organic substrates. Zhao *et al*. and Wu *et al*. (*122, 123*) demonstrated that agglomeration of GO was dependent on the concentration of the salt ions and natural organic matters (NOMs). This explains the DLS and the zeta potential results in which the GO in LB broth showed the least stability with highest amount of agglomeration with a hydrodynamic diameter followed by GO in ISO 10712 test media (table 2.4.3.2). As explained by Palmieri *et al*. (*121*) this agglomeration state affected the mechanism and the interaction of bacteria with GO, where the monodisperse GO would induce membrane damage and agglomeration would result in either wrapping mechanism for nutrient starvation or formation of scaffolding for growth enhancement. The toxicity tests (figure 2.4.3.2 and Appendix V) showed that the addition of GO in Milli-Q water to bacteria caused an inhibitory mechanism of membrane damage; direct contact GO with bacteria in ISO 10712 showed mixture of mechanisms and toxicity and GO with bacteria in LB broth showed growth enhancement with agglomeration (figure 2.4.3.2. and figure 2.4.3.5) likely to be due to scaffolding mechanism. Figure 2.4.4.1

below illustrates the three different conditions with the possible proposed mechanisms by which the GO and bacteria interact.

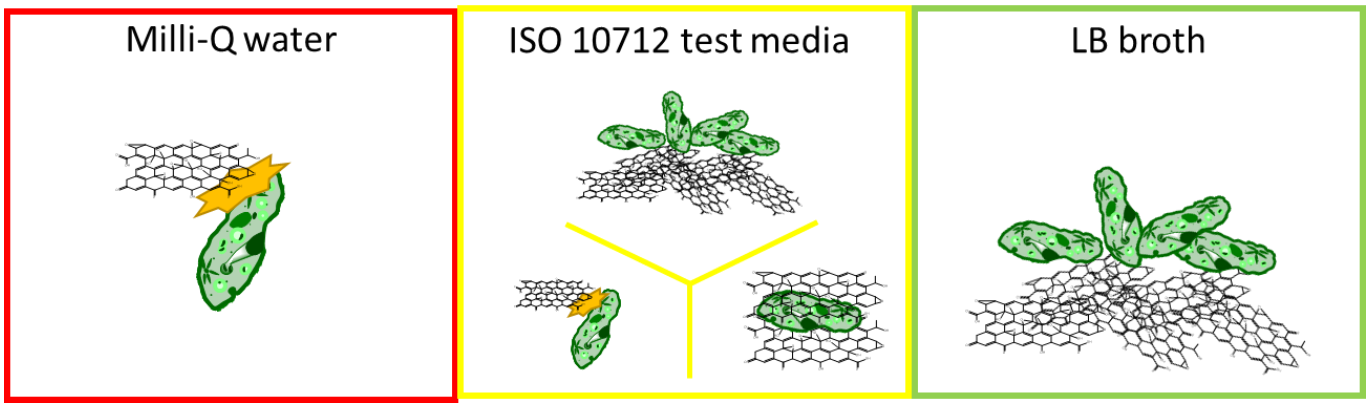


Figure 2.4.4.1 Illustration of GO interactions with soil bacteria with GO dispersed in Milli-Q water, ISO 10712 test media, and LB broth.

GOs showed different behaviour in their colloidal state depending on the media that the GOs were dispersed in as shown by the DLS and zeta potential results (table 2.4.3.2). Although comparison of effect of different salt content towards toxicity of GO against model pathogenic bacteria had been carried out, (*104*) there have been no reports of directly comparing three different media conditions covering nutrient rich condition (LB broth), environmental relevant condition (ISO 10712 test media), and no salt/minimum salt condition (Milli-Q water).

The behaviour of GO under three different conditions from abiotic results were successfully related to the toxicity result (figure 2.4.3.2 and Appendix V) by using optical images (figure 2.4.3.5), reference to other literatures using different salt contents, (*104, 121*) and TEM images (figure 2.4.3.6 and 2.4.3.7). The toxicity result from the bacteria exposed to GO under ISO 10712 test media condition was intermediatory when compared to Milli-Q water condition and LB broth condition. GO and bacteria in ISO 10712 test media showed milder inhibitory effect when compared to the Milli-Q water condition but did not show

growth enhancement to the same degree as in the LB broth. This finding certainly adds to the increasing complexity of different behaviours in which GO and bacteria could behave in an environmentally relevant condition, and adds to the need for wider range of environmentally relevant condition to be researched.

A direct comparison should be made to a study by Combarros *et al*. (*143*) which exposed GO to *P. putida* (DSM 4478) in simulated urban wastewater (SUW) and simulated industrial wastewater (SIW) to study the potential effect of GO on wastewater system. They showed a stronger inhibitory effect by the GO towards the bacteria under their condition used when compared to the ISO 10712 test condition result. Table 2.4.4.2 shows the composition of simulated wastewater from Combarros *et al*. (*143*)

	SUW (mg L^{-1})	**SIW (mg L^{-1})**		**Trace solution (mg L^{-1})**
Peptone	5000		$ZnSO_4.7H_2O$	8
Beef	3000		H_3BO_3	4
KH_2PO_4	422		$Na_2MoO_4.2H_2O$	4
K_2HPO_4	375	500	$CuSO_4.5H_2O$	4
$(NH_4)_2SO_4$	244	300	$MnCl_2.4H_2O$	4
$MgSO_4.7H_2O$	50	50	$CoCl_2.6H_2O$	4
$C_6H_{11}FeNO_7$	54			
$CaCl_2.2H_2O$	15	10		
NaCl	15			
$FeCl_3.6H_2O$		10		
Tryptone		50		
Salicylic acid		500mg L^{-1}		
Trace solution*		10mL L^{-1}		

Table 2.4.4.2 Composition of the Simulated Urban Wastewater (SUW) and the Simulated Industrial Wastewater (SIW) used by Combarros *et al*. (*143*)

Comparison of composition of ISO 10712 (table 2.4.4.1) and composition of media used by Combarros *et al.* (table 2.4.4.2) shows that ISO 10712 test media, SIW, SUW have some common salts such as $MgSO_4$ and K_2HPO_4 but also have different organic substances and other trace salts. The result by Combarros *et al*. showed that GO exhibited stronger inhibitory effect in SIW than in SUW indicating that presence of

organic substances such as peptone and beef may have interfered with the inhibitory interaction of GO with bacteria. However, comparison of ISO 10712 test media composition to SUW and SIW composition and the toxicity results from all of the three conditions indicates that sweeping statement explaining the different degree of effect by comparison of composition may not be suitable without consideration of other factors. Although the same species of bacteria was used the strain of the bacteria was different. This may have been the reason for the different degree of response. Another factor may have been the type of GO used. However, Combarros *et al*. only characterised their material using DLS and optical imaging meaning that no conclusion can be made on the direct comparison. Again, the lack of characterisation has made the comparison of different observations of toxicity difficult, as mentioned in the literature (chapter 2.1).

TEM images of GO with pathogenic bacteria had been reported previously but never for soil bacteria such as *P. putida* and *A. globiformis*. More importantly, TEM images of comparison under different media condition has also not been reported before. The difference in distance between the GO and the bacteria under different media condition (figure 2.4.3.6 and 2.4.3.7) showed that bacteria behaved differently under different media conditions in response to the GOs. The gap present indicated that bacteria may have a protective mechanism such as production of extracellular polymeric substance (EPS) under conditions with nutrients to allow them to actively defend themselves against GO. Due to the lack of nutrients for proliferation in Milli-Q water condition, both bacteria cannot activate its protective mechanism and defend themselves against GO in addition to the stable monolayer dispersion of monolayer GO. However, in environmental condition where there is sufficient nutrient, bacteria can produce EPS to form a protective layer and defend themselves against the GOs that are slowly agglomerating. Due to the lack of cutting mechanism and also the longer distance between the GO and the bacteria, wrapping mechanism is less likely to be effective and therefore the toxicity test result showed less inhibitory effect. Hypothetically, under LB broth condition, the distance between GO and bacteria may increase with more than one

bacterium within the envelope of GO showing proliferation. TEM images of bacteria under LB broth condition have not been reported, possibly due to the complexity involved in the preparation of sample of the GO-bacteria complex.

Another consideration point which has previously not been discussed in previous literature for GO under different media in including water is the effect of GO in adsorbing salt contents and nutrients from the bacteria cells. GO has been shown to adsorb salt and material end even form complexes. (*85, 150, 169*) Therefore, under conditions where there is no minerals and salt i.e. in Milli-Q water condition, GO could accelerate the diffusion of nutrients and salts from the cells, adsorb the nutrients and salts from the cells onto its surface, resulting in bactericidal effect. This extraction/adsorption mechanism differentiates itself from the conventional wrapping mechanism as this mechanism adds bactericidal effect on top of the wrapping bacteriostatic mechanism. This mechanism also explains the trend observed with addition of minerals and nutrients where toxicity of GO diminishes. With the presence of nutrients and salts around the cells and in the media, GO would adsorb the nutrients and salts outside of the cells first, slowly saturating its basal plane. The GOs still would have some toxicity towards the cells since it would still extract and adsorb the nutrients and salts but the toxicity would quickly diminish. In addition, production of EPS by the cell would further accelerate the saturation and the loss of toxicity of GO.

Two types of bacteria: *A. globiformis* and *P. putida* were used to study the different effect, if any, from the GO. It was not clear from the toxicity test results whether there was any difference between the two bacteria in term of its sensitivity towards GO but the TEM images showed that *A. globiformis* may be more susceptible to GO. The cutting mechanism was only observed in the GO with *A. globiformis* sample under TEM. However, this requires further investigation with more data points in the toxicity test in Milli-Q water

to estimate the half maximal Effective Concentration (EC50) for comparison. This is reported in subsequent chapter in chapter 3.

2.4.5 Conclusions

The comparison of interaction of GO with soil bacteria within three different media conditions ranging from nutrient rich condition to minimal salt condition showed that composition of the media such as the presence of salt and organic substrates greatly affects the GO-bacteria interaction. As well as the GO being affected by the different composition of the media, bacteria were also shown to exhibit different behaviour under the various media conditions tested. TEM images revealed for the first time, a "gap" between bacteria and GO indicating the presence of potential protective mechanism in which bacteria could defend themselves when nutrients are available. This mechanism has not been reported yet in regard to the interaction with GO and it may be unique to soil bacteria used in this study only but certainly adds to the increasing literature in an effort to understand the complex interaction between bacteria and GO. Careful attention to characterisation of material used and details of conditions as well as potential effect of experimental set-up are key to draw correct conclusion on the effect of GO on the environment and therefore the correct safety measures to be implemented. The results highlighted the need for wider environmental conditions and wider variety of bacteria to be tested against GO to understand the factors that affect the GO-bacteria interaction.

3 Effect of lateral size of GOs on toxicity

3.1 Introduction

The effect of physiochemical properties such as lateral size and oxidation degree on the toxicity of GO have been previously studied. Although there are very few literatures available on the effect of variation of different physiochemical properties on the toxicity of GO, the few literatures have suggested that lateral size of GO greatly impacts the toxicity of GO. (*92, 113, 120, 138*) No consensus have been reached in terms of how size affects the toxicity of GO towards bacteria but, as the literature review will show, the lateral size dependency of GO toxicity may differ depending on the condition and the bacteria. In order to assess the environmental risk that GFNs could pose, data on the lateral size dependency of GO toxicity towards soil bacteria are needed. Currently, there are no reports that studied the effect of different lateral size under environmental condition or even with nutrient rich condition. Therefore, the work presented here reports for the first time the toxicity effect of Large GO (LGO) and Small-GO (SGO) that differ only in lateral size. It was important for the LGO and SGO to only differ in lateral size to avoid replicating results from other existing literature which reported different lateral size GO with different degree of oxidation degrees. Again, thorough characterisation to distinguish the difference between the two lateral sizes of GO was carried out so that future comparison can be made from literatures. The toxicity results from the variation of lateral size were then corroborated with TEM images to understand the possible variation in mechanism between the two GOs. The results by the soil bacteria studied here were then compared to the pathogenic bacteria used in existing literatures and similarities and differences were highlighted. The work aimed to understand the effect of different lateral size of GO on the toxicity towards soil bacteria under

both environmental condition (ISO 10712 test) and also ideal toxicity condition (Milli-Q water). This comparison of size dependency across different media condition has also not been carried out before and provided important information on top of the results from Chapter 2.

In order to understand the effect of lateral size on the environmental bacteria similar literature review was carried out to the previous chapter in that literature related to mammalian cells and pathogenic bacteria were discussed. On top of that a further literature review was conducted to explore the different technique available to prepare different lateral sized GO for biological assay.

3.2 Literature review on the biological interactions of GO with varied lateral diameters

3.2.1 Lateral size dependency of GO towards model pathogenic mammalian cells

A few research papers have studied the effect of different lateral size of GO on their interaction with mammalian cells. Chang *et al*. (*90*) prepared three different size distributions of GO dispersions using a modified Hummer's method, by centrifuging the GO. As-synthesised dispersions of GO were centrifuged to prepare small-GO and large-GO by separating the supernatant and the residue. The three GO dispersions had mean values of 780 ± 410 nm, 430 ± 300 nm, and 160 ± 90 nm, measured by AFM, and mono to few layers GO. Raman, FTIR (Fourier Transform Infrared Spectroscopy), and XPS result showed that, even though there was a slight variation in chemical properties, they were mostly similar, and that the centrifugation step did not affect the chemical properties of the GO. Chang *et al* performed a series of assays ranging from cell viability to ROS production and membrane damage using the LDH leakage assay. (*90*) It was concluded that GO was biocompatible in the range of 10-200 mg L^{-1} with mammalian cells with

small-GO exhibiting more overt toxicity at higher concentration compared to the larger GOs. There was no indication that GO could be internalised by the bacteria for any GO diameter using TEM, but it was clear from the ROS and LDH assay that GOs could cause oxidative stress and also block some membrane channels. The paper did not explain the reason by which smaller GO could be more effective in causing cellular damage. (*90*)

Liao *et al*. (*92*) studied the impact of a range of GOs and their derivatives ton the health of skin fibroblasts and red blood cells (RBCs). Three distinct GO dispersions were prepared by bath sonication for 5 hours and 5 minutes, and probe sonication for 30 minutes. The three lateral diameter distributions, measured by DLS, were 748 ± 13 nm, 672 ± 13 nm, 342 ± 13 nm respectively. AFM showed that only probe sonicated GOs were monolayers. They also showed that in PBS, the hydrodynamic diameter increased for all of the GFNs studied. *In-vitro* haemolysis tests indicated that the lateral size of GO played a significant role in the haemolysis of the RBCs and that smaller GO caused greater haemolysis than larger GOs. The smaller GO presented more oxygen groups and therefore provided more interactions. With the fibroblasts, functionalisation by chitosan reduced its toxicity via agglomeration.

Yue *et al*. (*97*) performed a systematic study on the effect of lateral size of GO towards 6 different cell types. Lateral diameters of 2 μm and 350 nm GOs were obtained by centrifugation and exposed to two phagocytic macrophage cell lines and four non-phagocytic cells to study the cellular uptake, localisation inside the cells, and inflammation. The AFM showed that the GOs were a few layers thick with the two desired lateral dimensions. The cell study indicated that the only macrophages were able to internalise the GO. However, the amount of uptake by the two macrophages was not affected by the lateral size of the GO. The only significant difference between the two was that larger GO triggered stronger inflammation

responses, indicating better biocompatibility of the smaller GO. This was contradictory to the earlier study but highlighted the possibility of different size effects on different cell types. (*90*)

There is very little literature available studying the effect of lateral size of the GO on the cytotoxicity towards mammalian cells, and no general consensus about their relationship. One of the challenges in determining this size effect was the poor control of other factors such as the functional groups and the thickness of the GO flakes. Mittal *et al*. and Buccheri *et al*. (*91, 170*) both indicated that smaller GO exhibited higher cytotoxicity, but their method of synthesising different lateral sizes of GO resulted in significantly altered chemical structure. For this reason, these reports did not provide conclusions on whether the smaller GO was responsible for the observed change. Further is necessary, with more controlled synthesis of the GO to draw more accurate conclusions.

3.2.2 Lateral size dependency of GO towards model pathogenic bacteria

The antibacterial toxicity of GO has been related to the lateral dimensions of GO using computer simulations (*136, 139*), as well as experimentally (*113, 120*). Dallavalle *et al.* (*136*) used coarse-grained molecular dynamics (CGMD) to simulate the interaction of hexagonal graphene sheets with a phospholipid bilayer. Lateral diameters of graphene sheets between 0.9 nm to 13.3 nm have been used in this simulation. This simulation highlighted that, depending on the lateral size, graphene sheets can either insert themselves inside the membrane or adhere on top of the membrane. Below a sheet dimension of 5.2 nm, only the insertion mode was observed. Between 5.2 nm and 1.3 nm, both an insertion mode and the adhesion mode were seen depending on the orientation of the graphene sheet; above 13.3 nm, only the adhesion mode was observed.

Dallavalle *et al.* then simulated how each of the modes perturbs the membrane to assess the membrane damage. (*136*) They concluded that the larger graphene sheets affected the order of the membrane by flipping the phospholipids over, so that the hydrophobic tail interacted with the graphene sheets when they adhered on top of the membrane. Smaller graphene nanosheets did not cause disorder in the membrane during insertion. Although this simulation did not use GO, it was a good indication that size of 2DNMs affects the mode of mechanism of interaction with membranes, and worthy of future study experimentally.

Mao *et al.* also performed computer simulations similar to Dallavalle *et al.* using CGMD. However, Mao *et al.* looked at how different degrees of oxidation of graphene sheets (different GOs) affects their interaction with the phospholipid bilayer, as well as their size.(*139*) Graphene sheet sizes of between 3.5 nm to 10.5 nm were used, with varying degrees of oxidation, which were edge-only oxidation (eGO), 20% oxidation of the basal plane (sGO), and 40% oxidation of basal plane (dGO). Typical GO has C:O ratio between 2 to 3.(*54*) Therefore this simulation gave a better estimation of size dependency of GO for the phospholipid interaction. Compared to the simulation of graphene sheets by Dallavalle *et al*, even though change of mechanism of interaction was expected, the GO simulation indicated that the interaction switched from adhesion to membrane surface to 'lying' across the membrane surface which was different from previous findings. Both modes disrupted the membrane, but the difference was due to the degree of hydrophobic interaction and therefore the degree of oxidation on GO. More investigation into which specific interactions occurred between the membrane and GO is required. Nevertheless, both papers indicated that in the range between 10 nm to 3 nm, there were changes in mechanism for interaction with the membrane with different lateral sizes of GO and graphene.

Only a few experiments had been performed so far, to study the size dependency of antibacterial activity of GO. The two main literature on this topic are by Liu *et al*. (*120*) and Perreault *et al*. (*113*). Other work,

for example by Barbolina *et al*. show that there was no size dependency due to the influence of media. (*117*) Liu *et al*. prepared different lateral sizes of GO by varying the probe sonication time from 0 to 240 minutes. 6 different GO dispersions were prepared with labels: GO-0, GO-10, GO-30, GO-50, GO-120, GO-240 with the number indicating the sonication duration. The sonication process produced a narrower size distribution, and as the sonication time increased, it produced a smaller lateral size of GO. The mean lateral size of the GO decreased from 0.753 to 0.010 μm^2 with increasing sonication time. XPS data showed that there were no significant changes in the chemical properties of the GO with the sonication process, which indicated the usefulness of the process to prepare smaller lateral size GO.

Liu *et al*. exposed the GO with different lateral diameters to *E. coli*. and showed that smaller GO showed the least inhibitory effect towards the bacteria. They also studied the time and concentration dependency of GO on inhibition, which showed that increasing time and increasing concentration of GO resulted in more antibacterial effects across all sizes. Their hypothesis for the action of mechanism was that GO induced oxidative stress to membranes, which could be dependent on the surface area of the GO. Therefore, they measured the level of glutathione (GSH) to measure the oxidation capacity of GO depending on its size. GSH is a chemical mediator produced by bacteria in response to changes in the level of reactive oxygen species (ROS). Since the thiol groups on the GSH can be oxidised to glutathione disulphide, GSH measurements give a good indication of the "oxidation-stress capacity" of GO. However, their results indicated that the oxidation capacity of GO suspension did not differ with various lateral sizes. Moreover, XPS of different sized GO showed that there were no significant differences in chemical functionality between the sonicated GOs. Atomic Force Microscopy images of *E. coli* exposed to GO showed that the GO wrapped itself around the bacteria causing entrapment of the bacteria. With the larger sized GO, the cells were covered fully with a single sheet of GO, whereas with the smaller sized GO, the cells were covered with multiple smaller GOs. This was backed up by surface roughness analysis which showed that

single GO sheet coverage of cell showed less roughness than multiple smaller GO adhering to the surface. (*120*)

The hypothesis built by Liu *et al*. was that adhesion of GO on the surface of bacterial cells starves the cell of nutrients. GO is impermeable to many molecules like any other GFN and therefore blocks channels and pores in the bacteria membrane leading to inactivation of cells.(*120*) Due to the hydrophobic nature of the outer surface of the phospholipid bilayer, more hydrophobicity on the GO was hypothesised to increase the adhesion. The larger GO size was believed to have more sp^2 character and therefore exhibited stronger interaction leading to higher bacterial inactivation. However, no Raman measurements were taken of the various sized GO, and the XPS results showed very little variation in chemical composition with sonication time. Therefore, their hypothesis and conclusions were limited and required further investigation.

Another group that studied the relationship between size dependency and antibacterial toxicity was Perreault *et al*. (*113*). They also varied the lateral size of GO using various probe sonication times, characterized the lateral size using SEM (but not AFM), and exposed the GO to *E. coli*. The lateral area varied from 0.65 μm^2 to 0.01 μm^2 in a similar manner to the size distribution by Liu *et al*. However, as well as exposing bacteria to GO suspension, the bacteria were exposed to GO-coated filters as well. The different sized GO were vacuum filtered through a cellulose filter and air-dried so that a homogenous GO surface was prepared. The results from the non-suspension showed that cells in direct contact with GO surfaces had compromised cell integrity, but not those in contacted with the GO surfaces, meaning that direct contact was necessary for antibacterial inactivation *via* chemical or physical mechanisms. Moreover, the antibacterial activity increased with decreasing lateral dimensions of the GO on the surface, which was contradictory to the suspension exposure study conducted by Liu *et al*.. (*120*) To differentiate the suspension study to film study, Perreault *et al*. confirmed the difference in the interaction of GO in

suspension and GO filter paper by repeating the suspension exposure experiment and showed that the relationship between size and inhibitory effects reversed and that smaller GO decreased the inhibitory effect in the same way as shown by Liu *et al*.. (*113, 120*)

To investigate further the mechanism of the antibacterial activity of GO coated surfaces, the possibility of an oxidative stress mechanism was explored. Oxidation of GSH against various sized GO was measured using an Ellman's assay. The results showed that the smaller sized GO oxidised the GSH most avidly, which contradicted the findings of Liu *et al*. that found no relationship. Perreault *et al*. hypothesised that the oxidative pathway has a major contribution to the cell inactivation. Therefore, they analysed the various sized GO using Raman and XPS. XPS results showed comparable results to Liu *et al*. in that there were no significant differences between the samples. However, the Raman spectra of various sized GO showed increasing I_D/I_G ratio with decreasing GO size indicating smaller sized GO has more defects. Previous findings had indicated that defects in carbon structure allow oxygen to be adsorbed, which was an essential step in oxygen mediated oxidative stress, and the increase in defects led to more adsorption of oxygen.(*140*) Usually, defects in GO are the functional groups, such as the hydroxyl or the carboxyl groups that break the sp^2 character. However, as demonstrated by the XPS, there was no significant difference in the functional groups present between the different sizes. Therefore, it was likely that the defect observed in the Raman spectra was due to edge-site defects or basal-plane vacancies which resulted in smaller sp^2 domains, and the fragmentation process created more defects of those types responsible for oxidative stress. It should be noted that this hypothesis was used to explain the reverse trend of what has been observed in suspension, but Perreault *et al*. and Liu *et al*. both conducted their Ellman's assay in a suspension media. Therefore, the effect of change in lateral size towards defects and oxidative stress have been inconclusive thus far in suspension assays. Both Raman and XPS measurements should be taken when it comes to studying lateral size dependency of GO towards environmental bacteria.

An interesting remark made by this study and another study by Akhavan *et al*.(*135*) was the reactivation of bacteria after short period of bath sonication (~5 min) in a suspension exposure study. The suspension which contained both GO and the bacteria were sonicated to release the cells from the GO entrapment. This re-activation by sonication was only observed for the suspension study and therefore highlighted the difference in mechanism of toxicity of the surface and suspension systems. However, as with any other observation, Liu *et al*. reported otherwise and indicated that the interaction between GO and bacteria were very strong and the entrapment were irreversible. (*120*)

The reactivation seen in suspension could only be explained by the wrapping mechanism, so far as the other mechanisms proposed disrupt the cell membrane, leading to irreversible damage to the cells. However, Tu *et al*. (*137*) and others (*109, 125*), observed that there was evidence for loss of membrane integrity under the microscope, even using a suspension assay, which was contradictory to the re-activation results.

Tu *et al*. (*137*) carried out both computational and bacteria suspension exposures of GO interaction with *E. coli*. They used GO lateral sizes of 50 nm, 200 nm, 500 nm and the CFU method to show that larger GO had a higher inhibitory effect at 100 mg L^{-1} of GO. The higher inhibitory effect was attributed to the higher amount of sp^2 domain leading to more extraction and cutting in the membrane. TEM images showed that there was clear leakage in the cytoplasm of the cell. They concluded that there was a distinguishable difference between lipid extraction and cutting (nano-knife mechanism). Both of which were observed but no other mechanism, such as membrane embedding or wrapping, were observed.

Yu *et al*. (*138*) most recently showed that there were competing mechanisms between the wrapping and cutting mechanisms. They studied the effect of GOs with hydrodynamic diameter of 1295 nm, 2015 nm, 3074 nm, 4544 nm against *Streptococcus Mutans*. They used the CFU method for cell viability testing but was unclear which media was used during exposure. They showed that within the range of 12.5 to 50 mg

L^{-1}, the different GO sizes had a parabolic relationship, where the GO with hydrodynamic diameter of 2015 nm had the highest inhibition. Using SEM, it was shown that smaller GO showed more instances of membrane-cutting but fewer instances of the membrane-wrapping, whereas with the larger GO, the observation was reversed. They also studied the relationship between oxidative stress and the size but concluded that oxidative stress was not affected by the change in size. Therefore, Yu *et al*. concluded and showed that these mechanisms could compete.

Except for the embedding mechanism, it is claimed that all of the other mechanisms have been observed experimentally. However, as highlighted before, separate groups used different mechanisms to explain their results, which in some cases cannot be supported by other competing mechanisms. For example, insertion mechanism, cutting mechanism and phospholipid extraction mechanism rely on edge interaction, which suggests that more edges from smaller sized GO would increase the toxicity. However, the wrapping mechanism could be used to explain opposite trend where larger sized GO would increase the strength of adhesion due to more hydrophobic sp^2 domains and therefore strongly interacts to starve the cells of nutrients. Computational results have suggested the possibility of a change in the physical mechanism of action between different lateral sizes and degrees of oxidation of GO, however this has not been established experimentally.

In summary, evidence in the literature points to the fact that a change in lateral size would affect the outcome of the toxicity tests. Tu *et al*., Perreault *et al*., and Liu *et al*. all reported that, in suspension, larger lateral size GO showed higher toxicity towards model pathogenic bacteria, *E. coli*. (*113, 120, 137*) However, other reports such as Yu *et al*. that studied the effect of different lateral sized GO on another bacteria showed that the dependency was not as straightforward and that there may be favourable mechanisms depending on the lateral size of GO. (*138*) Even against *E. coli*, Tu *et al.* have shown a different

mechanism in comparison to Perreault *et al*. and Liu *et al*.. (*113, 120, 137*) Computational results have also suggested that mechanism of action could change depending on the lateral size. (*136, 139*) Since there has been no reported results on the effect of different lateral size GO on soil bacteria, it was important to investigate the effect of GOs lateral size on *A. globiformis* and *P. putida* using ISO 10712 but also in a similar condition to the ones reported in the literature. (*113, 120, 137*) This unique study on impacts of lateral size of GO on the health of environmental bacteria will also generate new underpinning understanding into how bacteria and GO interact to attempt to deconvolute the findings described in the literature.

In the next section, a literature review was performed to select the optimal method to produce the different lateral sizes of GO.

3.3 Preparation of different lateral sized GO

Both Perreault *et al*. (*113*) and Liu *et al*. (*120*) used probe sonication to break up the GO of various size ranging from few μm to few nm. They both varied the length of sonication time and reported that increasing sonication time decreased the area of GO monolayer. This was conducted using bath sonicator, as well, but for a longer period of time.(*171*) However, both sonication methods only broke the larger sheets into smaller fragments and failed to prepare narrow size distribution of larger dimeter GO. Therefore, a narrow distribution of only smaller 2DNM sheets could be obtained. A shorter sonication time retains the larger sheets in the range of μm but may still include smaller dimeter GO.

To separate out different lateral sizes of 2DNM, a fractionation process is commonly used. Several methods of fractionation have been explored for 2DNMs, mainly for GFN and GO. The physical methods included standard centrifugation and density gradient centrifugation, which separated out the materials depending

on their shape and density. Although for GO, the degree of oxidation, as well as the choice of media affects the separation of materials, it was a relatively quick way to fractionate GO by their size. (*172-174*) Other physical methods included phase separation between isotropic and liquid crystal phases. (*175*) However, this method required a long time for the phases to separate, and there was an uncertainty about the range of sizes of GO that this method was applicable to. Directional freezing method had also been explored, which used liquid nitrogen to freeze the dispersion. Due to the dependency of hydroxyl group on the basal plane with the size of GO, by controlling the freezing rate, different sizes of GO could be separated. (*176*) However, this method was subject to the degree of oxidation which was not always dependent on the lateral size. A simple filtration method using track etched membrane was very simple and quick way to fractionate different size GO. The only drawback was in controlling the rate of agitation to suit each membrane with different pore sizes, as too little agitation causes the pores to be blocked by large GO sheets, and too much agitation causes the large GO sheets to crumple up and pass through the pores. However, a relative simple system setup means that this could be easy to set up.

Chemical methods to fractionate included selective sedimentation by controlling the pH (*177*), or varying the solvents (*178*). Addition of spherical particles could also selectively adsorb different sizes of GO for fractionation. (*179*) However, all of these methods required an additional step to wash the additives or media away to ensure that the GO was pure. Controlling the size of GO during synthesis had also been tested by sieving graphite flakes. (*180*) However, this required careful consideration of oxidation and exfoliation steps, as these could break up the GO sheets, giving wide distribution of sizes. A scalable fractionation method was likely to employ controlled synthesis of well-defined parent 3D materials, as well as post-synthesis fractionation methods. A narrow distribution of different sized 2DNMs would allow optimisation of devices (*181*) and also membranes (*171*). However, for the purpose preparation of 2DNMs

for environmental toxicology studies in the laboratory, one or a combination of fractionation methods seemed sufficient.

Filtration by track-etched membranes, probe sonication, and centrifugation methods seemed to have been the most reliable and required the least number of steps. Both probe sonication had been employed more commonly by toxicity test in order to study the effect of lateral size of GO on bacteria. (*113, 120, 138*) Therefore, the probe sonication method was employed to prepare the smaller lateral size GO and compare the effect with the as-received GO from ACS material. From herein, the as-received GO which was the GO used in Chapter 1 is referred to as large-GO (LGO) and the probe sonicated GO is referred to as small-GO (SGO). Other methods of fractionation, such as centrifugation and filtration by track-etched membrane, were carried out to prepare different lateral sizes of GO but they were more time intensive and required more equipment as well as additional steps for controlling the concentration of the dispersion which was essential for the biological assay.

In the next section, methods, and results for the preparation of SGO was presented and discussed followed by a comparison between the characterisation and toxicity tests of LGO and SGO. Toxicity test results from both ISO 10712 and the pre-exposure with Milli-Q water were presented.

3.4 Method and Materials

3.4.1 Preparation of SGO

GO from ACS materials were sonicated as-received for up to 240 minutes using a probe sonicator (750 Watt Ultrasonic Processors – VCX Series, Sonics, Sonics & Materials Inc., USA) operated at 20% of 750W (150 W). The volume of GO (5 mg L^{-1}) was set at 20 mL so that the power to volume ratio was 7.5 W mL^{-}

[1]. This was comparable to the power used by Perreault *et al*. (*113*) Probe sonication time was varied at 1 minute, 10 minutes, 120 minutes, 240 minutes. At each time point, AFM measurements were taken. Only the 120 minutes probe sonicated SGO was taken for subsequent characterisation by XPS, Raman, DSL, and for zeta potential.

3.4.2 Characterisation of SGO

All characterisation steps were exactly replicated as the characterisation used in the chapter 2 with as-received GO.

3.4.3 Toxicity test for SGO

The same method was employed with as-received GO, described in Chapter 2. The only change was the number of concentration time points, with more intermediate concentration points between 0-200 mg L^{-1} of GO.

3.4.4 Statistical test

For comparison of toxicity response between results of different GO and different bacteria, EC50 of each condition with different bacteria and different GOs were calculated using logistic regression. The EC50 values were compared using statistical Z-test. All end-point assays were considered utilising the EC50 value and also the S.E.. All analysis were carried out using Microsoft excel and Origin 2022.

3.4.5 TEM image

The same protocol was followed to prepare samples for TEM image of both SGO and LGO with *A. globiformis* and *P. putida*.

3.5 Results

3.5.1 AFM result of probe sonication

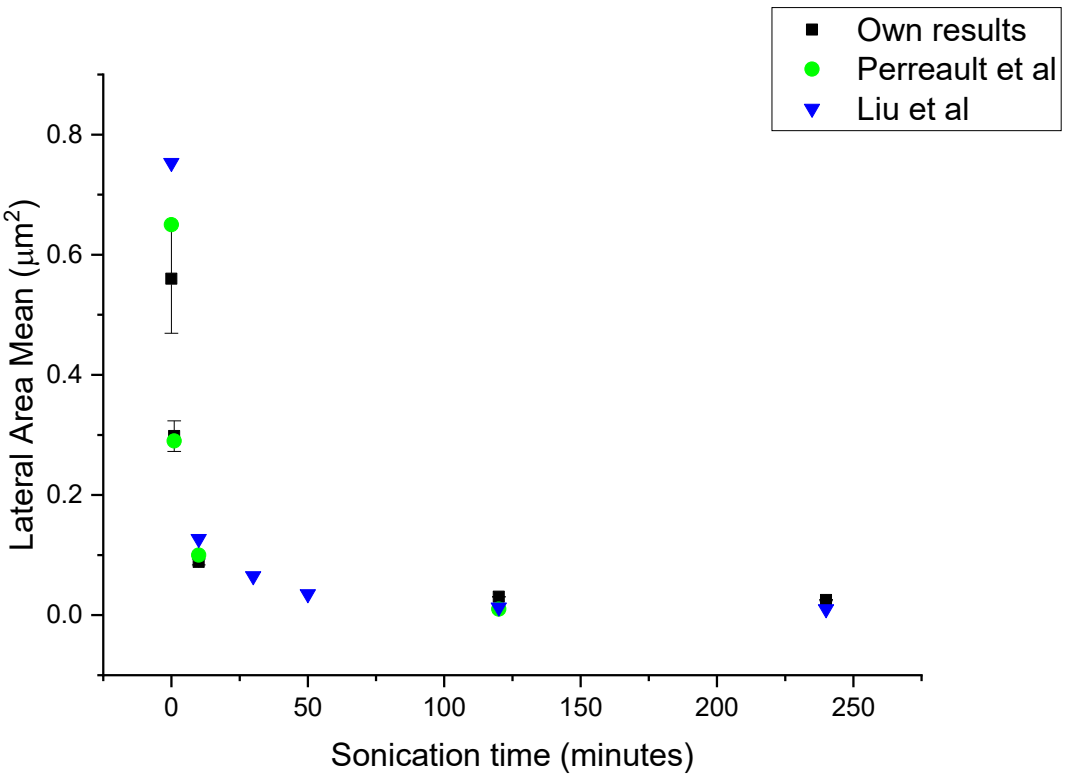


Figure 3.5.1.1 Plot of sonication time versus lateral size of the GO flakes given by lateral area measured using AFM of the results but also compared to two other data sets from the literature. (*113, 120*)

The plot of sonication time versus measured lateral size of GO flakes showed that increasing sonication time led to smaller GO flake size. Probe sonication was able to break up the GO flakes effectively with short amount of time of sonication (~1 minutes) where the flake size could decrease to nearly half of the starting size. The effect of probe sonication quickly diminished in an exponential manner in that longer sonication time did not lead to smaller GO beyond 120 minutes of sonication. Therefore, in the subsequent section 120-minutes sonicated GO was used as well as the As-Received GO. The 120-minutes sonicated GO was referred to as SGO and the ARGO was referred to as LGO.

The plot also showed the probe sonication result from Perreault *et al*. and Liu *et al*. (*113*) matched closely to one another but also to the result obtained here. Interestingly, although the starting material of GO dispersion varied in lateral size, the after the sonication, the GO flake size began to converge together and produced similar GO flake sizes. The method used within the project was matched as close as possible to the method employed by Perreault *et al*. but the power used in the Liu *et al*. was not reported. Coleman *et al*. showed that sonication power directly affected the size of the GO flakes and therefore, the three independent results plotted were likely to have had the same sonication power input. (*25*)

3.5.2 **Characterisation of SGO (120 minutes sonicated GO)**

Comparative AFM, Raman, XPS as well as DLS and zeta potential measurement of SGO were taken and presented

AFM

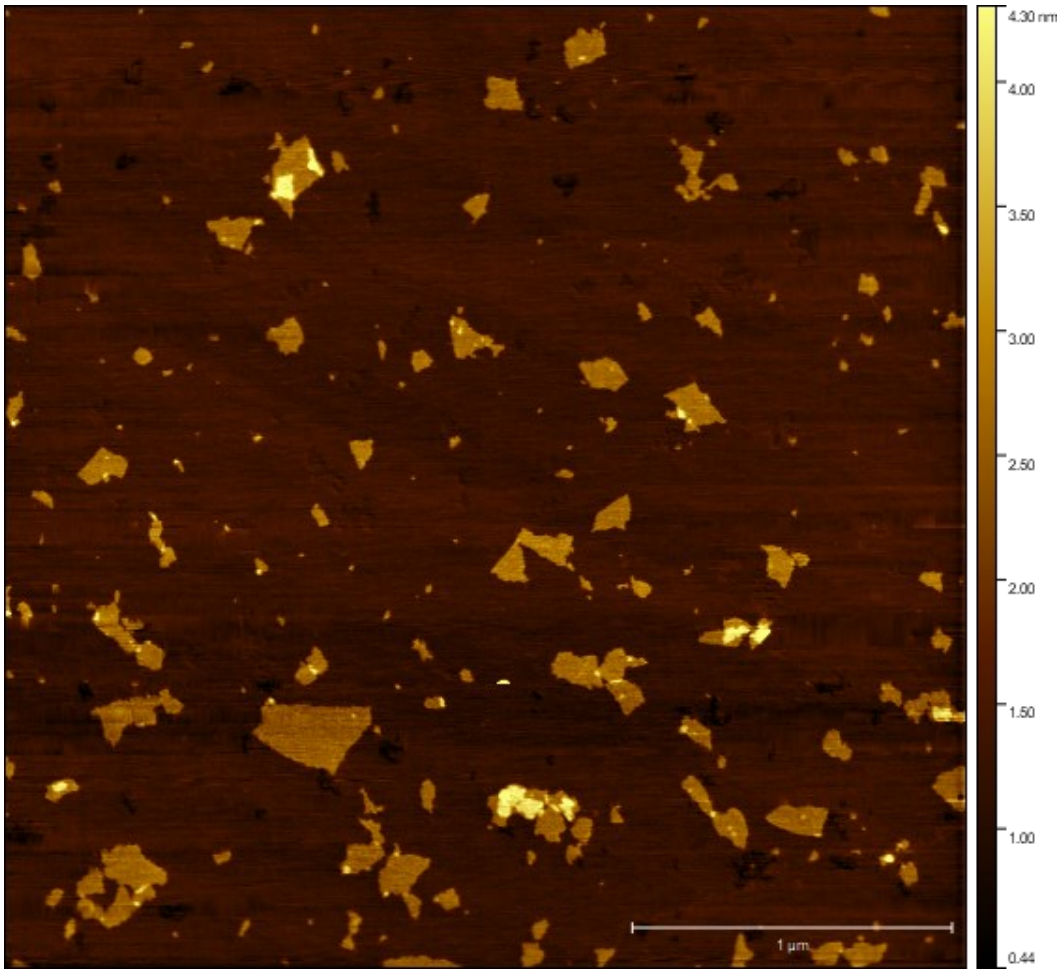


Figure 3.5.2.1 AFM image of SGO drop-casted on to freshly cleaved mica sheet at 1 mg L^{-1}.

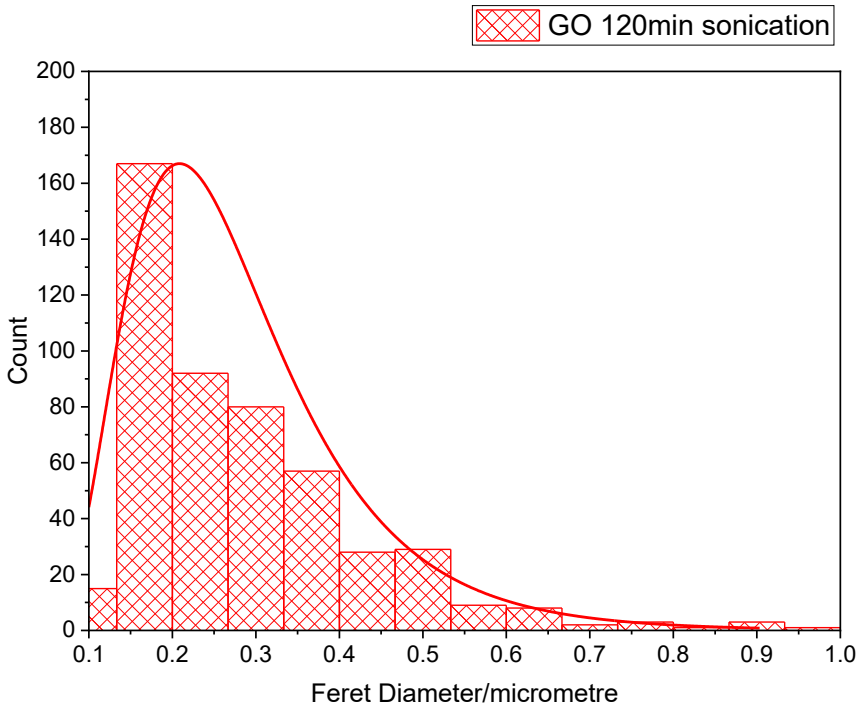


Figure 3.5.2.2 Distribution plot of lateral diameter of SGO (measured using Feret diameter) with sample size N = 495 with bin size of 14 (mean = 0.28, S.D. = 0.14).

AFM of SGO (figure 3.5.2.1 and 3.5.2.2) showed that 120 minutes of sonication resulted in smaller flakes of GO. Table 3.5.2.1 below shows a comparison of the mean value between the LGO and SGO, which indicated that the two samples of GO dispersion differed greatly in terms of the lateral size. Therefore, the use of probe sonication was successful in preparing small diameter GO.

	Mean lateral diameter	**S.D.**
LGO	0.96	0.80
SGO	0.28	0.14

Table 3.5.2.1 Mean and S.D. of both LGO and SGO from AFM measurements taken from figure 2.2.2.2 and 3.5.2.2

Raman

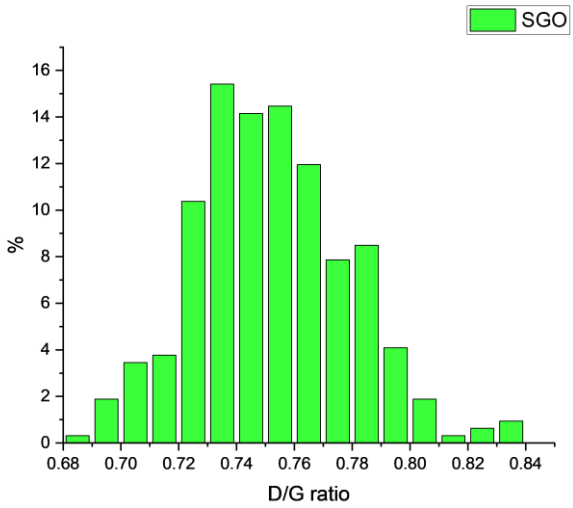
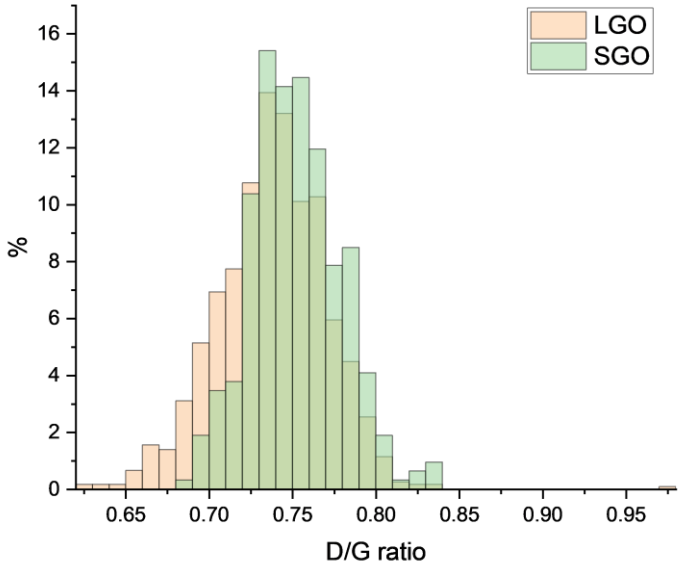


Figure 3.5.2.3 D/G ratio distribution plot of SGO deposited on silica wafer (5 mg mL^{-1}). Mean = 0.75, S.D. = 0.03, Sample size N = 318.



2945

Figure 3.5.2.4 Comparative D/G ratios of LGO (As-Received GO) and SGO on the same graph.

The Raman results (figure 3.5.2.3 and 3.5.2.4) showed that the sonication process did not affect the defect density of the GO. The average D/G ratio of LGO to SGO changed from 0.74 to 0.75 which was very little and within the error values obtained. Therefore, the sonication process was able to produce smaller GO flakes without altering the defect density of the GO.

XPS

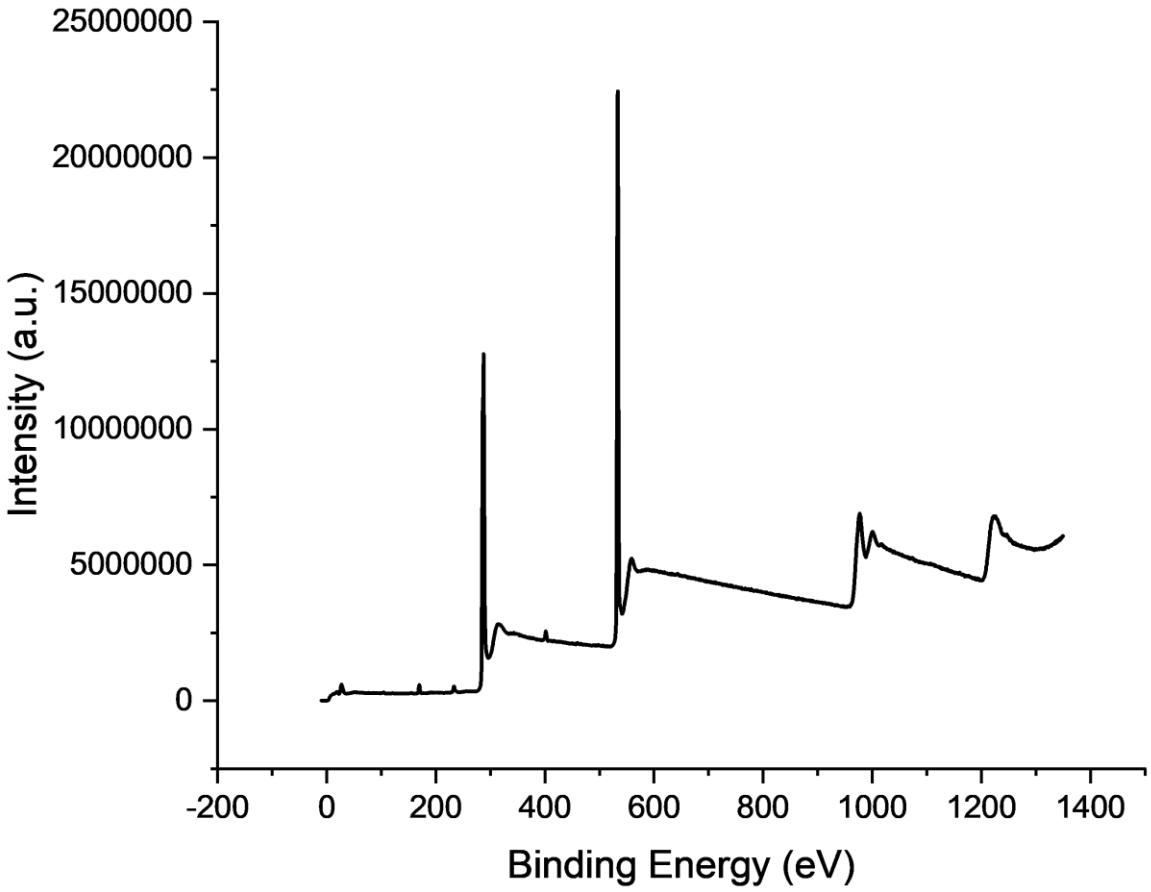


Figure 3.5.2.5 XPS survey spectra of SGO drop-cast onto a silica wafer with the main chemical transition peaks labelled.

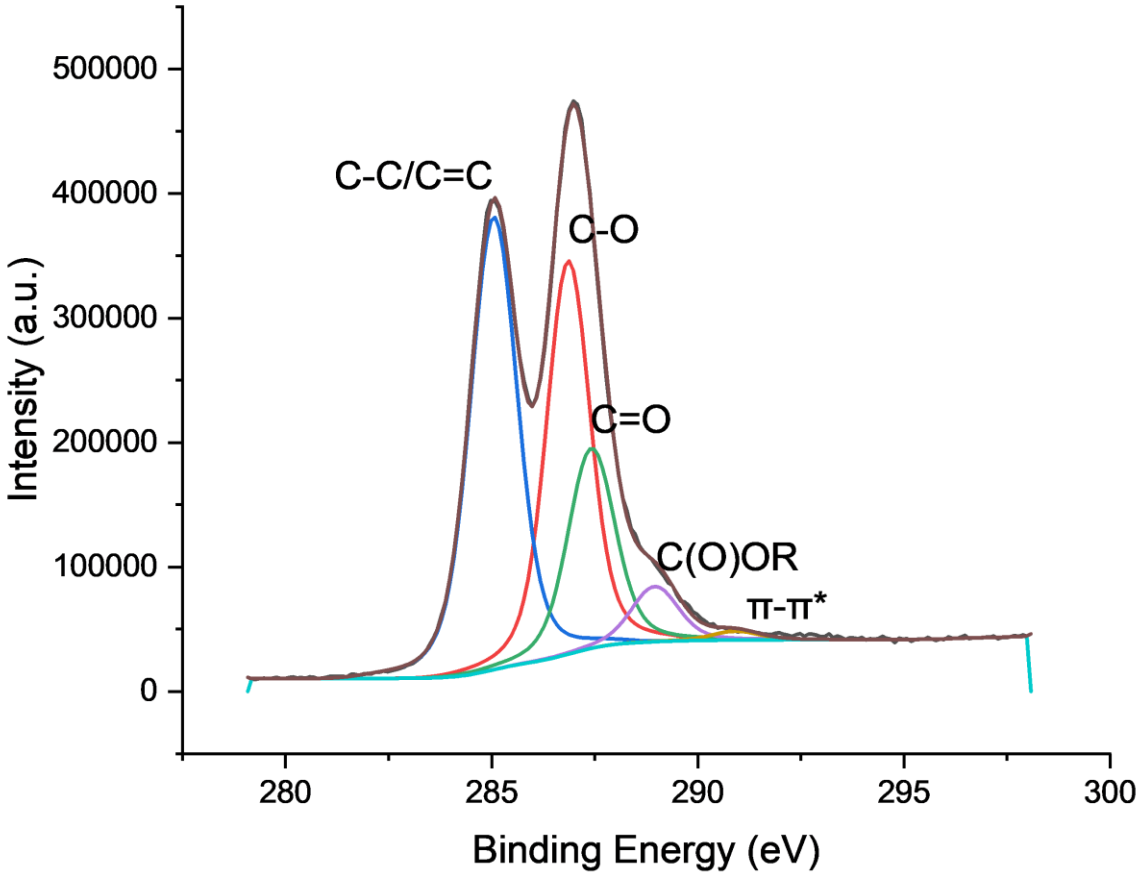


Figure 3.5.2.6 High resolution XPS spectra of C1s transition peak of SGO on silica wafer. The spectra had been deconvoluted and fitted to show the different chemical environment of C1s.

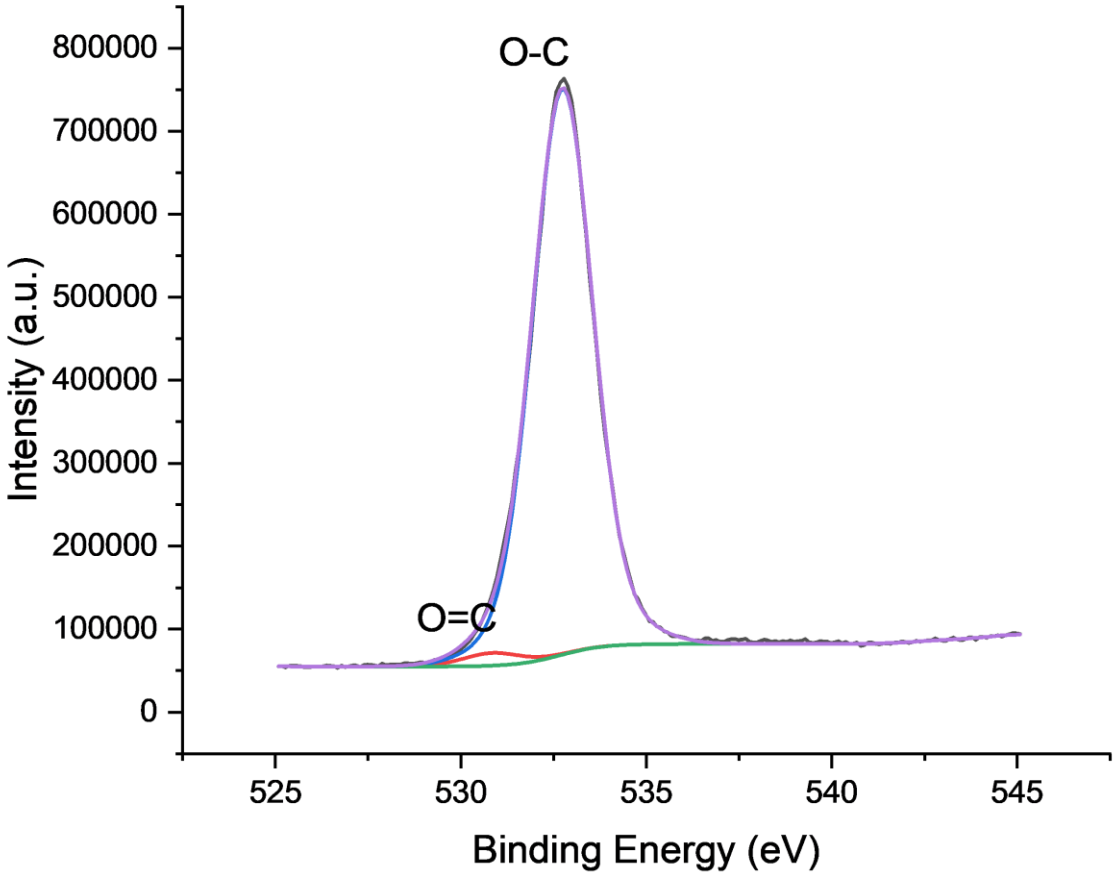


Figure 3.5.2.7 High resolution XPS spectra of O1s transition peak of SGO on silica wafer. The spectra had been deconvoluted and fitted to show the different chemical environment of O1s.

LGO	C/O ratio	O/C ratio
LGO	2.11	0.48
SGO	2.07	0.48

Table 3.5.2.2 C/O ratio and O/C ratio calculated from survey and C1s spectra of XPS obtained from SGO in comparison to LGO (As-Received GO).

XPS showed that the chemical composition of the GO changed minimally with the sonication process (figure 2.2.2.8 and 3.5.2.6). The comparison of C/O ratio (table 3.5.2.2) which was routinely used to

compare any chemical changes showed very little change. Usually for a chemical change such as reduction of GO, there were larger changes with a higher increase in C/O ratio, where the C content significantly increased and O content decreased. (*159*)

DLS/zeta potential

DLS and zeta potential data in both Milli-Q water and ISO 10712 test media was taken and presented in a similar manner to the LGO in figure 2.2.2.9.

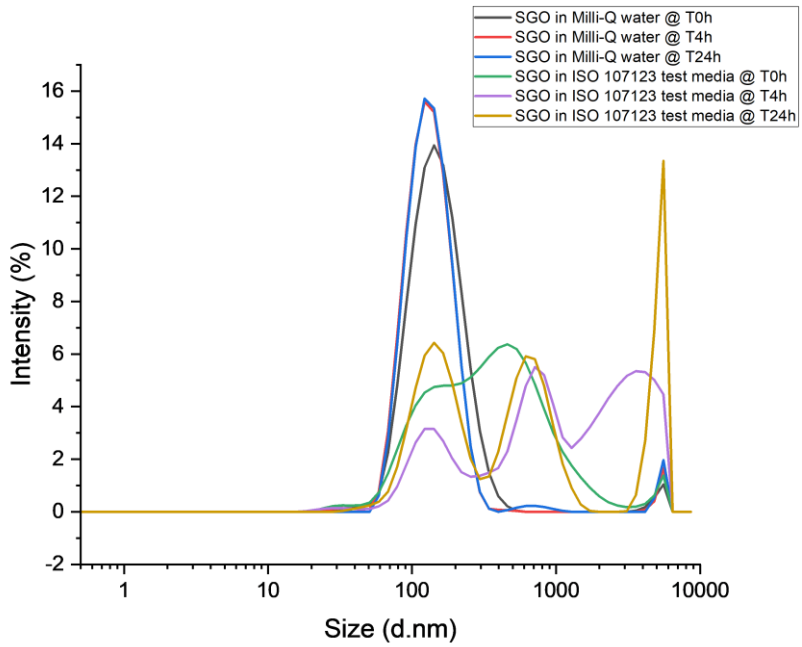


Figure 3.5.2.8 DLS hydrodynamic diameter plot by intensity of SGO dispersion in Milli-Q water and ISO 10712 test media at different time points of 0 hour, 4 hours, and 24 hours. Each plot was average of three repeated measurements at concentration of 50 mg L^{-1}.

	Time	Z-average	PDI	Zeta
SGO in Milli-Q water (50 mg L^{-1})	0h	149.28±10.28	0.28±0.02	-46.30±2.55
	4h	153.48±12.14	0.36±0.06	-44.10±2.37
	24h	142.96±3.49	0.36±0.03	-44.56±2.17

SGO in ISO 10712 Test media (50 mg L^{-1})	0h	250.74±15.54	0.55±0.03	-27.98±1.55
	4h	619.96±232.01	0.95±0.09	-28.58±1.31
	24h	606.94±50.81	0.89±0.07	-28.08±1.20

Table 3.5.2.3 DLS hydrodynamic diameter given by Z-average and PDI as well as Zeta potential measurements of SGO dispersion in Milli-Q water and ISO 10712 test media (50 mg L^{-1}) at 0h, 4h, and 24h.

The DLS plot of hydrodynamic diameter by intensity of SGO in Milli-Q water and ISO 10712 test media shown in figure 3.5.2.7 showed that the SGO agglomerate more under ISO 10712 test condition. In Milli-Q water, the intensity plot showed that the main peak was around 140 nm and remained to be the main peak with no significant shift. However, in the ISO 10712 test media, the size intensity plot of SGO showed multiple peaks indicating agglomeration and a polydisperse dispersion.

The table comparison of SGO and LGO (table 2.2.2.7 and 3.5.2.3) indicated that the SGO hydrodynamic diameter (indicated by Z-average value) was smaller for SGO in comparison to LGO. The table also showed that the SGO like LGO showed incipient instability and agglomerated over time. One noticeable difference between the LGO and SGO behaviour in ISO 10712 test media, apart from the smaller hydrodynamic size, was the PDI value. The PDI value of SGO in the test media was significantly higher than the PDI value of LGO indicating that the SGO formed multiple agglomerates of different sizes. This was reflected in the size intensity plot, as well with the visible multiple peaks shown for the plot of SGO. This may be due to the smaller GO having more surface area and more variety of interactions to form different sized agglomerates.

3.5.3 **Toxicity tests using ISO 10712**

In a similar manner to the results compiled for the LGO toxicity test with ISO 10712 protocol, the proliferation plot of all the repeated runs for SGO were plotted and presented in figure 3.5.3.1-3.5.3.4.

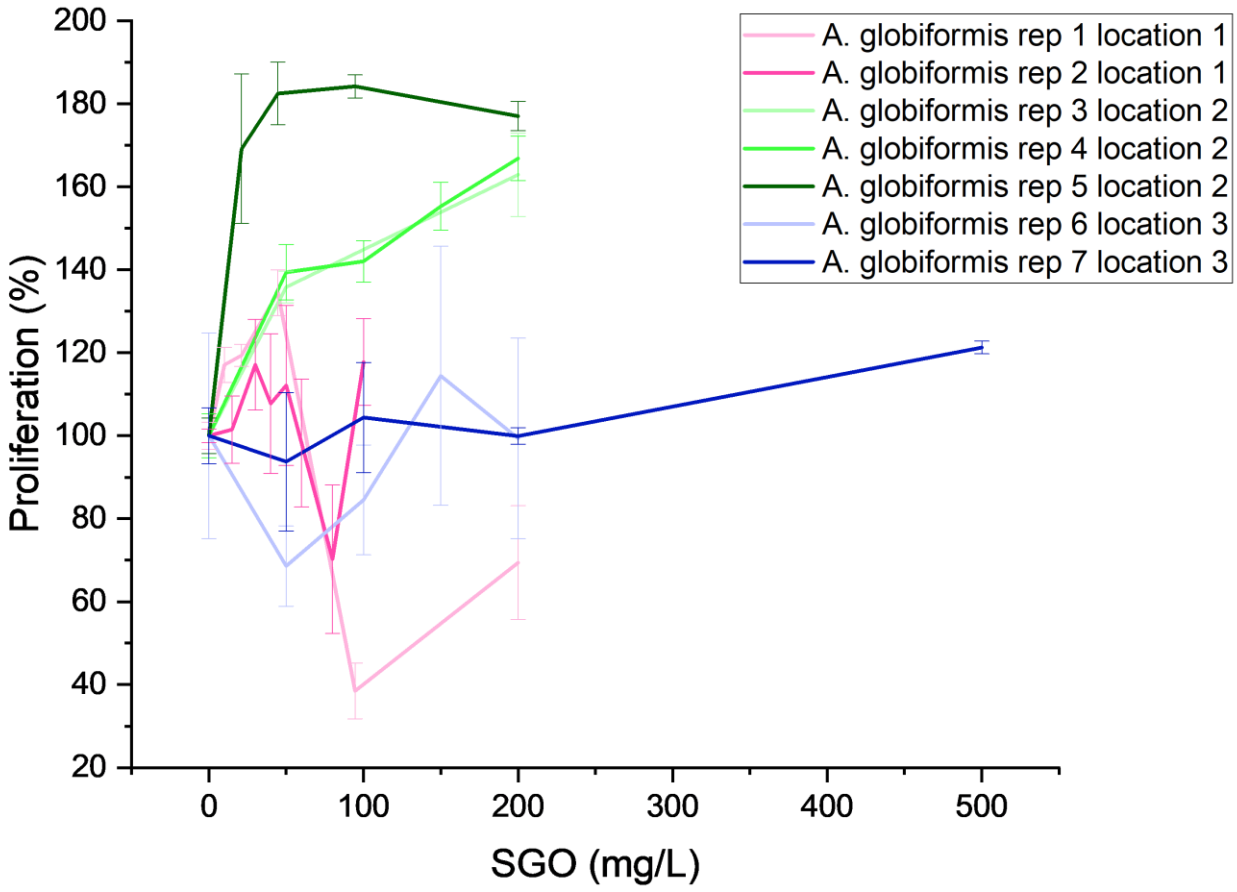


Figure 3.5.3.1 Proliferation plot of *A. globiformis* with SGO based on OD change results. Toxicity test results of all ISO 10712 runs against *A. globiformis*. This proliferation plot was based on the OD change data with 5 replicates for each of the data points with each error bar representing standard error. Each of the samples were run independently from the other. Each shade of colour represents the location and the time frame in which the experiment was carried out. Shade of pink represents experiments carried out at Location 1 in 2019. Shade of green represents experiments carried out at Location 2 in 2020. Shade of blue represents experiments carried out at Location 3 in 2021 and 2022.

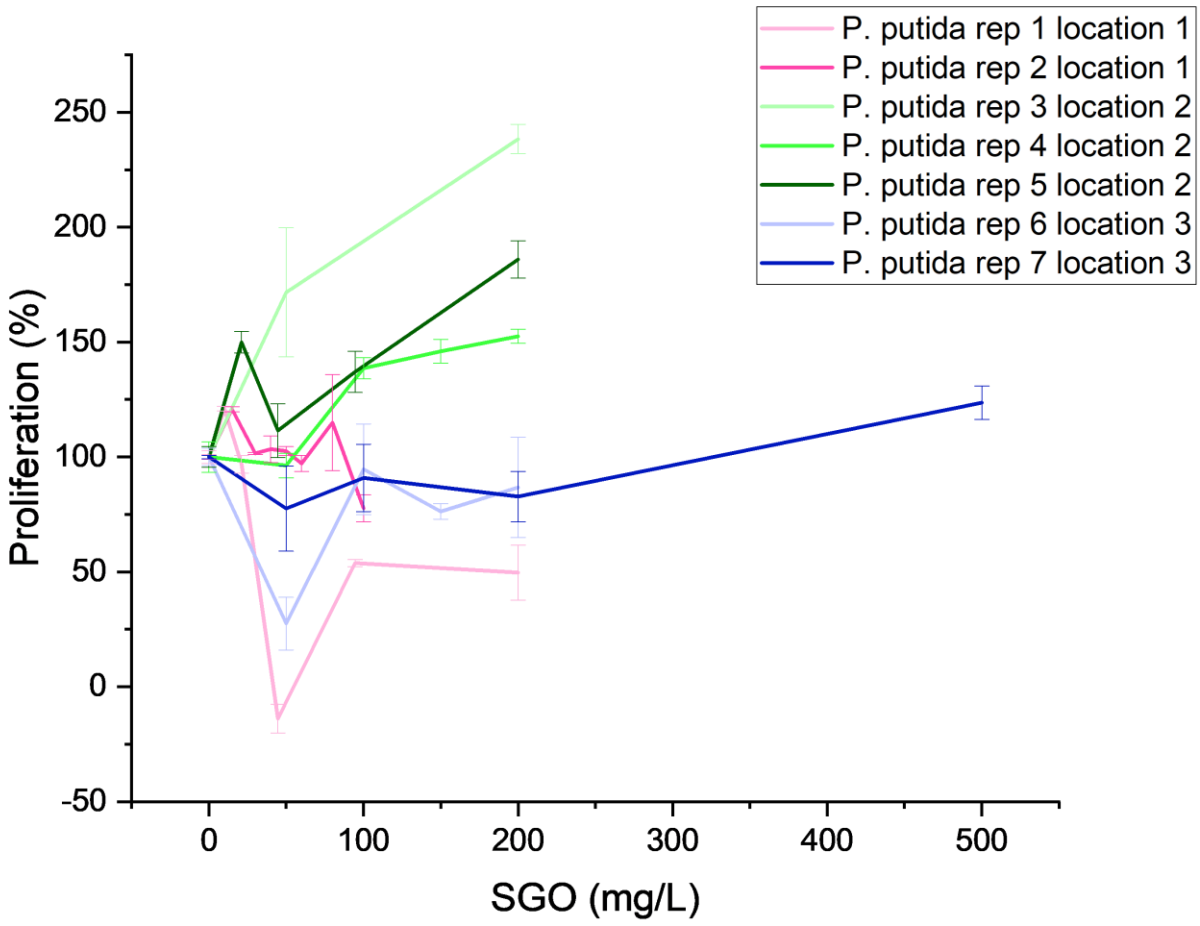


Figure 3.5.3.2 Proliferation plots of *P. putida* with SGO based on OD change results. Toxicity test results of all ISO 10712 runs against *P. putida*. This proliferation plot was based on the OD change data with 5 replicates for each of the data points with each error bar representing standard error. Each of the samples were run independently from the other. Each shade of colour represents the location and the time frame in which the experiment was carried out. Shade of pink represented experiments carried out at Location 1 in 2019. Shade of green represents experiments carried out at Location 2 in 2020. Shade of blue represents experiments carried out at Location 3 in 2021 and 2022.

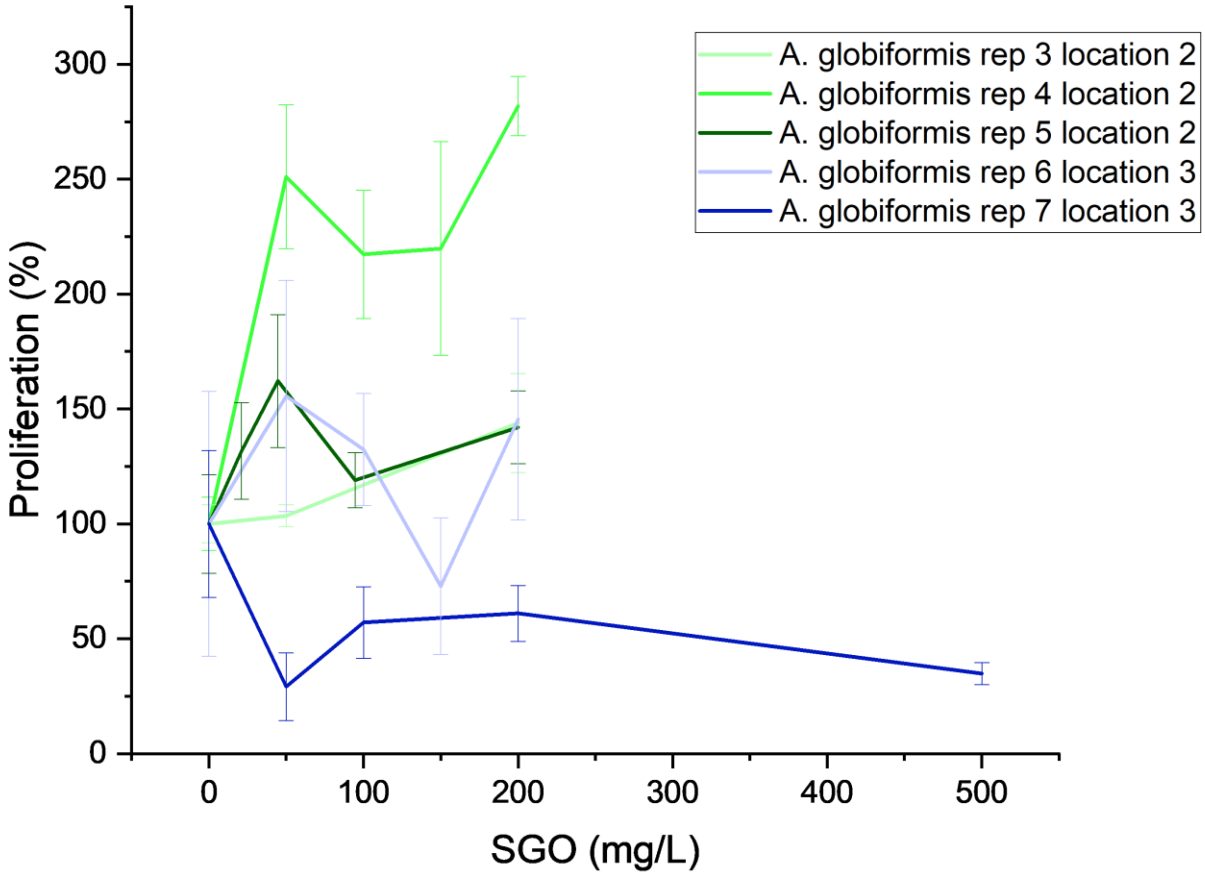


Figure 3.5.3.3 Proliferation plot of *A. globiformis* with SGO based on CFU results. Toxicity test results of all ISO 10712 runs against *A. globiformis*. This proliferation plot was based on the CFU data with 5 replicates for each of the data points with each error bar representing standard error. Each of the samples were run independently from the other. Each shade of colour represents the location and the time frame in which the experiment was carried out. Shade of pink represents experiments carried out at Location 1 in 2019. Shade of green represents experiments carried out at Location 2 in 2020. Shade of blue represents experiments carried out at Location 3 in 2021 and 2022.

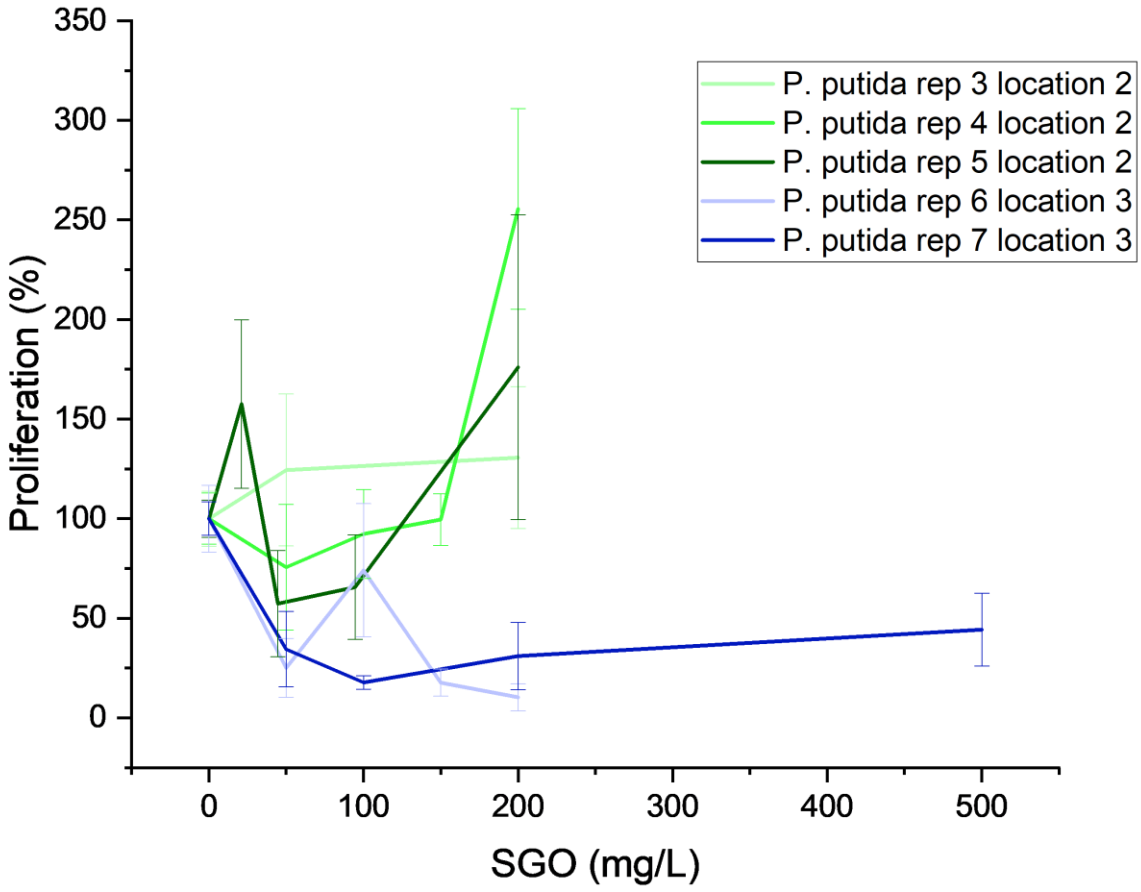


Figure 3.5.3.4 Proliferation plot of *P. putida* with SGO based on CFU results. Toxicity test results of all ISO 10712 runs against *P. putida*. This proliferation plot was based on the CFU data with 5 replicates for each of the data points with each error bar representing the standard error. Each of the samples were run independently from each other. Each shade of colour represents the location and the time frame in which the experiment was carried out. Shade of pink represented experiments carried out at Location 1 in 2019. Shade of green represents experiments carried out at Location 2 in 2020. Shade of blue represents experiments carried out at Location 3 in 2021 and 2022.

The compilation of ISO 10712 toxicity test results with SGO showed the same finding as LGO result with ISO 10712 toxicity tests. There was no complete inhibition effect observed and a mixture of trends with inhibitory effect as well growth enhancement suggesting mixture of mechanism present. This corroborated

with the hydrodynamic values given in the earlier result where the Z-average was similar between the LGO and SGO in ISO 10712 test media. (Table 2.2.2.7 and table 3.5.2.3) The only difference was that there could have been more variety of results from the SGO due to the increased PDI and range of agglomerate sizes as shown by the size intensity plot. The abiotic OD change result also showed that the behaviour of SGO in the ISO 10712 test media alone was not different from LGO interaction with the media and that a bacteria-GO interaction was predominant and unique to the biotic condition.

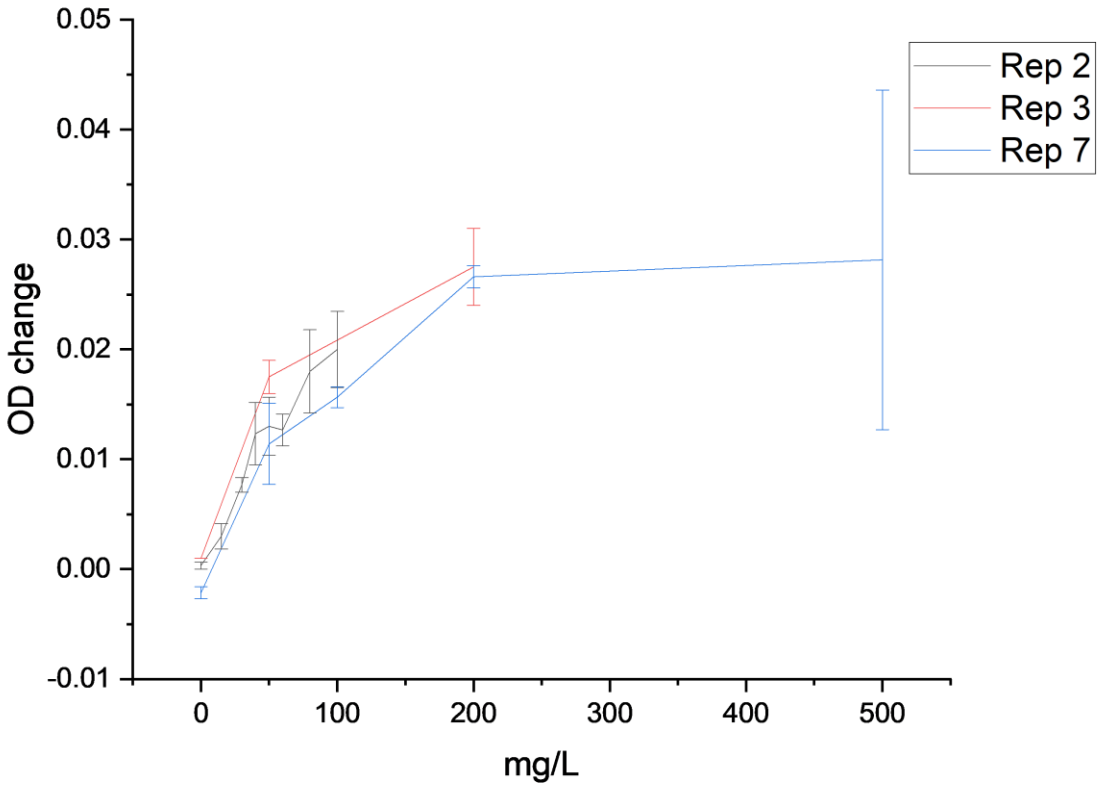


Figure 3.5.3.5 OD change of pristine SGO of concentration range between 0-200 mg L^{-1} in ISO 10712 test media. The OD change was calculated from OD reading at T0h and T24h sample (same sample left for 24-hour exposure) and each data point are average of 3 independent samples. The error bar represents the standard error.

3.5.4 Toxicity testing – Pre-exposure with Milli-Q water

A series of comparative plots shown in figure 3.5.4.1 between LGO and SGO results from OD changes, 24h CFU result and 3h CFU results (CFU reading after the 3-hour pre-exposure without re-introduction of ISO 10712 test media) showed that both LGO and SGO were effective inhibitors of bacterial growth when they were exposed to both environmental bacteria in Milli-Q water conditions. Each results method can be referred from figure 2.4.3.1.

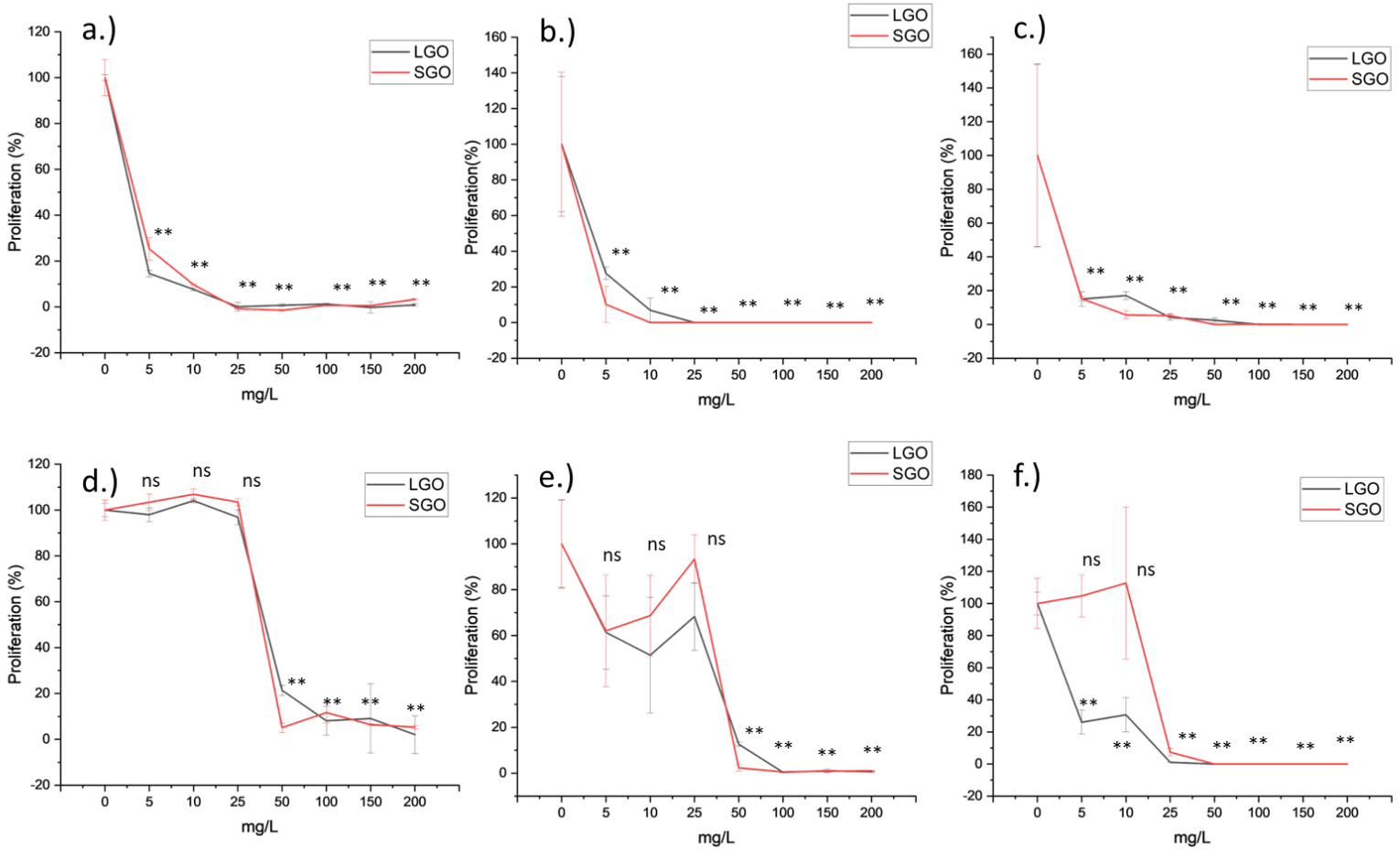


Figure 3.5.4.1 Proliferation plot of bacteria from a.) OD change results of A. globiformis exposed to LGO and SGO in Milli-Q water b.) 24h CFU results of A. globiformis exposed to LGO and SGO in Milli-Q water c.) 3h CFU results of A. globiformis exposed to LGO and SGO in Milli-Q d.) OD change results of P. putida exposed to LGO and SGO in Milli-Q water e.) 24h CFU results of P. putida exposed to LGO and SGO in Milli-Q water f.) 3h CFU results of P. putida exposed to LGO and SGO in Milli-Q water. Each data was an average of 3 measurements with error bars representing the S.E.. ANOVA statistical results were also plotted with "ns" = not statistically significant and "**" = statistically significant ($p<0.01$).

In order to draw comparison between the SGO and LGO, EC50 of each result plot was calculated and compiled below in Table 3.5.4.1.

	A. globiformis		**P. putida**	
	EC50 of LGO	**EC50 of SGO**	**EC50 of LGO**	**EC50 of SGO**
OD change	2.11	5.95	38.26	28.32
24h CFU	3.62	4.56	47.08	44.62
3h CFU	2.65	1.45	2.21	22.80

Table 3.5.4.1 EC50 calculated from each condition. Logistic regression function was used to best fit the plot using Origin 2022.

OD&24hCFU \ **3hCFU**	LGO with A. globiformis	SGO with A. globiformis	LGO with P. putida	SGO with P. putida
LGO with A. globiformis				
SGO with A. globiformis				
LGO with P. putida				
SGO with P. putida				

Table 3.5.4.2 Z-test statistical test result showing the statistical significance of differences between each of the EC50 values. Red indicates no statistical significance where $p>0.1$. Green indicates statistical significance where $p<0.01$ The left

bottom hand side of the table are results from OD change and 24h CFU result. The right top hand side of the table are results from 3h CFU result.

	3hCFU in comparison to 24hCFU and OD change result using EC50 values
LGO with A. globiformis	Ns
SGO with A. globiformis	Ns
LGO with P. putida	$p<0.01$
SGO with P. putida	Ns

Table 3.5.4.3 Statistical test (Z-test) of comparison of EC50 values between the results with the different end point assay. 3hCFU results are from direct exposure in Milli-Q water whereas 24hCFU and OD change results are from Milli-Q water exposure followed by media exposure (figure 2.4.3.1)

Figure 3.5.4.1 shows the proliferation plot of LGO and SGO against *A. globiformis* and *P. putida* in Milli-Q water with ANOVA statistical test results showing any statistically different data point compared to the control. Table 3.5.4.1 shows the EC50 of LGO and SGO against *A. globiformis* and *P. putida* in Milli-Q water. Table 3.5.4.2 shows the Z-test result of statistical test for comparison of EC50 between the different bacteria and different lateral sizes of GO. Table 3.5.4.3 shows the statistical difference if any between the methods used as depicted in figure 2.4.3.1.

The proliferation plot (figure 3.5.4.1) showed that both LGO and SGO could induce inhibitory effect which resulted in complete suppression of the proliferation. Both types of GOs showed statistically significant inhibition at 5 mg L^{-1} against *A. globiformis* and at 50 mg L^{-1} against *P. putida* (figure 3.5.4.1. a-e.) Only in 3h CFU results against *P. putida*, there was a difference in the concentration at which statistically significant inhibition was observed between LGO and SGO. Against *P. putida*, LGO showed statistically significant inhibition at 5 mg L^{-1} and SGO showed statistically significant inhibition at 25 mg L^{-1} (figure 3.5.4.1 f.)

Table 3.5.4.1 showed EC50 values of LGO and SGO against *A. globiformis* and *P. putida*. The EC50 values of LGO and SGO were an order of magnitude higher against *P. putida* than against *A. globiformis* for all results reported except in the 3h CFU result of LGO against *P. putida*. In order to compare between LGO and SGO against both bacteria Z-test were carried out on the EC50 values (Table 3.5.4.2). Table 3.5.4.2 showed that depending on the type of end-point assay used, different comparative observation could be made. The OD changes and their complementary CFU results (24h CFU) showed from table 3.5.4.1 and table 3.5.4.2 that: 1.) LGO were more effective in inhibition than SGO against *A. globiformis*, 2.) SGO were not more effective than LGO against *P. putida* and there was no statical significance 3.) Both GOs were more effective towards *A. globiformis*. However, for the 3h CFU result, where the proliferation of the culture was measured after the direct exposure with GOs, there was no statistical difference between the different lateral sized GO against *A. globiformis* and/or *P. putida*. Note that EC50 value from SGO against *P. putida* from 3h CFU result was considerably higher than other EC 50 values from the 3h CFU results but the S.E. was high resulting in non-statistically significant result.

In order to assess whether the 3h CFU results were different from the OD and 24h CFU results, another Z-test was carried out to compare the difference in result. Table 3.5.4.3 showed that only EC50 values from LGO against *P. putida* were significantly different. Other EC50 values were not statistically different. Therefore, this may indicate a considerable effect of the end-point assay used on the LGO with *P. putida* particularly.

3.5.5 TEM

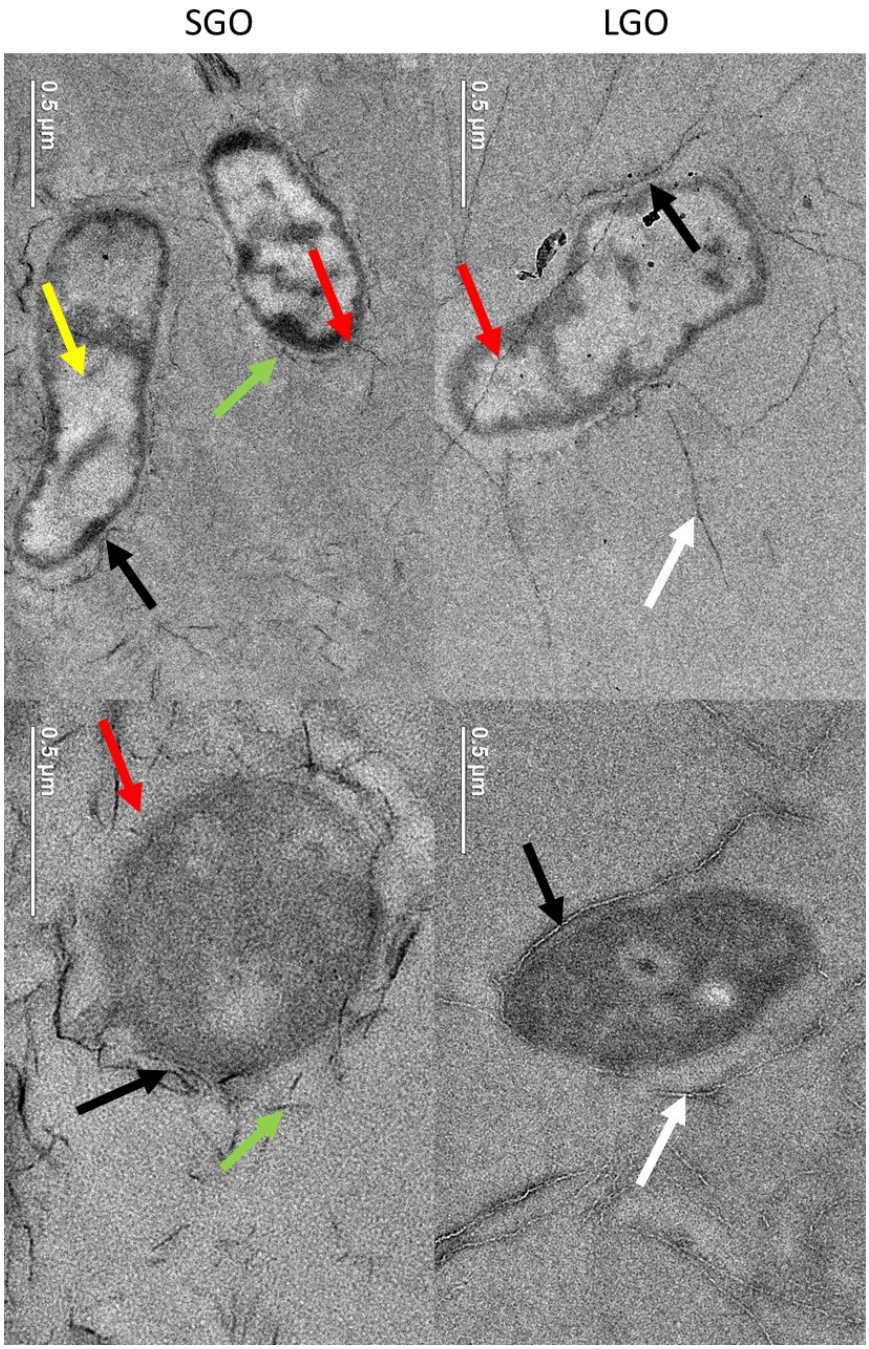


Figure 3.5.5.1 TEM images showing the different interaction of *A. globiformis* and *P. putida* bacteria with LGO and SGO. Images taken were of the samples after the 3h at 150 mg/L of GOs. White arrows show LGOs. Green arrows show SGOs. Black arrows show direct contact of GO with bacteria membrane. Red arrows show perpendicular contact of GO with bacteria membrane.

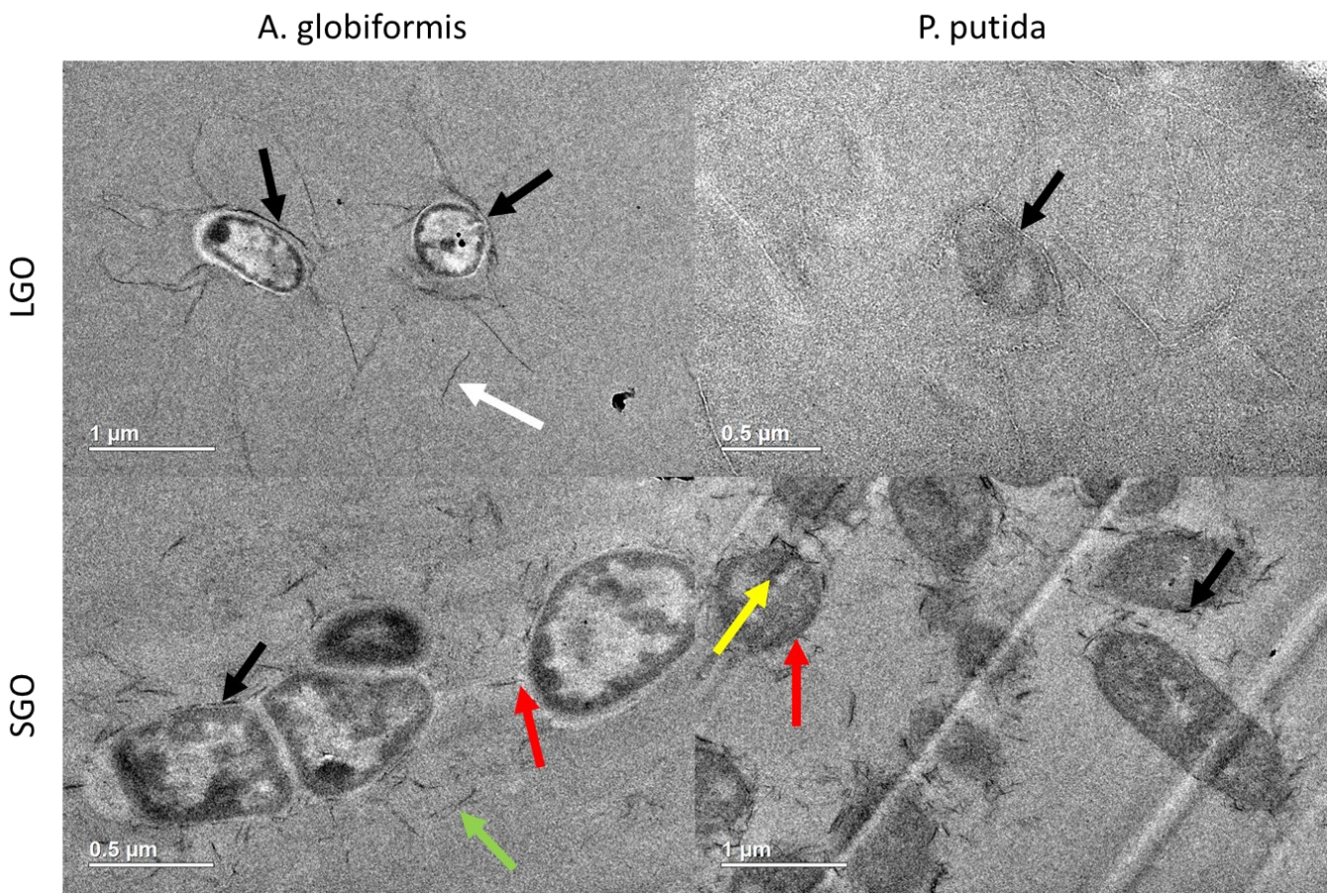


Figure 3.5.5.2 Lower magnification TEM images showing the different interaction of *A. globiformis* and *P. putida* bacteria with LGO and SGO. Images taken were of the samples after the 3h at 150 mg/L of GOs. White arrows show LGOs. Green arrows show SGOs. Black arrows show direct contact of GO with the bacterial membrane. Red arrows show perpendicular contact of GO with the bacterial membrane.

3090

The TEM images of interaction of LGO and SGO with *A. globiformis* and *P. putida* showed couple of key interaction which had not been reported together before by TEM images. Both LGO and SGO showed direct contact with its basal plane (black arrows) indicating a wrapping mechanism as previously reported by AFM and SEM but not TEM. (*113, 120*) There were also "piercing" of GO observed (red arrows) where the LGO and SGO were perpendicular to the membrane of the bacteria. This edge interaction was observed in both bacteria in multiple cells for SGO but only for LGO against *A. globiformis* and only in one instance as shown in figure 3.5.5.1. There was also some potential preferential internalisation of SGO (yellow arrows). The wrapping of bacteria was by the far the most observed. The wrapping of bacteria by LGO and SGO was observed to be different in that LGO were large in diameter and therefore did not completely encapsulate the bacteria whereas SGO were small in diameter and therefore required a multiple of SGOs to wrap around the bacteria. Both GOs were not observed to be completely enclosed and particularly with the SGO with *A. globiformis* in figure 3.5.5.2 showed potential splitting of cell within the SGOs. The splitting of cell imaged here under the condition may be the first ever reported and holds significance as it could show another mechanism where bacteria could unravel themselves from materials such as GO (and other 2DNM).

3.6 Discussion

The toxicity test result in ISO 10712 of LGO and SGO showed that there is no significant difference between the two-lateral sizes of GOs (chapter 3.5.3). Both size of GOs showed mixture of inhibitory effect, no effect on proliferation, and growth enhancement as previously discussed in chapter 2. Although SGO dispersion in Milli-Q water had significantly different lateral size (measured by both DLS and AFM), in ISO 10712 test media, the hydrodynamic diameter increased for both sizes of GO to a similar value showing

agglomeration. Similar to the findings towards LGO in chapter 2, the effect of media seemingly masked the effect of significant lateral size differences of GO on inhibitory effect.

The comparison of LGO and SGO toxicity result in Milli-Q water from OD change result and 24h CFU result indicated that both GOs showed statistically significant inhibition towards *A. globiformis* and *P. putida* at concentrations of 5 mg L^{-1} and 50 mg L^{-1} respectively. The estimated environmental concentration of release based on current production amount of GOs are between 1-1000 µg L^{-1} (based on Chapter 1 and (*182*)). Therefore, together with the ISO 10712 results, where there was less inhibitory effect observed, it could be concluded that depending on the salt and other nutrients condition in the environment, release of GOs within the lateral size range studied here (0.28-0.96 µm) should be carefully considered especially for an inhibition towards bacteria similar to *A. globiformis*. Further toxicity studies, using a lower range of concentration of GO, should be exposed to bacteria such as *A. globiformis* to pinpoint the exact concentration range where the GO starts to exhibit inhibitory effect. Against bacteria such as *P. putida* which are more resistant, concentration of GO released currently may not be of concern but if the production of GFNs were to increase further, consideration to minimise release should be taken place.

With regards to the interaction of soil bacteria with different lateral size GOs under pure water condition (Milli-Q water), it was shown that depending on the choice of end-point assay used, different conclusion could be made. From the OD change and 24h CFU results, it was shown that *P. putida* was significantly more resistant to the inhibitory effect of both types of GO by an order of magnitude compared to *A. globiformis*. It was also shown that LGO exhibited significantly higher inhibitory effect than SGO only against *A. globiformis*. LGO and SGO did not show significantly different inhibitory effect towards *P. putida*. However, the 3h CFU results showed that there were no statistically significant differences between the bacteria and also LGO and SGO as observed by OD change and 24h CFU results. It was also shown

that EC50 values changed significantly with the LGO and *P. putida* toxicity test. This change in the EC50 and proliferation results may be similar to the observation of reactivation by Perreault *et al*. (*113*), Akhavan *et al*. (*135*), and Liu *et al*. (*120*). They have collectively reported that bacteria can be reactivated in some instances depending on the condition. This point was not explored in detail as its reactivation was not considered as significant against model pathogenic bacteria but could be significant in soil bacteria.

As shown in figure 2.4.3.1, the 3h CFU results are taken directly from the pre-exposure step and both LGO and SGO would interact directly with the bacteria in a favourable condition under no media components. The TEM images taken (figure 3.5.5.1. and 3.5.5.2) were also taken after 3 hours of exposure representing the interaction in Milli-Q water only. During the interaction in Milli-Q water at pre-exposure step, LGO would predominantly interact with the bacteria *via* wrapping mechanism and the adsorption extraction mechanism with its basal plane as indicated by the TEM image. SGO would interact differently in that they could interact *via* edge interaction as well internalisation of SGO on top of the wrapping mechanism. After the direct interaction (pre-exposure step in Milli-Q water), the GO and bacteria were re-introduced in nutrient rich media (ISO 10712 test media) and left under the ISO 10712 protocol condition for 24 hours after which OD change and 24h CFU results are obtained. During this time, any bacteria that was inactivated would be allowed to re-activate under nutrient rich condition (in a similar manner to the reactivation step observed by Perreault *et al*. (*113*) and Akhavan *et al*. (*135*)). However, any bacteria that were completely killed with extraction/adsorption mechanism would not be able to reactivate (in a similar observation by Liu *et al*. (*120*)). Considering these points, the interaction between *A. globiformis* and both GO as well as *P. putida* and SGO were strong enough that introduction of nutrient did not reactivate the cells. However, interaction of *P. putida* and LGO were not as strong and therefore when the nutrients were introduced, *P. putida* were able to reactivate and showed the significance increase in the EC50 value and

also resulted in significantly different EC50 value between LGO interaction between two *P. putida* and *A. globiformis*.

The additional consideration of extraction/adsorption mechanism introduced earlier adds to the complexity of interaction between bacteria and GO. However, because the mechanism is bactericidal effect as opposed to the bacteriostatic wrapping mechanism, the extraction/adsorption mechanism explains the bactericidal effect observed where there was no growth after the reactivation step. This mechanism also is size-dependent where the increase in lateral size and therefore basal plane would increase the toxicity of the GO towards bacteria.

The edge interaction/nano-knife interaction observed in the TEM images taken (figure 3.5.5.1. and 3.5.5.2) also should be treated with consideration. Including the preparation of these TEM samples, most biological samples with GO for TEM include centrifugation steps. This step could potentially manufacture such nano-knife interaction as observed by forcing the GO to insert itself in the membrane. With the current techniques it is difficult to rule out this manufactured observation other than to optimise the preparation method which is often not reported. In this project the centrifugation step was optimised but other in-situ techniques such as use of high-speed AFM (*183*) with experimental set up where direct interaction of GO with bacteria can be observed would confirm the existence of nano-knife mechanism.

The difference in the strength of interaction was likely to be due to the difference in the structure of outer membrane as well as potentially an active protective mechanism. One of the main differences between *A. globiformis* and *P. putida* is that *A. globiformis* is gram-positive bacteria and *P. putida* is gram-negative bacteria. Gram-positive bacteria have peptidoglycan as the outer layer which has adhesive characteristic and gram-negative bacteria have lipopolysaccharide attached to its extra outer membrane which are negatively charged. (*132*) The adhesive characteristic of membrane of the gram-positive bacteria could

have resulted in equal and strong interactions between both sizes of the GO. Whereas the lipopolysaccharides and the extra outer membrane may have provided protection towards SGO that preferred to interact *via* edge interaction or insertion into the cell but not towards LGO that would predominantly interact *via a* wrapping mechanism. Therefore, this may explain the significant increase in the EC50 value for the LGO and *P. putida* from the 3h CFU result and OD change/24h CFU result.

Note that there was also a slight increase in the EC50 value of SGO with *A. globiformis* which resulted in significantly different EC50 value reported from OD change and 24h CFU between LGO and SGO against *A. globiformis* which was not significant at 3h CFU result. This may be due to the ability of A. globiformis to replicate even under wrapping mechanism as shown in figure 3.5.5.2. Of the bacteria cells that were wrapped, some were able to replicate in SGO due to the inefficiency of the SGO to wrap completely around the cells and were allowed to replicate and increase the EC50. The proliferation under wrapping warrants further work and possibly real-time imaging as this could also explain the reactivation mechanism together with the strength of interaction with membrane.

3.7 Conclusion

As-received GO (LGO) dispersion was successfully probe sonicated to produce SGO without significantly altering the chemical structure of the GO. Under favourable condition of interaction (Milli-Q water) GO exhibited both bacteriostatic and bactericidal effect with different degree of interaction and mechanism between gram-positive and gram-negative bacteria. *A. globiformis* (gram-positive bacteria with thick peptidoglycan layer) showed strong interaction with both sizes of GO with possibility of proliferation with SGO under nutrient rich condition. *P. putida* (gram-negative bacteria with extra outer membrane with lipopolysaccharides) showed very limited proliferation with LGO in comparison to SGO but upon

introduction of nutrients, the interaction with LGO was reversed and LGO and SGO showed comparable inhibitory effect due to the difference in the preferential mechanism displayed by the two different lateral size GO. Of the mechanism observed, it was apparent that wrapping mechanism was the dominant mechanism of interaction with smaller GO being able to display insertion or edge interaction with the bacteria cell. The wrapping mechanism was observed to reversible towards in some cases and smaller lateral size GO were shown to be potentially inefficient at stopping proliferation *via* wrapping mechanism. A higher modality of imaging with real-time monitoring of the change in interaction is needed to further support the current findings. Under environmental conditions, if the GOs were released to the environment where the interaction would occur under nutrient rich condition, there would be minor inhibitory effect with mixture of growth enhancement and possibly no observable effect (Chapter 2 and Chapter 3.5.3). However, if the GOs were released to the environment where the interaction with bacteria would occur under low salt or nutrient condition, the GOs would exhibit strong inhibitory effect. Change in the condition from low salt or nutrient condition to nutrient rich condition can recover some bacteria growth depending on the lateral size of the GO and the strength of the interaction between the bacteria and the GO but the inhibitory effects do still remain as GO exhibit both bacteriostatic and bactericidal effect.

4 Environmental toxicity of next emerging 2DNMs: MoS_2

4.1 Introduction to TMDs and MoS2

Another emerging 2-Dimensional nanomaterial (2DNM) that is next in line from the Graphene Family Nanomaterials (GFNs) are Transitional Metal Dichalcogenides (TMDs). TMDs are labelled as a potential contender in the field of semiconductors as their bandgaps range closely with that of Si and GaAs in their semiconducting phase. This is different to pristine graphene as their bandgap is zero in theory and careful chemical modifications are required to achieve a range of bandgaps from metallic to semiconductors through to insulators. (*184*) The beauty of TMDs is the variation of elemental combinations they can have. The general structure of TMDs consists of one transition metal layer sandwiched between two layers, made up of group 16 elements, otherwise known as chalcogens. The combinations of these are numerous and in terms of the number of bulk material of TMDs, there are over 60. (*184, 185*) Therefore, TMDs have a greater variety of 2D nanomaterials than GFNs that can be tuned and modified for more specific applications than GFNs. They can potentially fill the market-gap created by the GFNs and follow the production-growth.

4.2 Literature Review of MoS_2 and its biological interaction

4.2.1 MoS_2 structure

Of the TMDs, Molybdenum disulphides (MoS_2) have attracted a lot of attention since these materials can be derived quite easily like GFNs at ambient conditions, and from a source which are abundant in nature.(*186*) Like graphite, the parent bulk material of graphene, the bulk material of MoS_2 has been used

as lubricants for nearly a century, and coincidentally or not, both of the bulk materials, graphite and MoS_2, are similar in terms of physical appearance and behaviour. (*3, 187*) However, the single layer MoS_2 has noticeably different properties to graphene due to the difference in its physiochemical properties arising from the elements involved and the general structure.

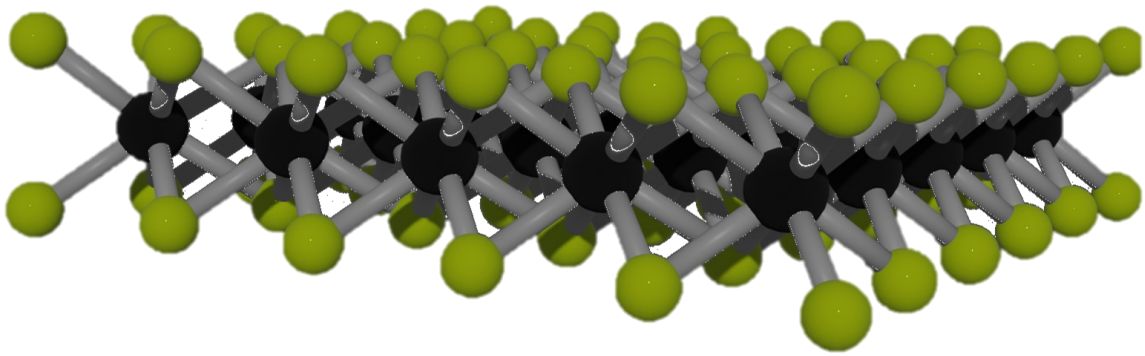


Figure 4.2.1.1 3D model of monolayer MoS_2. Mo in black and S in green.

As shown in figure 4.2.1.1, MoS_2 is similar to graphene in that the atoms are arranged periodically and their 2D plane expands in series of hexagonal shapes. However, MoS_2 has 2 elements of transitional metals and chalcogens instead of one carbon element (in graphene) to make up its network, and the arrangements between the two elements can result in several different phases. The discussion of different phases will become important in the subsequent sections where synthesis and applications are discussed.

4.2.2 MoS_2 synthesis and associated phases

2D MoS_2 layers can be made in a similar way to GFNs. However, MoS_2 has different phases in which the synthesis method can influence the dominant phase present in the product which is controlled to meet specific applications. For example the 2H phase is semiconducting and therefore used in electronic

applications, whereas the other 1T and 1T' phase are metallic and semi metallic and can be used to enhance catalytic activity. (*188, 189*) Naturally occurring bulk MoS_2 consists mainly of the 2H phase since this is the most thermodynamically stable phase. The 2H phase is hydrophobic and has trigonal prismatic geometry. However, the less stable 1T phase can be synthesised from the 2H phase *via* Li intercalation and because of this, chemical exfoliation usually results in a mixture of both phases. The 1T phase differs greatly from the 2H phase and has metallic and hydrophilic characteristics which facilitates the exfoliation process. The Li-intercalation process results in destabilisation and change in electronic structure of 2H MoS_2 to 1T MoS_2. (*190*) Some effort has been made to produce both phases separately and interchangeably at high yield, but currently the challenge remains in using a scalable synthesis method that produces high amounts of the desired yield. (*191, 192*)

Other synthesis methods other than chemical exfoliation include mechanical exfoliation, liquid exfoliation, chemical vapour deposition (CVD), and hydrothermal-solvothermal reaction. Mechanical exfoliation, liquid exfoliation and chemical exfoliation are top-down synthesis methods for which the bulk layered MoS_2 is exfoliated by breaking the inter-layer weak bonds formed by Van der Waals forces. This results in mono- or few layer MoS_2, depending on how well the synthesis conditions are controlled. The latter two synthesis methods mentioned are bottom-up, meaning that the layers are assembled from their atomic constituents. This allows for more control of the phase, size and crystallinity but these methods usually require harsher conditions.(*188*) It is worth noting that although chemical or liquid exfoliation methods are the most scalable, they are still unable to control the phase fully or use environmentally unfriendly materials.

MoS_2

4.2.3 MoS_2 applications

Applications of MoS_2, beyond its bulk material use as a lubricant, depend on its phase, and size and number of layers. For example, mechanical exfoliation can provide a large monolayer with minimal damage to the lattice and therefore defects for fundamental studies, but the synthesis method is itself is largely limited. Therefore, if no other synthesis methods became available, the potential for layered MoS_2 would not have become as widespread. Due to the development of the synthesis methods described earlier, the range of applications so far include, but are not limited to, energy storage, electronic devices, hydrogen evolution reaction, membrane materials, optoelectronics, electronics, sensors, catalysis, and environmental adsorbents. (*9, 189, 193-196*)

In terms of the safety of synthesis and scalability, energy storage/electronic devices, and catalysts made using chemical and liquid-based exfoliation are most promising for use in future industrial applications. This is because these two synthesis methods are currently most scalable and use less harsh conditions than other synthesis methods. In addition, these methods can now convert between phases in solution after exfoliation. (*192, 197*) Synthesis methods, such as CVD and hydrothermal-solvothermal reactions are capable of producing more controlled layers of MoS_2 from Mo and S-containing precursors, but the method uses high-temperature and potentially results in release of Sulphur containing fumes or solution. The clear advantage of synthesis in a solution phase is the potential for scalability and also the ease of post-processing for wide variety of uses. However, this does still raise concerns about whether these materials are safe to the environment. It was predicted that CNTs, a close relative of GFNs, are released to the soil compartment. In particular, since these materials can also be produced using liquid phase synthesis and provide similar applications, it is likely that MoS_2 are also released into aquatic and soil compartments during its production and use.

4.2.4 Applications of MoS_2 in the environment

In order to discuss the environmental impact and the pathways for these materials to be released in to the environment, their environmental applications also had to be highlighted. (*11, 198*) These applications are predominantly removal of environmental contaminants through adsorption or photocatalysis, disinfection during water treatment, environmental sensors, and antibacterial surfaces. (*4, 199-212*) These applications of MoS_2 are still in their early stages but it is clear that one of the main applications of MoS_2 nanomaterials would be in environmental applications. These materials could be released into air, soil, water and landfill, but it is most likely that they will end up in water and soil from water treatment applications. This means that they are more likely to be released into surface, ground, and wastewater. For this reason it is vital to consider the possible environmental fate, aging and transformation of MoS_2 along these pathways. (*213*)

4.2.5 Environmental Fate of MoS_2

There were number of considerations that needed to be addressed to assess the environmental impact of nanomaterials. Primary research is usually performed on pristine nanomaterials, but transformations such as dissolution and ageing, under environmentally relevant conditions should also be considered. (*36, 214, 215*) A review assessing the environmental interaction of 2DNMs, other than graphene, considered MoS_2 to be one of the more stable 2DNMs in solution. This was not as surprising, considering that the bulk material can be found in nature. (*4*) However, it was also important to note that bulk MoS_2, molybdenite, found in mining by-products, oxidised slowly in the environment (*216*) Therefore, it was highlighted that dissolution is still likely to occur via other dissolution pathways and for MoS_2, oxidative dissolution was hypothesised to be the dominant transformation pathway. (*4*)

Indeed this was the case as MoS_2 was later shown to undergo significant oxidation dissolution. (*36, 217, 218*) Wang *et al*. studied the oxidative dissolution pathway of chemically exfoliated MoS_2 in environmentally relevant media. Their aims were to systematically study the relative length-scale of the degradation to determine the rate, and to understand whether pH and different media had any effect on the rate of oxidative dissolution. They have found that two main points. 1.) The oxidative dissolution reaction resulted in production of protons which resulted in self-limiting reaction as well as destabilisation of colloidal dispersion. 2.) The dissolution was pH dependent with increasing pH leading to faster dissolution kinetics. The main dissolution reaction was identified as follows.

$$2MoS_2 + 9O_2 + 6H_2O \rightarrow 2MoO_4^{2-} + 4SO_4^{2-} + 12H^+ \quad \text{Equation 3}$$

This main oxidative pathway revealed that, not only does the MoS_2 dispersion lower its pH to self-limit the oxidative dissolution, but the commonly observed re-stacking and the aggregation seen during storage was due to the protons produced in the reaction. MoS_2 nanosheets had been shown to have negative charges at neutral pH, due to the charge transfer that occurs during intercalation. Therefore, the MoS_2 dispersion maintains its colloidal stability from repulsive forces between the negatively charged sheets. However, the presence of protons above certain threshold (measured by pH) destabilised the colloidal stability. Below a pH value of 1.9, it was identified from DLS and zeta potential measurements that MoS_2 nanosheets started to aggregate. This number of protons could be produced from MoS_2 dispersion concentrations of above 210 ppm which is very common for mass produced MoS_2 dispersion. Therefore, one could conclude from this

data that long term oxidative dissolution not only results in a decreased amount of MoS_2 sheets but also aggregation of the remaining sheets in the environment.

4.2.6 MoS_2 in a biological context

Understanding how monolayer MoS_2 interacts with microorganisms can help to assess its environmental impacts. *In vitro* studies of MoS_2 with cells, mammalian, or bacteria, provides a first step in understanding the possible impact that MoS_2 can have on the environment. Ideally, a literature review of *in vitro* study of MoS_2 exposed to environmental microbes would have been more focused and relevant but unfortunately, it was only recently that environmental concerns for these MoS_2 have been highlighted. These concerns arose from a cytotoxicity study of MoS_2 against humans as well as research into antibacterial application of MoS_2.

***In vitro* cytotoxicity test against mammalian cells**

It is only in the past decade that research into the toxicity of monolayer MoS_2 had been performed, and there was very little literature available on MoS_2. Monolayer, bulk and aggregated MoS_2 had all been shown to elicit low toxicity to both mammalian cells and bacteria. (*219, 220*) One important finding which applies to all experiments using traditional assays and test method to study the interaction of cells with novel materials was highlighted in a study by Teo *et al*. (*221*) Teo *et al.* compared the cytotoxicity of TMDs including MoS_2 and GOs towards mammalian cell. The MoS_2 was synthesised by Li-intercalation exfoliation to make multilayer flakes of around 5nm in thickness and 300nm in lateral size. They tested the TMDs against A549 cells - a type 2 lung epithelial cell line - using the Methylthiazolyldiphenyl-tetrazolium bromide (MTT) and the water-soluble tetrazolium salt (WST-8) assay that measure cell metabolic activity and cell viability, respectively, using colorimetric methods. MoS_2 did not cause significant toxicity to

epithelial cells up to a concentration of 200 mg L^{-1} using the WST-8 assay, although cell viability dropped below 80% to around 50% at 400 mg L^{-1}. With the MTT assay, the level of toxicity seemed to be enhanced, and in comparison, to the WST-8 assay, at every respective concentration of MoS_2, the cell viability was much lower. At 200 mg L^{-1} of MoS_2 the cell viability was already below 80% using the MTT assay. The difference in cell viability measurements from the MTT and WST-8 assays arose from the different formazan products in the respective assays. Both assays directly measured the cell viability by the MTT assay reagent or WST-8 reagent being reduced by active cells to produce insoluble purple formazan and soluble orange formazan respectively. It was reported previously that GO and Graphene could reduce the MTT reagent and produce insoluble formazan leading to a pronounced effect of toxicity and an inaccurate readout of cell viability. (*92*) A similar experiment studying the interaction of MoS_2 with the assays were carried out and the MoS_2 along with other TMDs (WS_2 and WSe_2) did reduce the MTT assay, to produce insoluble formazan, leading to a pronounced and inaccurate cell viability reading. A similar effect was not observed for the WST assay and there was no interaction observed for MoS_2 (WSe_2 was shown to reduce WST assay at high concentration of 400 mg L^{-1}). Therefore, when testing the toxicity of new materials, it is important to ensure that there was no interaction between the reagents used in the toxicity test employed and the MoS_2. This would be recommended for all 2DNMs in terms of studying the interaction of 2DNMs with common assays and the reagents used in cell viability assays.

Another important aspect in studying the toxicity of novel material was highlighted by Moore *et al.* that tested the effect of industrially produced 2D MoS_2 on the health of different mammalian cells, mimicking doses encountered during occupational exposure. (*222*) They tested MoS_2 with different lateral-diameters (in the range of 50 nm to 177nm) produced by liquid phase exfoliation. Unfortunately, there was no information on the thickness of the MoS_2, and the MoS_2 was insufficiently characterised which made it difficult to draw conclusions about which properties of the 2D MoS_2 were responsible for cytotoxicity.

However, the *in-vitro* part of the study highlighted some key points that were generally applicable for assessing the environmental safety of a novel materials. First of all, interaction of each cell type with MoS_2 was different. They assessed the toxicity of three different lateral-diameters of industrial grade MoS_2 dispersion towards THP-1, A549, and AGS cells (Human acute monocytic leukaemia, human lung adenocarcinoma, and human gastric adenocarcinoma cells respectively) using a high content screening method (a high-throughput microscopy technique using nuclear staining) and live/dead cell staining method (membrane permeable and impermeable fluorescent dye respectively) so that complications with interference seen previously in assays like the MTT was avoided. MoS_2 showed no toxicity towards A549 cells in the range of concentrations tested of up to 10 mg L^{-1}, a slight toxicity towards AGS cells with toxicity only observed at 10 mg L^{-1} of MoS_2, and a highest toxicity towards THP-1 macrophages with toxicities of above 1 mg L^{-1}. The observed differences in the sensitivity of cells towards the MoS_2 was hypothesised to be due to the different morphology of the cells. A549 cells had high amount of unsaturated fatty acid which likely protected them. The AGS cells were more resistant to microbes, in general, due to their protective function as a lining in the gastric system. THP-1 cells were the most sensitive due to their role as macrophages in the immune system; their ability to engulf foreign substances, such as Mos_2 nanosheets, increased their cellular interaction and led to subsequent cell damage. The above differences in response by different cell lines were confirmed by laser scanning confocal microscopy where the most significant changes in cell morphology was observed with the THP-1 cells. However, TEM images of the cell and the MoS_2 – made in an attempt to differentiate the internalisation mechanism between the cells - did not yield conclusive evidence. Moreover, there was no clear trend observed from the above techniques, in terms of the size effect on each of the cell line or a plausible explanation on the lack of trends. However, the paper highlighted that cell morphology could have a great influence on the interaction with the MoS_2, leading to different endpoint measurements in toxicity assays.

Second of all, the paper by Moore *et al*. highlighted that presence of contaminants in industrial grade MoS_2 could have an influence on the toxicity assessment. In this case the contaminants were endotoxin or otherwise known as lipopolysaccharides (LPS). They are commonly found on the most outer layer of gram-negative bacteria and the term endotoxin is used because it causes an inflammatory response in human cells. LPS are made of four main blocks arranged in a row from the outer membrane: Lipid A, Inner core, Outer core, and then O-specific antigen, and it is Lipid A that is mainly responsible for causing the inflammatory response. (*223*) Moore *et al*. showed that LPS were present in all three sample of MoS_2 with different lateral diameters with decreasing sizes leading to more available edges for the LPS to adhere to. Even though there were no *in-vitro* data to suggest that amount of LPS, and therefore size, had any clear trend in influencing the cell viability of the three human cell lines, it was concluded that consideration of endotoxin, as well as interaction from the MoS_2 itself, were needed during further cytotoxicity studies. Even though endotoxins would not affect bacteria and therefore did not need to be considered in the assessment of interaction between environmental bacteria and MoS_2, there could be other contaminants or by-products present in the MoS_2 dispersion that need to be accounted for. Moreover, consideration of endotoxins could lead to further understanding of interaction between bacteria and 2DNMs.

A review by Murali *et al*. and by Fojtu *et al*. summarised the recent key findings regarding interaction of MoS_2 and TMDs with human cells concisely. (*11, 224*) Out of all of the experiments which studied the effect of different physiochemical properties of MoS_2 on the cytotoxicity towards human cells, one main finding was that the phase of MoS_2 greatly affected the activity. It was found that 1T phase of the MoS_2 were more active due to higher efficiency in charge transfer and the ability to induce Reactive Oxygen Species (ROS) than the more naturally stable and abundant 2H phase. Other properties such as different synthesis method and degree of exfoliation had been studied to determine whether they affected the

cytotoxicity but currently, no clear conclusion could be drawn due to the difficulty in controlling the synthetic route to obtain different lateral diameter, or number of layers.

As summarised by Murali *et al*., and Fojtu *et al*. the physiochemical property relationship between MoS_2 and human cells should be explored further with more carefully designed materials preparation. However, to summarise the current findings on the MoS_2 interaction with human cells, it was found that MoS_2 were biocompatible even without modifications. The most active phase, 1T MoS_2, had been shown to be biocompatible up to 100 mg L^{-1} with greater than 95% cell viability. Functionalised MoS_2 showed improved biocompatibility with ranges up to 400 mg L^{-1}. Therefore, in terms of interaction of MoS_2 with human cells, the material of interest was more likely to move away from purely non-functionalised MoS_2 to more functionalised MoS_2 with biocompatible additives.

Bacteria-MoS_2 interactions

Interactions of 2D MoS_2 with bacteria have also been investigated. (*225, 226*) The reports principally focused on 2D MoS_2 used in antimicrobial applications, as films, hetero-multilayer 2D structures, and functionalised monolayer form as well as in its pristine, non-functionalised forms. In a similar development as the biocompatible application of MoS_2 towards human cells, antimicrobial applications had moved on from assessing the effect of pristine MoS_2 towards developing improved functionalised MoS_2 materials for better antimicrobial properties. From herein, the study of the bioreactivity of pristine 2D MoS_2 dispersions used in antimicrobial applications is discussed as they gave a good reference point for building up an understanding of the potential impact of 2D MoS_2 on the environment.

One of the earliest studies on the antibacterial activity of 2D MoS_2 was performed by Yang *et al*. (*210*) This work studied the antibacterial activity of monolayer MoS_2, as well as bulk and aggregated MoS_2, with

a thickness of couple of micrometres and tens of nanometres respectively. The main finding from this study was that chemically exfoliated MoS_2 showed time and concentration dependent toxicity towards *E. coli* with an exposure time of between 2 to 6 hours and a MoS_2 concentration up to 80 mg L^{-1}, and the mechanism of action involved a direct contact of the MoS_2 with the cells leading to cell membrane disruption and production of ROS through oxidative stress – similar to the proposed three step mechanism for 2D GOs. (*141*) However, other findings needed further study. The reported result on the higher antibacterial activity of monolayer chemically exfoliated MoS_2 compared to the aggregated MoS_2 and bulk MoS_2 were explained to be due to the higher 1T phase as well as higher stability in the dispersion allowing them to effectively transfer charges to induce oxidative stress. However, the observed result of aggregated MoS_2 (prepared from the monolayer MoS_2 and thus having similar 1T phase composition) having lower toxicity than the bulk MoS_2 (more layers and full 1H phase) were not fully explained fully. They had suspected that it would be due to difference in the physiochemical structure, but this meant that it would be a factor which would dominate over the higher amount of 1T phase present in the aggregated MoS_2. Moreover, the difference observed for the effect of incubation period were not fully explored. Even though the monolayer MoS_2 increased its antibacterial activity with increasing incubation time, aggregated and bulk MoS_2 showed opposite trends with increased incubation times. The authors explained this phenomenon to be due to the instability and therefore higher aggregation of the latter MoS_2 dispersions during the incubation period and a loss of effective surface area. However, they did not explain why the same aggregation states were not seen with monolayer MoS_2.

It was not clear from Yang *et al*. whether 1T phase was responsible for the higher toxicity observed or whether phase was predominant factor in antibacterial activity of MoS_2. Therefore, Kim *et al*. (*227, 228*) had performed an assessment of the antibacterial activity of common TMDs, including MoS_2 in its 1T phase and compared the results against antibacterial activity of MoS_2 with 1H phase. After 3 h exposure with *E.*

coli in Phosphate Buffer solution (PBS), 500 mg L^{-1} of 1T phase MoS_2 were able to completely reduce the cell viability measured using CFU plate method. In comparison, a similar concentration of 400 mg L^{-1} only reduced the cell viability to 50% compared to its control. Therefore, in a similar observation to the effect seen in *in vitro* studies towards human cells, 1T phase MoS_2 have higher activity towards bacteria due to higher charge transfer ability. However, it should be noted that the comparisons were not carried out in the same experiment, so an experiment that directly compares the two phases would further drive the understanding of phase on the activity of MoS_2 towards bacteria.

Kim *et al*. then further identified the possible mechanism of toxicity by the TMDs tested. (*227*) Since it was hypothesised that charge transfer played a significant role in the toxicity of TMDs, two oxidative stress measurements were made: 2,3-bis-(2-methoxy-4-nitro-5-sulfophenyl)-2H-tetrazolium-5-carboxanilide (XTT) assay, and Ellman's assay (which measures glutathione (GSH) level). The two tests determined whether the material tested causes oxidative stress *via* production ROS (ROS-dependent) or directly causes oxidative stress (ROS-independent), respectively. Both of the measurements matched with the cell viability measurements made by the CFU plate method, in terms of the trends shown between the different TMDs studied, and it was further confirmed by electrical resistive measurement performed on all three TMDs studied. The highest oxidative stress shown from all of the assays tested was WS_2 followed by MoS_2, and WSe_2 with electrical resistance increasing in the order $WS_2 > MoS_2 > WSe_2$. Therefore, it was concluded that MoS_2 caused toxicity *via* both ROS independent and ROS dependent oxidative stress. However, further study would be required to understand the difference in trend observed between the bacteria and human cells as the trend observed earlier towards human cells were $WSe_2 > MoS_2 >> WS_2$ with the reason being due to the presence of Selenium. (*221*)

Wu *et al*. (*229*) had studied the possible mechanism of interaction using computational simulation and exposure to a range of concentration of MoS_2 nanosheets (4.48 nm thickness, 100 nm lateral dimeter, AFM) towards *E. coli* and *Staphylococcus aureus* (*S. aureus*) in physiological saline for 2 hours. The computer simulations concluded that MoS_2 nanosheet attaches to the membrane from the edge and made a dent in the membrane Then the MoS_2 sheet extracted the phospholipid membrane via electrostatic interaction until the nanosheet was inserted in the membrane. The toxicity of MoS_2 towards the bacteria measured using a CFU plating method resulted in similar concentration and time dependent antibacterial properties, as previously observed with MoS_2 that showed higher toxicity towards the gram-positive *S. aureus* over the gram-negative *E. coli*. The exposure experiment also revealed that the membrane of bacteria was damaged after the exposure with MoS_2. Both SEM and TEM images of the bacteria with MoS_2 (60 mg L^{-1}) showed changes in the shape of the bacterial membrane and membrane disruption leading to cytoplasm leakage, respectively. Therefore, this paper showed that as well as oxidative stress pathways, there could be a physical insertion mechanism. This insertion or nano-knife mechanism was further observed by Kaur *et al*. (*230*) where they exposed human and bacteria cells to few layer MoS_2 dispersed in water. They showed, using SEM images, that MoS_2 nanosheets could damage the membrane by inserting into the membrane and causing leakage to the intracellular components. This effect was observed for both human cells (two cancerous cells: U937 and MCF7, and one non-cancerous cell – HaCaT cell), and bacteria (Salmonella typhimurium, wild and non-wild type) at 10-14 mg L^{-1} and 11.2-20 mg L^{-1} respectively.

The proposed mechanisms so for the interaction of bacteria and MoS_2 nanosheets are oxidative stress *via* ROS dependent and independent pathways, and mechanical insertion. The wrapping mechanism observed in GO have not been reported yet and it may be that this is due to the structural differences between MoS_2 and GO which could extend to TMDs and GFNs. It might also be that observation of different mechanism is due to the variation in the experimental set up. Even in the literature discussed above, the number of

layers of MoS_2 are different as well as the lateral diameter. Also, the consideration of phase is missing in some cases, and it is not clear whether this affects the physical mechanism. Moreover, types of bacteria may influence the preferred pathway of mechanism. Therefore, in order to understand the interaction of MoS_2 with environmental bacteria, we require 1.) a thorough characterisation of monolayer MoS_2, 2.) an assessment of effect of the toxicity assay used 3.) Images for mechanistic understanding of how this material interacts with the bacteria. This would fill a main gap in the knowledge with regards to *in-vitro* MoS_2 assessment towards bacteria in general where different mechanism is still being reported and allow direct comparison between GO and MoS_2.

4.2.7 Impacts of MoS_2 on bacteria in the environment

Considerations about the impact of novel materials on the environment is usually secondary to the development of their applications and a physical-chemical understanding of the materials properties. Nevertheless, with the increasing demand for safety and protection of the environment, consideration of the environmental impact of novel materials is required for their future development as their manufacture is up-scaled. Quite recently, Bae *et al*. (*220*) published the first and only study on the effects of MoS_2 on environmentally relevant bacteria. This work was of particular interest as soil bacteria were utilized as the target organism since they too identified that accidental or occasional release are likely to end up in waterbodies and soil. Their study found that exfoliated MoS_2 with a thickness of 3.1 ± 0.7 nm and lateral size of 0.88 ± 0.81 µm, caused concentration and time-dependent toxicity towards both *Bacillus cereus* (*B. cereus*) and *Pseudomonas aeruginosa* (*P. aeruginosa*) in the concentration range between 0 to 16 mg mL^{-1}. They have reported that median effective concentration (EC_{50}) of exfoliated MoS_2 to be 1.45 ± 0.19 mg mL^{-1} and 0.59 ± 0.16 mg L^{-1} against *B. cereus* and *P. aeruginosa* respectively at 8 h exposure time in peptone water. The study identified that the MoS_2 caused a decrease in cell viability through several

potential mechanisms using SEM images and pH measurements. The SEM images showed wrinkles on the membrane of the bacteria exposed to MoS_2 nanosheets, indicating that MoS_2 could block the cell wall either by mechanical or oxidative stress. The pH measurement revealed that with increasing concentration of MoS_2 from 1.6-16.0 mg mL^{-1}, the pH of the dispersion changed from 5.4 to 3.5. Because the bacteria studied here were mesophilic, the acidification process created unfavourable conditions for growth and caused decrease in cell viability. The author hypothesised that the acidification was caused by the dissolution of MoS_2 in water leading to production of protons and molybdenum oxide ions as well as further ability for the molybdenum oxide ions to release protons in aqueous media. This meant dissolution and oxidation of MoS_2 in the environment would lead to a persistent acidic nature and subsequent toxicity towards environmental bacteria. The dissolution and oxidation process of MoS_2 would be further discussed in the next section but this study by Bae *et al*. showed the potential nanotoxicity of MoS_2 nanosheets on environmentally relevant bacteria.

4.2.8 The ageing/oxidation process of MoS_2

Zhang *et al*. showed that freshly cleaved MoS_2 layers can age under aqueous conditions using AFM and XPS. (*36*) A process of oxidation occurred on the surface of MoS_2 sheets within 1 hour of contact with Milli-Q water (18.2 MΩcm, pH 5.65), and continued up to 12 hours. The *in-situ* AFM measurement revealed that after 1 hour of contact time, the surface morphology changed from smooth surface to protrusions appearing (20-50 nm in width, ~1.5 nm in height) on the surface with increasing number of protrusions and therefore roughness with time. It was also discovered that MoS_2 surface was etched under water and revealed the lower layers of MoS_2. However, the newly exposed surface did not show etching as the upper layer protected from further etching from occurring. XPS measurements were taken on a sample that was exposed to water for 4 days (the water droplet on the surface took 4 days to dry). After the

examination of deconvoluted peak of Mo 3d, S 2p, and O 1s spectra, it was concluded that the protrusions were various forms of hydrous MoO_3, and no other changes were observed for Sulphur species on the surface of the MoS_2. However, Atomic Absorption Spectrometry (AAS) as well as the pH diagram of molybdenum and sulphur in water at room temperature showed that as well as hydrous MoO_3 crystals on the surface of the MoS_2 layer, there were molybdate ions present during the oxidation process resulting in dissolution of the MoS_2. Moreover, the AAS measured dissolved Sulphur which was most likely to be SO_4^{2-}. Addition of Ba^{2+} resulted in precipitation of white precipitate indicating that the dissolved S species was SO_4^{2-}. Furthermore, there protons were produced, and this was confirmed by the decrease in measured pH to 4.08 after 24 hours. Note that the dissolution experiment was carried out using bulk MoS_2 powder, as the dissolution mechanism was thought to be the comparable. Therefore, this study showed that oxidation process of the MoS_2 could lead not only to dissolution of MoS_2 into SO_4^{2-} and Molybdate ions (VI) species but also formation of hydrous MoO_3 crystals on the surface of the MoS_2 sheets. The proposed oxidation process was summarised as follows in an equation.

$$MoS_2 + O_2 + H_2O \rightarrow MoO_3.H_2O + Mo(VI)_xO_y^{a-} + SO_4^{2-} + H^+ \qquad \text{Equation 4}$$

Domi *et al.* assessed the toxicology of commercially available MoS_2 from ACS material inc. against A549 lung epithelial cells and a unicellular fungus, *Saccharomyces cerevisiae* (*S. cerevisiae*), used in breweries. (*27*) This study was particularly interesting as the toxicity of aged MoS_2 sheets as well as the pristine material were evaluated. Theoretically different sized sheets were purchased from the same manufacturer, but materials characterisation revealed that both micro-MoS_2 and nano-MoS_2 did not display clear

differences. The TEM and AFM images showed significant aggregation of the MoS_2. Both types of MoS_2 were aged for 10 months and characterised using Raman and XPS. The Raman results showed that there were changes between the fresh and the aged MoS_2 sample for both types of MoS_2 with nano MoS_2 showing more changes. XPS provided further details on the observed ageing effect. The deconvolution of the Mo 3d peak indicated that there was a presence of MoO_3 at 233.1 ± 0.1 eV and a presence of MoS_2 at 229.0 ± 0.1 eV. In the S 2s peak, there were 2H-MoS_2 and S-O bonds (energy not mentioned). The author claimed that there was a progressive change in these values, which was pronounced more in nano-MoS_2 but unfortunately there were no quantitative measurement given. The same analysis was given for the S 2p peak where there were four deconvoluted peaks identified (S from MoS_2: 162.0 ± 0.1 eV, unsaturated S atom: 163.5 ± 0.1 eV, sulphates: 167.2 ± 0.1 eV, $[S_n(SO_3)_2]^{2-}$ or SO_2: 168.4 ± 0.1 eV), but no further comment was made. The author concluded that there were differences observed between the pristine and the aged sample with aged suspension being "enriched in a mixture of defected MoS_x species, and oxysulfides MoS_xO_y", but no further explanation on the mechanism or comparison with other ageing studies.

The toxicity test by Domi *et al*. (*27*) showing the effect of pristine and aged MoS_2 (10 months, 4 °C) dispersion against human cell (A549) and yeast cell (S cerevisiae) indicated that aged MoS_2 showed different toxicity compared to pristine MoS_2. The human cell interaction was studied by using Neutral Red assay - a measure of cell viability - and the 2,7-dichlorofluorescin diacetate (DCFH-DA) an (ROS-dependent assay) with exposure time of 24 h at °C. The yeast cell interaction was studied using CFU plate method and CM-H2DCFDA (General Oxidative Stress Indicator) at exposure time of 2 h and 24 h at 30 °C. The toxicity test against A549 cell revealed that all types of MoS_2 tested (micro and nano MoS_2, pristine and aged) did not affect the cell viability in the concentration range studied (up to 160 mg L^{-1}). However, the same concentration of 160 mg L^{-1} ROS production of A549 cells were greatly enhanced by the presence

of old MoS_2 for both types. This was attributed to the presence of MoO_3 in the aged sample which could induce ROS (although not confirmed). The toxicity test against the yeast cells revealed that 2 h exposure of all types of MoS_2 at concentration of 160 mg L^{-1} and 800 mg L^{-1} did not cause any significant changes to cell viability. However, when exposure was increased to 24 h, all types of MoS_2 caused decrease in cell viability with the same concentration range. The aged samples showed higher decrease in cell viability indicating that the aged samples were more toxic towards the cells. This also showed that the yeast cells were more sensitive to the presence of MoS_2. However, in contrast to the ROS results in human cell, the level of ROS detected were higher in the pristine samples for the yeast cell. This point was not discussed much further than the fact that there were differences in the mechanism of action between the pristine and the aged samples. In conclusion, this study showed the complexity involved in the study of effect of ageing MoS_2 and the importance in the thorough characterisation and explanation of the findings.

An alternative ageing effect was also reported by Ye *et al*. (*231*). They explored the ageing in air where the MoS_2 can adsorb hydrocarbons. They used computational modelling to study the difference in interaction of fresh and aged MoS_2. The fresh MoS_2 interacted more with phospholipid membranes and inserted itself inside the membrane more deeply than the aged MoS_2. This was attributed to the stronger Van der Waals interaction between the fresh MoS_2 and the membrane. Although this ageing process in the air and absorption of hydrocarbon on the surface is less widely reported on, this may also impact the toxicity of the MoS_2 in aged samples.

4.3 Aims

As the literature review above demonstrated, there are two main gaps in the study of interaction of bacteria and MoS_2. One main gap lies in the toxicity mechanism of exfoliated MoS_2, and the second one lies in the

effect of aged MoS_2 and its oxidation/dissolution products in an aqueous phase on the bacteria. The proposed toxicity mechanism of exfoliated MoS_2 are as follows: 1.) Insertion/Embedding of MoS_2 in the membrane to cause disruption in the membrane. It is unclear if complete membrane breakage or blocking of membrane function by disfigurement occurs; 2.) ROS-dependent oxidative stress. The exact mechanism of which ROS species is unclear; 3.) ROS- independent oxidative stress. The mechanism of this pathway is still unclear. The literature on this is still scarce and therefore no definitive conclusion can be drawn on whether which mechanism dominates over the other.

The effect of aged MoS_2 on bacteria is even scarcer in literature since the dissolution/oxidation study of MoS_2 nanosheets is still yet to be eluded especially in other aqueous media than water. The ageing mechanism has been hypothesised as follows: 1.) Oxidation of MoS_2 nanosheets occurs at the defective sites; 2.) The MoO_3 crystals form on the surface of MoS_2; 3.) Part of MoS_2 forms ions in the solution, with a range of products such as molybdate ions and sulphate ions and protons, as well other sulphides. It is still unclear which part of the aged dispersions causes the changes in the toxicity, such as the increased acidity or the presence of molybdate ions and sulphides and sulphates, but it has been observed that aged dispersion can cause change in toxicity.

Therefore, in order to fill the knowledge gap in the literature on the interaction of bacteria with MoS_2 as well as assessing the toxicity of MoS_2 towards environmentally relevant bacteria, exfoliated as-received MoS_2 dispersion from ACS material Inc. was characterised using XPS, AFM, DLS, and Zeta potential measurements, and exposed to soil bacteria using an ISO protocol. Then, changes in the toxicity of aged MoS_2 were assessed by ageing the dispersion in the dark at room temperature to study the potential impact which the aged sample could have on the soil bacteria. Comparison of as-received and aged samples was performed to assess whether persistence of these materials could be a problem in the environment.

4.4 Methods and Materials – MoS_2

This section was reproduced from mixture of methods and materials already described in the work with GO but mentioned explicitly for completeness of the MoS_2 work.

4.4.1 Materials

Chemicals and Hardware

MoS_2 dispersion in water was obtained from ACS materials, US. For the toxicity test of ISO 10712, all chemicals used, including LB agar and LB broth, were purchased from Sigma Aldrich at biological grade suitable for microbial work. A standard Milli Q water was used for any dilution or media preparation. Pipettes, plates, and other materials used in toxicity assay were purchased from VWR, UK.

Bacteria

Gram-positive bacteria, *Arthrobacter globiformis* (*A. globiformis*), and gram-negative bacteria, *Pseudomonas putida* (*P. putida*) were obtained from DMSZ, Germany in a freeze-dried form and rehydrated for preparation of the assays. Freeze-dried bacteria were rehydrated in Luria-Bertani (LB) broth and half of the culture was plated onto LB Agar plate and incubated at 25° for 48 hours, while the other half remained in the LB broth and mixed with glycerine for long term storage at -80°C. The plated cultures were re-plated again and incubated for another 48 hours and then stored at 4°C until used for the assays. The plated culture was re-plated every 4-6 weeks to obtain fresh cultures. All toxicity tests for MoS_2 were run on the same batch of bacteria.

4.4.2 Methods

ISO 10712

Preparation of Media

Media used for ISO 10712 was prepared using an existing method routinely used at Centre for Ecology and Hydrology (CEH, Wallingford, Oxfordshire). Pre-culture, and Test media were prepared. The composition of both media are shown in Table 4.4.2.1 and the media were made up with different amounts of solution I-IV. Table 4.4.2.2 shows the composition of each solutions I-IV. All solutions were sterilised using an autoclave (Prestige Medical, Media Autoclave, UK), except for solution III in which a sterile filtration was used as the constituents would decompose high temperature. All solutions and media were stored in a fridge at 4°C until use and a new batch was made up every 6 months.

	Constituent	**Amount**
Solution I (500 mL)	$NaNO_3$	10.0 g
	$K_2HPO_4.3H_2O$	3.14 g
	KH_2PO_4	1.20 g
	Yeast	1.0 g
	Milli Q water	500 mL
Solution II (500 mL)	$NaNO_3$	10.0 g
	$K_2HPO_4.3H_2O$	3.14 g
	KH_2PO_4	1.20 g
	Milli Q water	500 mL
Solution III (500 mL)	D-glucose	36.6 g
	Milli Q water	500 mL
Solution IV (1000 mL)	$MgSO_4.7H_2O$	4.0 g
	Iron (III) citrate	0.01 g
	Milli Q water	1000 mL

Table 4.4.2.1 Composition of Solution I-IV

	Solution	Volume
Pre-culture media (500 mL)	Solution I	13.75 mL
	Solution III	13.75 mL
	Solution IV	27.5 mL
	Milli Q water	445 mL
Test nutrient media (500 mL)	Solution II	15.5 mL
	Solution III	15.5 mL
	Solution IV	31.0 mL
	Milli Q water	438 mL

Table 4.4.2.2 Composition of the pre-culture media and test media.

Toxicity assays

Bacteria cultures from plates stored in the fridge were suspended in pre-culture media and incubated for 16 hours at 25°C. The bacteria suspensions were then adjusted in concentration so that Optical Density (OD) was 0.5 in the test media as per the protocol. This was to allow a measurement of OD change from the growth of bacteria. The MoS_2 dispersion for testing was then diluted to the desired concentration in the test media. MoS_2 dispersion was sonicated for 30 seconds prior to the dilution. The bacteria suspensions were then added to the MoS_2 suspension which was T0h. There were 5 replicates of each concentration, including the negative control without the MoS_2, as well as a blank sample for sterility or cross-contamination checking. All samples were incubated for 24 hours at 25°C in the dark at a shaking speed of 150 rpm (Incu-Shake Maxi Refrigerated Incubating shaker, SciQuip, UK) and at a 24-hour time point, OD and CFU readings were taken.

Optical Density reading

A volume of 200 µL was pipetted out from each replicate of the mixture and onto 96 well plate for the OD readings using a plate reader (Spectramax M2 Microplate reader, Molecular Devices, US). This was performed at T0h and T24h. The difference between OD of T24h and T0h was taken to represent the growth and change in each mixture. This meant that any change was measured by the OD and the measurements were independent of each other. OD measurements of MoS_2 dispersions only were also taken to ensure that the changes were due to the presence of bacteria alone.

Colony Forming Unit reading

After 24 hours incubation, the mixtures were serially diluted to the specified concentration. For *A. globiformis*, the mixture was diluted 3-fold, and for *P. putida*, the mixture was diluted 5 folds. Then 50 µL from the diluted samples were taken out and plated out on to LB agar. All plates were incubated for 48 hours or longer until sufficient colonies formed for counting. The CFU readings were converted back to the original dilution for results.

Optical imaging

Optical images of bacteria with MoS_2 dispersion were taken using an inverted microscope (Nikon Eclipse TS100, Nikon, Japan) with objective lens at x20 magnification piece. This was used to give a representative image of the interaction of MoS_2 dispersion with the bacteria. Images were taken directly from the well after the 24 hours exposure time period.

Statistical Test

For all toxicity test result with OD and CFU readings, One-way ANOVA statistical test was carried out. A Dunnett test, where the means of control were compared to all other variants, was used to determine whether the presence of MoS_2 caused a significant change compared to the control sample. A P-value of 0.05 and 0.01 was used to denote significance, which is commonly used in biological tests (p-value at 5% and 1%). Table 4.4.2.3 shows the denotation used in the result sections with the statistical meaning.

Statistical Denotation	Statistical Meaning
Ns	$p>0.05$ (not significant)
*	$p<0.05$ (statistically significant)
**	$p<0.01$ (statistically significant)

Table 4.4.2.3 Statistical denotation used in the toxicity test results in OD and CFU.

Ageing materials

MoS_2 dispersions in water were aged under ambient conditions at room temperature and pressure (RTP) and in the fridge in the dark wrapped in foil. Samples were taken and used for the toxicity runs and XPS and AFM characterisation at time points of As-Received (AR), 1 months, 2 months, 3 months, 4 months, and 3 years (Aged from May 2018 to June 2021).

Material characterisation

XPS samples were prepared by drop-cast method onto silica wafer. The samples were dried and measured using a K-alpha+ XPS spectrometer equipped with a MXR3 Al Kα monochromated X-ray source (hν = 1486.6 eV). The X-ray gun power was set to 72 W (6 mA and 12 kV) and charge compensation was

achieved using the FG03 flood gun using a combination of low-energy electrons and the ion flood source. Mapping was used to avoid beam damage and the beam spot size was adjusted to 400 µm. All spectra were analysed using Avantage Software. The Mo peak was deconvoluted and analysed for quantification of ageing, as well as comparison with literature. (*27, 36*)

AFM

AFM samples were prepared by diluting the MoS_2 dispersion to 10 mg L^{-1} then drop-casting on to freshly cleaved Mica sheets (Agar, UK). The samples were measured using Asylum MFP 3D AFM in AC air topography mode. All images were processed using Gwyddion (Gwyddion, Czech Republic) and Image J software. Size distribution for lateral diameter was calculated using the same method employed for GOs size distribution. Gwyddion was used to process the images then thresholding was used to create a mask. The masked images were exported to Image J and then using the particle analyser built-in, and the Feret diameter of the particles were calculated. Briefly, the Feret diameter is the distance measured between two parallel planes in which the long and the short distance is averaged to represent the lateral size of an irregular object. It is commonly used in microscopy particle analysis. (*25*)

DLS and Zeta potential

Samples for Dynamic Light Scattering (DLS) were prepared by diluting the dispersion to 50 mg L^{-1}. Measurements were made using a Zetasizer (to take both DLS measurements of the hydrodynamic diameter and zeta potential measurements simultaneously). Because DLS and zeta potential provides a measurement of behaviour of nanomaterials in different media, these techniques were used to characterise the zeta potential and hydrodynamic diameter of the nanomaterial in test media as well. (*28, 29*)

ICP

Inductively Coupled Plasma Spectroscopy was used to measure the amount of Molybdenum that had leached out of as-received exfoliated MoS_2 dispersion in a dialysis membrane (1,00,000 Da, MWCo). The content of Mo in the leachate was analysed using inductively coupled plasma-atomic emission spectroscopy (ICP-AES; ThermoScientific iCAP 6300 Duo). Samples taken were at as-received, 3 months old, and 3 years old with each time point having 5 replicates.

4.5 Results

4.5.1 Material characterisation of AR exfoliated MoS_2

Manufacturer Specification

MoS_2 dispersions in water, obtained from ACS Material (Monolayer Molybdenum Disulfide, Water Dispersion, 1mg mL^{-1}, SKU GLMSW0A2), were characterised using AFM, XPS, and a Zetasizer. The manufacturers' information are listed below in Table 4.5.1.1.

MoS_2 dispersion ACS Materials	**Manufacturer specification**
Synthesis	Chemical exfoliation
Appearance	Black dispersion
Lateral dimension	0.2-5.0 μm
Thickness	~1 nm
Monolayer ratio	~90 %
Stabiliser	Trace LiOH
2H/1T phase ratio	60/40

Table 4.5.1.1 Material properties specified by the manufacturer

The table shows the summary of characterisation of MoS_2 dispersion in water obtained from ACS material. The MoS_2 dispersion was synthesised using a chemical exfoliation method using Lithium intercalation. The lateral diameter of the flakes ranged from 0.2-5.0 μm and the thickness of the flakes were around 1 nm, determined by AFM. The monolayer ratio of the entire dispersion was around 90% meaning most of the MoS_2 flakes in the water were monolayered. The manufacturer specified that there was mixture of phases of 2H (semiconducting/natural) and 1T (metallic/metastable) phases present in the dispersion. This was expected as chemical exfoliation usually resulted in a mixture of phases being produced.

Materials Characterisation

MoS_2 in water dispersion

Optical images of the as-received exfoliated MoS_2 dispersion in water as well as the DLS and zeta potential measurements are shown below in figure 4.5.1.1 and table 4.5.1.2.

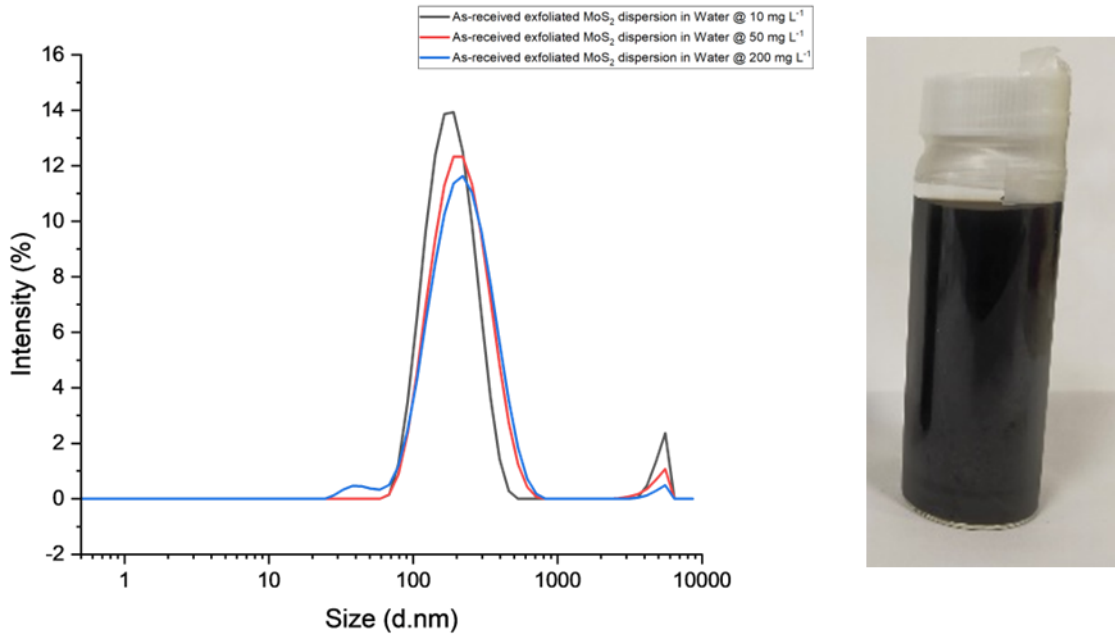


Figure 4.5.1.1 DLS hydrodynamic diameter by intensity of MoS_2 dispersion in water at three different concentrations (10, 50 and 200 mgL^{-1}), together with a photo of as-received dispersion of MoS_2 in DI water. Each plot was an average of three repeated measurements.

The plot shows the DLS measurement of the MoS_2 dispersion in water by intensity. Three concentrations of 10, 50, 200 mg L^{-1} of MoS_2 was measured to study the behaviour of the particle in the range of concentrations used for the toxicity assay. The plot shows a large peak at around 190 nm for all three concentrations of the MoS_2 dispersion and also a smaller peak at 5560 nm. The larger peak at 190 nm is from the monolayer MoS_2 which dominates the proportion of the particles dispersed. The smaller peak at 5560 nm is likely to be from the small proportion of poorly exfoliated MoS_2 or restacked MoS_2 sheets. There is slightly increasing trend of the large peak at 190 nm because of the increasing concentration effect of the MoS_2 in DI water. DLS measures changes in scattering intensity of a particle moving in Brownian motion in a solution. Therefore, an increase in concentration can limit the Brownian motion and affect the measurement. Moreover, a unique effect seen for 2DNMs can also be seen where a higher concentration

can lead to a weaker separation of sheets. The shift to the smaller diameter with increasing concentration reflects the slight stacking that may be occurring in the water at higher concentration with an increase in the intensity.

Concentration	Z-average (nm)	S.D.	PDI	S.D.	Zeta potential (mV)	S.D.
10 mg L^{-1}	179.93	±1.76	0.33	±0.04	-45.03	±0.29
50 mg L^{-1}	187.47	±1.31	0.28	±0.01	-42.17	±1.23
200 mg L^{-1}	185.53	±2.45	0.25	±0.00	-41.13	±0.42

Table 4.5.1.2 Z-average, Polydispersity Index (PDI), and Zeta-potential measurement of MoS_2 dispersion in water at three different concentrations. The values for all measurements were average of three measurements with the information taken from intensity reading.

As well as the DLS size intensity plot shown in figure 4.5.1.1, table 4.5.1.2 shows the average hydrodynamic diameter given by Z-average, Polydispersity Index (PDI), and Zeta potential of the same MoS_2 dispersion in water. The hydrodynamic diameter is usually used to determine the hydrodynamic diameter of a spherical particle accurately. However, for a non-spherical particle like MoS_2, the hydrodynamic diameter given by Z-average value corresponds to a spherical particle with the same scattering intensity pattern. This means that the hydrodynamic diameter given here is of a spherical particle with the same scattering pattern to the MoS_2 and is not necessarily a direct measurement of its size. This value is also affected by the salt present, pH, and other factors that affect the colloidal state and the surrounding electrical double layer of the particle. This is one of the main reasons that diameter measurements for nanoparticles from direct imaging such as TEM or AFM differs from the DLS size measurement.

The spherical particle assumption is also applied to the size intensity distribution as well and both results show the size of particle in the dispersion. However, the correlative fitting of the change of scattering

intensity over time is longer for the size intensity measurement. Therefore, for a polydisperse and unstable colloidal dispersion, the size intensity distribution plot can provide more accurate representative size of the particle. However, for the case of MoS_2 dispersion in water, the Z-average value and the main peak in the size intensity plot matches very closely at around 180 – 190 nm. This means that the MoS_2 dispersion measured here was monodisperse. This is reflected in the value of PDI where the PDI is low with very little deviation.

The zeta potential given here indicated that the MoS_2 dispersion is very stable in water with a negative surface charge. The structure of exfoliated MoS_2 has sulphur atoms on the basal planes. This is likely to give the negative zeta potential measurement with colloidal stability in water. As mentioned in the technique section, any zeta potential value grater in magnitude than ±30 mV indicates a very stable colloidal dispersion. Therefore, the MoS_2 dispersion obtained from ACS material was very stable in water.

AFM

Figure 4.5.1.2. shows a representative example of AFM images of as-received MoS_2 monolayers from ACS material on freshly cleaved mica with the height profile and figure 4.5.1.3 shows the Feret diameter distribution taken from multiple AFM images to show the average lateral size of MoS_2.

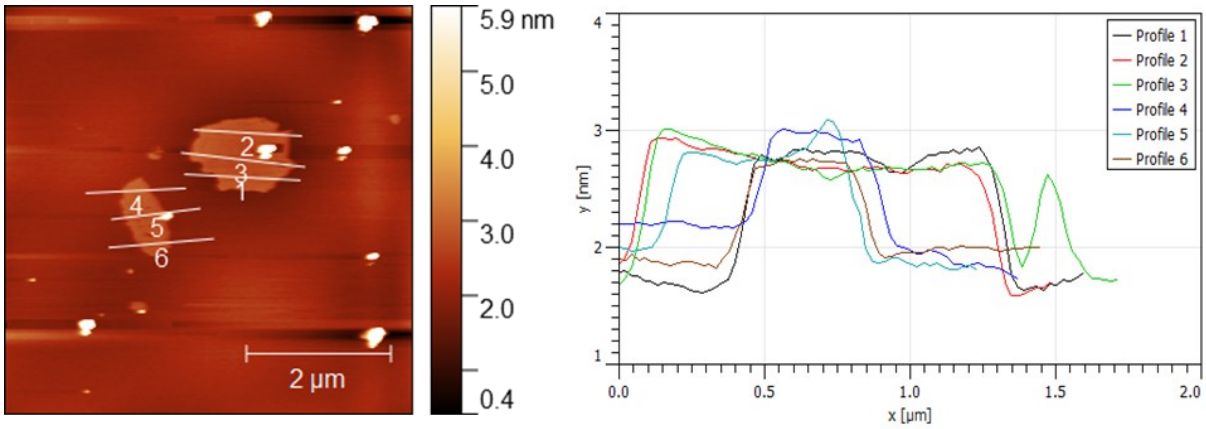


Figure 4.5.1.2 AFM image of as-received MoS_2 from ACS material drop-casted on freshly cleaved mica with the height profile taken from the MoS_2 flakes to show the monolayer nature of the material for 6 different profiles across the MoS_2.

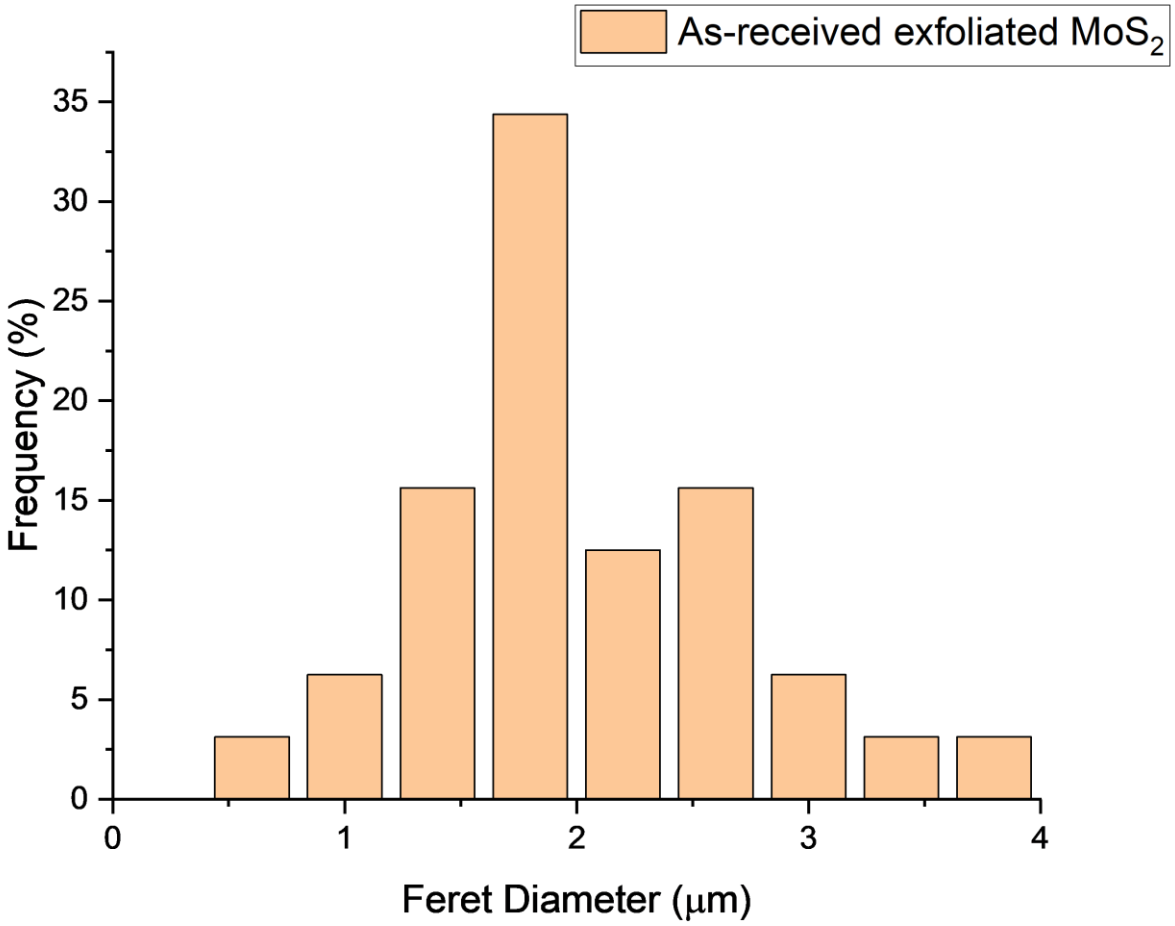


Figure 4.5.1.3 Lateral size distribution of monolayer MoS_2 flakes represented by Feret diameter measurements taken from 32 AFM images. (Mean = 2.00, S.D. = 0.72, N = 32)

The representative AFM image and the height profile (figure 4.5.1.2) shows the monolayer nature of the MoS_2 dispersion in water obtained from ACS material when deposited on freshly cleaved mica. The height profile shows that the MoS_2 are monolayers with thickness of 1 nm. This agreed well with the DLS results showing good exfoliation of the MoS_2 dispersion in water as all the images taken under AFM were monolayers of the same quality as the represented image. The Feret diameter distribution (figure 4.5.1.3) showed that the lateral size of monolayer MoS_2 flakes ranged from 0.2 to 3.8 μm with mean size of 2.0 μm.

XPS

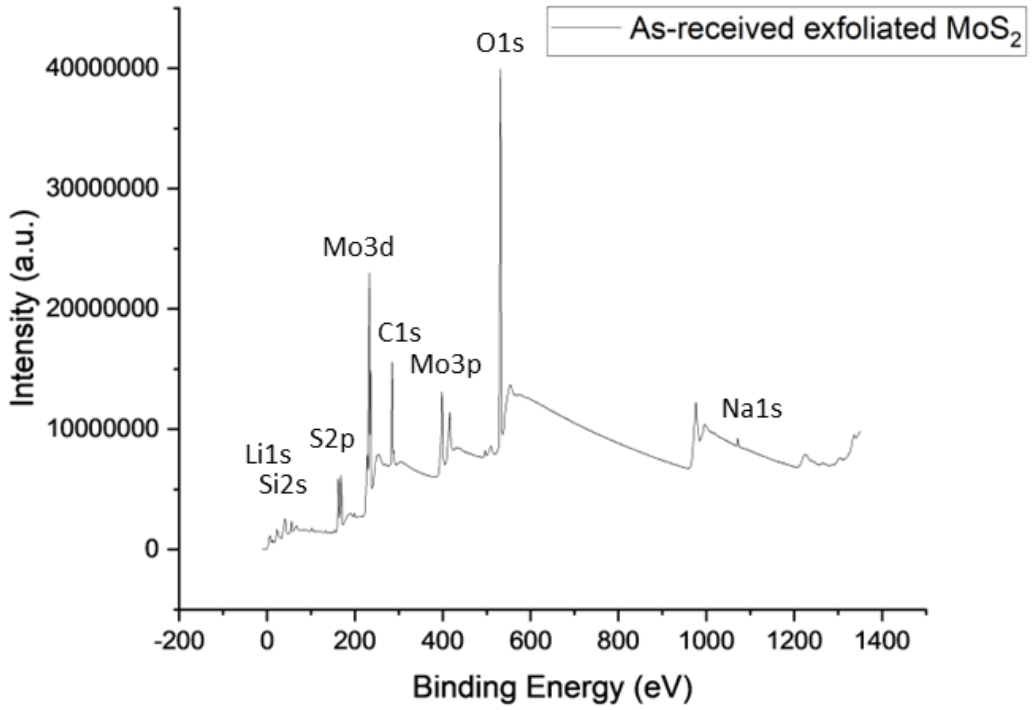


Figure 4.5.1.4 XPS survey spectra of as-received exfoliated MoS_2 drop-cast on silica wafer with the main transition peaks labelled

The survey spectra from the XPS of the as-received exfoliated MoS_2 on silica wafer (figure 4.5.1.4) showed that the main elements present in the sample prepared was Mo, S, O, C, Li, Na, Si. The Mo and S were mainly attributed to the MoS_2 dispersed in water. Li and O was from the LiOH stabiliser in the water dispersion as well as O from water. Na was attributed to a synthesis impurity and the C was from contamination from atmosphere or the carbon tape used in mounting the sample. (*232, 233*)

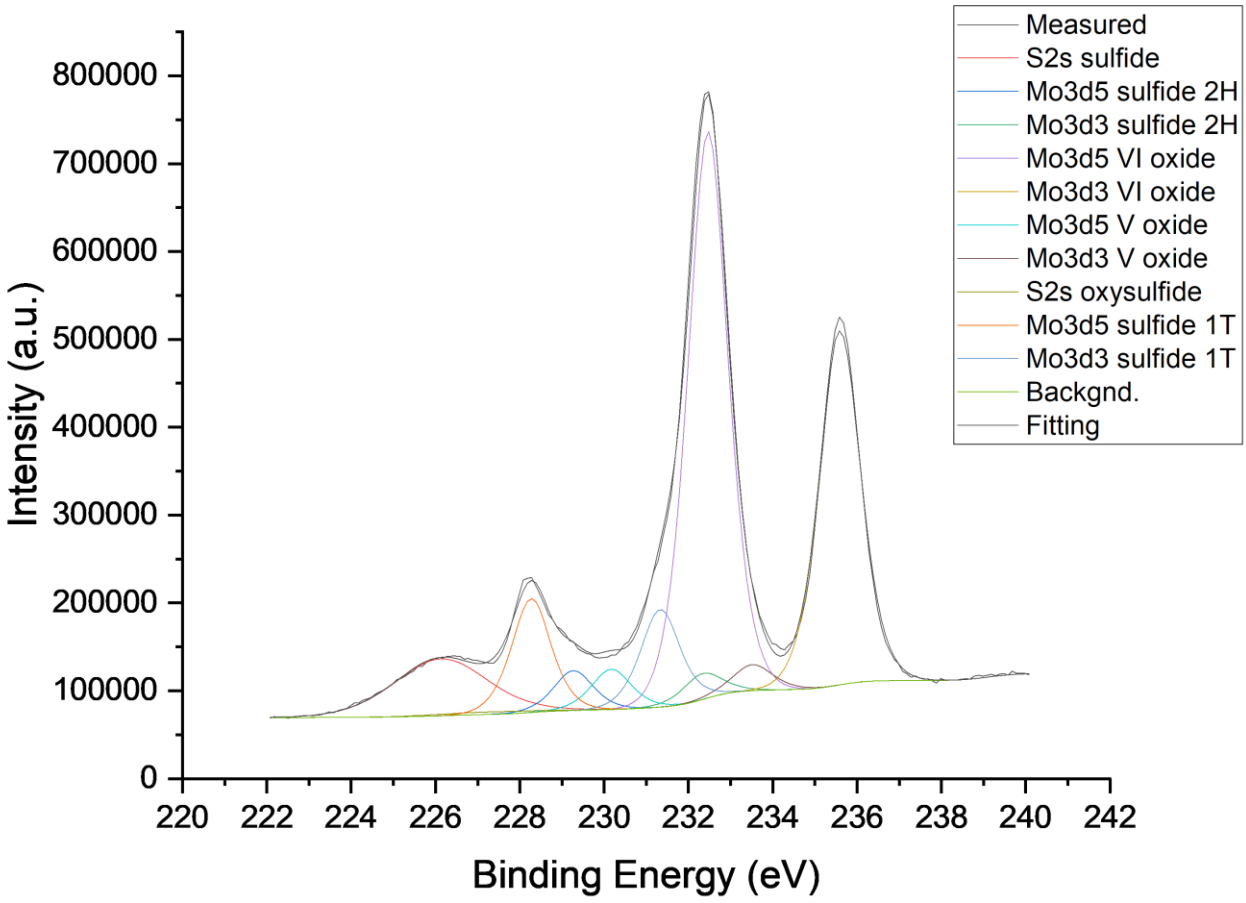


Figure 4.5.1.5 High resolution XPS spectra of the Mo3d peak of as-received exfoliated MoS_2 sample on silica wafer. The spectra have been deconvoluted and fitted to show the different chemical environment of Mo3d, as well as S2s where the B.E. overlap..

High-resolution spectra of both the Mo3d region (figure 4.5.1.5) was taken to analyse the different chemical environment of Mo in the MoS_2. This is common for analysis of MoS_2 and various fitting methods from number of literatures was used to deconvolute the measured spectra. (*27, 36, 234, 235*) As shown in the high-resolution spectra, the number of different chemical environment present is numerous. No one particular fitting from the literature provided the best fit, since there was still no appropriate fitting

described for MoS_2 dispersion in water. The current fittings were based on characterisation of MoS_2 powder, bulk, CVD-grown MoS_2 and dispersed MoS_2 in water. (*27, 36, 234, 235*) The combination of all provided the best fitting for both high resolution which indicated that the MoS_2 dispersion in water have many different chemical environments for Mo. These are affected by the base or the edge of nanosheets as well as the phases present and the different oxidation degree. The change in high-resolution spectra and the respective different chemical environment became essential in the ageing oxidation study which will be discussed in the later section.

The high-resolution Mo3d spectra (figure 4.5.1.5) showed 4 distinctive chemical environments for Mo3d which has two spin orbital splitting (3d5/2 and 3d3/2 labelled as 3d5 and 3d3 on the figure). The 4 distinctive chemical environments of Mo are a.) Mo (IV) associated with 2H phase MoS_2, b.) Mo (IV) associated with 1T phase MoS_2, c.) Mo (V) associated with incompletely oxidised Molybdenum oxide d.) Mo (VI) associated with Molybdenum oxide mainly of MoO_3. The B.E. peak position is shown in table 4.5.1.3 below. Note that the Mo3d region overlaps with S2s transition as well which was included in the deconvolution of the spectra. There were two identifiable chemical environments for the S which were associated with MoS_2 and oxysulfide. As the high-resolution spectra of S2p showed, it was expected that there was sulfate peak as well, but this overlaps significantly with the Mo (IV) peak.

Name	**Peak BE (eV)**
S2s sulfide	226.13
Mo3d5 sulfide 2H	229.27
Mo3d3 sulfide 2H	232.33
Mo3d5 VI oxide	232.46
Mo3d3 VI oxide	235.6
Mo3d5 V oxide	230.17
Mo3d3 V oxide	233.52
S2s oxysulfide	227.28
Mo3d5 sulfide 1T	228.27
Mo3d3 sulfide 1T	231.33

Table 4.5.1.3 The Peak B.E. of different deconvoluted chemical environments of Mo in Mo3d transition together with the S2s peak positions showing S environments.

The high-resolution spectra of Mo3d showed that there were multiple Mo environment that resulted from as-received exfoliated MoS_2 of different phase and oxidation of MoS_2 leading to production of sulfate, molybdate, and other intermediatory products such as oxysulfide. The ratio of 2H/1T ratio was 0.30 (30% 2H/1T composition) with higher 1T phase then 2H phase which was significantly different than the manufacturer specification of 60% 2H/1T. However, this value was common amongst the literature discussed meaning that the quality of MoS_2 was still good and comparable to other literature. (*236*) It should be noted that value of 2H/1T phase was not as commonly reported as other physiochemical characteristics such as thickness or size but it was reported that this can affect the biological interaction and therefore should be reported to build further understanding. (*227*)

MoS_2 dispersion in media condition of ISO10712

The Zeta potential and DLS size measurements of the same MoS_2 in the ISO 10712 test media (pH 7.08 ± 0.03) is shown below.

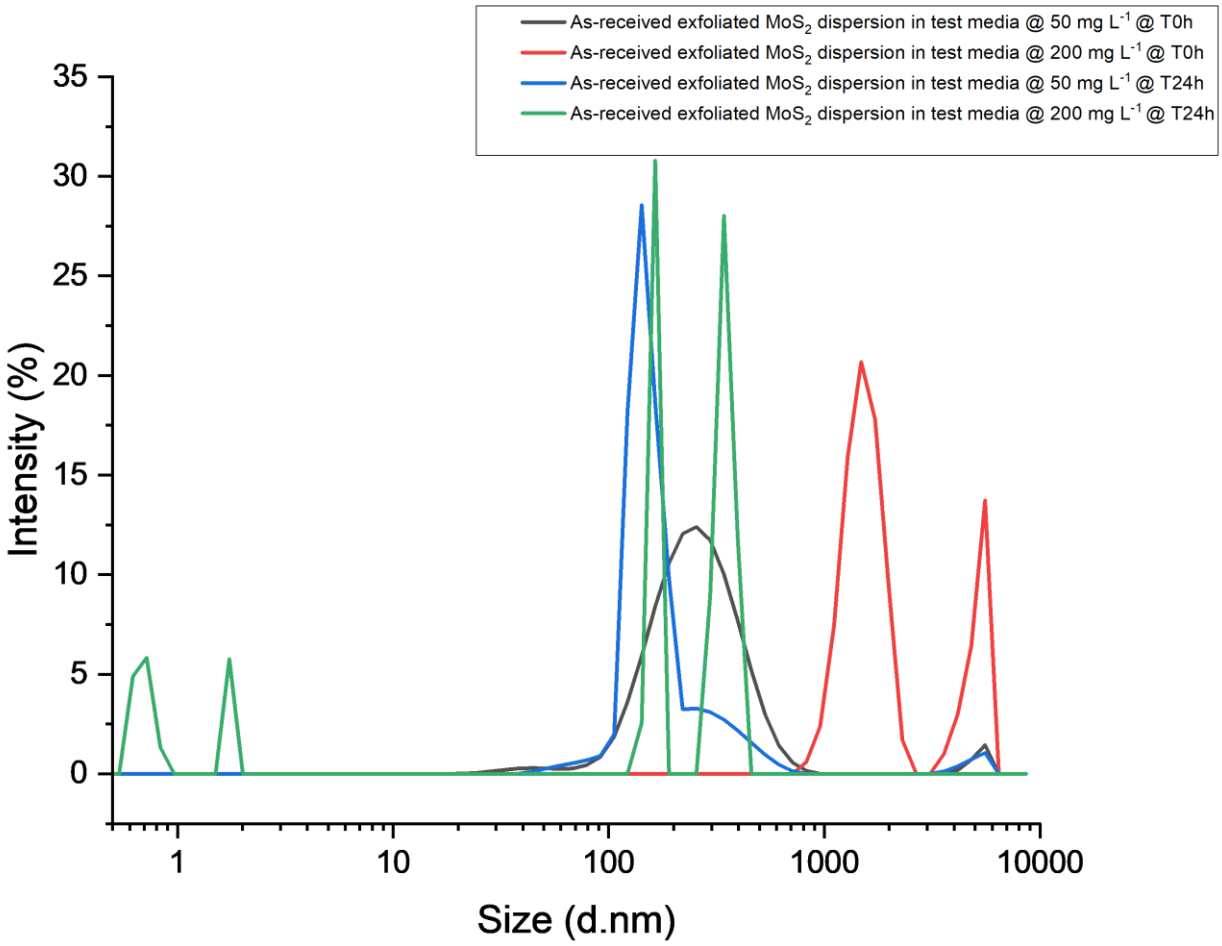


Figure 4.5.1.6 DLS hydrodynamic diameter by intensity of MoS_2 dispersion in ISO 10712 test media at two different concentrations (50 and 200 mgL^{-1}). Each plot was an average of three repeated measurements.

	Concentration (mg L^{-1})	Z-average (nm)	SD	PDI	SD	Zeta potential (mV)	SD
As-received exfoliated MoS_2 in ISO 10712 test media @ T0h	50	233.10	±4.00	0.33	±0.05	-26.97	±1.28
	200	3818.67	±412.28	0.48	±0.03	-20.80	±0.49
As-received exfoliated MoS_2 in ISO 10712 test media @ T24h	50	802.50	±513.61	0.72	±0.22	-28.17	±1.56
	200	8397.67	±271.17	0.62	±0.03	-24.77	±0.90

Table 4.5.1.4 Z-average, Polydispersity Index (PDI), and Zeta-potential measurement of MoS_2 dispersion in ISO 10712 test media (pH 7.01) at two different concentrations between time points of 0 hour and 24 hours. The samples were incubated at 25 °C under shaking in the dark to replicate exposure conditions in the toxicity tests. The values for all measurements are an average of three measurements.

The DLS size plot by intensity (figure 4.5.1.7) of MoS_2 in ISO 10712 test media of two concentration at 50 mg L^{-1} and 200 mg L^{-1} at time point of T0h and T24h under toxicity test condition showed the dispersion behaviour of $MoS2_2$ under abiotic conditions of the toxicity test. The two concentrations were 50 and 200 mg L^{-1} so that they replicated the range of concentrations in the toxicity assay and also so that the T0h samples can be directly compared with the DLS result from MoS_2 in water dispersion. As the DLS intensity size plot shows in figure 4.5.1.7, the MoS_2 dispersion in ISO 10712 test media at T0h with concentration of 50 mg L^{-1} (black line) shows a large peak at 255 nm with a small shoulder peak at 5560 nm. The T0h sample of the 200 mg L^{-1} (red line) shows a large peak at 1480 nm and a small shoulder peak at 5560 nm. The 24h samples of 50 mg L^{-1} (blue line) shows a large peak at 142 nm with a shoulder peak at 5560 nm, and the 24h sample of 200 mg L^{-1} (green line) shows two large peaks at 190 nm and 342 nm with two smaller peaks at 0.719 and 1.74 nm.

The intensity size plot of the T0h samples showed that in ISO 10712 test media, the MoS_2 dispersion agglomerate slightly with increasing concentration from 50 to 200 mg L^{-1}. There was a shift in the main large peak to show that the MoS_2 agglomerated. Comparison between the T0h and T24h samples for both concentrations showed that the MoS_2 became increasingly unstable in the media especially at the 200 mg L^{-1} with increased polydispersity in the sample. In fact, this change was more clearly shown in the table 4.5.1.5. The table shows hydrodynamic diameter (given by Z-average), PDI (polydispersity of the sample), and the zeta potential (surface charge of the MoS_2). The Z-average value and PDI value showed an increase in size from 50 mg L^{-1} to 200 mg L^{-1} as well as T0h to T24h sample. This indicated that the MoS_2 agglomerated to form different sized MoS_2 clusters to increase the PDI. The zeta potential value also reflects the instability of the MoS_2 in the media as all of the values were between -15 mV and -30 mV meaning that the MoS_2 is not meta-stable and can agglomerate. The DLS and zeta potential results showed that the MoS_2 dispersion agglomerated increasingly with higher concentrations and under abiotic conditions of toxicity test.

4.5.2 As-received exfoliated MoS_2 toxicity test results against soil bacteria

The Optical Density (OD) data representing the growth of *A. globiformis* and *P. putida* bacteria exposed to the MoS_2 dispersion in ISO is shown in figure 4.5.2.1.

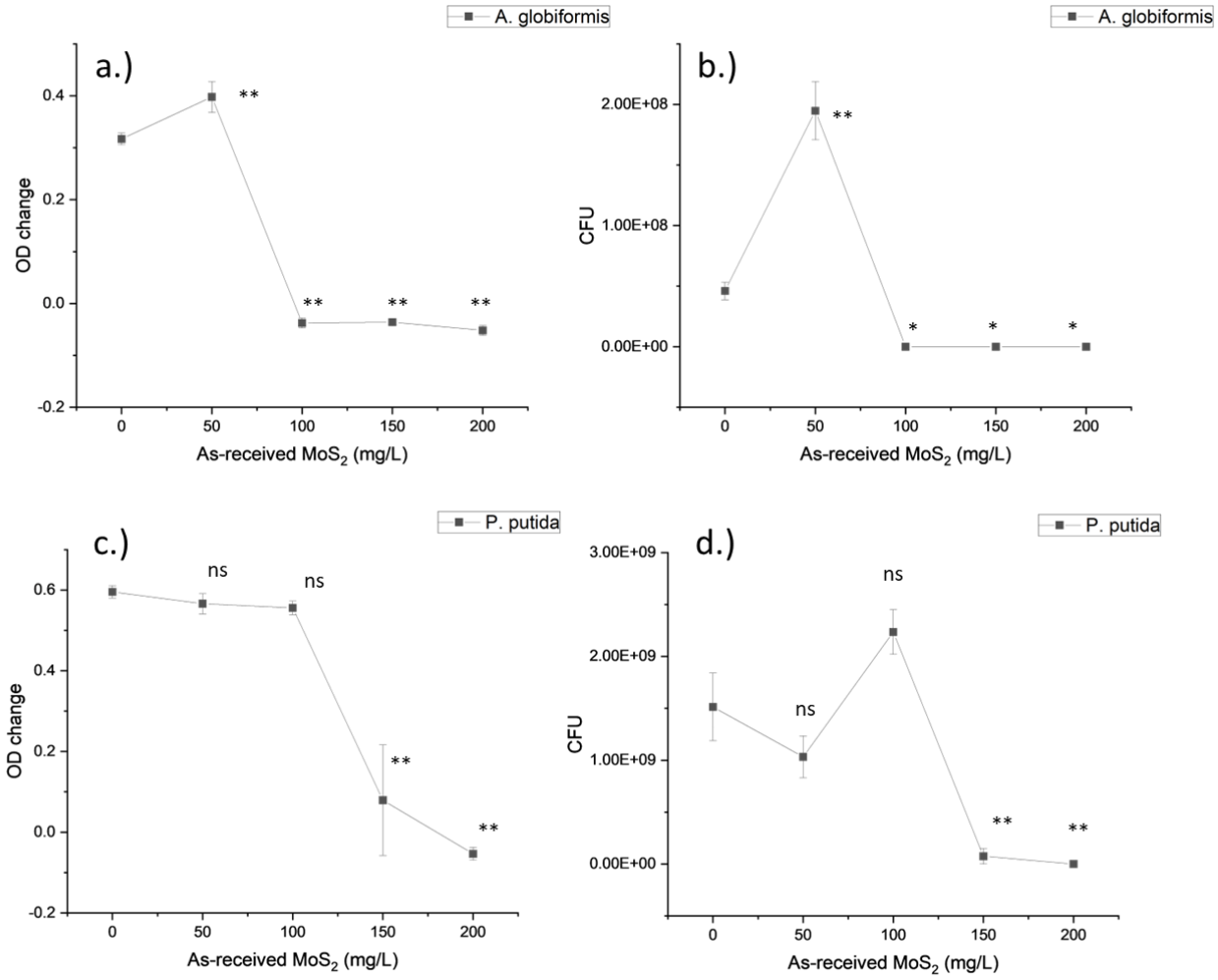


Figure 4.5.2.1 Toxicity test result in ISO 10712 of a.) OD change of *A. globiformis* with increasing dose of as-received exfoliated MoS_2 dispersion in the concentration range between 0-200 mg L^{-1} b.) CFU of *A. globiformis* with increasing dose of as-received exfoliated MoS_2 dispersion in the concentration range between 0-200 mg L^{-1} c.) OD change of *P. putida* with as-received exfoliated MoS_2 dispersion of concentration range between 0-200 mg L^{-1} d.) CFU of *P. putida* with increasing dose of as-received exfoliated MoS_2 dispersion in the concentration range between 0-200 mg L^{-1}. The OD change was calculated from OD reading at T0h and T24h sample with the same sample left for 24 hour exposure. Each data point is an average of 5 independent samples. CFU was calculated from the plate reading method and each data point are average of 5 independent samples. The error bars represent the standard error. The annotations indicate the following for p-value of comparison of means: ns = $p>0.05$, * = $p<0.05$, ** = $p<0.01$ as shown in table 4.4.2.3.

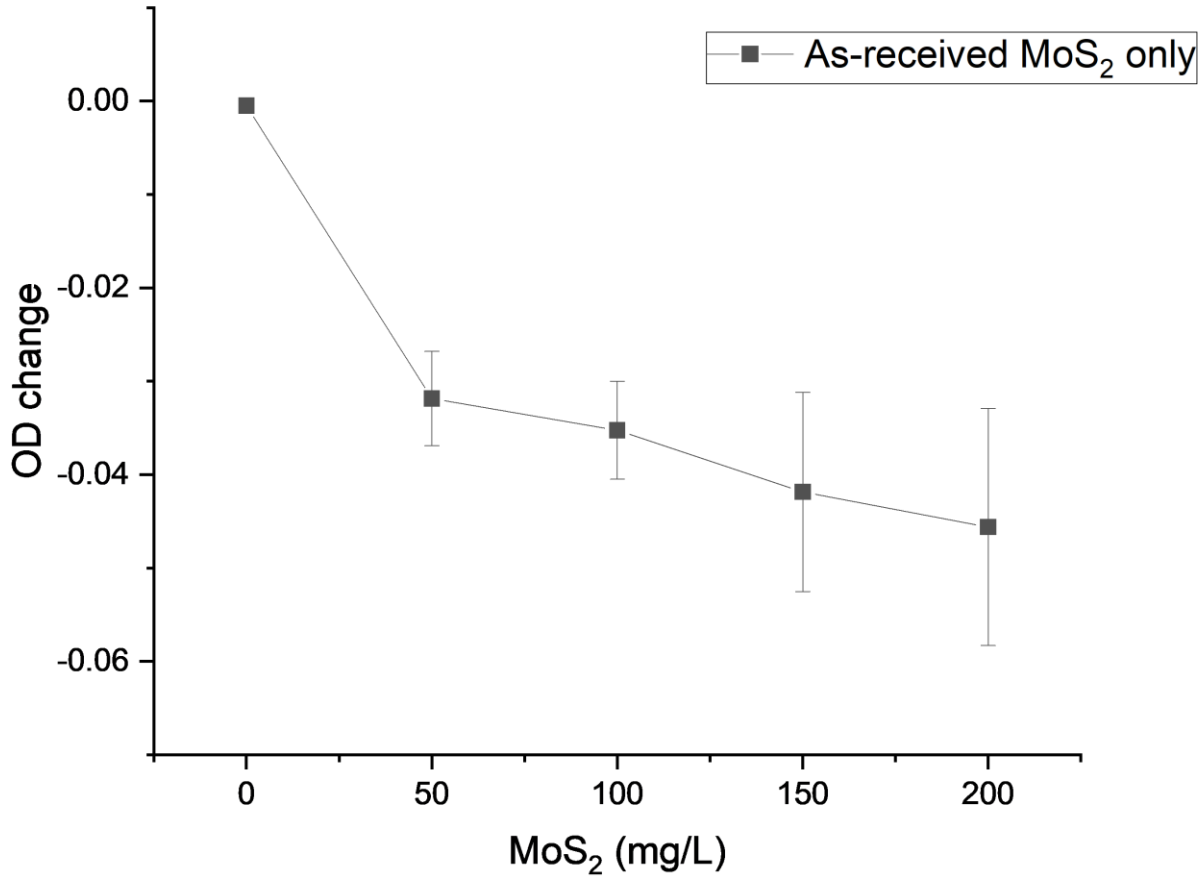


Figure 4.5.2.2 OD change of as-received exfoliated MoS_2 dispersion of concentration range between 0-200 mg L^{-1} in ISO 10712 test media. The OD change was calculated from OD reading at T0h and T24h sample (same sample left for 24-hours' exposure) and each data point are average of 3 independent samples. The error bars represent the standard error.

The OD change plot for *A. globiformis* (figure 4.5.2.1 a.) showed compete inhibition of bacterial growth at concentration of as-received exfoliated MoS_2 higher than 100 mg L^{-1}. There is a visible increase in the amount of growth compared to the control (0 mg L^{-1} of as-received exfoliated MoS_2) at 50 mg L^{-1} of as-received exfoliated MoS_2 with *A. globiformis*. EC50, the effective concentration of the toxin that gives half of the maximal response, was calculated using logistic regression fit of the plot using a statistical analysis

software. The EC50 for the as-received exfoliated MoS_2 against *A. globiformis* was 74.01 mg L^{-1} from the OD change plot.

The OD change plot for *P. putida* (figure 4.5.2.1 c.) showed inhibition of growth of bacteria at concentration of as-received exfoliated MoS_2 higher than 150 mg L^{-1} with complete inhibition at 200 mg L^{-1}. Unlike with the result from *A. globiformis*, there was no visible increase in proliferation in the lower concentrations at 50 or 100 mg L^{-1}. The EC50 of the as-received exfoliated MoS_2 against *P. putida* was 132.80 mg L^{-1} from the OD change plot with a logistic regression fit.

This EC50 concentration is two to three order of magnitude higher than for the same bacteria, using the same experimental set up, exposed to series of functionalised and non-functionalised silver nanoparticles. (*46, 47*) Bae *et al*. exposed two other environmental bacteria to MoS_2 nanosheets and their EC50 values were 1.45 and 0.59 mg mL^{-1}, respectively, for gram-positive B. cereus and gram-negative *P. aeruginosa*. Therefore, the reported EC50 here was much lower than the previously reported EC50. They conducted their exposure in peptone water with MoS_2 with 0.88 ± 0.81 μm lateral size and 3.1 ± 0.7 nm thickness so it is likely that media and/or lateral size as well type of bacteria affected the difference in EC50 values. Note that there were other studies for antibacterial activity of MoS_2, but they did not report EC50 values.

The OD without the bacteria, (figure 4.5.2.2) in the abiotic condition, showed a change caused by the MoS_2 nanosheets and media alone. The figure showed that there was very little OD change measured for the interaction between MoS_2 and media alone. The OD change was an order of magnitude smaller than the OD measured in biotic conditions. The slight decrease in OD change as the concentration of MoS_2 increased could be attributed to the increased agglomeration of the MoS_2 seen in the 24-hour time period by DLS s. Therefore, this abiotic condition experiment showed that all OD changes observed arose due to an interaction between bacteria, media, and MoS_2.

The Colony Forming Unit (CFU) data (figure 4.5.2.1 b and d.) were obtained to validate and cross-check the results obtained from OD changes (figures 4.5.2.1 a and c.). The CFU results are more widely reported as it requires less expensive equipment and more conventional than other assays. The errors in CFU result tend to be greater than OD changes, as the protocol for taking CFU measurements involves multiple dilution steps which can introduce human error and also colony counting errors from insufficiently grown cells. However, as the results presented here show, the CFU method errors were relatively small, especially when compared to the GO results. This point was discussed further in the discussion section to highlight the difference bacteria interactions between the two materials, but this smaller error indicated that the MoS_2 were relatively stable in dispersion even in the presence of bacteria.

The CFU plots of both bacteria showed similar results to their respective OD change plot. The CFU plot of the MoS_2 exposed to *A. globiformis* showed that complete inhibition was observed at 100 mg L^{-1} with increase in growth observed at 50 mg L^{-1} which was the same with the observation from OD change plot. The CFU plot of the MoS_2 exposed to *P. putida* showed that inhibitory effect was observed at 150 mg L^{-1} with complete inhibition at 200 mg L^{-1}. Again, this was the same observation of results from the OD change plot. The EC50 results of the MoS_2 against *A. globiformis,* and *P. putida* were 67.68 mg L^{-1} and 142.91 mg L^{-1}. These values were similar to the EC50 obtained from OD change plot.

Optical images of the interaction between the soil bacteria and the MoS_2 dispersion are summarised below.

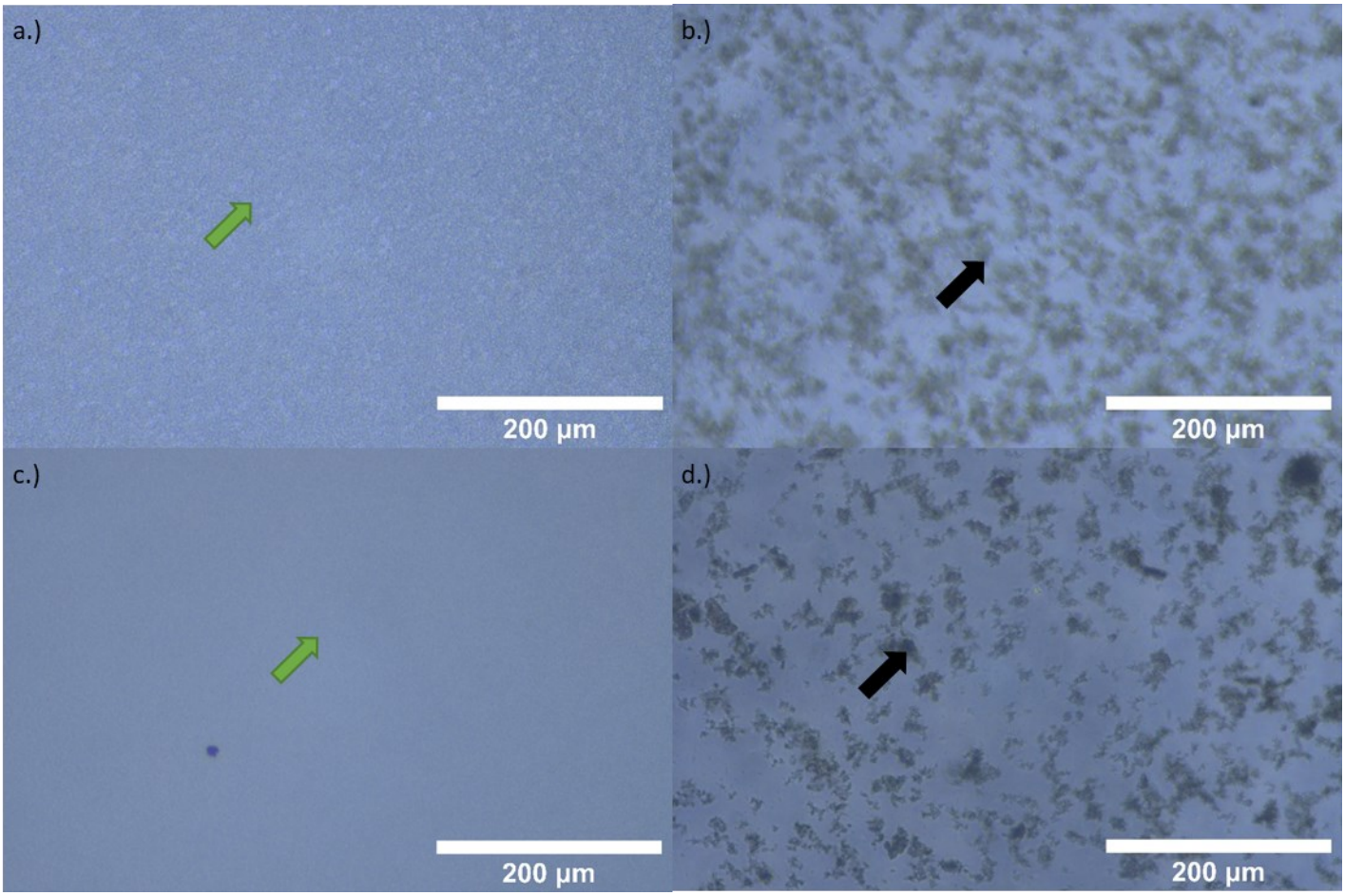


Figure 4.5.2.3 Optical images of soil bacteria with MoS_2 dispersion after 24-hour exposure taken directly in the 96 well plate used to measure the OD changes. a.) *A. globiformis* with 50 mg L^{-1} of MoS_2. b.) *A. globiformis* with 200 mg L^{-1} of MoS_2. c.) *P. putida* with 50 mg L^{-1} of MoS_2. d.) *P. putida* with 200 mg L^{-1} of MoS_2. Green arrows indicate bacteria. Black arrows indicate MoS_2 agglomeration.

The optical images taken of the MoS_2 with bacteria in the well plate used to measure OD change after 24-hours' exposure is shown in figure 4.5.2.3. The two concentrations of 50 mg L^{-1} and 200 mg L^{-1} were chosen because the OD change plot showed that these two concentrations would show bacteria with and without growth, respectively. The images show that at 50 mg L^{-1}, there were bacteria growth from both *A. globiformis* and *P. putida* and the MoS_2 had not agglomerated. However, in the MoS_2 of 200 mg L^{-1}, no bacterial growth was observed and there was MoS_2 agglomeration. The agglomeration of the MoS_2 seems

similar to that of the observed agglomeration from the optical image of the GO (figure 2.4.3.5) except for the absence of bacteria growth in the MoS_2 sample.

4.5.3 Effect of ageing/oxidation on MoS_2

Toxicity testing

Toxicity test results from all of the aged samples are shown below with the OD and CFU results together with the as-received exfoliated material (figures 4.5.3.1). The time point used to quantify the ageing time was from the time that freshly prepared MoS_2 dispersion arrived at the laboratory. The manufacturer usually dispatched the material within a month of synthesis of MoS_2 dispersion, so all the time points indicated thereafter were roughly 1 month after the synthesis date. The MoS_2 sample studied in this series of experiments were As-received exfoliated (As Received), 1 month old, 2 months old, 3 months old, and 3 years old. All ISO 10712 toxicity test for the samples were run in the same manner to the reported results in the previous section with OD change between T0h (OD at time 0h) and T24h (OD at time 24h) and the CFU results. For comparison, the test results were normalised against the controls and converted into percentage of proliferation. Proliferation is the same as survival rate or cell viability in other reported literature.

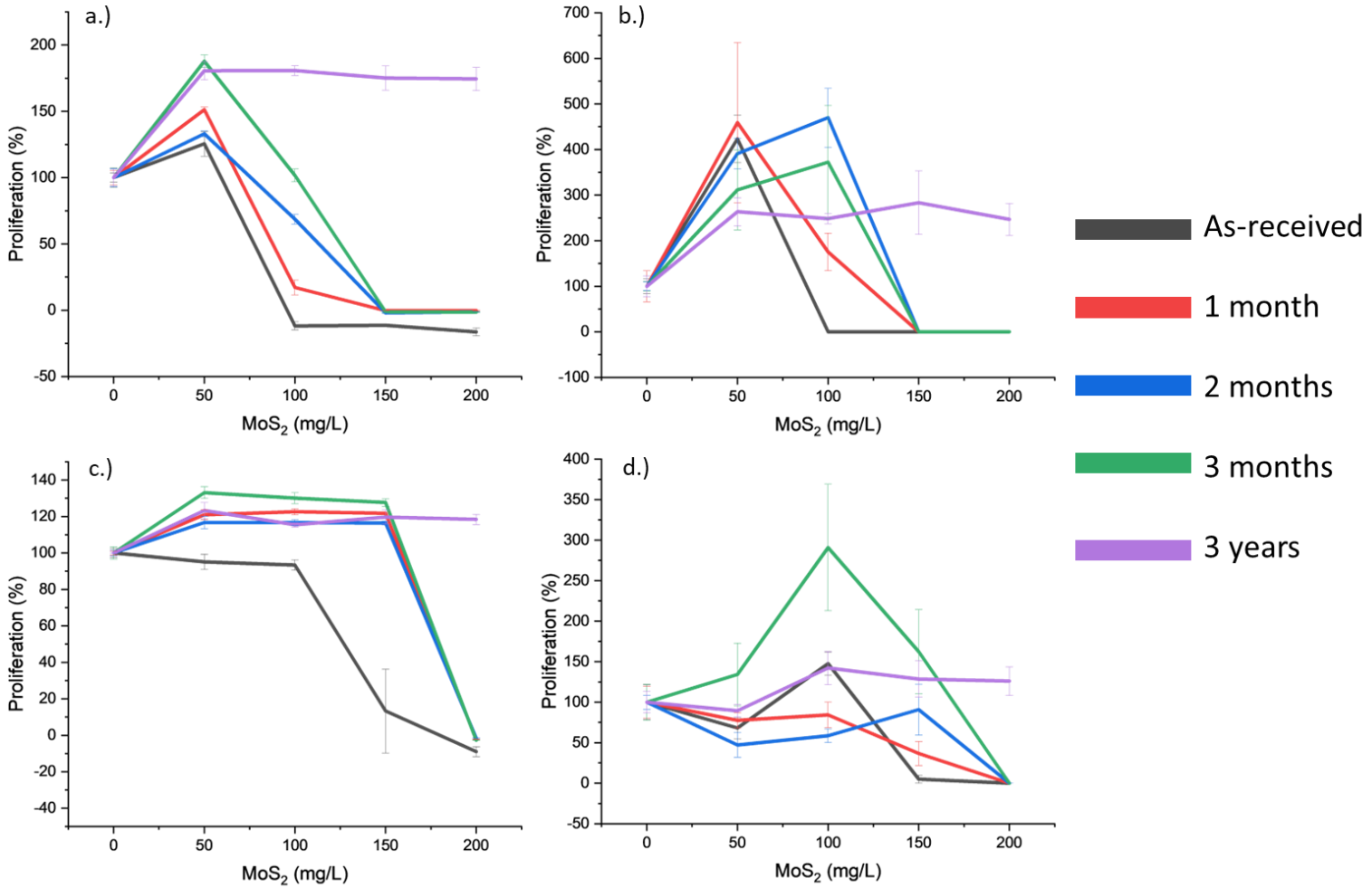


Figure 4.5.3.1 Toxicity test results of all samples of MoS_2 (As-received, 1 month old, 2 months old, 3 months old, and 3 years old) against a.) *A. globiformis* based on OD change results b.) *A. globiformis* based on CFU results c.) *P. putida* based on OD change results d.) *P. putida* based on CFU results. All proliferation plot was based on 5 replicates for each of the data points with each error bar representing the standard error. Each of the samples were run independently from the other.

The proliferation plot of *A. globiformis* with MoS_2 based on OD change results (figure 4.5.3.1 a.) showed that the inhibitory effect of MoS_2 changed as they aged. As the age of MoS_2 dispersion increased from 0 month (as-received exfoliated) to 3 months old, there was a visible proliferation percentage increase at 100 mg L^{-1} indicating the loss of inhibitory effect when the MoS_2 was aged in water. The concentration at which the complete inhibition for each of the samples of MoS_2 was observed was all the same at 150 mg L^{-1}. For the 3 years old sample there were no inhibitory effect observed. The increase in proliferation compared to control was observed for As-received exfoliated, 1 month old, 2 months old, and 3 months old MoS_2 at 50 mg L^{-1} and also for all concentration of 3 years old MoS_2 dispersion. The increase in proliferation were more pronounced in 3 months and 3 years old samples but the effect does not seem to be concentration dependent in the 3 years old sample. The EC50 deduced from the OD change proliferation plot for each of the samples were 74.02, 95.18, 100.24, 103.05 (as-received exfoliated, 1 month, 2 months, and 3 months respectively), and no EC50 for 3 years as there were no inhibition observed.

The proliferation plot of *P. putida* with MoS_2 based on OD change results (figure 4.5.3.1.c.) showed that the inhibitory effect also changed with MoS_2 ageing time against *P. putida*. However, the change in inhibitory effect against *P. putida* was less pronounced than compared to *A. globiformis*. The as-received exfoliated MoS_2 showed no effect up to concentration of 100 mg L^{-1} with visible inhibitory effect at 150 mg L^{-1} and complete inhibition at 200 mg L^{-1}. For the 1-3 months old MoS_2 with *P. putida*, there was growth enhancement observed between the concentration of 50 mg L^{-1} to 150 mg L^{-1} of MoS_2. At 200 mg L^{-1}, 1-3 months old MoS_2 still showed complete inhibition in the same way as the as-received exfoliated MoS_2. The 3 years old sample showed no inhibitory effect but growth enhancement at all concentrations of MoS_2 tested. However, in the same observation to the growth enhancement from the 3 years old MoS_2 on *A. globiformis*, the growth enhancement by the 3 years old MoS_2 on the *P. putida* was concentration independent. The EC50 deduced from the OD change plot with *P. putida* were 132.80, 218.47, 212.96,

240.43 (as-received exfoliated, 1 month, 2 months, 3 months respectively) and no inhibitory effect from the 3 years old sample.

The proliferation plot from the CFU results for all the MoS_2 samples showed the same results as the proliferation plot from the OD change plot (figure 4.5.3.1 b and d.). The only difference was that because the error values in the CFU results were greater for the reasons described earlier such as human error associated with agglomeration of materials or the bacteria, the ANOVA statistical test did not yield the same result. For example, the p-value for the complete inhibition resulted in statistically non-significant at 0.05 level confidence in some cases, because the error values in the control was too large. However, the CFU result showed that there are no bacteria, so these scenarios demonstrate the importance of running both the OD and CFU measurements. The EC50 values deduced from the CFU results together with the EC50 values deduced from the OD change results is summarised in table 4.5.3.1.

		EC50 (mg L^{-1})				
		As-received exfoliated	1 month	2 months	3 months	3 years
OD	A. globiformis	74.02	95.18	100.24	103.05	No EC50
	P. putida	132.80	218.47	212.96	240.43	No EC50
CFU	A. globiformis	67.68	102.04	112.04	116.37	No EC50
	P. putida	142.91	147.27	654.49*	160.54	No EC50

Table 4.5.3.1 EC50 values from individual logistic regression fit of all samples of MoS_2 (As-received exfoliated, 1 month, 2 months, 3 months, and 3 years old). Both OD and CFU results were used to deduce the EC50 for each toxicity assessment technique. *Note the 2 months old MoS_2 with *P. putida* result from CFU method did not yield a good fit.

The summary of EC50 values shown in table 4.5.3.1 confirmed the loss of inhibitory effect from the ageing of MoS_2 dispersion in water. The EC50 values of MoS_2 dispersion against both bacteria showed As-received exfoliated < 1 month old < 2months old < 3 months old with no inhibitory effect at 3 years old sample of MoS_2 in water. At all of the time points of ageing, EC50 of MoS_2 with gram positive bacteria, *A.*

globiformis, was lower, suggesting that MoS_2 inhibition of growth is more effective against gram positive bacteria.

Ageing of MoS_2 by XPS

The origin of ageing/oxidation effect of MoS_2 dispersion in water was investigated using XPS to characterise the as-received exfoliated, 3 months old, and 3 years old sample of MoS_2. High resolution XPS spectra of all three samples showing Mo3d and S2p peak region are shown in figure 4.5.3.2 and also the chemical transition associated with deconvolution.

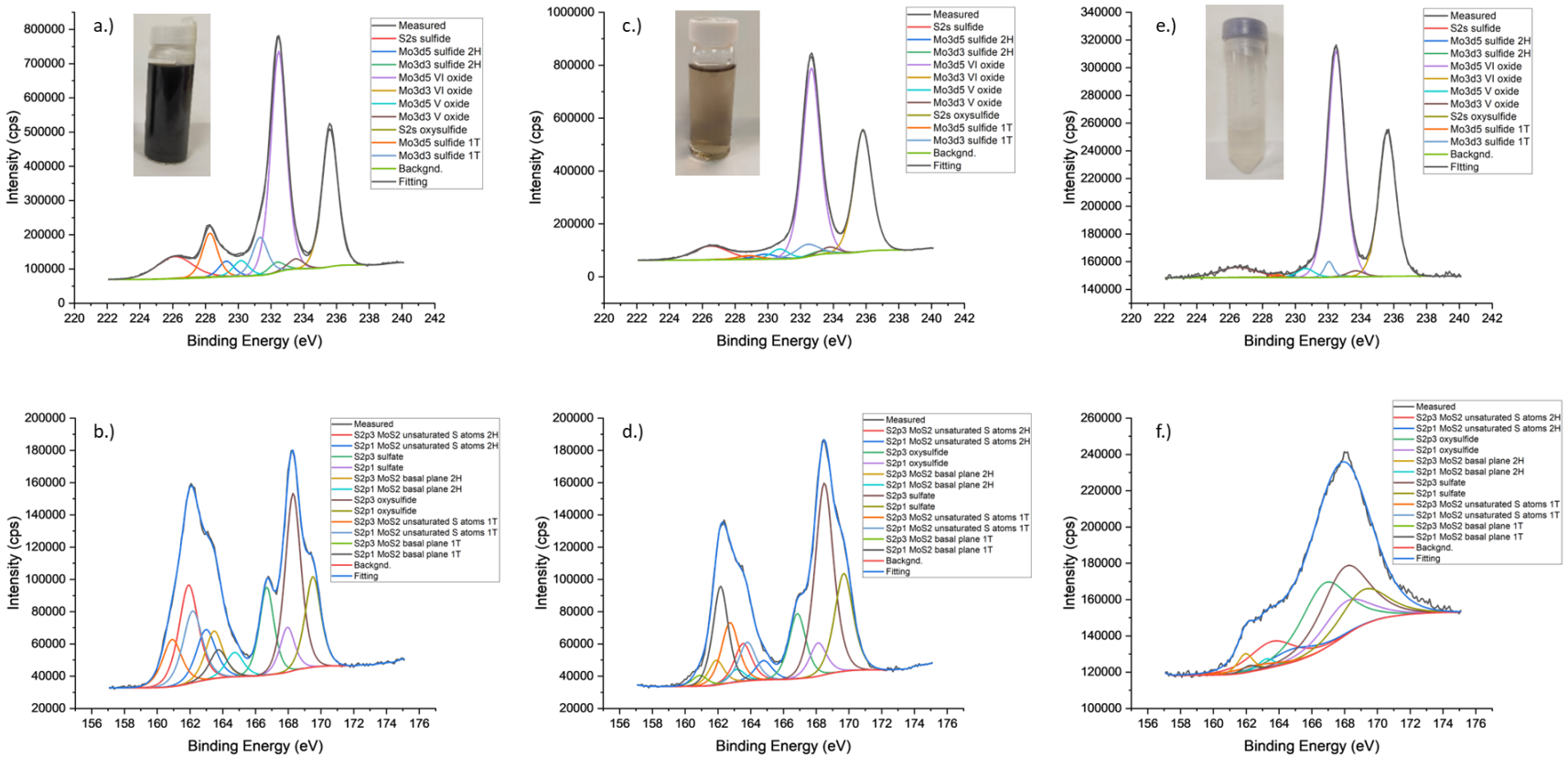


Figure 4.5.3.2 High resolution XPS of As-received, 3 months old, and 3 years old MoS_2 on silica wafer. a.) High resolution XPS spectra of Mo3d peak with deconvolutions as well as S2s peak of pristine MoS_2. Inset image shows the pristine MoS_2 dispersion in water at 1 mg mL^{-1} b.) High resolution XPS spectra of S2p peak with deconvolutions of pristine MoS_2 c.) High resolution XPS spectra of Mo3d peak with deconvolutions as well as S2s peak of 3 months old MoS_2. Inset image shows the 3 months old MoS_2 dispersion in water 1 mg mL^{-1} d.) High resolution XPS spectra of S2p peak with deconvolutions of 3 months old MoS_2 e.) High resolution XPS spectra of Mo3d peak with deconvolutions as well as S2s peak of 3 years old MoS_2. Inset image shows the 3 years old MoS_2 dispersion in water 1 mg mL^{-1} f.) High resolution XPS spectra of S2p peak with deconvolutions of 3 years old MoS_2

	As-received exfoliated	3 months	3 years
Chemical environment in Mo3d and S2s peak region	**Amount (%)**	**Amount (%)**	**Amount (%)**
Sulfide	29.63	23.91	19.70
Oxysulfide	1.30	1.05	0.86
Mo (IV)	15.02	7.19	2.60
Mo (V)	3.59	3.46	2.99
Mo (VI)	50.48	64.40	73.86

Table 4.5.3.2 % of each main chemical species deduced from the area under the graph of deconvoluted high resolution XPS spectra of Mo3d and S2s peaks. The environments and the amount were deduced using protocols described in Zhang *et al*. (*36*). Sulfide and oxysulfide were from the S2s peak while the Mo (IV), Mo (V), Mo (VI) were from the Mo3d peak.

	As-received exfoliated	3 months	3 years
Chemical environment in S2p region	**Amount (%)**	**Amount (%)**	**Amount (%)**
Sulfate	30.57	42.24	67.25
Oxysulfide	14.01	13.19	11.99
Sulfide	55.43	44.56	20.77

Table 4.5.3.3 % of each main chemical species deduced from the area under the graph of the deconvoluted high resolution XPS spectra of S2s peaks. The species and the amount was deduced using protocols described by Zhang *et al*. (*36*).

	As-received exfoliated	3 months	3 years
Phases in MoS_2 nanosheets	**Amount (%)**	**Amount (%)**	**Amount (%)**
2H	3.50	2.21	0.27
1T	11.52	4.98	2.33
	Ratio	**Ratio**	**Ratio**
2H/1T	0.30	0.44	0.12

Table 4.5.3.4 % of each phase calculated from Mo3d peak based on Domi *et al*. (*27*) and the ratio of 2H/1T phase present.

The insets of the figure 4.5.3.2 showed the colour change of the MoS_2 dispersion at 1 mg L^{-1} as they aged and oxidised from as-received exfoliated sample to 3 months old sample then to 3 years old sample. The MoS_2 dispersion starts off dark brown colour at as-received exfoliated condition then slowly discolours to

a yellowish and more clear dispersion at 3 months old and at 3 years old turns completely colourless solution.

The high-resolution spectra of Mo3d and S2s region (220-242 eV) and S2p region (155-175 eV) for all three samples of MoS_2 (as-received exfoliated. 3 months old and 3 years old) were deconvoluted with the same method using the combination of common analysis. (*27, 36, 234, 235*) shown in figure 4.5.3.2. Only the time points stated were measured since the measurements could only be taken at those time points due to equipment availability, but these three time points demonstrated the start, mid, and end point of the ageing process in the 3 years period. Although it was not clear whether ageing for longer than 3 years had further effect on the dispersion, this type of prolonged storage length had never been explored before. The longest ageing that been reported was 10 months at 4 °C. (*27*)

Ageing process measured by XPS highlighted couple of key changes in the MoS_2 dispersion. One of them was the oxidation of the Mo (IV) in MoS_2 into Mo (VI). There were some Mo (V) species present in small amount which also oxidised into Mo (VI). These Mo (V) species exist in bulk MoS_2 which occurs naturally. (*185*) The oxidation of Mo (IV) species in MoS_2 agreed well with observation by Zhang *et al*. (*36*) and therefore follows the same oxidation process. MoS_2 species are converted into MoO_4^{2-} species that are soluble in water together with formation of SO_4^{2-} species. In the XPS spectra of Mo3d region in figure and also table 4.5.3.2 showing the relative amount of different oxidation species of Mo, it was clear that as the amount of Mo (IV) species decreased, the amount of Mo (VI) species increased. It was also clear from the S2s peak deconvolution and S2p peak deconvolution that the amount of sulfide decreased and S2p deconvolution showed that the sulfate amount increased. The sulfate peak in the S2s peak overlapped significantly with the Mo (IV) peak hence the amount could not be deduced from S2s spectra. Both S2p and S2s spectra deconvolution table 4.5.3.2 and 4.5.3.3 also showed that there was small amount of

oxysulfide which did decrease in amount as the MoS_2 aged. These observations confirmed that the MoS_2 underwent oxidation process which resulted in production of MoO_4 species and sulphate species mainly with small amount oxysulfide possibly as an intermediate or by product.

There was also a change in the number of phases present in the MoS_2 dispersion as shown in table 4.5.3.4. Overall, the amount of MoS_2 decreased and therefore each of the 2H and 1T phases but the ratio of the two phases, 2H/1T, changed throughout the oxidation process. Within the 3 months period, the amount of 1T phase decreased more than the amount of decrease of 2H phase. This was reflected by an increase in the 2H/1T ratio. This is likely due to the metastability of 1T phase and that 1T phase MoS_2 is less stable than the 2H phase and therefore more susceptible to the oxidation process. At 3 years old, the amount of both phases decreased to a much lower amount with 1T phase still decreasing by more than the 2H phase. However, because most of the MoS_2 have been oxidised, the absolute amount of MoS_2 was low and therefore the ratio value changed to 0.12. This could indicate the kinetic change in the oxidation process as the time of ageing process increases. This XPS result showed that oxidation process previously reported might be dependent on the phase proportion present in the MoS_2 and that oxidation process favours the oxidation of 1T phase over 2H phase. This also indicated that the loss of toxicity was from oxidation process of MoS_2 but more importantly the oxidation of 1T phase over 2H phase. The higher toxicity of 1T phase had been previously reported for both human and bacteria cells (*11, 210, 224, 227*), so this hypothesis that the loss of 1T phase in MoS_2 detoxifies the MoS_2 certainly seems plausible with further research required with different grades of as-received exfoliated MoS_2.

Ageing of MoS_2 by ICP and pH

To complement the XPS result and elucidate the mechanism of ageing of exfoliated MoS_2, pH measurements to determine the pH change in the as-received exfoliated MoS_2 dispersion and ICP

measurements to determine the amount of Mo released from the as-received exfoliated MoS_2 using dialysis membrane. Table 4.5.3.5 and table 4.5.3.6 shows the pH and ICP results respectively.

	pH	S.D.
As-received	11.8	0.08
3 months	12.1	0.14
3 years	12.1	0.06

Table 4.5.3.5 pH of MoS_2 dispersion in water at 1 mg L^{-1}. Each result consist of at least 3 repeated measurements at 25 °C.

	ppm of Mo	S.D.
As-received	0.126	0.001
3 months	0.602	0.001
3 years	1.236	0.006

Table 4.5.3.6 Concentration of Mo ions present in each of the MoS_2 dispersion leachate from as-received, 3 months aged, and 3 years aged. For conversion to mM, 1 ppm of Mo roughly eauls to 0.01 mM of Mo. All measurements were at least 5 replicates with average and the S.D. shown.

As shown in the pH result (table 4.5.3.5), the MoS_2 dispersion did not change in its pH during the ageing process. However, the ICP result (table 4.5.3.6) showed that the ageing mechanism is likely to release Mo ions during the ageing process. The ageing process resulted in ten folds increase in the amount of Mo in the leachate meaning that there has been significant dissolution of MoS_2.

4.6 Discussion

The exfoliated MoS_2 dispersion in water received from ACS material had physiochemical properties which matched very closely with the manufacturer specification given. The MoS_2 dispersion was monolayer with average lateral diameter size of 2.0 μm. The MoS_2 was stable in water in the testing concentration range

with negative zeta potential value. The XPS results suggested that there was less 1T phase than the manufacturer specification. This could be due to the time lag in the receiving the material as the lead time for the synthesis to arrival of the material was roughly 1 month so there would be some oxidation of MoS_2 during those shipping time. This was also reflected in the initial amount of both Mo (VI) and Mo (IV) which represent the oxidised Mo and Mo present in MoS_2 respectively where the Mo (VI) was present in significant proportion. The amount of oxidised Mo could be lower in a freshly produced MoS_2. However, this is not reported adnywhere else even in literature.

The MoS_2 dispersion in test media of ISO 10712 was less stable in comparison to the stability in water within the test concentration range. This was likely due to the presence of the salt ions with positive charges such as the Na^+, K^{2+}, and Mg^{2+}promoting agglomeration of the MoS_2 nanosheets in a similar manner to colloidal behaviour of GFNs. (*122, 123, 218*) At higher concentration (200 mg L^{-1}), the agglomeration is more indicated by the larger value of Z-average since the destabilised MoS_2 from the salt ions increase with more amount of MoS_2.

The as-received exfoliated MoS_2 showed inhibitory effect towards both bacteria, *A. globiformis* (gram positive) and *P. putida* (gram negative). The complete inhibition of both bacteria, *A. globiformis* and *P. putida*, by MoS_2 were observed at 100 mg L^{-1} and 200 mg L^{-1} with EC50 of 74.02 mg L^{-1} and 132.80 mg L^{-1} respectively based on the OD change result. The CFU result agreed well with the observed level of inhibitory effect which indicated that the observed MoS_2 toxicity is bactericidal as the bacteria growth could not be recovered.

It was also clear that unlike GO, agglomeration of MoS_2 in test media observed by the DLS did not affect the toxicity effect of MoS_2. This could be due to the difference in mechanism of action where the MoS_2 does not heavily rely on the physical mechanism such as insertion or wrapping mechanism. Although there

were reports of insertion mechanism of MoS_2 (*212, 231*) there were also reports of oxidative stress with 1T phase exhibiting higher inhibitory effect than the 2H phase due to the higher electrical conductivity and charge transfer ability. (*210, 227, 228*) The toxicity results reported here suggest that MoS_2 could still exhibit inhibitory effect even at aggregated state. It may be that there is a competing effect or amount of aggregation and amount of 1T MoS_2 which requires further study, possibly with different media to explore the media effect and change in agglomeration state in a similar manner to the GO part of the experiment.

Ageing of MoS_2 dispersion in water led to oxidation of MoS_2 into MoO_4^{2-} and SO_4^{2-} in a similar manner to the observation by Zhang *et al*. (*36*) from the XPS results. It was also observed that the amount 1T phase decreased significantly. This type of detailed effect of oxidation has not been reported previously possibly due to the difficulty in controlling the synthesis of MoS_2 but also the lack of analysis of MoS_2 using XPS. 1T phase of the MoS_2 is meta stable and more susceptible to the oxidation process than the 2H phase as well being more active towards bacteria. Therefore, the loss of inhibitory effect observed in the toxicity results were due to the loss of 1T phase. Although this results partially contradicts with the toxicity observation by Domi *et al*. (*27*) in that they showed aged MoS_2 being more toxic towards yeast and human cell, their reported results of higher ROS production by aged MoS_2 might indicate similar ageing mechanism in that there was a loss of 1T phase. The difference in observation may be due to other physiochemical differences such as thickness and size as they struggled to characterise the material, or the type of cells tested.

Additionally, the ICP result indicated that on top of the loss of 1T phase shown in XPS result, the MoS_2 dispersion was likely going through dissolution during the ageing. The ICP result showed that MoS_2 dispersion is releasing Mo ions during ageing. Based on both XPS results and ICP, after 3 years of ageing, there is no 2D MoS_2 exfoliated dispersion left because a.) XPS result showed no presence of 1T phase

which is indicative of stable exfoliated MoS_2 dispersion b.) ICP result showed significant increase in the amount of Mo ions released on the aged samples compared to the as-received MoS_2 sample. It is likely that at 3 years time of ageing, there is virtually no 2D MoS_2 left and most Mo and S ions are in dissolution form. Mechanistically, this means that during ageing of MoS_2 dispersion, 1T phase is oxidised and converted into MoO_4^{2-} and SO_4^{2-}. The oxidation process of 2H phase is not clear yet as this level of detailed analysis have not been carried out yet but additional Raman measurements can determine the presence of 2D MoS_2 and the changes during the ageing process and it can complement the ageing experiment to elucidate whether the MoS_2 is completely dissolved.

The growth enhancement effect of MoS_2 was also observed only for the *A. globiformis* but was observed in both the *A. globiformis* and *P. putida* in the more aged and oxidised MoS_2 samples. It was clear from the 3 years old sample that the effect was not concentration dependent unlike the inhibitory effect. This observation has not yet been reported but growth enhancement has been reported for graphene oxide where the GOs could form scaffolds to support growth under agglomerated conditions. It is unlikely that this same mechanism of growth enhancement applies to growth enhancement observed for MoS_2 as the effect is only observed at low concentration and it is concentration independent. The growth enhancement of GO is concentration dependent with higher amount of GO showing more growth enhancement. A likely alternative mechanism for growth enhancement is from the presence of Mo (VI) species or the product of oxidation species. Molybdenum, Mo (VI) is an environmental pollutants and essential mineral for bacteria growth. (*237-240*) Since both bacteria, *A. globiformis* and *P. putida*, are soil-dwelling bacteria important in bioremediation and nitrogen fixation, it is possible that certain level of Mo ion present can help the growth of bacteria. It is not clear whether this is self-limiting and therefore not concentration dependent but the increased effect of enhanced growth with increased oxidation, especially visible in the *P. putida* results

with ageing test, suggested that formation of Mo (VI) may have a significant role in the interaction of MoS_2 in the environment and its biological system.

It was worth noting that *A. globiformis* was more susceptible to the inhibitory effect of the *P. putida*. The enhanced growth effect at low concentration was also only visible in the *A. globiformis* culture in the as-received exfoliated MoS_2 mixture. Therefore, within the experimental procedure of modified ISO 10712, it could be concluded that the *A. globiformis* was more susceptible to the effect by MoS_2. This may be due to the difference in the cell structure as *A. globiformis* is a gram-positive with thick peptidoglycan but no outer cell wall like *P. putida* which is a gram-negative bacterium. Gram-negative bacteria have more cell wall integrity with outer cell wall having negatively charged lipopolysaccharides. Therefore, interaction of MoS_2 may be stronger with gram-positive bacteria than gram-negative bacteria. The observation of the higher inhibitory effect on *A. globiformis* is consistent with previous report of silver nanoparticles but different from the GO results. (*46, 47*) The difference in observation is due to the combination of difference in interaction but also the different cell structure which each bacteria culture goes through at different stages of growth. (*133*)

4.7 Conclusions

The effect of fresh MoS_2 as well as aged MoS_2 on the environmental system were assessed using ISO 10712, one of the routinely used in-vitro material toxicity tests against soil bacteria. As-received exfoliated MoS_2 showed inhibitory effect towards gram-positive bacteria, *A. globiformis*, and gram-negative bacteria, *P. putida* with EC50 of 74.02 mg L^{-1} and 132.80 mg L^{-1} respectively using the standard OD method. It was confirmed by the CFU that MoS_2 was bactericidal rather than bacteriostatic. As the MoS_2 was aged, the

inhibitory effect of MoS_2 was gradually lost with the oldest sample of 3 years old MoS_2 showing complete loss of inhibitory effect within the test range (0-200 mg L^{-1}). Using XPS, it was revealed that the toxicity effect of MoS_2 was mainly due to the presence of 1T phase which has higher charge transfer ability than the 2H phase. The ageing process resulted in oxidation of MoS_2 to MoO_4^{2-} and SO_4^{2-} with predominantly more loss of 1T phase leading to loss of toxicity and dissolution of MoS_2 with most dissolving in 3 years. As well as the XPS results, the DLS results suggested that the main toxicity mechanism was oxidative stress rather than a physical mechanism. This work was the first to report the importance of 1T phase and the loss of 1T phase in the ageing process in water. It also demonstrated the versatility of the newly developed modified ISO 10712 for emerging 2DNMs as well as the importance of through characterisation and analysis of 2DNMs used in biological toxicity test.

5 Comparison between GO work and MoS_2

In order to bring together the above work, assessing the toxicity of GO and MoS_2 on soil bacteria with focuses on the effect of media on GO toxicity (chapter 2.4), effect of lateral size on GO toxicity (chapter 3), and effect of ageing on MoS_2 (chapter 4), a plot compiling all of the main toxicity results was produced for OD change and 24h CFU results and presented in figure 5.1. This helped to draw conclusions about which factors such as choice of exposure condition or lateral dimension of 2DNMs are important in assessing the impact of novel 2DNMs to the environment.

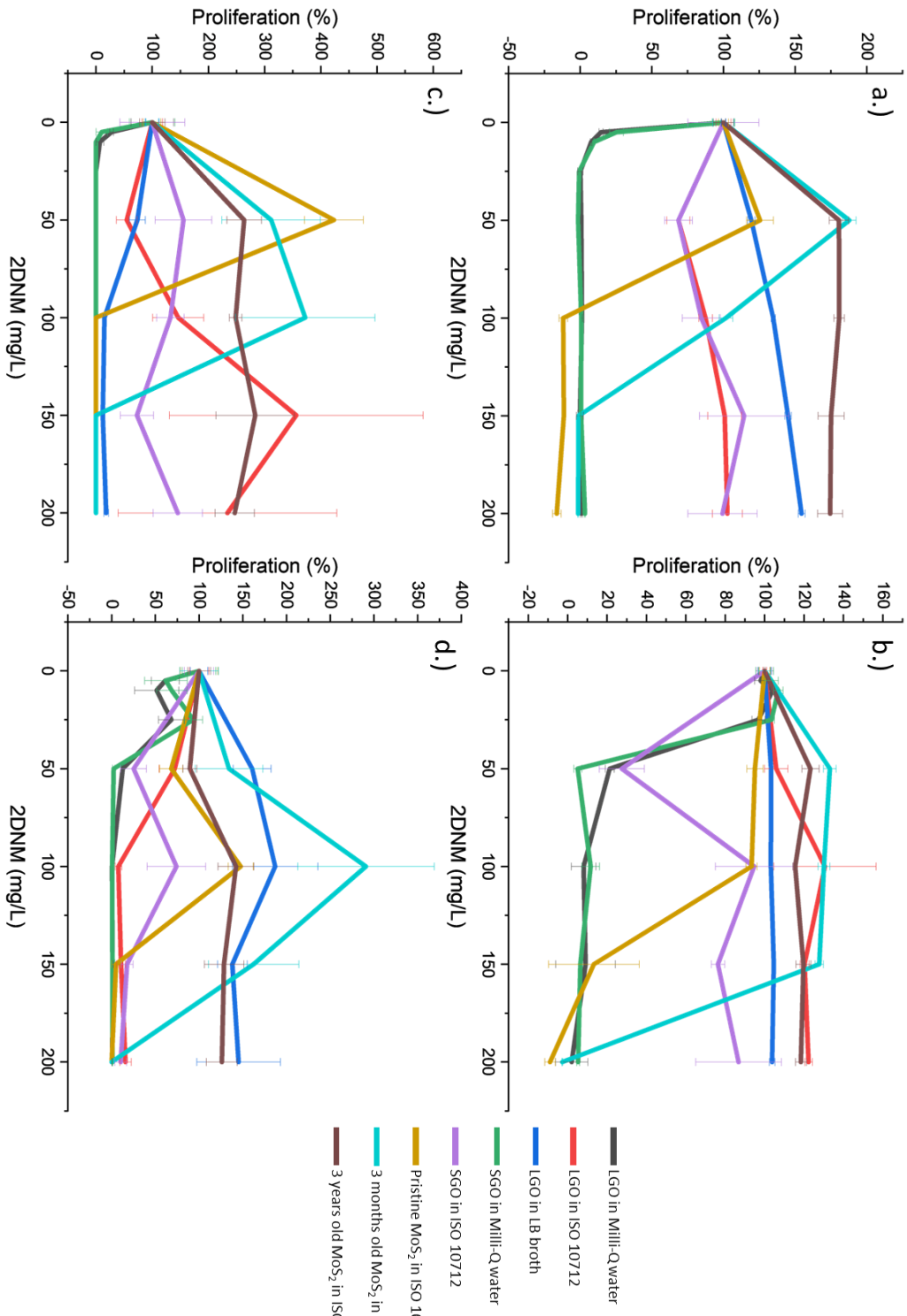


Figure 5. 1 Proliferation plot of 2DNMs (pristine and aged MoS_2 and GO of different lateral size) against a.) *A. globiformis* given by the OD change results; b.) *A. globiformis* given by 24h CFU results; c.) *P. putida* given by the OD change results; d.) *P. putida* given by 24h CFU results, under different media conditions (Milli-Q water, ISO 10712, and LB broth)

The comparative plot (figure 5.1) showed that when assessing the toxicity behaviour of 2DNMs, it is important to consider: 1.) The effect of media on the 2DNM (exposure condition); 2.) The effect of age if any on the 2DNM; 3.) The effect of lateral size of 2DNMs. The type of bacteria should be considered in order to understand the different interactions. In terms of which factor should be prioritised in order to assess the safety of the different 2DNMs under environmental conditions can be ranked as follows: Effect of media such as different level of salt and organic substate> Effect of ageing>> Species of bacteria> lateral size of 2DNMs. The ranking was identified by using figure 5.1 and comparing the difference in the reported EC50 values. Effect of media greatly affected the behaviour of GO and masked any difference in the interaction by different lateral size. Further research replicating the procedure to study the effect of MoS_2 toxicity in Milli-Q water and also much more nutrient-rich condition such LB broth or ISO 10712 with additional NOMs is likely to provide interesting results. It is likely that MoS_2 possess a property that their toxicity in the ISO 10712 does not interfere with the presence of nutrients as much as with GOs since MoS_2 was able to show inhibitory effect under the ISO 10712 condition.

Effect of ageing also greatly affected the toxicity of MoS_2. MoS_2 had been shown to lose its toxicity over time with molecular constituent dissolving. It should be noted that GO did not age under the 3-year time period studied within this project as no observable change in the physiochemical property or toxicity response was observed. The characterisation results of ageing study of GOs are included in Appendix VII and chapter 2.3 shows all toxicity test carried out in the time span of 3 years with the same GO dispersion in water. There are currently no reports of ageing of GO in water reported which suggests that there is no observable or noticeable change that occur with GO in water. However, GO has been shown to be affected by other process such as photochemical reactions by natural sunlight, as well as the presence of chlorine. (*147-149, 215*) The work has only been carried out in water with *E. coli,* so assessment against *A. globiformis* and *P. putida* in different media will provide data on whether transformed GO behave similarly

towards range of bacteria and whether presence of nutrients or salts could also supress the toxicity of transformed GO. Similar assessment should be carried out for MoS_2.

The difference in between the interaction of bacteria of *A. globiformis* and *P. putida* showed that *P. putida* does seem to be more resistant to the toxicity of MoS_2 and GO. However, as stated in the literature review, this conclusion cannot be extrapolated to state that gram-negative bacteria are more resistant to 2DNMs. More amount of research needs to be carried out with systematic approach to the experiment controlling the above factors so that literature comparison can be made.

Lastly, lateral size had the least effect on the toxicity against soil bacteria. The difference may be larger if larger difference in lateral size can be prepared but effect of media as well as other external factors are likely to affect the toxicity more than the lateral size. However, effect of lateral size for MoS_2 toxicity should still be explored as this has not been reported yet fully. This may be difficult to do since ageing/oxidation occur in water and the probe sonication technique does require the material to be dispersed in solution. However, the ageing effect takes place over a period of time and therefore if the starting material was controlled there could be an interesting toxicity results from the effect of lateral size of MoS_2.

6 Overall Conclusions & Future Outlook

Within this thesis, two emerging 2DNMs, Graphene Oxides (GOs), and MoS_2, which are gaining ever increasing interest in research and for commercialisation were assessed against environmentally relevant bacteria under environmentally relevant conditions. During the assessment of these 2DNMs using ISO protocol 10712, which was routinely used to assess the toxic material on water quality in soil, it became apparent that effect of the media used needed to be understood in more depth. A series of experiments revealed that GO and MoS_2 exhibited very different interactions under ISO 10712 protocol testing. GO exhibited range of effect from inhibitory effect to growth enhancement whereas MoS_2 exhibited significant inhibitory effects. Further experiments with GO showed that GO were found to display antibacterial effects in minimum salt condition (Milli-Q water) with complete inhibition of growth on soil bacteria, whereas with nutrient rich media (LB broth), GO displayed growth enhancement effect on the bacteria. Colloidal characterisation study and TEM image revealed that depending on the composition of the solution which the GO was dispersed in, GO would either exhibit edge interaction and wrapping interaction for antibacterial effects, and scaffolding interaction to promote growth enhancement effect on the bacteria. It was also reported here, for the first time, the potential protective mechanism in which bacteria could produce EPS under nutrient rich condition to protect against the GOs.

For GO, further experiments that varied lateral size revealed that smaller lateral size GO (SGO) would exhibit different mechanism of interaction compared to larger GO (LGO). The two distinctive lateral size GOs were prepared using probe sonication which resulted in SGO and LGO that were chemically indifferent but only different in lateral size. The toxicity tests under favourable condition (Milli-Q water) showed that different sized GO showed different preferential interaction of mechanism for antibacterial effect. SGOs were shown to interact through edge and insertion mechanism by their edges, as well as

wrapping whereas LGOs, were shown to interact mainly through wrapping mechanism by their basal planes. The two soil bacteria, *Arthrobacter globiformis* and *Pseudomonas putida*, gram-positive and gram-negative respectively, showed different interactions with SGO and LGO. *A. globiformis* showed no preferential interaction with either of LGO and SGO and exhibited strong interaction which was irreversible. However, *P. putida* showed preferential interaction with LGO through wrapping mechanism which was reversible and showed significant change in its EC50 value. TEM images also reported for the first time the potential for bacteria to still reproduce within the wrapping mechanism. These findings were important in many ways as they highlighted the complexity of understanding the biological interaction when considering variation of physiochemical size with different bacteria other than model pathogenic bacteria.

For MoS_2, it was shown that as-received exfoliated MoS_2 could inhibit the growth soil bacteria completely under ISO 10712 test condition unlike GO and also showed stronger inhibition towards *A. globiformis* than *P. putida*. Then the ageing effect, one of the physiochemical change prominent for MoS_2, was considered in a series of further experiments. MoS_2 oxidised/dissolved under aqueous conditions over time and showed to lose its initial toxicity over a range of long time (within 3 years). The oxidation process resulted in mainly conversion of MoS_2 to MoO_4^{2-} and sulphate ions which resulted in loss of the 2DNM. Although it was unclear whether MoS_2 displayed similar types of mechanism of interaction with GOs, its 2DNM property was an important determinant of its antibacterial activity and therefore warrants further investigation. Consideration of 1T phase in MoS_2 through systematic study of relating the amount of 1T phase with its inhibitory effect should elucidate the unique biological interaction of 2DNM MoS_2. These findings highlighted the importance of considering changes of these 2DNMs and again the complexity of understanding the potential effect of emerging 2DNMs on the environment.

In terms environmental assessment and recommendations, for MoS_2 it was shown that as-received exfoliated MoS_2 would pose the highest threat to the soil bacteria currently. As-received exfoliated MoS_2 was able to exhibit strong inhibitory effect even in ISO 10712 test condition which GO did not exhibit. However, MoS_2 has shown to oxidise and dissolve over time which indicated that MoS_2 do not persist in the environment and poses very little threat to the microbial communities in the environment. MoS_2 release in its pure 2D form can harm microbial community in the environment but quickly loses its toxicity over time.

For GO, there is no observable ageing/dissolution to mitigate the toxicity observed. However, as the series of toxicity test using different media solution showed, GO is likely to have the highest toxicity with little/no salts present. The GO sheet can interact directly with the bacteria via physical mechanism or moreover actively force the salts and nutrients out of microbials and cause bactericidal effect. With increase in surroundings of other salts and other organic matters, the toxicity effect is reduced and virtually becomes non-toxic and rather acts as nutrient carrier. Moreover, this effect of saturation of GO sheet with the surrounding salts and nutrients can occur even in low salt content media because the mechanism of GO actively extracting and adsorbing the essential nutrients out of the bacteria over time would result in saturation of the GO sheet when left for long enough duration. Figure 6.1 shows the interaction of GO with time demonstrating the effect of saturation of GO sheet with available salt.

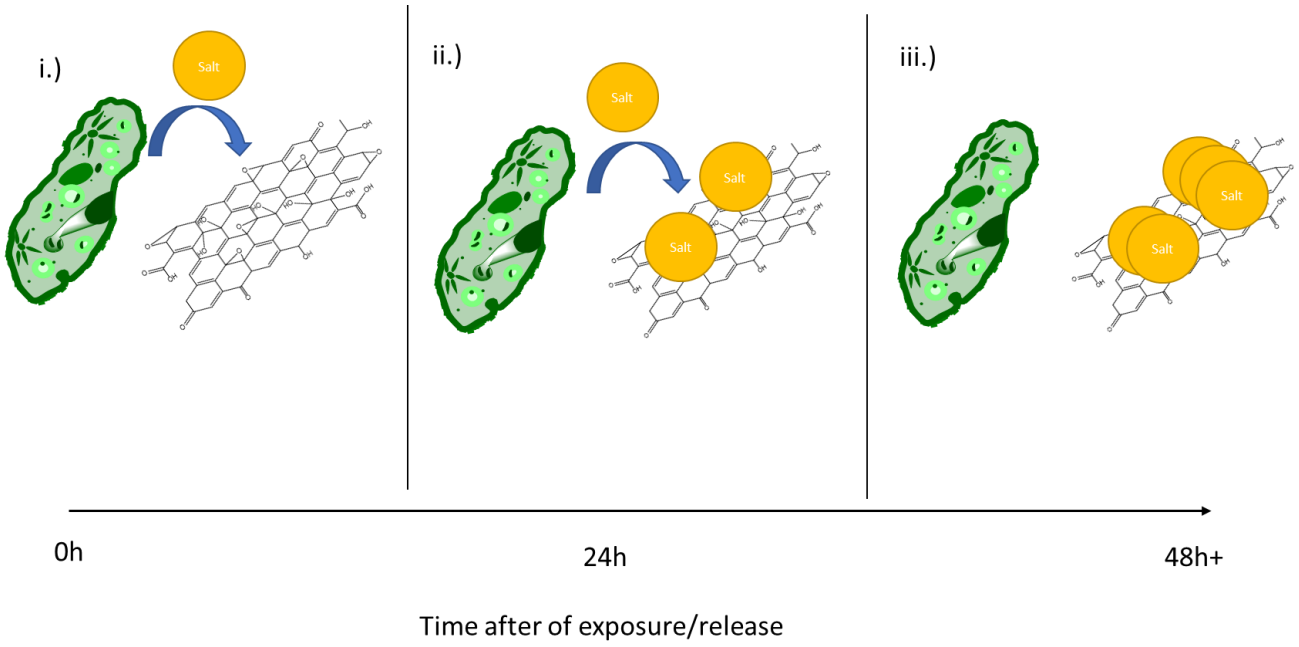


Figure 6. 1 Diagram showing the change in toxicity of GO over time. i.) with little to no salt content on the basal plane of GO, GO can actively extract salt content from the bacteria causing osmotic pressure and bactericidal effect on bacteria ii.) GO basal plane gradually saturated with salt and the extraction process and the toxicity decreasing iii.) Little to no extraction of salt due to GO basal plane being fully saturated and GO no longer has bactericidal effect.

As demonstrated in figure 6.1, as a function of time, the toxicity of GO diminishes. This is based on the current understanding and observation where the toxicity is of GO is heavily influenced by the presence/absence of salt and the mechanism observed where the GO would seemingly wrap itself around the bacteria. The electrostatic imbalance caused by adsorbing the salt on one side of the GO basal plane can cause the GO to bend around the bacteria. As more salts are adsorbed on to the GO, the GO gradually loses its toxicity. Again, this indicates that the GO too poses very little threat to the environment as environmental media usually have salt and organic matters present preventing toxic interaction between GO and bacteria.

One thing which does need to be taken account for is the potential mechanism of metal hitchhiking of other harmful metals on the GO sheets. As discussed, GO sheets present on its own with other unharmful substance would result in no real environmental threat of GOs but GO has been shown to be an excellent material for heavy metal adsorption in its application for environmental filters. (*241, 242*) This does raise concerns for potential scenario where GO present in the environment may act as a transport system for heavy metals. However, affinity of these heavy metals to GO sheets compared to other non-harmful materials in the environment need to be evaluated and also consideration of re-stacking of GO sheets under presence of salt is very likely leading to reduced mobility of GO in the environment. In reality, it is likely that GO in the environment may even lead to reduced mobility of heavy metals in the environment.

Comparison of all results from GO and MoS_2 under different experiment conditions revealed that key factors that affect the inhibitory effect of 2DNMs can be ranked as follows: level of salt, organic substrate, and other substances in the media > ageing of 2DNMs >> species of bacteria > lateral size of 2DNMs. This ranking should serve as a basis in which more key factors can be added to help assess the impact of 2DNMs against environment.

To approach more realistic environmental release scenarios, real waste such as GO ink could be used instead of as-synthesised GO. Moreover, effect of additional environmental condition should be considered such as presence of natural light and presence of NOMs. These conditions would be particular interesting for MoS_2 as these potential transformations have not been reported yet. It would also be interesting to understand the kinetics of the ageing effect of MoS_2 and whether this process can be delayed or even stopped and consider whether the ageing could halt under some environmental conditions and thus pose more threat.

As well as the above future work mentioned, adding more 2DNMs for testing, expanding the range of physiochemical properties of the GO and MoS_2 and the variation of target biological system should be considered. Particular attention should be paid to the detailed characterisation of the material but also its behaviour in the solution during exposure to understand the effect of the experimental procedure used. Different types of bacteria with different morphology as well as different maturity of culture should also be used to further the understanding of effect of membrane structure on the interaction with 2DNMs. Complementary TEM also provided some powerful insights into the interaction between GO and soil bacteria and therefore high-resolution image work as well as additional correlative imaging would be a necessary tool to understand the interaction. Certainly, even within this work, higher resolution imaging or 3D tomography would provide much more detailed understanding of the different mechanism observed. EELS mapping could provide confirmation on the internalisation of SGO inside the cells. EDX mapping or fluorescent imaging could be done to identify the number of EPS produced under different media. Some other technique such SIMS (Secondary Ion Mass Spectroscopy) could provide detailed analysis on the interaction of GO with the membrane and whether it is truly penetrating the membrane. Raman mapping coupled with confocal microscope could provide a much faster way to detect internalisation of GO or other 2DNMs inside the cells and also used to differentiate cells of different species to study real soil sample where there would various bacteria mixed.

In-situ imaging techniques such as Cryo-EM and High-speed AFM can also elucidate the exact nature of interaction of bacteria and 2DNMs, As mentioned previously, post-exposure processing of nanomaterials with bacteria can potentially lead to artificial observation such as rupturing of membrane. An in-situ imaging process would by-pass the problem encountered in sample preparation for number of biological imaging technique and capture more accurate representation of the interaction. Moreover, for time-

dependent toxicity discussed for GO and also ageing of MoS_2, an in-situ monitoring via imaging would be a powerful technique to complement the findings presented.

It should be noted that traditional protocols that assess the risk of materials towards environment were often developed during the times where nanomaterials did not exist. Therefore, together with every other research area, where steps are taken to adapt and improve the process or procedure to better control the quality of manufacture and use of 2DNMs, routine testing procedures and environmental protocol too should be adapted to provide a better understanding of the safety of the emerging material.

References

1. A. K. Geim, K. S. Novoselov, The rise of graphene. *Nature materials* **6**, 183 (2007).

2. D. McManus *et al.*, Water-based and biocompatible 2D crystal inks for all-inkjet-printed heterostructures. *Nature nanotechnology* **12**, 343 (2017).

3. P. K. Kannan, D. J. Late, H. Morgan, C. S. Rout, Recent developments in 2D layered inorganic nanomaterials for sensing. *Nanoscale* **7**, 13293-13312 (2015).

4. Z. Wang *et al.*, Biological and environmental interactions of emerging two-dimensional nanomaterials. *Chemical Society Reviews* **45**, 1750-1780 (2016).

5. Y. Zhan, Z. Liu, S. Najmaei, P. M. Ajayan, J. Lou, Large-area vapor-phase growth and characterization of MoS2 atomic layers on a SiO2 substrate. *Small* **8**, 966-971 (2012).

6. S. Bae *et al.*, Roll-to-roll production of 30-inch graphene films for transparent electrodes. *Nature nanotechnology* **5**, 574 (2010).

7. D. Dumcenco *et al.*, Large-area epitaxial monolayer MoS2. *ACS nano* **9**, 4611-4620 (2015).

8. T. Ohta, A. Bostwick, T. Seyller, K. Horn, E. Rotenberg, Controlling the electronic structure of bilayer graphene. *Science* **313**, 951-954 (2006).

9. J. N. Coleman *et al.*, Two-dimensional nanosheets produced by liquid exfoliation of layered materials. *Science* **331**, 568-571 (2011).

10. Y. Hernandez *et al.*, High-yield production of graphene by liquid-phase exfoliation of graphite. *Nature nanotechnology* **3**, 563 (2008).

11. M. Fojtů, W. Z. Teo, M. Pumera, Environmental impact and potential health risks of 2D nanomaterials. *Environmental Science: Nano* **4**, 1617-1633 (2017).

12. A. Malakar, S. R. Kanel, C. Ray, D. D. Snow, M. N. Nadagouda, Nanomaterials in the environment, human exposure pathway, and health effects: A review. *Science of the Total Environment* **759**, 143470 (2021).

13. S. E. Lowe, Y. L. Zhong, Challenges of Industrial-Scale Graphene Oxide Production. *Graphene Oxide: Fundamentals and Applications*, 410 (2016).

14. M. Segal, Selling graphene by the ton. *Nature nanotechnology* **4**, 612 (2009).

15. A. Zurutuza, C. Marinelli, Challenges and opportunities in graphene commercialization. *Nature nanotechnology* **9**, 730 (2014).

16. A. Dowling *et al.* (London, UK: Royal Academy of Engineering, 2004).

17. F. Gottschalk, T. Sonderer, R. W. Scholz, B. Nowack, Modeled environmental concentrations of engineered nanomaterials (TiO2, ZnO, Ag, CNT, fullerenes) for different regions. *Environmental science & technology* **43**, 9216-9222 (2009).

18. K. S. Novoselov *et al.*, Electric field effect in atomically thin carbon films. *science* **306**, 666-669 (2004).

19. S. Iijima, Helical microtubules of graphitic carbon. *nature* **354**, 56 (1991).

20. S. Iijima, T. Ichihashi, Single-shell carbon nanotubes of 1-nm diameter. *nature* **363**, 603 (1993).

21. A. A. Keller, A. Lazareva, Predicted releases of engineered nanomaterials: from global to regional to local. *Environmental Science & Technology Letters* **1**, 65-70 (2013).

22. A. A. Keller, S. McFerran, A. Lazareva, S. Suh, Global life cycle releases of engineered nanomaterials. *Journal of Nanoparticle Research* **15**, 1692 (2013).

23. F. Gottschalk, T. Sun, B. Nowack, Environmental concentrations of engineered nanomaterials: review of modeling and analytical studies. *Environmental Pollution* **181**, 287-300 (2013).

24. D. Chen, H. Feng, J. Li, Graphene oxide: preparation, functionalization, and electrochemical applications. *Chemical reviews* **112**, 6027-6053 (2012).

25. B. R. Coleman, T. Knight, V. Gies, Z. J. Jakubek, S. Zou, Manipulation and quantification of graphene oxide flake size: Photoluminescence and cytotoxicity. *ACS applied materials & interfaces* **9**, 28911-28921 (2017).

26. T. S. Miller *et al.*, Single crystal, luminescent carbon nitride nanosheets formed by spontaneous dissolution. *Nano letters* **17**, 5891-5896 (2017).

27. B. Domi *et al.*, Fate assessment of commercial 2D MoS2 aqueous dispersions at physicochemical and toxicological level. *Nanotechnology* **31**, 445101 (2020).

28. D. Gonzalez-Carter *et al.*, Quantification of blood–brain barrier transport and neuronal toxicity of unlabelled multiwalled carbon nanotubes as a function of surface charge. *Nanoscale* **11**, 22054-22069 (2019).

29. R. C. Murdock, L. Braydich-Stolle, A. M. Schrand, J. J. Schlager, S. M. Hussain, Characterization of nanomaterial dispersion in solution prior to in vitro exposure using dynamic light scattering technique. *Toxicological sciences* **101**, 239-253 (2008).

30. M. Lotya, A. Rakovich, J. F. Donegan, J. N. Coleman, Measuring the lateral size of liquid-exfoliated nanosheets with dynamic light scattering. *Nanotechnology* **24**, 265703 (2013).

31. S. Badaire, P. Poulin, M. Maugey, C. Zakri, In situ measurements of nanotube dimensions in suspensions by depolarized dynamic light scattering. *Langmuir* **20**, 10367-10370 (2004).

32. D. J. Morgan, X-ray photoelectron spectroscopy (xps): an introduction. *Cardiff Catalysis Institute, School of Chemistry, Cardiff University, Cardiff*, (2014).

33. K. Krishnamoorthy, M. Veerapandian, K. Yun, S.-J. Kim, The chemical and structural analysis of graphene oxide with different degrees of oxidation. *Carbon* **53**, 38-49 (2013).

34. N. Rubio *et al.*, Effect of graphene flake size on functionalisation: quantifying reaction extent and imaging locus with single Pt atom tags. *Chemical science* **12**, 14907-14919 (2021).

35. A. J. Clancy, H. Au, N. Rubio, G. O. Coulter, M. S. Shaffer, Understanding and controlling the covalent functionalisation of graphene. *Dalton Transactions* **49**, 10308-10318 (2020).

36. X. Zhang, F. Jia, B. Yang, S. Song, Oxidation of molybdenum disulfide sheet in water under in situ atomic force microscopy observation. *The Journal of Physical Chemistry C* **121**, 9938-9943 (2017).

37. A. C. Ferrari, D. M. Basko, Raman spectroscopy as a versatile tool for studying the properties of graphene. *Nature nanotechnology* **8**, 235-246 (2013).

38. K. Erickson *et al.*, Determination of the local chemical structure of graphene oxide and reduced graphene oxide. *Advanced Materials* **22**, 4467-4472 (2010).

39. K. A. Mkhoyan *et al.*, Atomic and electronic structure of graphene-oxide. *Nano letters* **9**, 1058-1063 (2009).

40. Y. Cheng *et al.*, Origin of the phase transition in lithiated molybdenum disulfide. *ACS nano* **8**, 11447-11453 (2014).

41. S. Chen *et al.*, Aqueous cationic, anionic and non-ionic multi-walled carbon nanotubes, functionalised with minimal framework damage, for biomedical application. *Biomaterials* **35**, 4729-4738 (2014).

42. A. E. Porter *et al.*, Uptake of noncytotoxic acid-treated single-walled carbon nanotubes into the cytoplasm of human macrophage cells. *Acs Nano* **3**, 1485-1492 (2009).

43. A. M. Schrand, J. J. Schlager, L. Dai, S. M. Hussain, Preparation of cells for assessing ultrastructural localization of nanoparticles with transmission electron microscopy. *Nature protocols* **5**, 744-757 (2010).

44. P. Kovalakova *et al.*, Occurrence and toxicity of antibiotics in the aquatic environment: A review. *Chemosphere* **251**, 126351 (2020).

45. B. S. B. E. ISO, Water quality–Pseudomonas putida growth inhibition test (Pseudomonas cell multiplication inhibition test). (1995).

46. M. Matzke, K. Jurkschat, T. Backhaus, Toxicity of differently sized and coated silver nanoparticles to the bacterium Pseudomonas putida: risks for the aquatic environment? *Ecotoxicology* **23**, 818-829 (2014).

47. C. L. Schultz *et al.*, Aging reduces the toxicity of pristine but not sulphidised silver nanoparticles to soil bacteria. *Environmental Science: Nano* **5**, 2618-2630 (2018).

48. A. Winding, J. J. Modrzyński, J. H. Christensen, K. K. Brandt, P. Mayer, Soil bacteria and protists show different sensitivity to polycyclic aromatic hydrocarbons at controlled chemical activity. *FEMS Microbiology Letters* **366**, fnz214 (2019).

49. K. K. Brandt *et al.*, Ecotoxicological assessment of antibiotics: a call for improved consideration of microorganisms. *Environment International* **85**, 189-205 (2015).

50. D. Labeda, K.-C. Liu, L. Casida Jr, Colonization of soil by Arthrobacter and Pseudomonas under varying conditions of water and nutrient availability as studied by plate counts and transmission electron microscopy. *Applied and Environmental Microbiology* **31**, 551-561 (1976).

51. J. Fabrega, S. R. Fawcett, J. C. Renshaw, J. R. Lead, Silver nanoparticle impact on bacterial growth: effect of pH, concentration, and organic matter. *Environmental science & technology* **43**, 7285-7290 (2009).

52. J. Fabrega, J. C. Renshaw, J. R. Lead, Interactions of silver nanoparticles with Pseudomonas putida biofilms. *Environmental science & technology* **43**, 9004-9009 (2009).

53. X. Chen *et al.*, Tolerance and biosorption of copper and zinc by Pseudomonas putida CZ1 isolated from metal-polluted soil. *Canadian journal of microbiology* **52**, 308-316 (2006).

54. A. Bianco *et al.* (Elsevier, 2013).

55. K. S. Novoselov *et al.*, A roadmap for graphene. *Nature* **490**, 192 (2012).

56. D. Li, M. B. Müller, S. Gilje, R. B. Kaner, G. G. Wallace, Processable aqueous dispersions of graphene nanosheets. *Nature nanotechnology* **3**, 101 (2008).

57. W. Ren, H.-M. Cheng, The global growth of graphene. *Nature nanotechnology* **9**, 726 (2014).

58. K. R. Paton *et al.*, Scalable production of large quantities of defect-free few-layer graphene by shear exfoliation in liquids. *Nature materials* **13**, 624 (2014).

59. L. M. Viculis, J. J. Mack, O. M. Mayer, H. T. Hahn, R. B. Kaner, Intercalation and exfoliation routes to graphite nanoplatelets. *Journal of Materials Chemistry* **15**, 974-978 (2005).

60. A. C. Ferrari *et al.*, Science and technology roadmap for graphene, related two-dimensional crystals, and hybrid systems. *Nanoscale* **7**, 4598-4810 (2015).

61. H. J. Yoon, J. H. Yang, Z. Zhou, S. S. Yang, M. M.-C. Cheng, Carbon dioxide gas sensor using a graphene sheet. *Sensors and Actuators B: Chemical* **157**, 310-313 (2011).

62. K. H. Kim, Y. Oh, M. Islam, Graphene coating makes carbon nanotube aerogels superelastic and resistant to fatigue. *Nature nanotechnology* **7**, 562 (2012).

63. S. Garaj *et al.*, Graphene as a subnanometre trans-electrode membrane. *Nature* **467**, 190 (2010).

64. N. I. Kovtyukhova *et al.*, Layer-by-layer assembly of ultrathin composite films from micron-sized graphite oxide sheets and polycations. *Chemistry of materials* **11**, 771-778 (1999).

65. W. S. Hummers Jr, R. E. Offeman, Preparation of graphitic oxide. *Journal of the american chemical society* **80**, 1339-1339 (1958).

66. K. Fu *et al.*, Graphene oxide-based electrode inks for 3D-printed lithium-ion batteries. *Advanced materials* **28**, 2587-2594 (2016).

67. V. Dua *et al.*, All-organic vapor sensor using inkjet-printed reduced graphene oxide. *Angewandte Chemie* **122**, 2200-2203 (2010).

68. Y. Singhbabu *et al.*, Efficient anti-corrosive coating of cold-rolled steel in a seawater environment using an oil-based graphene oxide ink. *Nanoscale* **7**, 8035-8047 (2015).

69. W. Gao, in *Graphene oxide*. (Springer, 2015), pp. 61-95.

70. G. Eda, M. Chhowalla, Chemically derived graphene oxide: towards large-area thin-film electronics and optoelectronics. *Advanced materials* **22**, 2392-2415 (2010).

71. S. Chen, J. Zhu, X. Wu, Q. Han, X. Wang, Graphene oxide− MnO2 nanocomposites for supercapacitors. *ACS nano* **4**, 2822-2830 (2010).

72. H. Y. Jeong *et al.*, Graphene oxide thin films for flexible nonvolatile memory applications. *Nano letters* **10**, 4381-4386 (2010).

73. U. Khan, P. May, A. O'Neill, J. N. Coleman, Development of stiff, strong, yet tough composites by the addition of solvent exfoliated graphene to polyurethane. *Carbon* **48**, 4035-4041 (2010).

74. K. Krishnamoorthy, R. Mohan, S.-J. Kim, Graphene oxide as a photocatalytic material. *Applied Physics Letters* **98**, 244101 (2011).

75. Y. Song, K. Qu, C. Zhao, J. Ren, X. Qu, Graphene oxide: intrinsic peroxidase catalytic activity and its application to glucose detection. *Advanced Materials* **22**, 2206-2210 (2010).

76. S. Shukla, S. Saxena, Spectroscopic investigation of confinement effects on optical properties of graphene oxide. *Applied Physics Letters* **98**, 073104 (2011).

77. S. Stankovich *et al.*, Synthesis of graphene-based nanosheets via chemical reduction of exfoliated graphite oxide. *carbon* **45**, 1558-1565 (2007).

78. W. Chen, L. Yan, P. R. Bangal, Preparation of graphene by the rapid and mild thermal reduction of graphene oxide induced by microwaves. *Carbon* **48**, 1146-1152 (2010).

79. Y. Zhu *et al.*, Exfoliation of graphite oxide in propylene carbonate and thermal reduction of the resulting graphene oxide platelets. *ACS nano* **4**, 1227-1233 (2010).

80. X. Zhou *et al.*, Photo-Fenton reaction of graphene oxide: a new strategy to prepare graphene quantum dots for DNA cleavage. *ACS nano* **6**, 6592-6599 (2012).

81. E. C. Salas, Z. Sun, A. Lüttge, J. M. Tour, Reduction of graphene oxide via bacterial respiration. *ACS nano* **4**, 4852-4856 (2010).

82. S. Park, R. S. Ruoff, Chemical methods for the production of graphenes. *Nature nanotechnology* **4**, 217 (2009).

83. X.-Y. Wang, A. Narita, K. Müllen, Precision synthesis versus bulk-scale fabrication of graphenes. *Nature Reviews Chemistry* **2**, 0100 (2017).

84. Z. Yin, C. Cui, H. Chen, X. Yu, W. Qian, The application of carbon nanotube/graphene-based nanomaterials in wastewater treatment. *Small* **16**, 1902301 (2020).

85. A. Khan *et al.*, The role of graphene oxide and graphene oxide-based nanomaterials in the removal of pharmaceuticals from aqueous media: a review. *Environmental Science and Pollution Research* **24**, 7938-7958 (2017).

86. Y. Zhao, Y. Liu, X. Zhang, W. Liao, Environmental transformation of graphene oxide in the aquatic environment. *Chemosphere* **262**, 127885 (2021).

87. A. Rhazouani *et al.*, Synthesis and toxicity of graphene oxide nanoparticles: A literature review of in vitro and in vivo studies. *BioMed Research International* **2021**, (2021).

88. O. N. Ruiz *et al.*, Graphene oxide: a nonspecific enhancer of cellular growth. *ACS nano* **5**, 8100-8107 (2011).

89. G.-Y. Chen, D.-P. Pang, S.-M. Hwang, H.-Y. Tuan, Y.-C. Hu, A graphene-based platform for induced pluripotent stem cells culture and differentiation. *Biomaterials* **33**, 418-427 (2012).

90. Y. Chang *et al.*, In vitro toxicity evaluation of graphene oxide on A549 cells. *Toxicology letters* **200**, 201-210 (2011).

91. S. Mittal *et al.*, Physico-chemical properties based differential toxicity of graphene oxide/reduced graphene oxide in human lung cells mediated through oxidative stress. *Scientific reports* **6**, 1-16 (2016).

92. K.-H. Liao, Y.-S. Lin, C. W. Macosko, C. L. Haynes, Cytotoxicity of graphene oxide and graphene in human erythrocytes and skin fibroblasts. *ACS applied materials & interfaces* **3**, 2607-2615 (2011).

93. X. Guo *et al.*, Organic electrochemical transistor for in situ detection of H2O2 released from adherent cells and its application in evaluating the in vitro cytotoxicity of nanomaterial. *Analytical Chemistry* **92**, 908-915 (2019).

94. E. Puigpelat, J. Ignés-Mullol, F. Sagués, R. Reigada, Interaction of graphene nanoparticles and lipid membranes displaying different liquid orderings: a molecular dynamics study. *Langmuir* **35**, 16661-16668 (2019).

95. A. B. Seabra, A. J. Paula, R. de Lima, O. L. Alves, N. Durán, Nanotoxicity of graphene and graphene oxide. *Chemical research in toxicology* **27**, 159-168 (2014).

96. V. C. Sanchez, A. Jachak, R. H. Hurt, A. B. Kane, Biological interactions of graphene-family nanomaterials: an interdisciplinary review. *Chemical research in toxicology* **25**, 15-34 (2012).

97. H. Yue *et al.*, The role of the lateral dimension of graphene oxide in the regulation of cellular responses. *Biomaterials* **33**, 4013-4021 (2012).

98. A. Wang *et al.*, Role of surface charge and oxidative stress in cytotoxicity and genotoxicity of graphene oxide towards human lung fibroblast cells. *Journal of Applied Toxicology* **33**, 1156-1164 (2013).

99. J. Ma *et al.*, Crucial role of lateral size for graphene oxide in activating macrophages and stimulating pro-inflammatory responses in cells and animals. *Acs Nano* **9**, 10498-10515 (2015).

100. Q. Mu *et al.*, Size-dependent cell uptake of protein-coated graphene oxide nanosheets. *ACS applied materials & interfaces* **4**, 2259-2266 (2012).

101. M. Xu *et al.*, Improved in vitro and in vivo biocompatibility of graphene oxide through surface modification: poly (acrylic acid)-functionalization is superior to PEGylation. *Acs Nano* **10**, 3267-3281 (2016).

102. X. Zou, L. Zhang, Z. Wang, Y. Luo, Mechanisms of the antimicrobial activities of graphene materials. *Journal of the american chemical society* **138**, 2064-2077 (2016).

103. E. P. Nguyen, C. d. C. C. Silva, A. Merkoçi, Recent advancement in biomedical applications on the surface of two-dimensional materials: from biosensing to tissue engineering. *Nanoscale* **12**, 19043-19067 (2020).

104. V. Palmieri *et al.*, The graphene oxide contradictory effects against human pathogens. *Nanotechnology* **28**, 152001 (2017).

105. T. Seifi, A. R. Kamali, Anti-pathogenic activity of graphene nanomaterials: A review. *Colloids and Surfaces B: Biointerfaces* **199**, 111509 (2021).

106. T. Pulingam, K. L. Thong, J. N. Appaturi, C. W. Lai, B. F. Leo, Mechanistic actions and contributing factors affecting the antibacterial property and cytotoxicity of graphene oxide. *Chemosphere* **281**, 130739 (2021).

107. J. Chen, X. Wang, H. Han, A new function of graphene oxide emerges: inactivating phytopathogenic bacterium Xanthomonas oryzae pv. Oryzae. *Journal of nanoparticle research* **15**, 1658 (2013).

108. Y. L. F. Musico, C. M. Santos, M. L. P. Dalida, D. F. Rodrigues, Surface modification of membrane filters using graphene and graphene oxide-based nanomaterials for bacterial inactivation and removal. *ACS Sustainable Chemistry & Engineering* **2**, 1559-1565 (2014).

109. X. Wang, X. Liu, H. J. C. a. S. B. B. Han, Evaluation of antibacterial effects of carbon nanomaterials against copper-resistant Ralstonia solanacearum. **103**, 136-142 (2013).

110. S. Gurunathan, J. W. Han, V. Eppakayala, J.-H. Kim, Microbial reduction of graphene oxide by Escherichia coli: a green chemistry approach. *Colloids and Surfaces B: Biointerfaces* **102**, 772-777 (2013).

111. S. Gurunathan, J. W. Han, A. A. Dayem, V. Eppakayala, J.-H. Kim, Oxidative stress-mediated antibacterial activity of graphene oxide and reduced graphene oxide in Pseudomonas aeruginosa. *International journal of nanomedicine* **7**, 5901 (2012).

112. Q. Mei, Z. Zhang, Photoluminescent graphene oxide ink to print sensors onto microporous membranes for versatile visualization bioassays. *Angewandte Chemie International Edition* **51**, 5602-5606 (2012).

113. F. Perreault, A. F. De Faria, S. Nejati, M. Elimelech, Antimicrobial properties of graphene oxide nanosheets: why size matters. *ACS nano* **9**, 7226-7236 (2015).

114. O. Akhavan, E. Ghaderi, Toxicity of graphene and graphene oxide nanowalls against bacteria. *ACS nano* **4**, 5731-5736 (2010).

115. H.-q. Chen *et al.*, Graphene oxide as an anaerobic membrane scaffold for the enhancement of B. adolescentis proliferation and antagonistic effects against pathogens E. coli and S. aureus. *Nanotechnology* **25**, 165101 (2014).

116. T. H. Nguyen, M. Lin, A. Mustapha, Toxicity of graphene oxide on intestinal bacteria and Caco-2 cells. *Journal of Food Protection* **78**, 996-1002 (2015).

117. I. Barbolina *et al.*, Purity of graphene oxide determines its antibacterial activity. *2D Materials* **3**, 025025 (2016).

118. J. Campos-Delgado *et al.*, Effect of graphene oxide on bacteria and peripheral blood mononuclear cells. *Journal of Applied Biomaterials & Functional Materials* **14**, 423-430 (2016).

119. L. Hui *et al.*, Availability of the basal planes of graphene oxide determines whether it is antibacterial. *ACS applied materials & interfaces* **6**, 13183-13190 (2014).

120. S. Liu *et al.*, Lateral dimension-dependent antibacterial activity of graphene oxide sheets. *Langmuir* **28**, 12364-12372 (2012).

121. V. Palmieri *et al.*, Bacteria meet graphene: modulation of graphene oxide nanosheet interaction with human pathogens for effective antimicrobial therapy. *ACS Biomaterials Science & Engineering* **3**, 619-627 (2017).

122. L. Wu *et al.*, Aggregation kinetics of graphene oxides in aqueous solutions: experiments, mechanisms, and modeling. *Langmuir* **29**, 15174-15181 (2013).

123. J. Zhao, Z. Wang, J. C. White, B. Xing, Graphene in the aquatic environment: adsorption, dispersion, toxicity and transformation. *Environmental science & technology* **48**, 9995-10009 (2014).

124. Y. Luo *et al.*, Functionalized graphene oxide in microbial engineering: An effective stimulator for bacterial growth. *Carbon* **103**, 172-180 (2016).

125. J. He *et al.*, Killing dental pathogens using antibacterial graphene oxide. *ACS applied materials & interfaces* **7**, 5605-5611 (2015).

126. S. S. Nanda, S. S. A. An, D. K. Yi, Oxidative stress and antibacterial properties of a graphene oxide-cystamine nanohybrid. *International journal of nanomedicine* **10**, 549 (2015).

127. H. E. Karahan *et al.*, Bacterial physiology is a key modulator of the antibacterial activity of graphene oxide. *Nanoscale* **8**, 17181-17189 (2016).

128. M. Veerapandian, L. Zhang, K. Krishnamoorthy, K. Yun, Surface activation of graphene oxide nanosheets by ultraviolet irradiation for highly efficient anti-bacterials. *Nanotechnology* **24**, 395706 (2013).

129. K. Krishnamoorthy, M. Veerapandian, L.-H. Zhang, K. Yun, S. J. Kim, Antibacterial efficiency of graphene nanosheets against pathogenic bacteria via lipid peroxidation. *The journal of physical chemistry C* **116**, 17280-17287 (2012).

130. W. Hu *et al.*, Graphene-based antibacterial paper. *ACS nano* **4**, 4317-4323 (2010).

131. T. Pulingam *et al.*, Graphene oxide exhibits differential mechanistic action towards Gram-positive and Gram-negative bacteria. *Colloids and Surfaces B: Biointerfaces* **181**, 6-15 (2019).

132. I. E. M. Carpio, C. M. Santos, X. Wei, D. F. Rodrigues, Toxicity of a polymer–graphene oxide composite against bacterial planktonic cells, biofilms, and mammalian cells. *Nanoscale* **4**, 4746-4756 (2012).

133. K. Krishnamoorthy, N. Umasuthan, R. Mohan, J. Lee, S.-J. Kim, Antibacterial activity of graphene oxide nanosheets. *Science of Advanced Materials* **4**, 1111-1117 (2012).

134. O. Akhavan, E. Ghaderi, A. J. T. J. o. P. C. B. Esfandiar, Wrapping bacteria by graphene nanosheets for isolation from environment, reactivation by sonication, and inactivation by near-infrared irradiation. **115**, 6279-6288 (2011).

135. M. Dallavalle, M. Calvaresi, A. Bottoni, M. Melle-Franco, F. Zerbetto, Graphene can wreak havoc with cell membranes. *ACS applied materials & interfaces* **7**, 4406-4414 (2015).

136. Y. Tu *et al.*, Destructive extraction of phospholipids from Escherichia coli membranes by graphene nanosheets. **8**, 594 (2013).

137. C.-H. Yu *et al.*, Understanding the sheet size-antibacterial activity relationship of graphene oxide and the nano-bio interaction-based physical mechanisms. *Colloids and Surfaces B: Biointerfaces* **191**, 111009 (2020).

138. J. Mao, R. Guo, L.-T. Yan, Simulation and analysis of cellular internalization pathways and membrane perturbation for graphene nanosheets. *Biomaterials* **35**, 6069-6077 (2014).

139. X. Liu *et al.*, Antioxidant deactivation on graphenic nanocarbon surfaces. **7**, 2775-2785 (2011).

140. S. Liu *et al.*, Antibacterial activity of graphite, graphite oxide, graphene oxide, and reduced graphene oxide: membrane and oxidative stress. *ACS nano* **5**, 6971-6980 (2011).

141. A. Sharma *et al.*, Structural, electronic structure and antibacterial properties of graphene-oxide nano-sheets. *Chemical Physics Letters* **698**, 85-92 (2018).

142. R. Combarros, S. Collado, M. Díaz, Toxicity of graphene oxide on growth and metabolism of Pseudomonas putida. *Journal of hazardous materials* **310**, 246-252 (2016).

143. A. Yilihamu *et al.*, Interaction between graphene oxide and nitrogen-fixing bacterium Azotobacter chroococcum: Transformation, toxicity and nitrogen fixation. *Carbon* **160**, 5-13 (2020).

144. J. Du, X. Hu, Q. Zhou, Graphene oxide regulates the bacterial community and exhibits property changes in soil. *Rsc Advances* **5**, 27009-27017 (2015).

145. S. Gurunathan, Cytotoxicity of graphene oxide nanoparticles on plant growth promoting rhizobacteria. *Journal of Industrial and Engineering Chemistry* **32**, 282-291 (2015).

146. W.-C. Hou *et al.*, The contribution of indirect photolysis to the degradation of graphene oxide in sunlight. *Carbon* **110**, 426-437 (2016).

147. W.-C. Hou, P.-L. Lee, Y.-C. Chou, Y.-S. Wang, Antibacterial property of graphene oxide: the role of phototransformation. *Environmental Science: Nano* **4**, 647-657 (2017).

148. W.-C. Hou *et al.*, Photochemical transformation of graphene oxide in sunlight. *Environmental science & technology* **49**, 3435-3443 (2015).

149. I. Chowdhury, M. C. Duch, N. D. Mansukhani, M. C. Hersam, D. Bouchard, Colloidal properties and stability of graphene oxide nanomaterials in the aquatic environment. *Environmental science & technology* **47**, 6288-6296 (2013).

150. G. Wang, F. Qian, C. W. Saltikov, Y. Jiao, Y. Li, Microbial reduction of graphene oxide by Shewanella. *Nano Research* **4**, 563-570 (2011).

151. S. Fogden, R. Verdejo, B. Cottam, M. Shaffer, Purification of single walled carbon nanotubes: The problem with oxidation debris. *Chemical Physics Letters* **460**, 162-167 (2008).

152. J. P. Rourke *et al.*, The real graphene oxide revealed: stripping the oxidative debris from the graphene-like sheets. *Angewandte Chemie* **123**, 3231-3235 (2011).

153. E. Aliyev *et al.*, Structural characterization of graphene oxide: Surface functional groups and fractionated oxidative debris. *Nanomaterials* **9**, 1180 (2019).

154. A. F. Faria, F. o. Perreault, M. Elimelech, Elucidating the Role of Oxidative Debris in the Antimicrobial Properties of Graphene Oxide. *ACS Applied Nano Materials* **1**, 1164-1174 (2018).

155. K. Pulskamp, S. Diabaté, H. F. Krug, Carbon nanotubes show no sign of acute toxicity but induce intracellular reactive oxygen species in dependence on contaminants. *Toxicology letters* **168**, 58-74 (2007).

156. W. Norwood, U. Borgmann, D. Dixon, Chronic toxicity of arsenic, cobalt, chromium and manganese to Hyalella azteca in relation to exposure and bioaccumulation. *Environmental Pollution* **147**, 262-272 (2007).

157. A. Lerf, H. He, M. Forster, J. Klinowski, Structure of graphite oxide revisited. *The Journal of Physical Chemistry B* **102**, 4477-4482 (1998).

158. R. Muzyka, S. Drewniak, T. Pustelny, M. Sajdak, Ł. Drewniak, Characterization of graphite oxide and reduced graphene oxide obtained from different graphite precursors and oxidized by different methods using Raman spectroscopy statistical analysis. *Materials* **14**, 769 (2021).

159. I. Childres, L. A. Jauregui, W. Park, H. Cao, Y. P. Chen, Raman spectroscopy of graphene and related materials. *New developments in photon and materials research* **1**, 1-20 (2013).

160. P. Wick *et al.*, Classification framework for graphene-based materials. *Angewandte Chemie International Edition* **53**, 7714-7718 (2014).

161. A. Kovtun *et al.*, Accurate chemical analysis of oxygenated graphene-based materials using X-ray photoelectron spectroscopy. *Carbon* **143**, 268-275 (2019).

162. A. Kumar, C. K. Dixit, in *Advances in nanomedicine for the delivery of therapeutic nucleic acids*. (Elsevier, 2017), pp. 43-58.

163. A. M. Dimiev, L. B. Alemany, J. M. Tour, Graphene oxide. Origin of acidity, its instability in water, and a new dynamic structural model. *ACS nano* **7**, 576-588 (2013).

164. B. Konkena, S. Vasudevan, Understanding aqueous dispersibility of graphene oxide and reduced graphene oxide through p K a measurements. *The journal of physical chemistry letters* **3**, 867-872 (2012).

165. C.-J. Shih, S. Lin, R. Sharma, M. S. Strano, D. Blankschtein, Understanding the pH-dependent behavior of graphene oxide aqueous solutions: a comparative experimental and molecular dynamics simulation study. *Langmuir* **28**, 235-241 (2012).

166. I. Martin-Gullon, J. M. Pérez, D. Domene, A. J. Salgado-Casanova, L. R. Radovic, New insights into oxygen surface coverage and the resulting two-component structure of graphene oxide. *Carbon* **158**, 406-417 (2020).

167. Q. Bao, D. Zhang, P. Qi, Synthesis and characterization of silver nanoparticle and graphene oxide nanosheet composites as a bactericidal agent for water disinfection. *Journal of colloid and interface science* **360**, 463-470 (2011).

168. M. A. Buccheri *et al.*, Modification of graphene oxide by laser irradiation: a new route to enhance antibacterial activity. *Nanotechnology* **27**, 245704 (2016).

169. A. Gogoi, T. J. Konch, K. Raidongia, K. A. Reddy, Water and salt dynamics in multilayer graphene oxide (GO) membrane: role of lateral sheet dimensions. *Journal of Membrane Science*, (2018).

170. X. Lin *et al.*, Fabrication of highly-aligned, conductive, and strong graphene papers using ultralarge graphene oxide sheets. *ACS nano* **6**, 10708-10719 (2012).

171. X. Sun *et al.*, Nano-graphene oxide for cellular imaging and drug delivery. *Nano research* **1**, 203-212 (2008).

172. E. Bidram *et al.*, Fractionation of graphene oxide single nano-sheets in water-glycerol solutions using gradient centrifugation. *Carbon* **103**, 363-371 (2016).

173. K. E. Lee *et al.*, Liquid crystal size selection of large-size graphene oxide for size-dependent N-doping and oxygen reduction catalysis. *Acs Nano* **8**, 9073-9080 (2014).

174. H. Geng *et al.*, Size Fractionation of Graphene Oxide Nanosheets via Controlled Directional Freezing. *Journal of the American Chemical Society* **139**, 12517-12523 (2017).

175. X. Wang, H. Bai, G. Shi, Size fractionation of graphene oxide sheets by pH-assisted selective sedimentation. *Journal of the American Chemical Society* **133**, 6338-6342 (2011).

176. W. Zhang *et al.*, Size fractionation of graphene oxide sheets by the polar solvent-selective natural deposition method. *Rsc Advances* **5**, 146-152 (2015).

177. S. Kim, J. Lee, S.-S. Lee, Fractionation of graphene oxides by size-selective adhesion with spherical particles. *Macromolecular Research* **24**, 1098-1104 (2016).

178. J. Chen *et al.*, Synthesis of graphene oxide sheets with controlled sizes from sieved graphite flakes. *Carbon* **110**, 34-40 (2016).

179. F. Lin, X. Tong, Y. Wang, J. Bao, Z. M. Wang, Graphene oxide liquid crystals: synthesis, phase transition, rheological property, and applications in optoelectronics and display. *Nanoscale research letters* **10**, 435 (2015).

180. X. Zhang, Q. Zhou, W. Zou, X. Hu, Molecular mechanisms of developmental toxicity induced by graphene oxide at predicted environmental concentrations. *Environmental science & technology* **51**, 7861-7871 (2017).

181. Y. Wang *et al.*, Two-dimensional nanomaterials with engineered bandgap: Synthesis, properties, applications. *Nano Today* **37**, 101059 (2021).

182. D. Gupta, V. Chauhan, R. Kumar, A comprehensive review on synthesis and applications of molybdenum disulfide (MoS2) material: Past and recent developments. *Inorg. Chem. Commun* **121**, 108200 (2020).

183. Y. Venkata Subbaiah, K. Saji, A. Tiwari, Atomically thin MoS2: A versatile nongraphene 2D material. *Advanced Functional Materials* **26**, 2046-2069 (2016).

184. W. O. Winer, Molybdenum disulfide as a lubricant: a review of the fundamental knowledge. *Wear* **10**, 422-452 (1967).

185. Z. Wang, B. Mi, Environmental applications of 2D molybdenum disulfide (MoS2) nanosheets. *Environmental science & technology* **51**, 8229-8244 (2017).

186. K. Chang *et al.*, Targeted synthesis of 2H-and 1T-phase MoS2 monolayers for catalytic hydrogen evolution. *Advanced Materials* **28**, 10033-10041 (2016).

187. S. S. Chou *et al.*, Controlling the metal to semiconductor transition of MoS2 and WS2 in solution. *Journal of the American Chemical Society* **137**, 1742-1745 (2015).

188. G. Eda *et al.*, Photoluminescence from chemically exfoliated MoS2. *Nano letters* **11**, 5111-5116 (2011).

189. D. Voiry *et al.*, Enhanced catalytic activity in strained chemically exfoliated WS 2 nanosheets for hydrogen evolution. *Nature materials* **12**, 850-855 (2013).

190. Y. H. Lee *et al.*, Synthesis of large-area MoS2 atomic layers with chemical vapor deposition. *Advanced materials* **24**, 2320-2325 (2012).

191. Y. Shi, H. Li, L.-J. Li, Recent advances in controlled synthesis of two-dimensional transition metal dichalcogenides via vapour deposition techniques. *Chemical Society Reviews* **44**, 2744-2756 (2015).

192. J. Xie *et al.*, Defect-rich MoS2 ultrathin nanosheets with additional active edge sites for enhanced electrocatalytic hydrogen evolution. *Advanced materials* **25**, 5807-5813 (2013).

193. D. Xu *et al.*, Microwave-assisted 1T to 2H phase reversion of MoS2 in solution: a fast route to processable dispersions of 2H-MoS2 nanosheets and nanocomposites. *Nanotechnology* **27**, 385604 (2016).

194. M. Miseljic, S. I. Olsen, Life-cycle assessment of engineered nanomaterials: a literature review of assessment status. *Journal of nanoparticle research* **16**, 1-33 (2014).

195. K. Ai, C. Ruan, M. Shen, L. Lu, MoS2 nanosheets with widened interlayer spacing for high-efficiency removal of mercury in aquatic systems. *Advanced Functional Materials* **26**, 5542-5549 (2016).

196. H. J. Song, S. You, X. H. Jia, J. Yang, MoS2 nanosheets decorated with magnetic Fe3O4 nanoparticles and their ultrafast adsorption for wastewater treatment. *Ceramics International* **41**, 13896-13902 (2015).

197. X. Wang *et al.*, High supercapacitor and adsorption behaviors of flower-like MoS 2 nanostructures. *Journal of Materials Chemistry A* **2**, 15958-15963 (2014).

198. X. Gao, X. Wang, X. Ouyang, C. Wen, Flexible superhydrophobic and superoleophilic MoS 2 sponge for highly efficient oil-water separation. *Scientific reports* **6**, 1-8 (2016).

199. T. Thurston, J. Wilcoxon, Photooxidation of organic chemicals catalyzed by nanoscale MoS2. *The Journal of Physical Chemistry B* **103**, 11-17 (1999).

200. A. Midya, A. Ghorai, S. Mukherjee, R. Maiti, S. K. Ray, Hydrothermal growth of few layer 2H-MoS 2 for heterojunction photodetector and visible light induced photocatalytic applications. *Journal of Materials Chemistry A* **4**, 4534-4543 (2016).

201. M. R. Hoffmann, S. T. Martin, W. Choi, D. W. Bahnemann, Environmental applications of semiconductor photocatalysis. *Chemical reviews* **95**, 69-96 (1995).

202. W. Li, Y. Yang, J. K. Weber, G. Zhang, R. Zhou, Tunable, strain-controlled nanoporous MoS2 filter for water desalination. *ACS nano* **10**, 1829-1835 (2016).

203. L. Sun, H. Huang, X. Peng, Laminar MoS 2 membranes for molecule separation. *Chemical communications* **49**, 10718-10720 (2013).

204. S. Jiang, R. Cheng, R. Ng, Y. Huang, X. Duan, Highly sensitive detection of mercury (II) ions with few-layer molybdenum disulfide. *Nano Research* **8**, 257-262 (2015).

205. H. Li *et al.*, Fabrication of single-and multilayer MoS2 film-based field-effect transistors for sensing NO at room temperature. *small* **8**, 63-67 (2012).

206. X. Yang *et al.*, Antibacterial activity of two-dimensional MoS 2 sheets. *Nanoscale* **6**, 10126-10133 (2014).

207. S. Pandit, S. Karunakaran, S. K. Boda, B. Basu, M. De, High antibacterial activity of functionalized chemically exfoliated MoS2. *ACS applied materials & interfaces* **8**, 31567-31573 (2016).

208. N. Wu *et al.*, Investigating the influence of MoS2 nanosheets on E. coli from metabolomics level. *PloS one* **11**, e0167245 (2016).

209. G. V. Lowry, K. B. Gregory, S. C. Apte, J. R. Lead. (ACS Publications, 2012).

210. Z. Wang, A. Von Dem Bussche, P. K. Kabadi, A. B. Kane, R. H. Hurt, Biological and environmental transformations of copper-based nanomaterials. *ACS nano* **7**, 8715-8727 (2013).

211. T. Du *et al.*, Photochlorination-induced transformation of graphene oxide: Mechanism and environmental fate. *Water research* **124**, 372-380 (2017).

212. G. S. Simate, S. Ndlovu, Acid mine drainage: Challenges and opportunities. *Journal of Environmental Chemical Engineering* **2**, 1785-1803 (2014).

213. M. Cao *et al.*, Molybdenum derived from nanomaterials incorporates into molybdenum enzymes and affects their activities in vivo. *Nature Nanotechnology* **16**, 708-716 (2021).

214. Z. Wang *et al.*, Chemical dissolution pathways of MoS2 nanosheets in biological and environmental media. *Environmental science & technology* **50**, 7208-7217 (2016).

215. X. Wang *et al.*, Differences in the toxicological potential of 2D versus aggregated molybdenum disulfide in the lung. *Small* **11**, 5079-5087 (2015).

216. M. Bae *et al.*, Nanotoxicity of 2D Molybdenum Disulfide, MoS2, Nanosheets on Beneficial Soil Bacteria, Bacillus cereus and Pseudomonas aeruginosa. *Nanomaterials* **11**, 1453 (2021).

217. W. Z. Teo, E. L. K. Chng, Z. Sofer, M. Pumera, Cytotoxicity of exfoliated transition-metal dichalcogenides (MoS2, WS2, and WSe2) is lower than that of graphene and its analogues. *Chemistry–A European Journal* **20**, 9627-9632 (2014).

218. C. Moore *et al.*, Industrial grade 2D molybdenum disulphide (MoS2): an in vitro exploration of the impact on cellular uptake, cytotoxicity, and inflammation. *2D Materials* **4**, 025065 (2017).

219. Y. Li, D. Boraschi, Endotoxin contamination: a key element in the interpretation of nanosafety studies. *Nanomedicine* **11**, 269-287 (2016).

220. A. Murali, G. Lokhande, K. A. Deo, A. Brokesh, A. K. Gaharwar, Emerging 2D nanomaterials for biomedical applications. *Materials Today* **50**, 276-302 (2021).

221. J. Zheng *et al.*, Post-graphene 2D materials-based antimicrobial agents: focus on fabrication strategies and biosafety assessments. *Journal of Materials Science* **55**, 7226-7246 (2020).

222. H. Miao, Z. Teng, C. Wang, H. Chong, G. Wang, Recent Progress in Two-Dimensional Antimicrobial Nanomaterials. *Chemistry–A European Journal* **25**, 929-944 (2019).

223. T. I. Kim, J. Kim, I.-J. Park, K.-O. Cho, S.-Y. Choi, Chemically exfoliated 1T-phase transition metal dichalcogenide nanosheets for transparent antibacterial applications. *2D Materials* **6**, 025025 (2019).

224. T. I. Kim *et al.*, Antibacterial activities of graphene oxide–molybdenum disulfide nanocomposite films. *ACS applied materials & interfaces* **9**, 7908-7917 (2017).

225. R. Wu *et al.*, Membrane destruction and phospholipid extraction by using two-dimensional MoS 2 nanosheets. *Nanoscale* **10**, 20162-20170 (2018).

226. J. Kaur *et al.*, Biological interactions of biocompatible and water-dispersed MoS 2 nanosheets with bacteria and human cells. *Scientific reports* **8**, 1-15 (2018).

227. R. Ye, W. Song, X. Ou, Z. Gu, D. Zhang, Membrane Insertion of MoS2 Nanosheets: Fresh vs. Aged. *Frontiers in chemistry* **9**, 499 (2021).

228. C. E. Taylor, S. D. Garvey, J. E. Pemberton, Carbon contamination at silver surfaces: surface preparation procedures evaluated by Raman spectroscopy and X-ray photoelectron spectroscopy. *Analytical chemistry* **68**, 2401-2408 (1996).

229. U. Krishnan, M. Kaur, K. Singh, M. Kumar, A. Kumar, A synoptic review of MoS2: Synthesis to applications. *Superlattices and Microstructures* **128**, 274-297 (2019).

230. W. Zou, Q. Zhou, X. Zhang, X. Hu, Environmental transformations and algal toxicity of single-layer molybdenum disulfide regulated by humic acid. *Environmental science & technology* **52**, 2638-2648 (2018).

231. D. Voiry *et al.*, Covalent functionalization of monolayered transition metal dichalcogenides by phase engineering. *Nature chemistry* **7**, 45-49 (2015).

232. J. Bellenger, T. Wichard, A. Kustka, A. Kraepiel, Uptake of molybdenum and vanadium by a nitrogen-fixing soil bacterium using siderophores. *Nature Geoscience* **1**, 243-246 (2008).

233. Y. Li, Q. Jin, D. Yang, J. Cui, Molybdenum sulfide induce growth enhancement effect of rice (Oryza sativa L.) through regulating the synthesis of chlorophyll and the expression of aquaporin gene. *Journal of agricultural and food chemistry* **66**, 4013-4021 (2018).

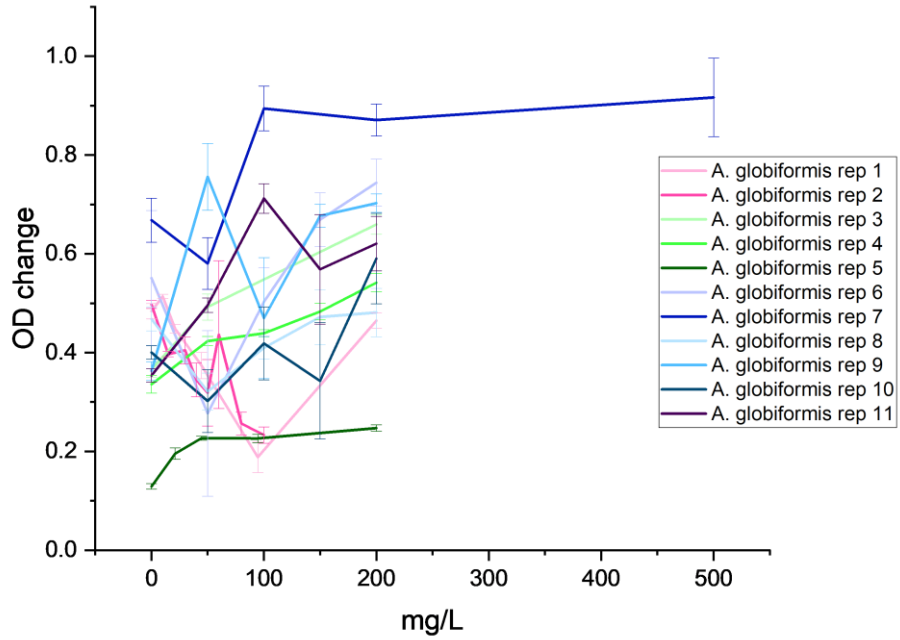
234. K. Koenig, J. R. Andreesen, Molybdenum involvement in aerobic degradation of 2-furoic acid by Pseudomonas putida Fu1. *Applied and environmental microbiology* **55**, 1829-1834 (1989).

235. H. Niewerth *et al.*, Complete genome sequence and metabolic potential of the quinaldine-degrading bacterium Arthrobacter sp. Rue61a. *BMC genomics* **13**, 1-19 (2012).

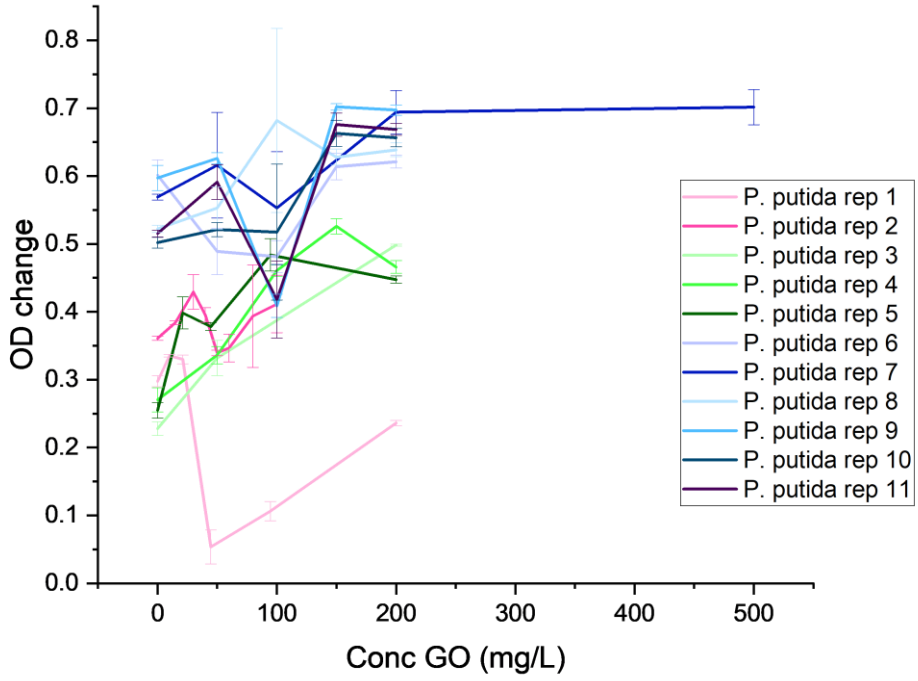
4885

7 Appendix

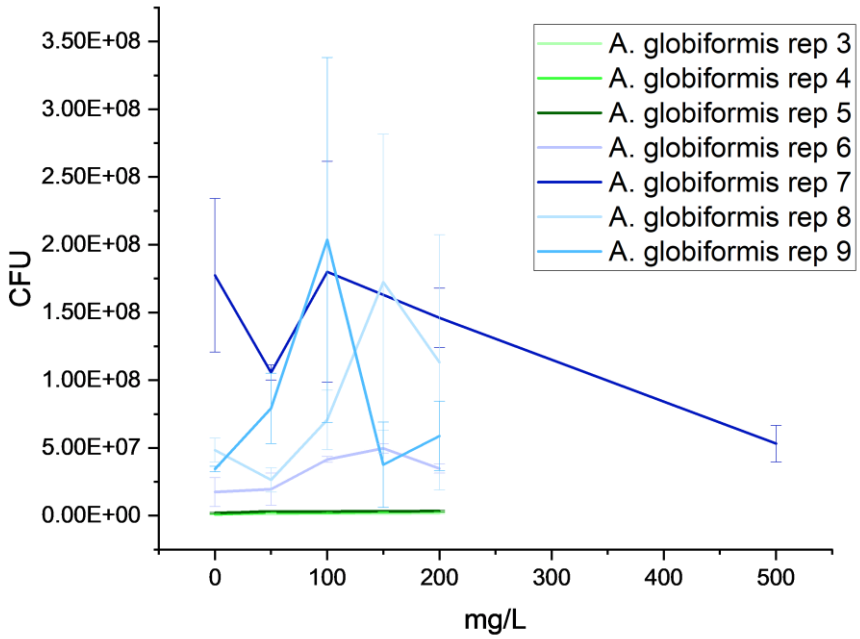
Appendix I: Raw data for repeated ARGO (LGO) measurements (Chapter 2.2)



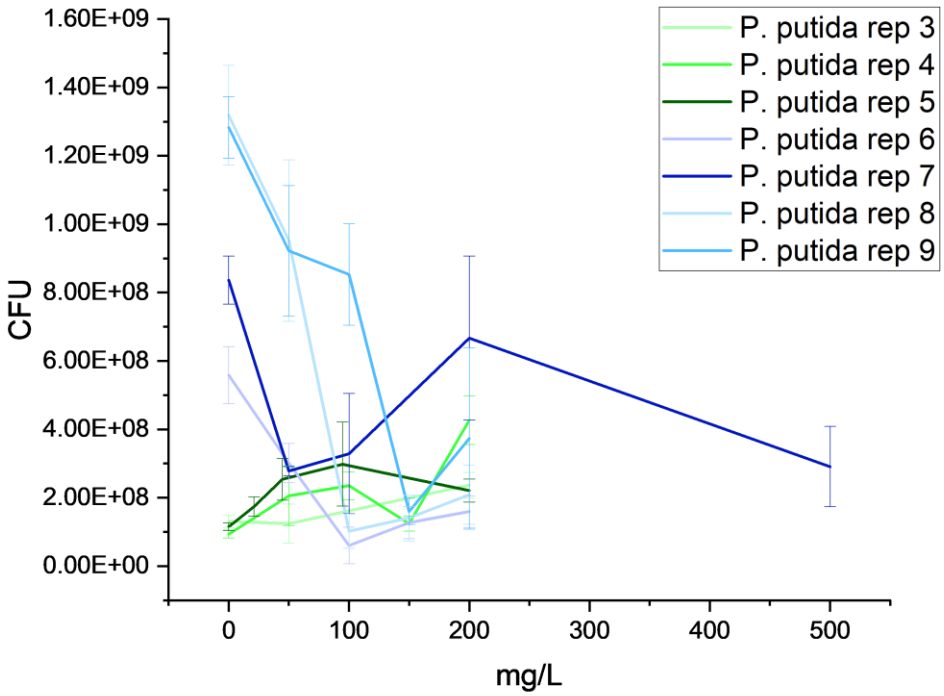
SI Figure I a.) Raw data plot of A. globiformis with GO from ACS material based on OD change results. This was based on 5 replicates for each of the data points with each error bar representing standard error. Each of the samples were run independently from the other. Each shade of colour represents the location and the time frame in which the experiment was carried out. Shade of pink represented experiments carried out at Location 1 in 2019. Shade of green represented experiments carried out at Location 2 in 2020. Shade of blue represented experiments carried out at Location 3 in 2021 and 2022.



SI Figure I b.) Raw data plot of P. putida with GO from ACS material based on OD change results. This was based on 5 replicates for each of the data points with each error bar representing standard error. Each of the samples were run independently of each other. Each shade of colour represents the location and the time frame in which the experiment was carried out. Shade of pink represented experiments carried out at Location 1 in 2019. Shade of green represented experiments carried out at Location 2 in 2020. Shade of blue represented experiments carried out at Location 3 in 2021 and 2022.

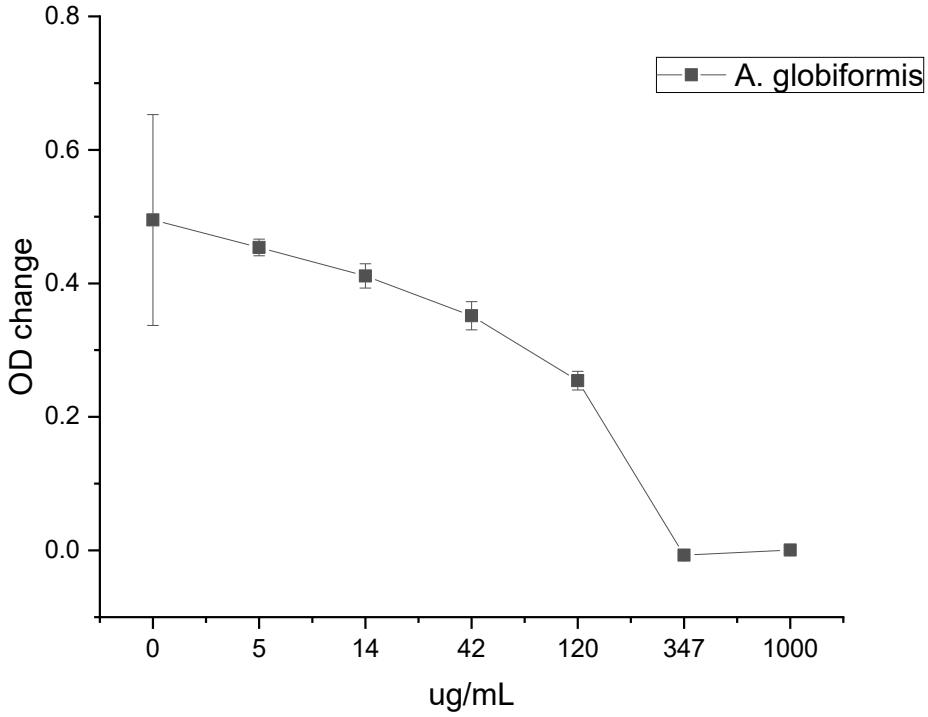


SI Figure I c.) Raw data plot of A. globiformis with GO from ACS material based on CFU results. This was based on 5 replicates for each of the data points with each error bar representing standard error. Each of the samples were run independently from the other. Each shade of colour represents the location and the time frame in which the experiment was carried out. Shade of pink represented experiments carried out at Location 1 in 2019. Shade of green represented experiments carried out at Location 2 in 2020. Shade of blue represented experiments carried out at Location 3 in 2021 and 2022.

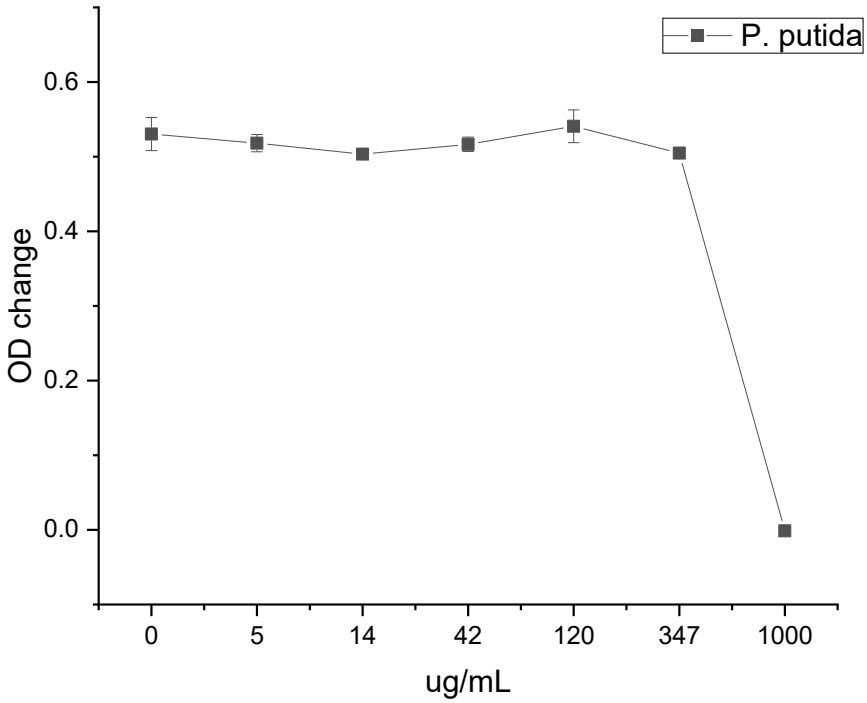


SI Figure I d.) Raw data plot of P. putida with GO from ACS material based on CFU results. This was based on 5 replicates for each of the data points with each error bar representing standard error. Each of the samples were run independently from the other. Each shade of colour represents the location and the time frame in which the experiment was carried out. Shade of pink represented experiments carried out at Location 1 in 2019. Shade of green represented experiments carried out at Location 2 in 2020. Shade of blue represented experiments carried out at Location 3 in 2021 and 2022.

Appendix II: Results from silver nitrate (positive control) (Chapter 2.2)

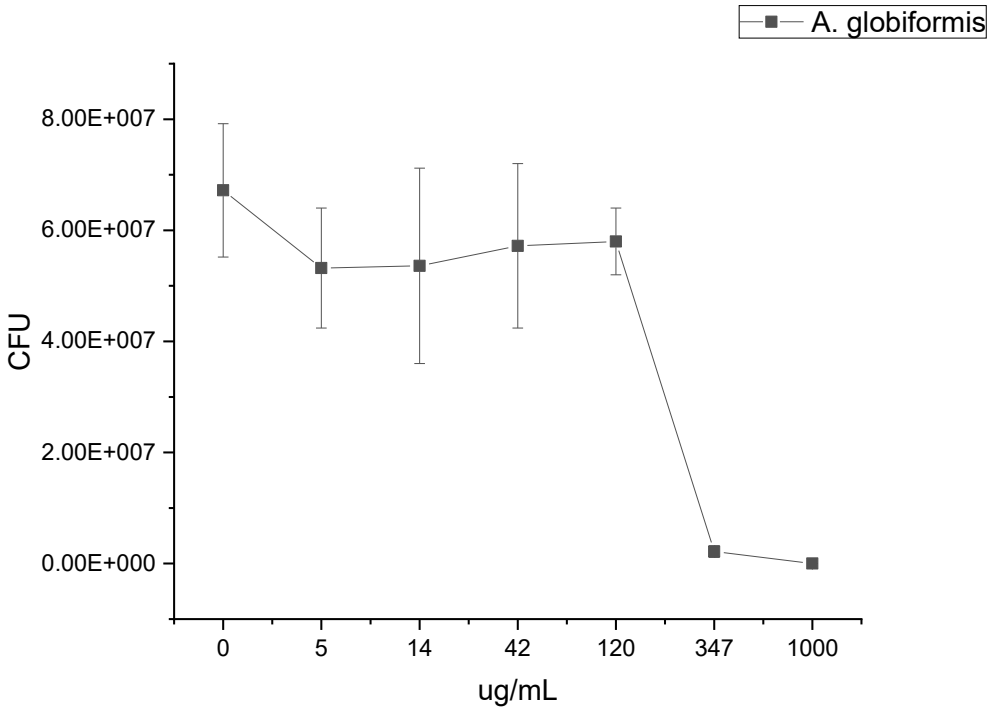


SI Figure II a.) Raw data plot of A. globiformis with silver nitrate based on OD change result. This was based on 5 replicates for each of the data points with each error bar representing standard error.

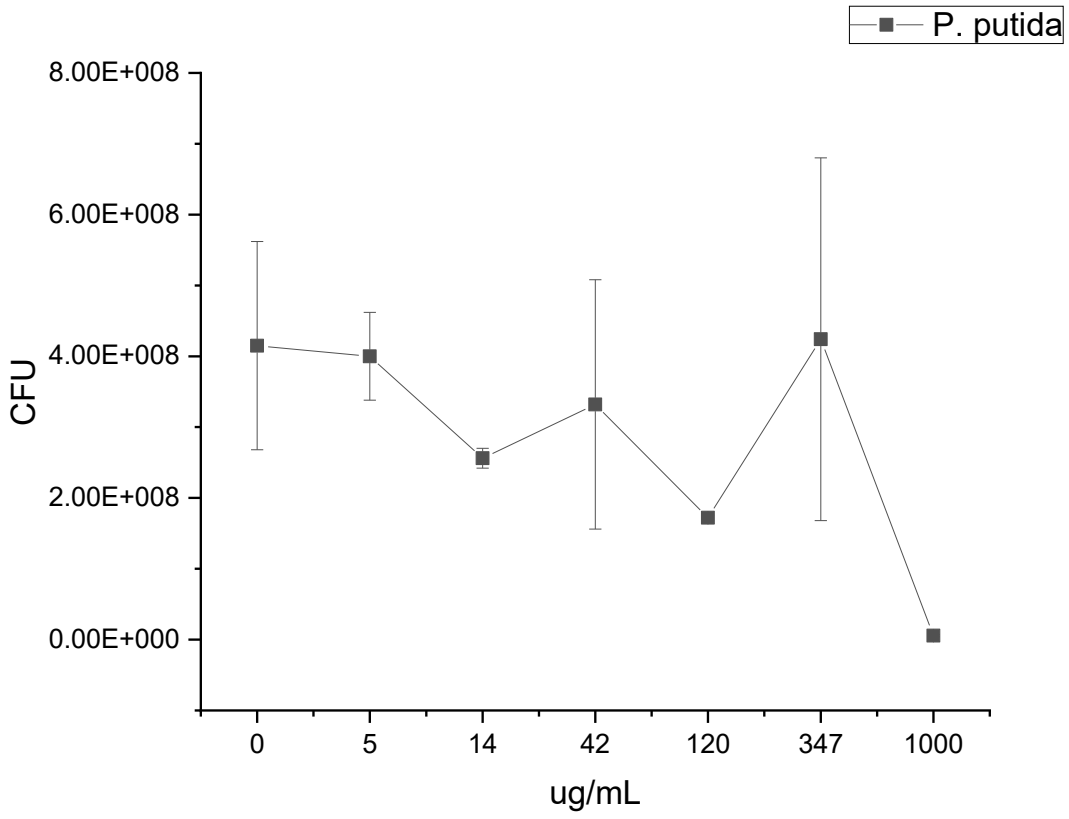


4925

SI Figure II b.) Raw data plot of P. putida with silver nitrate based on OD changes. This was based on 5 replicates for each of the data points with each error bar representing standard error.



SI Figure II c.) Raw data plot of A. globiformis with silver nitrate based on CFU measurements. This was based on 5 replicates for each of the data points with each error bar representing the standard error.



SI Figure II d.) Raw data plot of P. putida with silver nitrate based on CFU result. Toxicity test results of all ISO 10712 runs against P. putida. This was based on 5 replicates for each of the data points with each error bar representing the standard error.

Appendix III: Other nanoparticles with ISO 10712 (Chapter 2.2)

Introduction

One of the steps used to assess the impact of 2DNMs in the environment was to evaluate the suitability of the existing protocol against 2DNMs. The GO test with ISO 10712 resulted in not no growth inhibition. This is contrary to most of the results discussed in the literature review of the GOs that showed that GOs are likely to be an effective antimicrobial towards bacteria. The possible reasons for these contradictory results were identified as follows: a.) due to different bacteria, b.) due to the types of GO, c.) non-optimised experimental parameters. The first reason was unlikely, since the literature discussed covered only a few types of bacteria, as well as other microbes, and most of them which are similar to the two soil bacteria discussed did respond to the presence of GOs. Moreover, the fact that both bacteria were not inhibited indicate other factors are involved. The second possible reason regarding different types of GO was a possibility since there were some discrepancies in terms of the inhibitory concentration from the literature discussed. This was likely to be due to the different physiochemical properties of different GOs which resulted in different degree of interaction. The third reason of non-optimised parameters of the protocol was also a likely reason since the protocol was first developed for non-nanomaterials. In fact, the protocol was developed in 1995 and was described as a test "a test method for determining the inhibitory effect of surface, ground and wastewater on Pseudomonas putida growth. Not suitable for highly coloured samples or samples containing undissolved or volatile substances which react with the nutrient solution or undergo

changes such as biochemical degradation. Also suitable for testing substances soluble in water.".(*45*) This meant that for any new emerging materials such as 2DNMs, the suitability of the test should be evaluated and accounted for.

In order to understand the suitability of the ISO 10712 towards 2DNMs, it was sensible to test other ENMs which were not 2DNMs. This would remove some of the factors unique to 2DNMs such re-stacking as well as wider variety of ENMs to have a deeper understanding of the method. From herein, a brief discussion and literature survey of the ENMs tested other than 2DNMs are discussed. These would include comparative points to the results discussed later which served as validation data.

Silver Nanoparticles

Silver nanoparticles had been used extensively in products for its antimicrobial property in a similar way to its ionic form being an excellent antimicrobial. (*243*) Therefore, the literature volume assessing the effect of silver nanoparticles for their interaction with bacteria, as well as impact on the environment were greater than 2DNMs. (*46, 51, 244-249*) These literature on studies of impact of silver nanoparticles on the environment not only have studied the *in-vitro* interactions, but also their interactions with microbes in soil communities and aquatic communities. On top of that, despite having few mechanisms of action for its antimicrobial activity, the mechanisms had been well explained and systematically studied. (*250-254*) Since the focus of this project was 2DNMs and there were already numbers of comprehensive review on the topic of impact of silver nanoparticles on the environment, extensive literature review regarding silver nanoparticles were not undertaken. However, instead of discussing the general overview of interaction of silver nanoparticles with the environment, two papers published by Centre for Ecology and Hydrology (CEH) were reviewed to draw comparative points as they used ISO 10712 protocol to test the toxicity of silver nanoparticles.

Matzke *et al*. (*46*) published the fundamental part of work regarding the use of ISO 10712 to assess the toxicity of silver nanoparticles. This was by means not the first work studying the interaction of silver nanoparticles with bacteria, but it was the first work to assess the interaction of silver nanoparticles against Pseudomonas species relevant to the environment. Pseudomonas putida (P. putida) is commonly found in soil and surface water and therefore in the ISO 10712 protocol, as the primary species to test. The most notable finding from the results here was the fact that their results did not match with the previously found trends and results. Although there was inconclusive evidence in terms of the mechanism of action by the silver nanoparticles, there was a general understanding in the trend of toxicity with size, shapes, and additional coatings. Because one of the main contributing factors to the toxicity of silver nanoparticles is their ability to release silver ions, any variation causing changes in toxicity could be explained by changes in surface area. For example, smaller silver nanoparticles were shown to have higher toxicity because of their increased surface area leading to higher release rate of silver ions. (*255*) However, this was not observed in the results by Matke *et al*. and indicated that there were more complex interaction occurring within the test. This is similar to the initial findings from the GO study as the results did not match with the current literature landscape. Because ISO 10712 is an environmental assessment tool representative of surface, ground, and wastewater, it may be that these results highlight the need to build more complex toxicity data set using more representative media of the environment.

Schultz *et al*. (*47*) followed up on the work by Matzke and studied the behaviour of pristine and sulphidised silver nanoparticles with ageing against soil bacteria. As well as the gram-negative P. putida bacteria, they have chosen to add another environmentally ubiquitous gram-positive bacterium, Arthrobacter globiformis (A. globiformis), to increase the effectiveness of the test in assessing the environmental impact of the material. Their study tested series of modified silver nanoparticles that were likely to be released into the environment and carried out the toxicity test with ageing and also with addition of Fulvic acid (FA) to

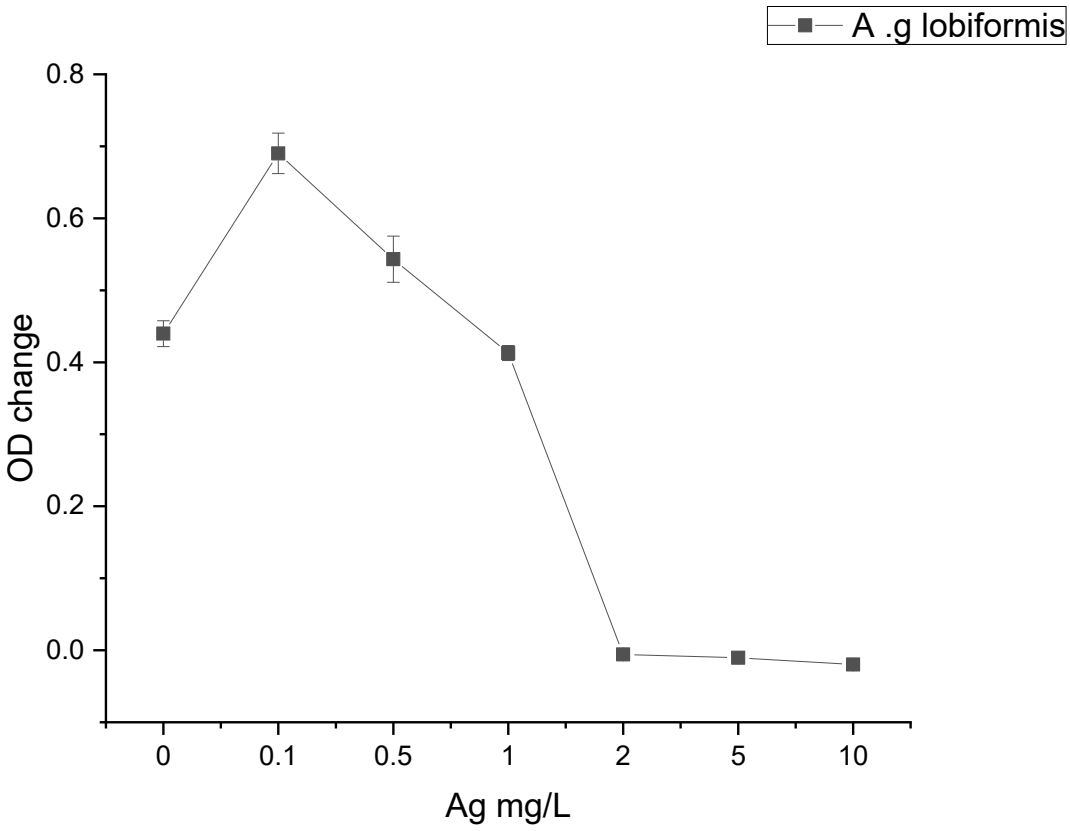
mimic the presence of natural organic matter (NOM). This study was designed to fill the gaps in the knowledge of the impact of silver nanoparticles in the environment by environmentally relevant design. The ageing and the addition of FA led to series of findings where the author highlighted the importance of further understanding the interaction and behaviour of bacteria with the nanoparticles in an environmentally relevant media. It seems that this gap in the knowledge of environmental relevancy is not only present in the 2DNMs, but also for other ENMs.

Titania nanoparticles

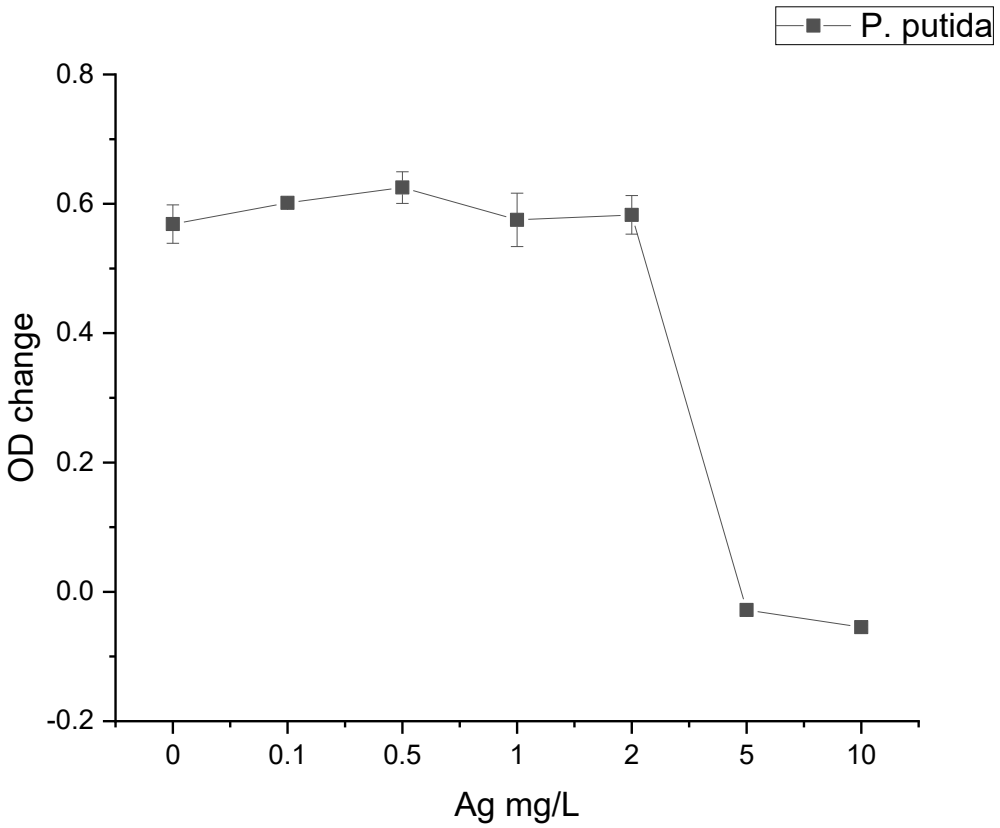
Titania nanoparticles or otherwise known as titanium dioxide nanoparticles are another nanoparticle commonly used and already assessed for its toxicity towards environmentally relevant organisms. Unlike, silver nanoparticles, they are opaque in appearance and therefore used widely for pigments. The nanoparticle was chosen as the next nanoparticle of interest because it was as widely studied as silver nanoparticles, but it was opaque in colour and therefore were expected to present challenges in colorimetric measurement method.

Unfortunately there was no literature available on titania nanoparticles with ISO 10712 but Combarros *et al*. (*256*) showed that titania were toxic to P. putida culture simulated industrial wastewater. Titania nanoparticles are photoactive meaning that only in the presence of light, they would be antimicrobial. (*257*) Combarros *et al*. used flow cytometry to assess the effectiveness of titania nanoparticle in environmentally relevant wastewater and showed that in the presence of light, titania nanoparticles could inhibit the bacteria completely at 500 mg L^{-1}.

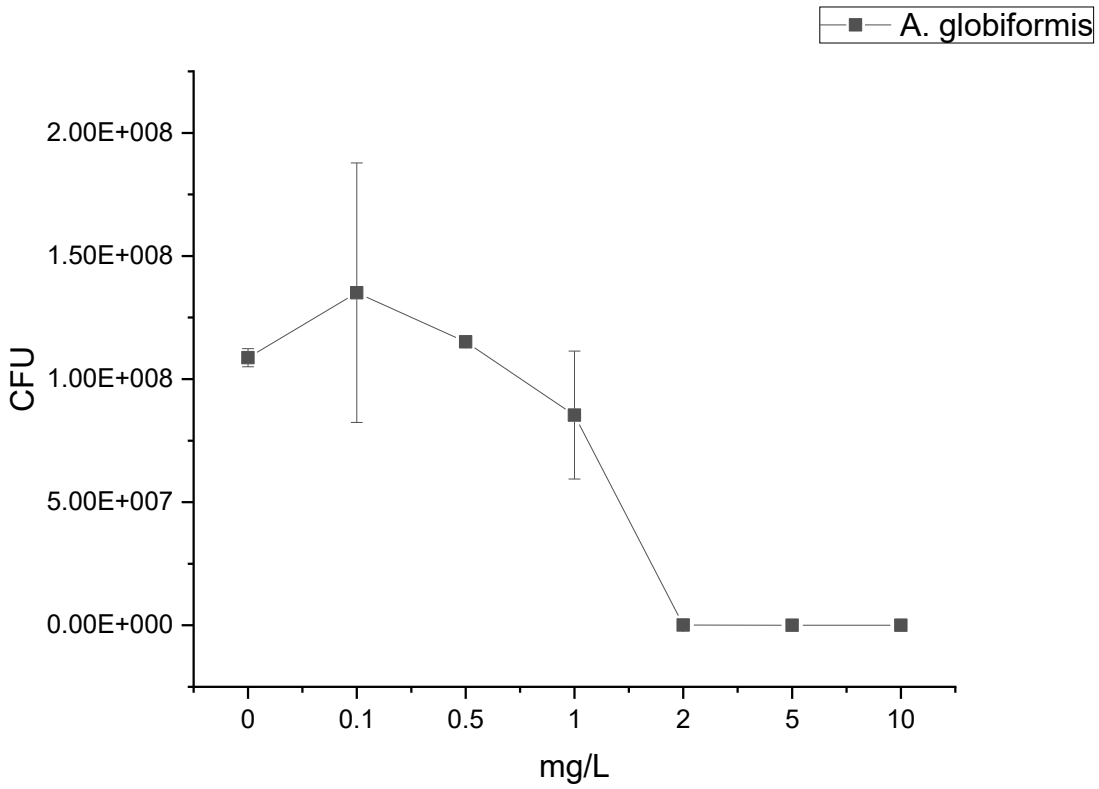
Results with ISO 10712 – silver nanoparticle



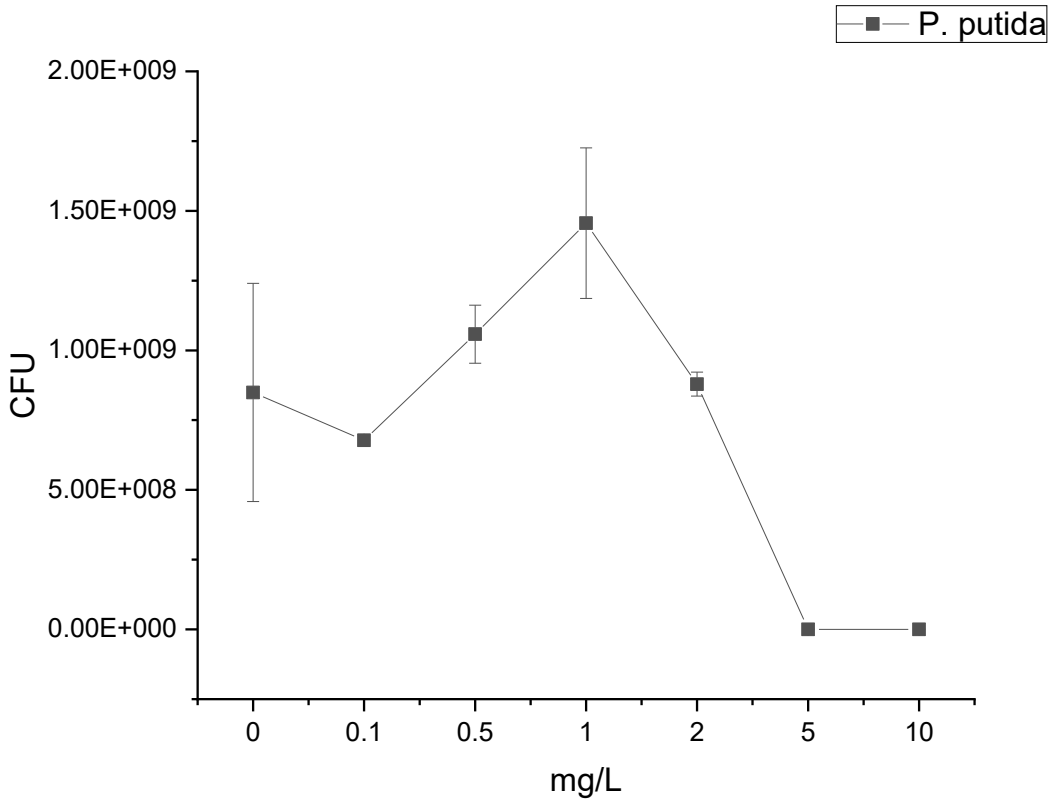
SI Figure III a.) Raw data plot of A. globiformis with silver nanoparticle based on OD changes. This was based on 5 replicates for each of the data points with each error bar representing standard error.



SI Figure III b.) Raw data plot of P. putida with silver nanoparticles based on OD change results. This was based on 5 replicates for each of the data points with each error bar representing the standard error.



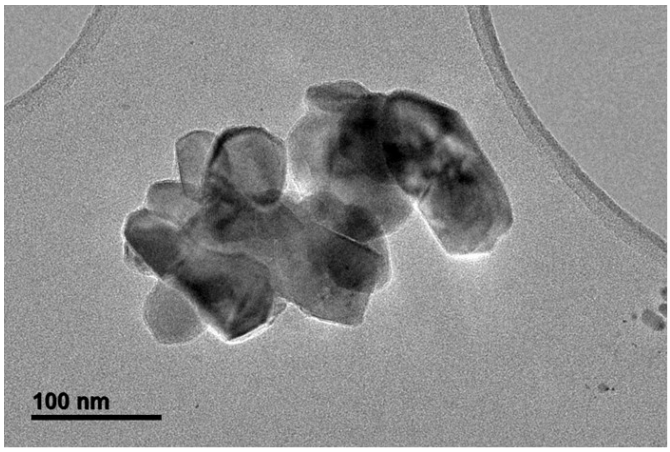
SI Figure III c.) Raw data plot of A. globiformis with silver nanoparticle based on CFU measurements. This was based on 5 replicates for each of the data points with each error bar representing the standard error.

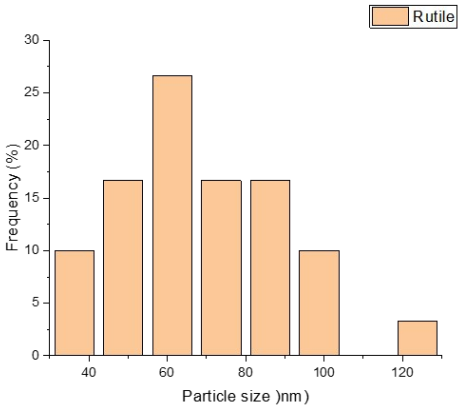


SI Figure III d.) Raw data plot of P. putida with silver nanoparticle based on CFU result. This was based on 5 replicates for each of the data points with each error bar representing the standard error.

5040

Results with ISO 10712 & Characterisation – titania nanoparticles

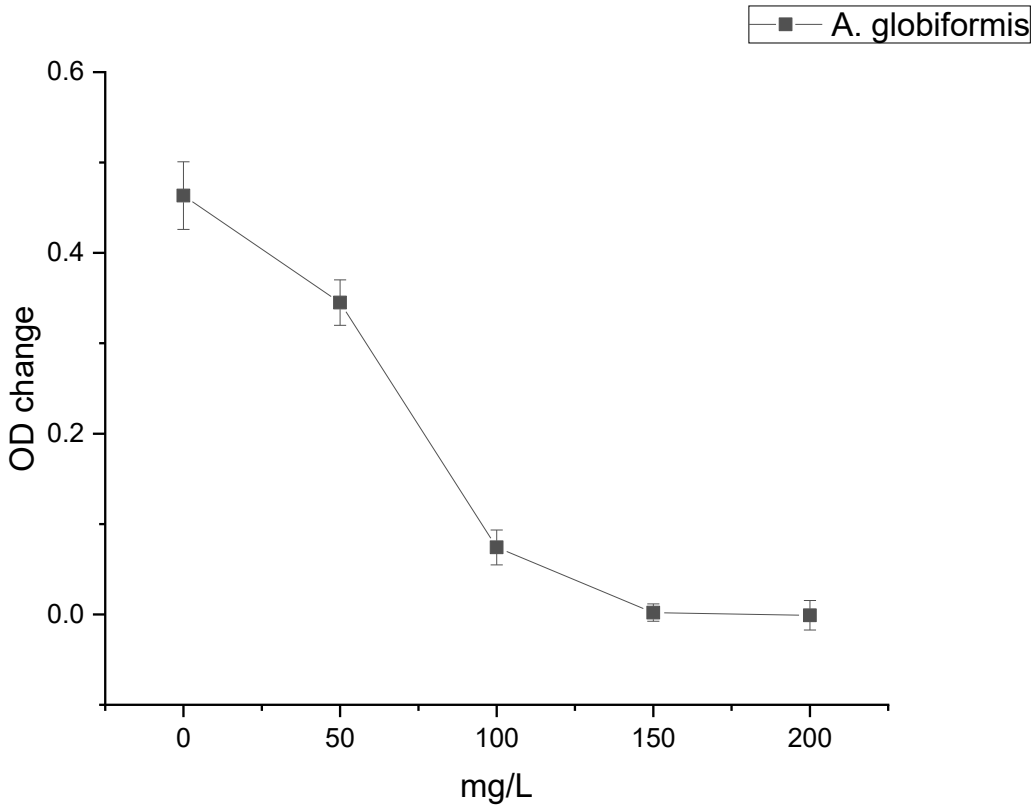




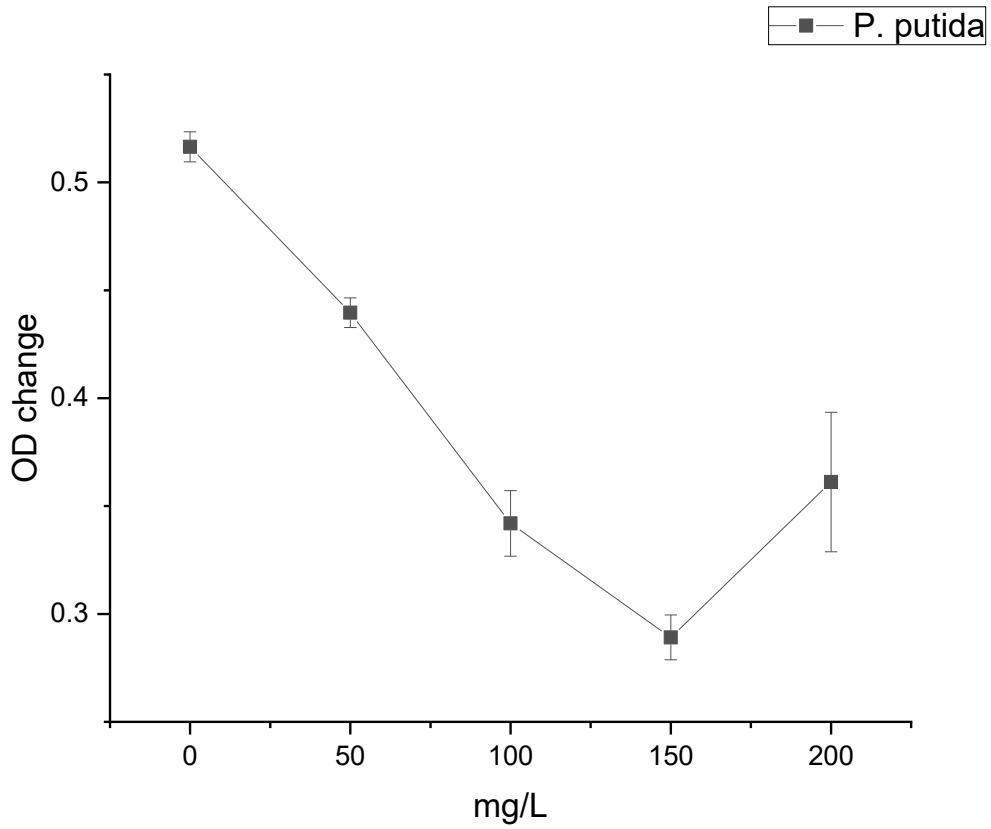
SI Figure III e.) TEM image of rutile titania nanoparticle after 30 seconds of bath sonication on holey carbon grid with size distribution taken from several TEM images. Mean = 68.26, SD = 21.19, N = 30.

	Primary peak position in nm (percentage of total intensity)	**Z-average (nm)**	**PDI**	**Zeta (mV)**
Rutile As-received	784.0±161.7 (20.6±%)	690.5±140.2	0.67±0.14	-34.2±1.4
Rutile After 30s Bath sonication	367.5±34.6 (47.8±%)	355.0±13.8	0.303±0.03	-38.2±0.3

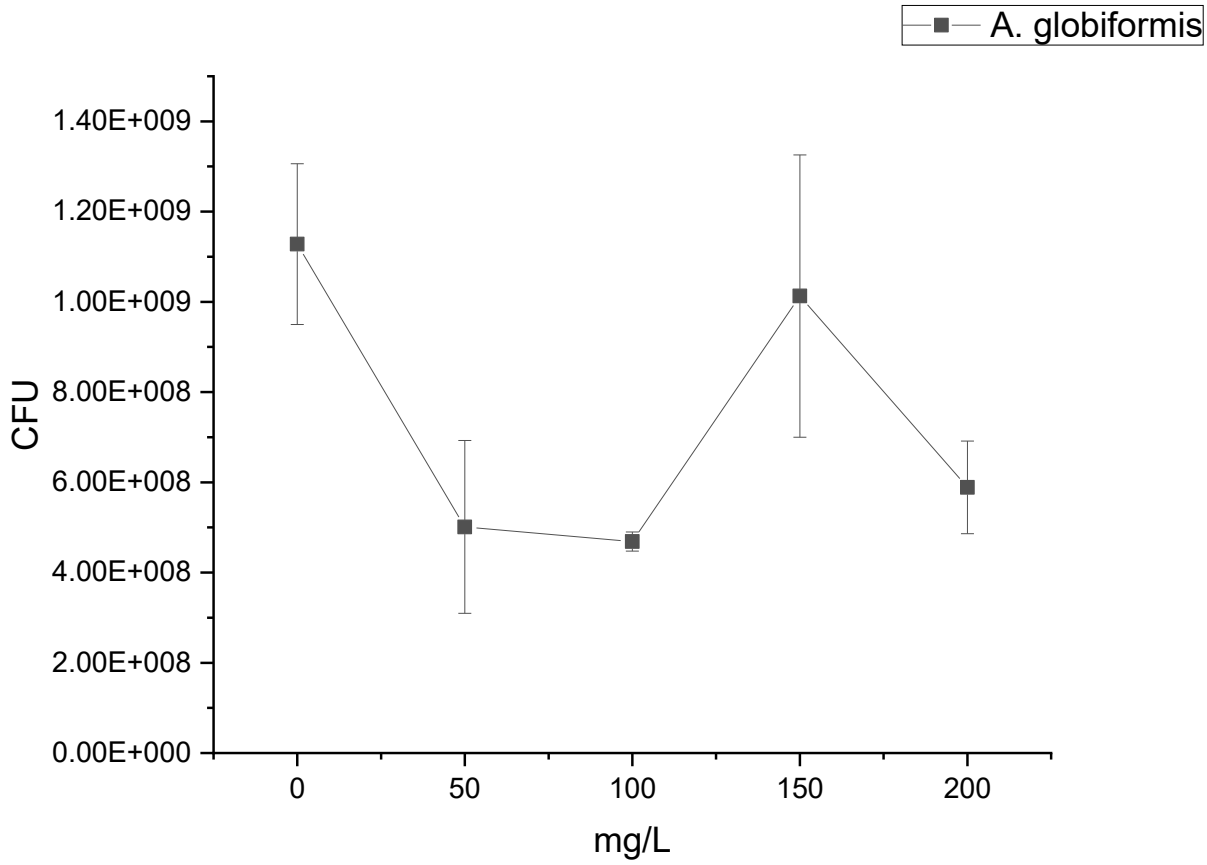
SI Figure III f.) TEM image of rutile titania nanoparticle with size distribution taken from several TEM images. Mean = 68.26, SD = 21.19, N = 30.



SI Figure III g.) Raw data plot of A. globiformis with titania nanoparticle based on OD change result. This was based on 5 replicates for each of the data points with each error bar representing the standard error.

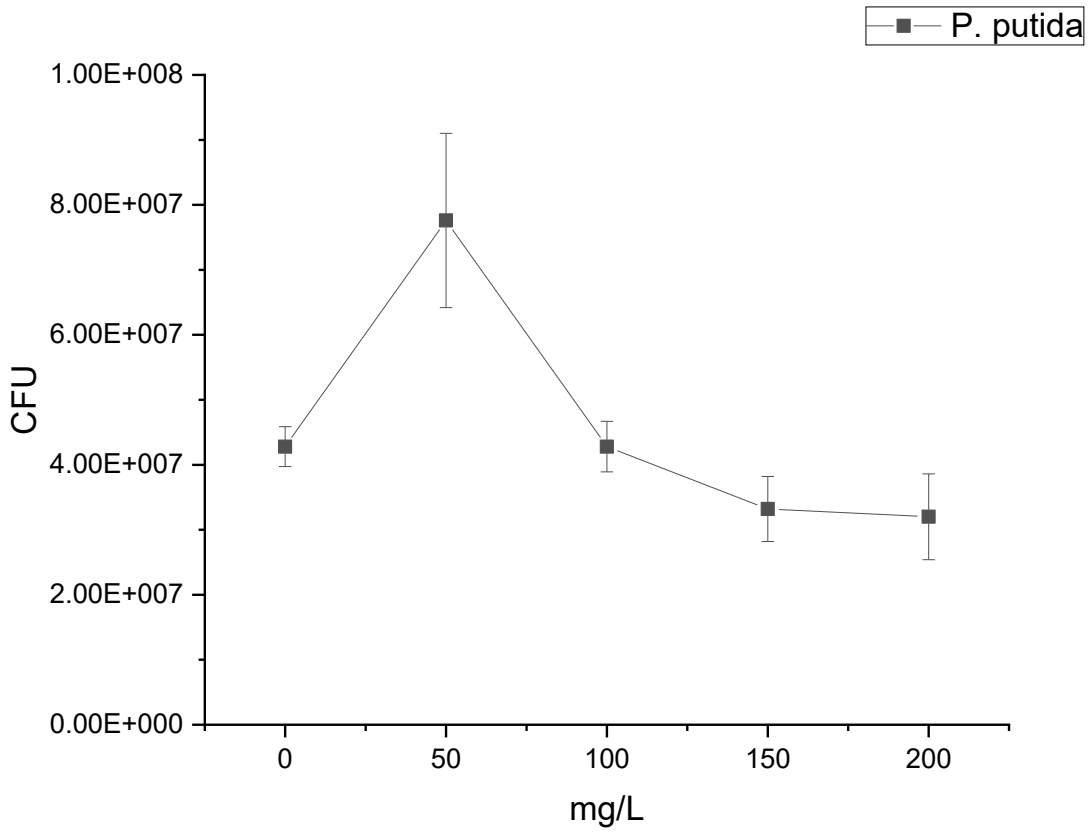


SI Figure III h.) Raw data plot of P. putida with titania nanoparticle based on OD change result. This was based on 5 replicates for each of the data points with each error bar representing the standard error.



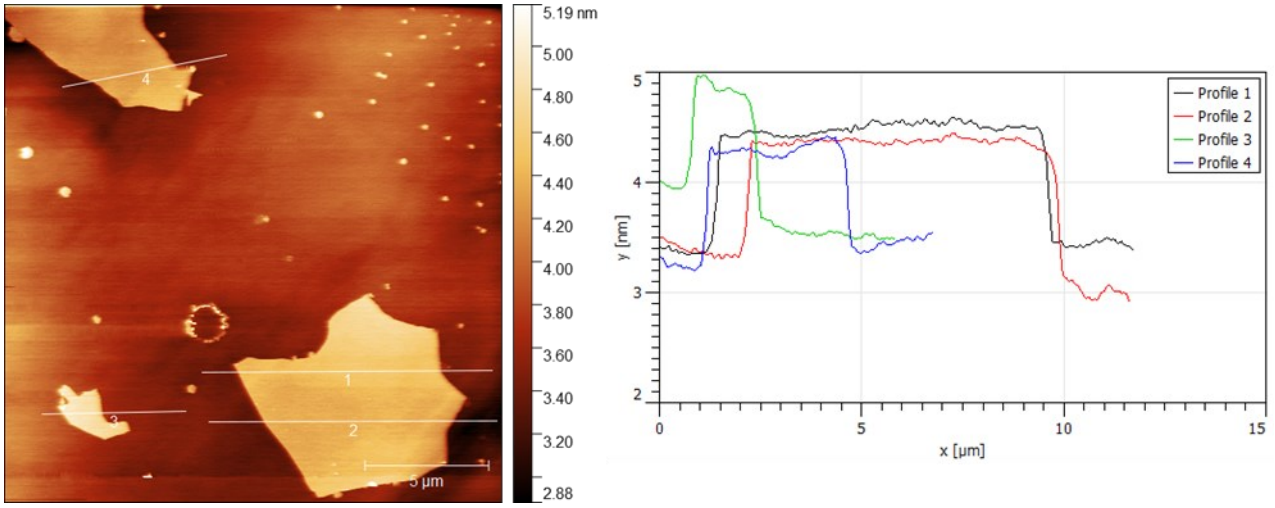
SI Figure III i.) Raw data plot of A. globiformis with titania nanoparticle based on CFU result. This was based on 5 replicates for each of the data points with each error bar representing the standard error.

5060

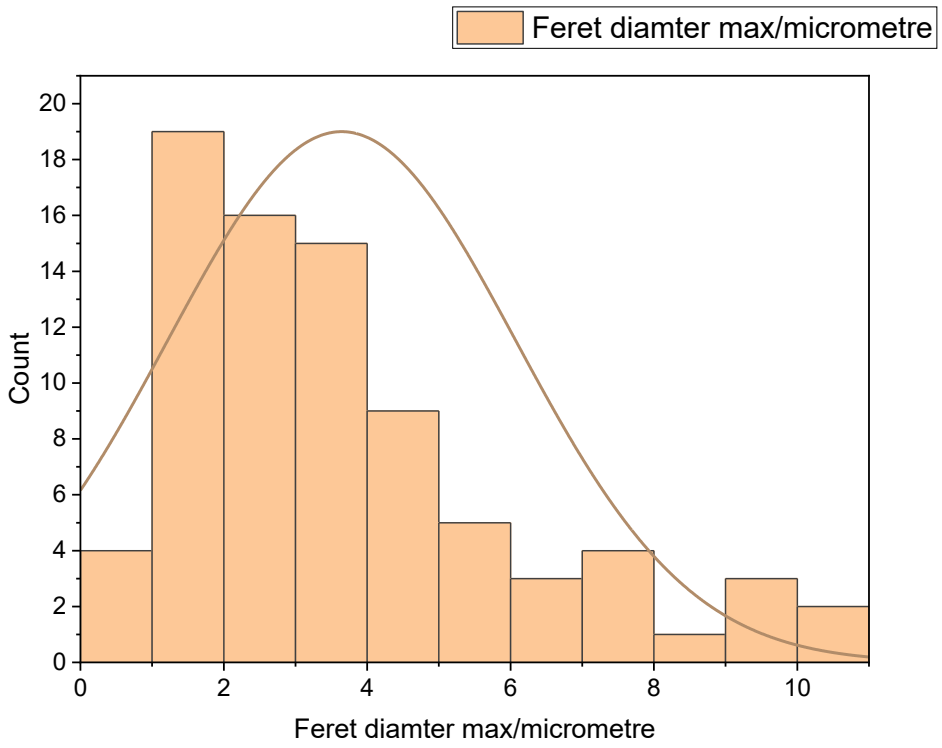


SI Figure III j.) Raw data plot of P. putida with titania nanoparticle based on the CFU result. This was based on 5 replicates for each of the data points with each error bar representing the standard error.

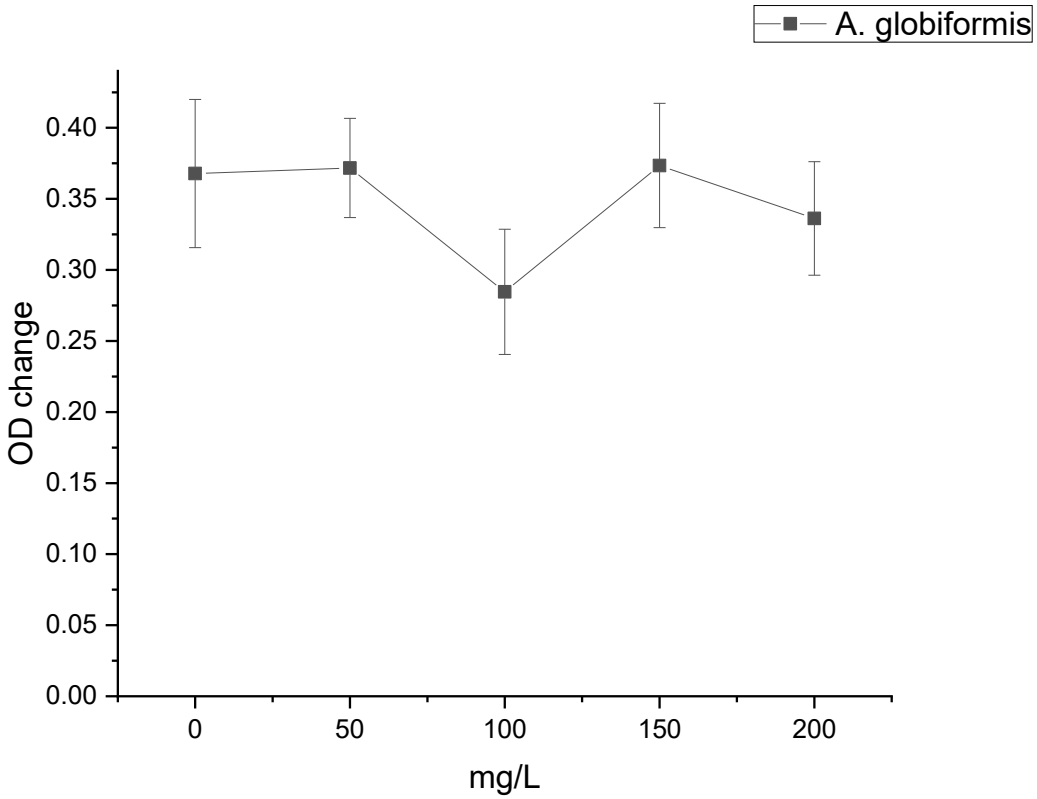
Appendix IV: ISO 10712 with different GO (Graphenea) (Chapter 2.2)



SI Figure IV a.) AFM image of Graphenea GO on freshly cleaved mica sheet. The plot shows height profile taken from the AFM image showing monolayer thickness of GO.

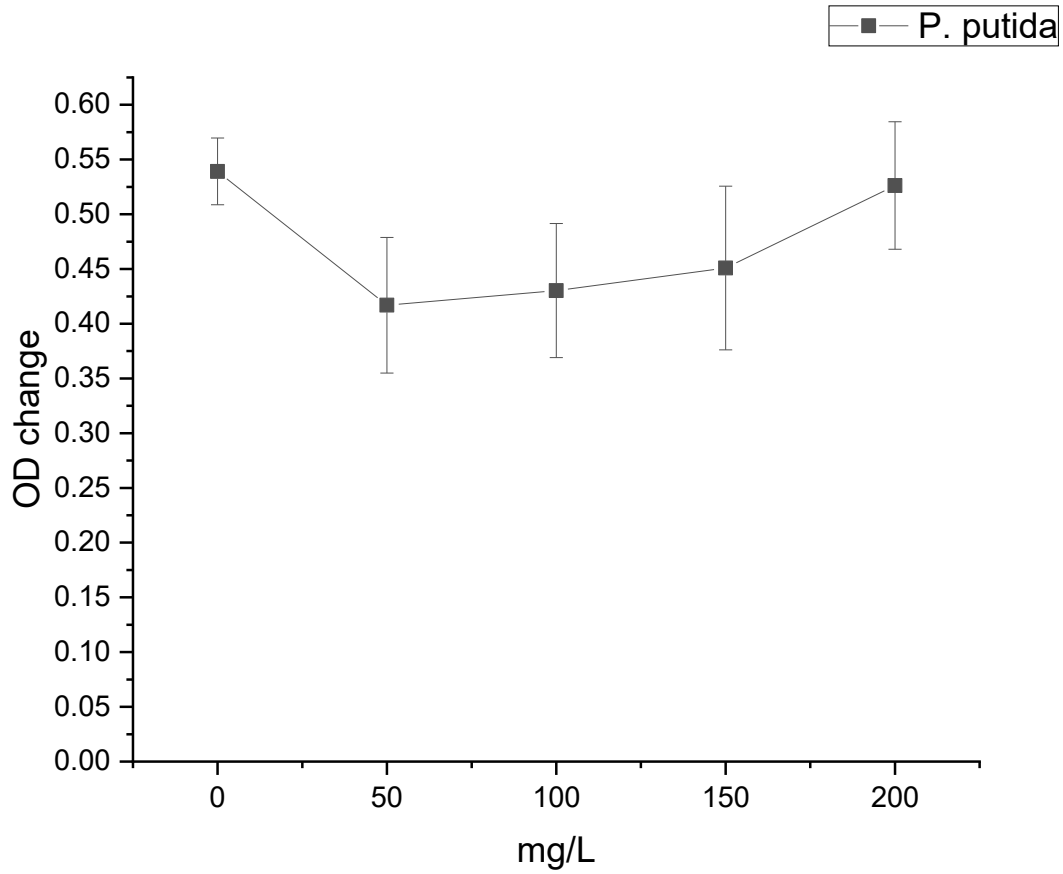


SI Figure IV b.) Size distribution of Graphene GO given by Feret diameter of the lateral size. Total N = 81, Mean = 3.64, S.D. = 2.42

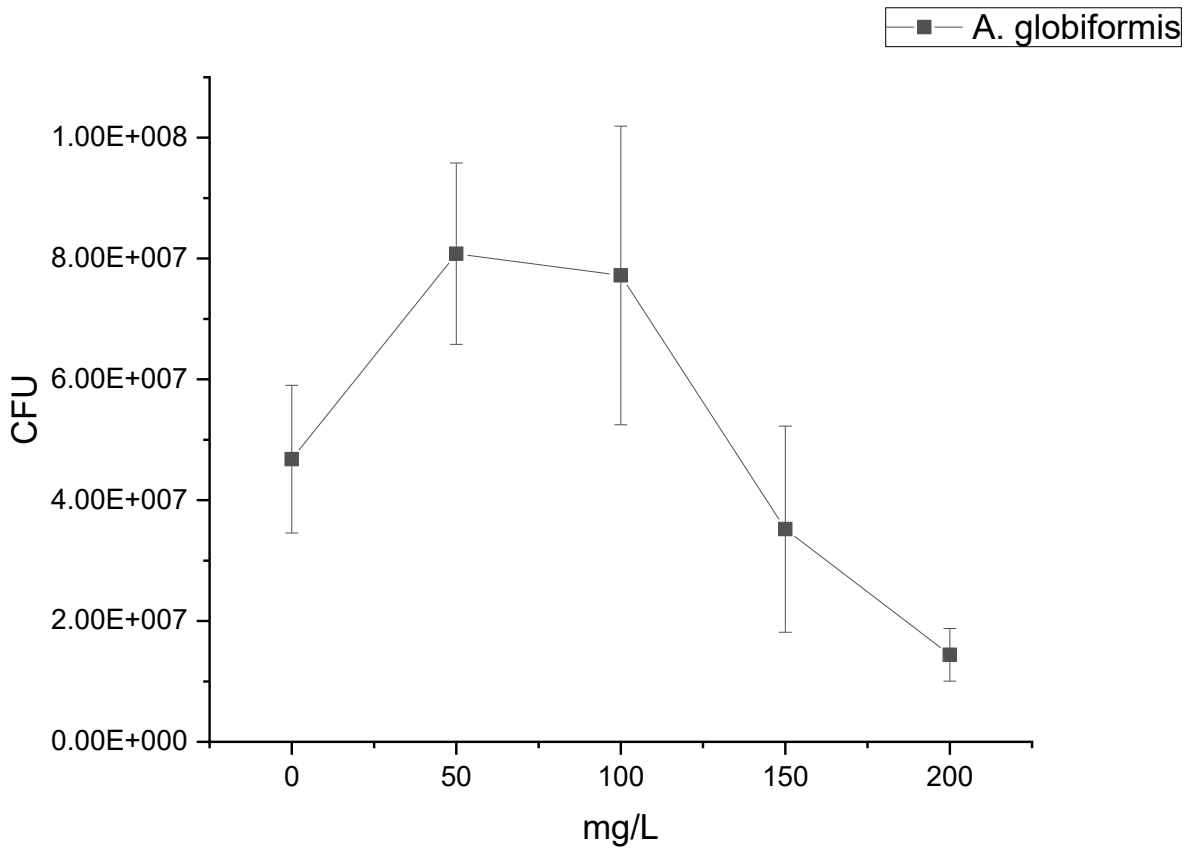


SI Figure IV c.) Raw data plot of A. globiformis with Graphenea GO based on OD changes. This was based on 5 replicates for each of the data points with each error bar representing the standard error.

5075

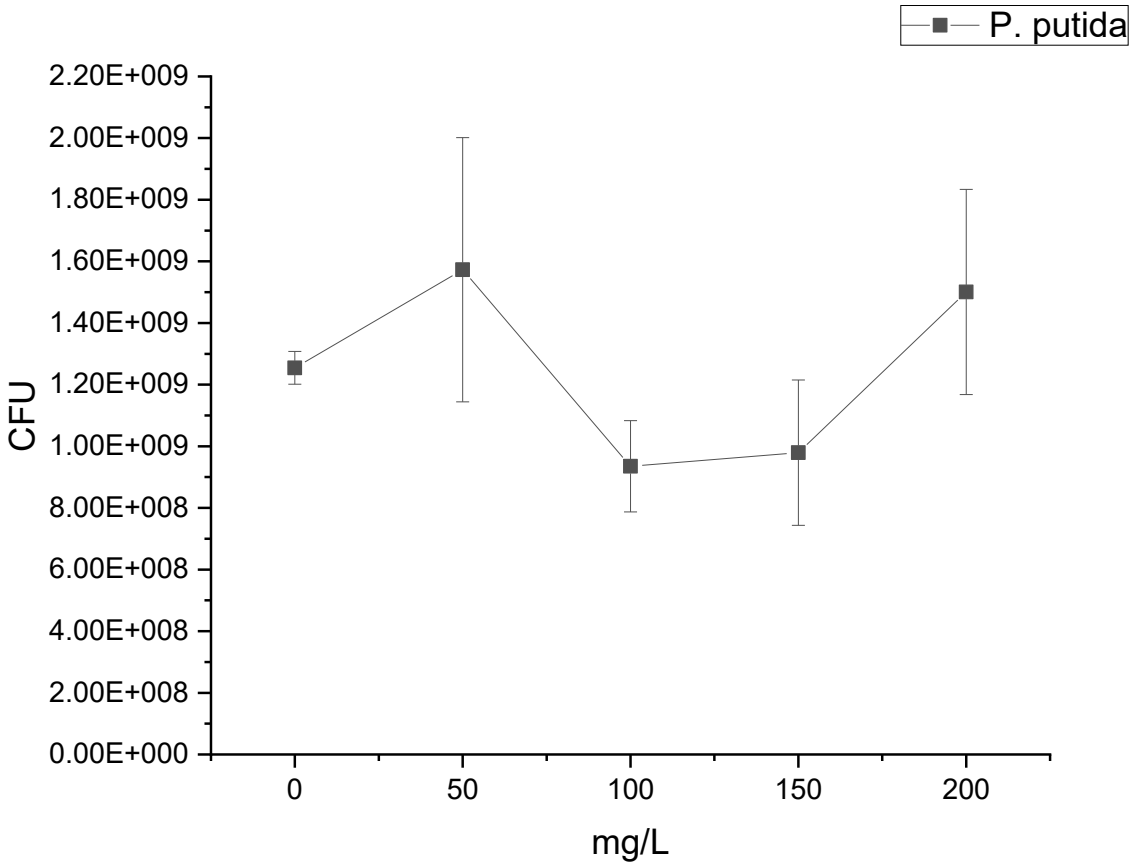


SI Figure IV d.) Raw data plot of P. putida with Graphenea GO based on OD changes. This was based on 5 replicates for each of the data points with each error bar representing the standard error.



5080

SI Figure IV e.) Raw data plot of A. globiformis with Graphenea GO based on CFU measurements. This was based on 5 replicates for each of the data points with each error bar representing the standard error.



SI Figure IV f.) Raw data plot of P. putida with Graphenea GO based on CFU result. This was based on 5 replicates for each of the data points with each error bar representing the standard error.

Appendix V: ANOVA statistic results of the effect of different media & abiotic conditions on OD changes (Chapter 2.3)

Toxicity test results in different media.

A. globiformis		Media					
OD results	mg/L	Water	ANOVA	ISO 10712	ANOVA	LB Broth	ANOVA
	50	-1.43394	**	68.60793	ns	119.4821	**
	100	-0.75148	**	87.53205	ns	134.7667	**
	150	0.49843	**	100.8546	ns	145.0846	**
	200	0.38341	**	102.7859	ns	154.5308	**

SI Table V a.) Table of proliferation values of the OD change result from range of concentrations of GO against A. globiformis with three different media: Water, ISO 10712 test media, LB broth. Each value was associated with the ANOVA test results to determine the difference in their mean values at 95% confidence level ($p<0.05$) as well as 99% confidence level ($p<0.01$).

P. putida		Media					
OD results	mg/L	Water	ANOVA	ISO 10712	ANOVA	LB Broth	ANOVA
	50	17.34119	**	105.8947	ns	103.2875	**
	100	20.19906	**	130.5922	ns	103.1418	**
	150	7.08431	**	120.2314	ns	104.6183	**
	200	9.64944	**	122.315	ns	103.8127	**

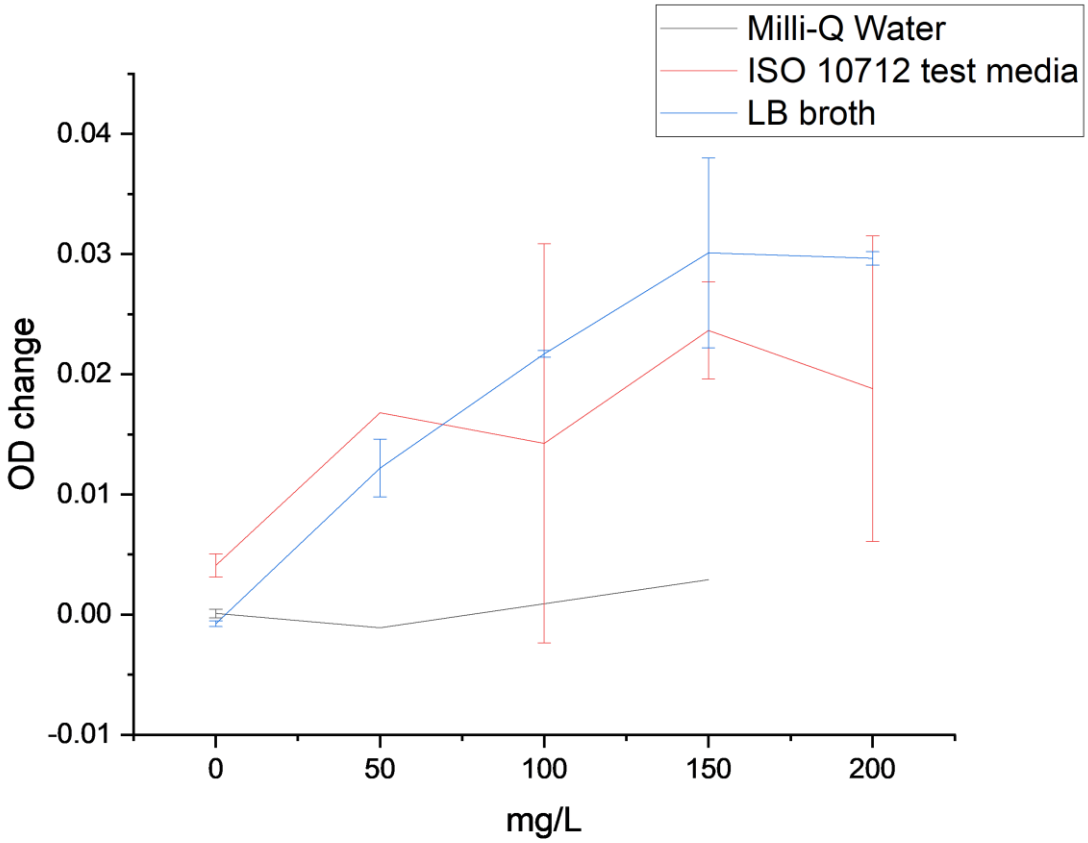
SI Table b.) Table of proliferation values of the OD change result from range of concentrations of GO against P. putida with three different media: Water, ISO 10712 test media, LB broth. Each value was associated with the ANOVA test results to determine the difference in their mean values at 95% confidence level ($p<0.05$) as well as 99% confidence level ($p<0.01$).

A. globiformis		Media					
CFU results	mg/L	Water	ANOVA	ISO 10712	ANOVA	LB Broth	ANOVA
	50	0	**	54.54545	ns	73.59551	ns
	100	0	**	146.281	ns	14.92275	**
	150	0	**	356.1984	ns	12.00843	**
	200	0	**	233.8843	ns	17.87219	**

SI Table c.) Table of proliferation values of the CFU results from range of concentrations of GO against A. globiformis with three different media: Water, ISO 10712 test media, LB broth. Each value was associated with the ANOVA test results to determine the difference in their mean values at 95% confidence level ($p<0.05$) as well as 99% confidence level ($p<0.01$).

P. putida		Media					
CFU results	mg/L	Water	ANOVA	ISO 10712	ANOVA	LB Broth	ANOVA
	50	25.9144	**	72.23908	ns	160.7194	ns
	100	9.18288	**	7.73665	**	187.0504	*
	150	5.87549	**	10.67961	**	138.1295	ns
	200	4.78599	**	15.83738	**	145.1799	ns

SI Table d.) Table of proliferation values of the CFU results from range of concentrations of GO against P. putida with three different media: Water, ISO 10712 test media, LB broth. Each value was associated with the ANOVA test results to determine the difference in their mean values at 95% confidence level ($p<0.05$) as well as 99% confidence level ($p<0.01$).

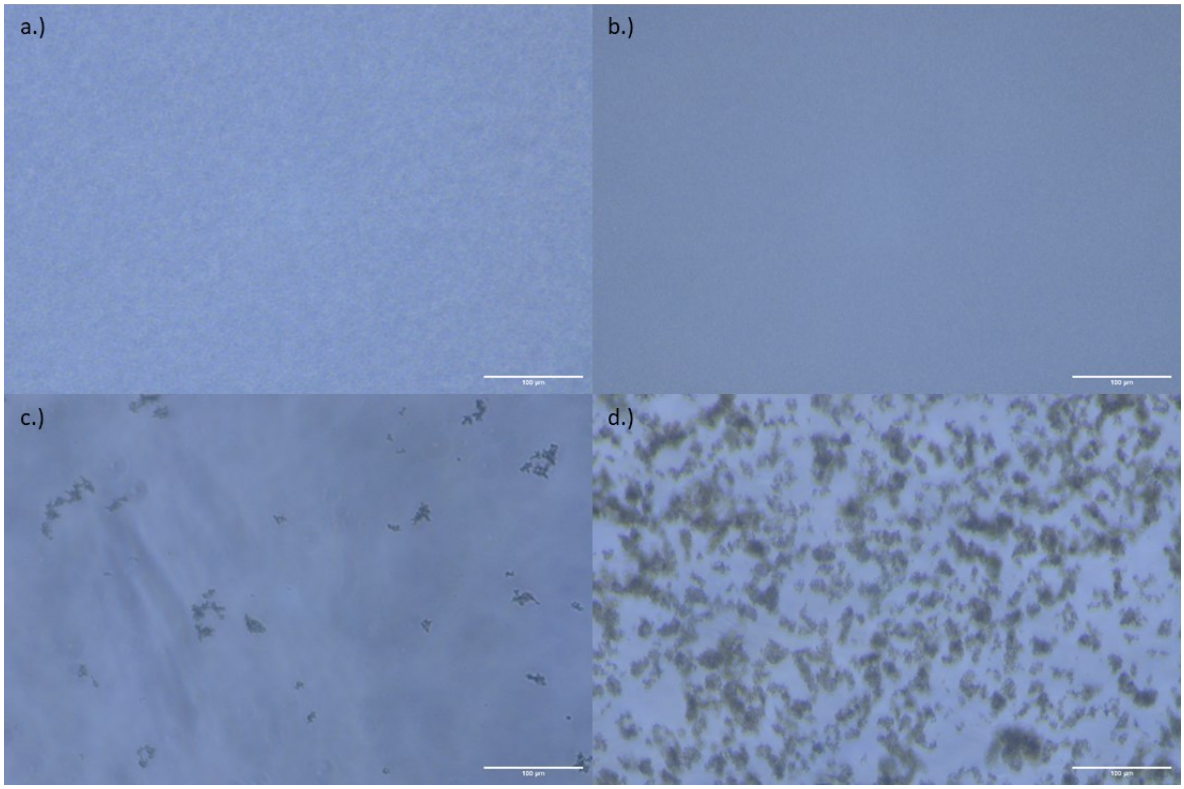


SI Figure V

a.) OD change result of abiotic condition of GO in Milli-Q water, ISO 10712 test media and LB broth.

Appendix VI: Complementary results to the MoS_2 toxicity data (Chapter 4)

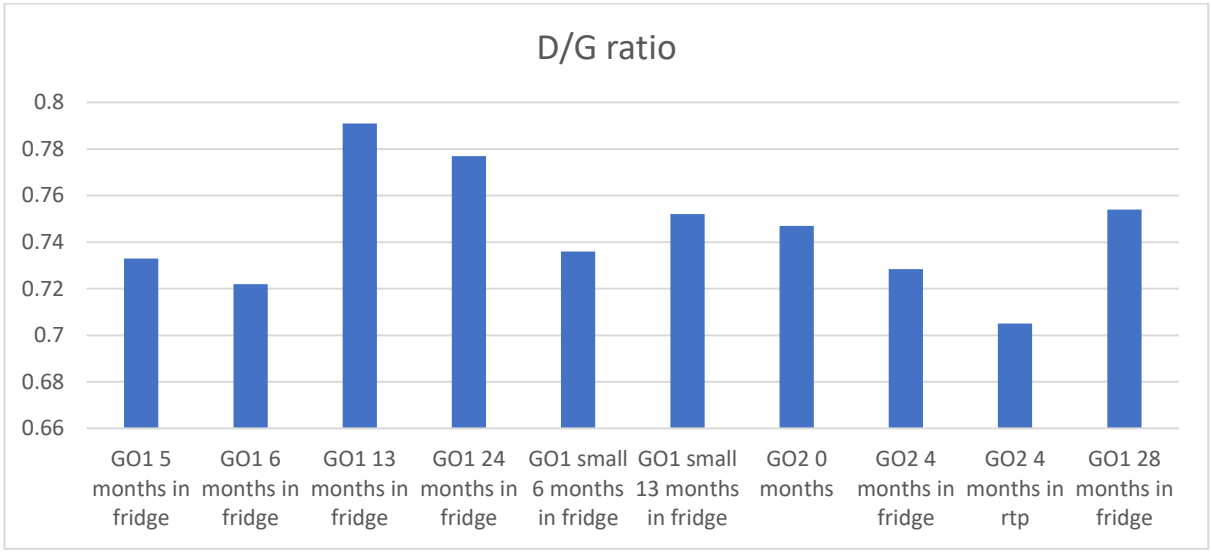
Optical image



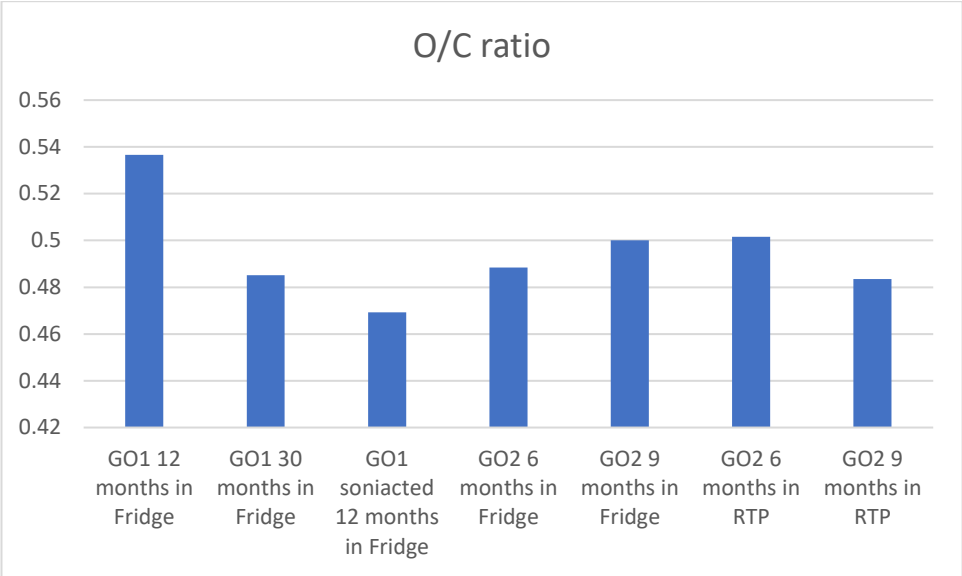
SI Figure VI a.) Optical image of control samples of soil bacteria with MoS_2 dispersion. a.) Image of A. globiformis. b.) Image of P. putida. c.) Image of 50 mg L^{-1} of MoS_2 in test media. d.) Image of 200 mg L^{-1} of MoS_2 in test media.

Appendix VII: Ageing of GO (Chapter 5)

Raman data given by D/G ratio and XPS data given by O/C ratio of all sample of GO samples characterised.



SI Table VII a.) D/G ratio of all sample of GO characterised using Raman spectra using the mapping technique. GO1 = GO batch 1, GO2 = GO batch 2, GO3 = GO batch 3, Fridge and RTP denotes storage conditions.



SI Table VII b.) O/C ration from XPS measurements taken by the mapping technique. GO1 = GO batch 1, GO2 = GO batch 2, GO3 = GO batch 3, Fridge and RTP denotes storage conditions.

Appendix References

1. A. K. Geim, K. S. Novoselov, The rise of graphene. *Nature materials* **6**, 183 (2007).

2. D. McManus *et al.*, Water-based and biocompatible 2D crystal inks for all-inkjet-printed heterostructures. *Nature nanotechnology* **12**, 343 (2017).

3. P. K. Kannan, D. J. Late, H. Morgan, C. S. Rout, Recent developments in 2D layered inorganic nanomaterials for sensing. *Nanoscale* **7**, 13293-13312 (2015).

4. Z. Wang *et al.*, Biological and environmental interactions of emerging two-dimensional nanomaterials. *Chemical Society Reviews* **45**, 1750-1780 (2016).

5. Y. Zhan, Z. Liu, S. Najmaei, P. M. Ajayan, J. Lou, Large‐area vapor‐phase growth and characterization of MoS2 atomic layers on a SiO2 substrate. *Small* **8**, 966-971 (2012).

6. S. Bae *et al.*, Roll-to-roll production of 30-inch graphene films for transparent electrodes. *Nature nanotechnology* **5**, 574 (2010).

7. D. Dumcenco *et al.*, Large-area epitaxial monolayer MoS2. *ACS nano* **9**, 4611-4620 (2015).

8. T. Ohta, A. Bostwick, T. Seyller, K. Horn, E. Rotenberg, Controlling the electronic structure of bilayer graphene. *Science* **313**, 951-954 (2006).

9. J. N. Coleman *et al.*, Two-dimensional nanosheets produced by liquid exfoliation of layered materials. *Science* **331**, 568-571 (2011).

10. Y. Hernandez *et al.*, High-yield production of graphene by liquid-phase exfoliation of graphite. *Nature nanotechnology* **3**, 563 (2008).

11. M. Fojtů, W. Z. Teo, M. Pumera, Environmental impact and potential health risks of 2D nanomaterials. *Environmental Science: Nano* **4**, 1617-1633 (2017).

12. A. Malakar, S. R. Kanel, C. Ray, D. D. Snow, M. N. Nadagouda, Nanomaterials in the environment, human exposure pathway, and health effects: A review. *Science of the Total Environment* **759**, 143470 (2021).

13. S. E. Lowe, Y. L. Zhong, Challenges of Industrial‐Scale Graphene Oxide Production. *Graphene Oxide: Fundamentals and Applications*, 410 (2016).

14. M. Segal, Selling graphene by the ton. *Nature nanotechnology* **4**, 612 (2009).

15. A. Zurutuza, C. Marinelli, Challenges and opportunities in graphene commercialization. *Nature nanotechnology* **9**, 730 (2014).

16. A. Dowling *et al.* (London, UK: Royal Academy of Engineering, 2004).

17. F. Gottschalk, T. Sonderer, R. W. Scholz, B. Nowack, Modeled environmental concentrations of engineered nanomaterials (TiO2, ZnO, Ag, CNT, fullerenes) for different regions. *Environmental science & technology* **43**, 9216-9222 (2009).

18. K. S. Novoselov *et al.*, Electric field effect in atomically thin carbon films. *science* **306**, 666-669 (2004).

19. S. Iijima, Helical microtubules of graphitic carbon. *nature* **354**, 56 (1991).

20. S. Iijima, T. Ichihashi, Single-shell carbon nanotubes of 1-nm diameter. *nature* **363**, 603 (1993).

21. A. A. Keller, A. Lazareva, Predicted releases of engineered nanomaterials: from global to regional to local. *Environmental Science & Technology Letters* **1**, 65-70 (2013).

22. A. A. Keller, S. McFerran, A. Lazareva, S. Suh, Global life cycle releases of engineered nanomaterials. *Journal of Nanoparticle Research* **15**, 1692 (2013).

23. F. Gottschalk, T. Sun, B. Nowack, Environmental concentrations of engineered nanomaterials: review of modeling and analytical studies. *Environmental Pollution* **181**, 287-300 (2013).

24. D. Chen, H. Feng, J. Li, Graphene oxide: preparation, functionalization, and electrochemical applications. *Chemical reviews* **112**, 6027-6053 (2012).

25. B. R. Coleman, T. Knight, V. Gies, Z. J. Jakubek, S. Zou, Manipulation and quantification of graphene oxide flake size: Photoluminescence and cytotoxicity. *ACS applied materials & interfaces* **9**, 28911-28921 (2017).

26. T. S. Miller *et al.*, Single crystal, luminescent carbon nitride nanosheets formed by spontaneous dissolution. *Nano letters* **17**, 5891-5896 (2017).

27. B. Domi *et al.*, Fate assessment of commercial 2D MoS2 aqueous dispersions at physicochemical and toxicological level. *Nanotechnology* **31**, 445101 (2020).

28. D. Gonzalez-Carter *et al.*, Quantification of blood–brain barrier transport and neuronal toxicity of unlabelled multiwalled carbon nanotubes as a function of surface charge. *Nanoscale* **11**, 22054-22069 (2019).

29. R. C. Murdock, L. Braydich-Stolle, A. M. Schrand, J. J. Schlager, S. M. Hussain, Characterization of nanomaterial dispersion in solution prior to in vitro exposure using dynamic light scattering technique. *Toxicological sciences* **101**, 239-253 (2008).

30. M. Lotya, A. Rakovich, J. F. Donegan, J. N. Coleman, Measuring the lateral size of liquid-exfoliated nanosheets with dynamic light scattering. *Nanotechnology* **24**, 265703 (2013).

31. S. Badaire, P. Poulin, M. Maugey, C. Zakri, In situ measurements of nanotube dimensions in suspensions by depolarized dynamic light scattering. *Langmuir* **20**, 10367-10370 (2004).

32. D. J. Morgan, X-ray photoelectron spectroscopy (xps): an introduction. *Cardiff Catalysis Institute, School of Chemistry, Cardiff University, Cardiff*, (2014).

33. K. Krishnamoorthy, M. Veerapandian, K. Yun, S.-J. Kim, The chemical and structural analysis of graphene oxide with different degrees of oxidation. *Carbon* **53**, 38-49 (2013).

34. N. Rubio *et al.*, Effect of graphene flake size on functionalisation: quantifying reaction extent and imaging locus with single Pt atom tags. *Chemical science* **12**, 14907-14919 (2021).

35. A. J. Clancy, H. Au, N. Rubio, G. O. Coulter, M. S. Shaffer, Understanding and controlling the covalent functionalisation of graphene. *Dalton Transactions* **49**, 10308-10318 (2020).

36. X. Zhang, F. Jia, B. Yang, S. Song, Oxidation of molybdenum disulfide sheet in water under in situ atomic force microscopy observation. *The Journal of Physical Chemistry C* **121**, 9938-9943 (2017).

37. A. C. Ferrari, D. M. Basko, Raman spectroscopy as a versatile tool for studying the properties of graphene. *Nature nanotechnology* **8**, 235-246 (2013).

38. K. Erickson *et al.*, Determination of the local chemical structure of graphene oxide and reduced graphene oxide. *Advanced Materials* **22**, 4467-4472 (2010).

39. K. A. Mkhoyan *et al.*, Atomic and electronic structure of graphene-oxide. *Nano letters* **9**, 1058-1063 (2009).

40. Y. Cheng *et al.*, Origin of the phase transition in lithiated molybdenum disulfide. *ACS nano* **8**, 11447-11453 (2014).

41. S. Chen *et al.*, Aqueous cationic, anionic and non-ionic multi-walled carbon nanotubes, functionalised with minimal framework damage, for biomedical application. *Biomaterials* **35**, 4729-4738 (2014).

42. A. E. Porter *et al.*, Uptake of noncytotoxic acid-treated single-walled carbon nanotubes into the cytoplasm of human macrophage cells. *Acs Nano* **3**, 1485-1492 (2009).

43. A. M. Schrand, J. J. Schlager, L. Dai, S. M. Hussain, Preparation of cells for assessing ultrastructural localization of nanoparticles with transmission electron microscopy. *Nature protocols* **5**, 744-757 (2010).

44. P. Kovalakova *et al.*, Occurrence and toxicity of antibiotics in the aquatic environment: A review. *Chemosphere* **251**, 126351 (2020).

45. B. S. B. E. ISO, Water quality–Pseudomonas putida growth inhibition test (Pseudomonas cell multiplication inhibition test). (1995).

46. M. Matzke, K. Jurkschat, T. Backhaus, Toxicity of differently sized and coated silver nanoparticles to the bacterium Pseudomonas putida: risks for the aquatic environment? *Ecotoxicology* **23**, 818-829 (2014).

47. C. L. Schultz *et al.*, Aging reduces the toxicity of pristine but not sulphidised silver nanoparticles to soil bacteria. *Environmental Science: Nano* **5**, 2618-2630 (2018).

48. A. Winding, J. J. Modrzyński, J. H. Christensen, K. K. Brandt, P. Mayer, Soil bacteria and protists show different sensitivity to polycyclic aromatic hydrocarbons at controlled chemical activity. *FEMS Microbiology Letters* **366**, fnz214 (2019).

49. K. K. Brandt *et al.*, Ecotoxicological assessment of antibiotics: a call for improved consideration of microorganisms. *Environment International* **85**, 189-205 (2015).

50. D. Labeda, K.-C. Liu, L. Casida Jr, Colonization of soil by Arthrobacter and Pseudomonas under varying conditions of water and nutrient availability as studied by plate counts and transmission electron microscopy. *Applied and Environmental Microbiology* **31**, 551-561 (1976).

51. J. Fabrega, S. R. Fawcett, J. C. Renshaw, J. R. Lead, Silver nanoparticle impact on bacterial growth: effect of pH, concentration, and organic matter. *Environmental science & technology* **43**, 7285-7290 (2009).

52. J. Fabrega, J. C. Renshaw, J. R. Lead, Interactions of silver nanoparticles with Pseudomonas putida biofilms. *Environmental science & technology* **43**, 9004-9009 (2009).

53. X. Chen *et al.*, Tolerance and biosorption of copper and zinc by Pseudomonas putida CZ1 isolated from metal-polluted soil. *Canadian journal of microbiology* **52**, 308-316 (2006).

54. A. Bianco *et al.* (Elsevier, 2013).

55. K. S. Novoselov *et al.*, A roadmap for graphene. *Nature* **490**, 192 (2012).

56. D. Li, M. B. Müller, S. Gilje, R. B. Kaner, G. G. Wallace, Processable aqueous dispersions of graphene nanosheets. *Nature nanotechnology* **3**, 101 (2008).

57. W. Ren, H.-M. Cheng, The global growth of graphene. *Nature nanotechnology* **9**, 726 (2014).

58. K. R. Paton *et al.*, Scalable production of large quantities of defect-free few-layer graphene by shear exfoliation in liquids. *Nature materials* **13**, 624 (2014).

59. L. M. Viculis, J. J. Mack, O. M. Mayer, H. T. Hahn, R. B. Kaner, Intercalation and exfoliation routes to graphite nanoplatelets. *Journal of Materials Chemistry* **15**, 974-978 (2005).

60. A. C. Ferrari *et al.*, Science and technology roadmap for graphene, related two-dimensional crystals, and hybrid systems. *Nanoscale* **7**, 4598-4810 (2015).

61. H. J. Yoon, J. H. Yang, Z. Zhou, S. S. Yang, M. M.-C. Cheng, Carbon dioxide gas sensor using a graphene sheet. *Sensors and Actuators B: Chemical* **157**, 310-313 (2011).

62. K. H. Kim, Y. Oh, M. Islam, Graphene coating makes carbon nanotube aerogels superelastic and resistant to fatigue. *Nature nanotechnology* **7**, 562 (2012).

63. S. Garaj *et al.*, Graphene as a subnanometre trans-electrode membrane. *Nature* **467**, 190 (2010).

64. N. I. Kovtyukhova *et al.*, Layer-by-layer assembly of ultrathin composite films from micron-sized graphite oxide sheets and polycations. *Chemistry of materials* **11**, 771-778 (1999).

65. W. S. Hummers Jr, R. E. Offeman, Preparation of graphitic oxide. *Journal of the american chemical society* **80**, 1339-1339 (1958).

66. K. Fu *et al.*, Graphene oxide‐based electrode inks for 3D‐printed lithium‐ion batteries. *Advanced materials* **28**, 2587-2594 (2016).

67. V. Dua *et al.*, All‐organic vapor sensor using inkjet‐printed reduced graphene oxide. *Angewandte Chemie* **122**, 2200-2203 (2010).

68. Y. Singhbabu *et al.*, Efficient anti-corrosive coating of cold-rolled steel in a seawater environment using an oil-based graphene oxide ink. *Nanoscale* **7**, 8035-8047 (2015).

69. W. Gao, in *Graphene oxide*. (Springer, 2015), pp. 61-95.

70. G. Eda, M. Chhowalla, Chemically derived graphene oxide: towards large‐area thin‐film electronics and optoelectronics. *Advanced materials* **22**, 2392-2415 (2010).

71. S. Chen, J. Zhu, X. Wu, Q. Han, X. Wang, Graphene oxide− MnO2 nanocomposites for supercapacitors. *ACS nano* **4**, 2822-2830 (2010).

72. H. Y. Jeong *et al.*, Graphene oxide thin films for flexible nonvolatile memory applications. *Nano letters* **10**, 4381-4386 (2010).

73. U. Khan, P. May, A. O'Neill, J. N. Coleman, Development of stiff, strong, yet tough composites by the addition of solvent exfoliated graphene to polyurethane. *Carbon* **48**, 4035-4041 (2010).

74. K. Krishnamoorthy, R. Mohan, S.-J. Kim, Graphene oxide as a photocatalytic material. *Applied Physics Letters* **98**, 244101 (2011).

75. Y. Song, K. Qu, C. Zhao, J. Ren, X. Qu, Graphene oxide: intrinsic peroxidase catalytic activity and its application to glucose detection. *Advanced Materials* **22**, 2206-2210 (2010).

76. S. Shukla, S. Saxena, Spectroscopic investigation of confinement effects on optical properties of graphene oxide. *Applied Physics Letters* **98**, 073104 (2011).

77. S. Stankovich *et al.*, Synthesis of graphene-based nanosheets via chemical reduction of exfoliated graphite oxide. *carbon* **45**, 1558-1565 (2007).

78. W. Chen, L. Yan, P. R. Bangal, Preparation of graphene by the rapid and mild thermal reduction of graphene oxide induced by microwaves. *Carbon* **48**, 1146-1152 (2010).

79. Y. Zhu *et al.*, Exfoliation of graphite oxide in propylene carbonate and thermal reduction of the resulting graphene oxide platelets. *ACS nano* **4**, 1227-1233 (2010).

80. X. Zhou *et al.*, Photo-Fenton reaction of graphene oxide: a new strategy to prepare graphene quantum dots for DNA cleavage. *ACS nano* **6**, 6592-6599 (2012).

81. E. C. Salas, Z. Sun, A. Lüttge, J. M. Tour, Reduction of graphene oxide via bacterial respiration. *ACS nano* **4**, 4852-4856 (2010).

82. S. Park, R. S. Ruoff, Chemical methods for the production of graphenes. *Nature nanotechnology* **4**, 217 (2009).

83. X.-Y. Wang, A. Narita, K. Müllen, Precision synthesis versus bulk-scale fabrication of graphenes. *Nature Reviews Chemistry* **2**, 0100 (2017).

84. Z. Yin, C. Cui, H. Chen, X. Yu, W. Qian, The application of carbon nanotube/graphene‐based nanomaterials in wastewater treatment. *Small* **16**, 1902301 (2020).

85. A. Khan *et al.*, The role of graphene oxide and graphene oxide-based nanomaterials in the removal of pharmaceuticals from aqueous media: a review. *Environmental Science and Pollution Research* **24**, 7938-7958 (2017).

86. Y. Zhao, Y. Liu, X. Zhang, W. Liao, Environmental transformation of graphene oxide in the aquatic environment. *Chemosphere* **262**, 127885 (2021).

87. A. Rhazouani *et al.*, Synthesis and toxicity of graphene oxide nanoparticles: A literature review of in vitro and in vivo studies. *BioMed Research International* **2021**, (2021).

88. O. N. Ruiz *et al.*, Graphene oxide: a nonspecific enhancer of cellular growth. *ACS nano* **5**, 8100-8107 (2011).

89. G.-Y. Chen, D.-P. Pang, S.-M. Hwang, H.-Y. Tuan, Y.-C. Hu, A graphene-based platform for induced pluripotent stem cells culture and differentiation. *Biomaterials* **33**, 418-427 (2012).

90. Y. Chang *et al.*, In vitro toxicity evaluation of graphene oxide on A549 cells. *Toxicology letters* **200**, 201-210 (2011).

91. S. Mittal *et al.*, Physico-chemical properties based differential toxicity of graphene oxide/reduced graphene oxide in human lung cells mediated through oxidative stress. *Scientific reports* **6**, 1-16 (2016).

92. K.-H. Liao, Y.-S. Lin, C. W. Macosko, C. L. Haynes, Cytotoxicity of graphene oxide and graphene in human erythrocytes and skin fibroblasts. *ACS applied materials & interfaces* **3**, 2607-2615 (2011).

93. X. Guo *et al.*, Organic electrochemical transistor for in situ detection of H2O2 released from adherent cells and its application in evaluating the in vitro cytotoxicity of nanomaterial. *Analytical Chemistry* **92**, 908-915 (2019).

94. E. Puigpelat, J. Ignés-Mullol, F. Sagués, R. Reigada, Interaction of graphene nanoparticles and lipid membranes displaying different liquid orderings: a molecular dynamics study. *Langmuir* **35**, 16661-16668 (2019).

95. A. B. Seabra, A. J. Paula, R. de Lima, O. L. Alves, N. Durán, Nanotoxicity of graphene and graphene oxide. *Chemical research in toxicology* **27**, 159-168 (2014).

96. V. C. Sanchez, A. Jachak, R. H. Hurt, A. B. Kane, Biological interactions of graphene-family nanomaterials: an interdisciplinary review. *Chemical research in toxicology* **25**, 15-34 (2012).

97. H. Yue *et al.*, The role of the lateral dimension of graphene oxide in the regulation of cellular responses. *Biomaterials* **33**, 4013-4021 (2012).

98. A. Wang *et al.*, Role of surface charge and oxidative stress in cytotoxicity and genotoxicity of graphene oxide towards human lung fibroblast cells. *Journal of Applied Toxicology* **33**, 1156-1164 (2013).

99. J. Ma *et al.*, Crucial role of lateral size for graphene oxide in activating macrophages and stimulating pro-inflammatory responses in cells and animals. *Acs Nano* **9**, 10498-10515 (2015).

100. Q. Mu *et al.*, Size-dependent cell uptake of protein-coated graphene oxide nanosheets. *ACS applied materials & interfaces* **4**, 2259-2266 (2012).

101. M. Xu *et al.*, Improved in vitro and in vivo biocompatibility of graphene oxide through surface modification: poly (acrylic acid)-functionalization is superior to PEGylation. *Acs Nano* **10**, 3267-3281 (2016).

102. X. Zou, L. Zhang, Z. Wang, Y. Luo, Mechanisms of the antimicrobial activities of graphene materials. *Journal of the american chemical society* **138**, 2064-2077 (2016).

103. E. P. Nguyen, C. d. C. C. Silva, A. Merkoçi, Recent advancement in biomedical applications on the surface of two-dimensional materials: from biosensing to tissue engineering. *Nanoscale* **12**, 19043-19067 (2020).

104. V. Palmieri *et al.*, The graphene oxide contradictory effects against human pathogens. *Nanotechnology* **28**, 152001 (2017).

105. T. Seifi, A. R. Kamali, Anti-pathogenic activity of graphene nanomaterials: A review. *Colloids and Surfaces B: Biointerfaces* **199**, 111509 (2021).

106. T. Pulingam, K. L. Thong, J. N. Appaturi, C. W. Lai, B. F. Leo, Mechanistic actions and contributing factors affecting the antibacterial property and cytotoxicity of graphene oxide. *Chemosphere* **281**, 130739 (2021).

107. J. Chen, X. Wang, H. Han, A new function of graphene oxide emerges: inactivating phytopathogenic bacterium Xanthomonas oryzae pv. Oryzae. *Journal of nanoparticle research* **15**, 1658 (2013).

108. Y. L. F. Musico, C. M. Santos, M. L. P. Dalida, D. F. Rodrigues, Surface modification of membrane filters using graphene and graphene oxide-based nanomaterials for bacterial inactivation and removal. *ACS Sustainable Chemistry & Engineering* **2**, 1559-1565 (2014).

109. X. Wang, X. Liu, H. J. C. a. S. B. B. Han, Evaluation of antibacterial effects of carbon nanomaterials against copper-resistant Ralstonia solanacearum. **103**, 136-142 (2013).

110. S. Gurunathan, J. W. Han, V. Eppakayala, J.-H. Kim, Microbial reduction of graphene oxide by Escherichia coli: a green chemistry approach. *Colloids and Surfaces B: Biointerfaces* **102**, 772-777 (2013).

111. S. Gurunathan, J. W. Han, A. A. Dayem, V. Eppakayala, J.-H. Kim, Oxidative stress-mediated antibacterial activity of graphene oxide and reduced graphene oxide in Pseudomonas aeruginosa. *International journal of nanomedicine* **7**, 5901 (2012).

112. Q. Mei, Z. Zhang, Photoluminescent graphene oxide ink to print sensors onto microporous membranes for versatile visualization bioassays. *Angewandte Chemie International Edition* **51**, 5602-5606 (2012).

113. F. Perreault, A. F. De Faria, S. Nejati, M. Elimelech, Antimicrobial properties of graphene oxide nanosheets: why size matters. *ACS nano* **9**, 7226-7236 (2015).

114. O. Akhavan, E. Ghaderi, Toxicity of graphene and graphene oxide nanowalls against bacteria. *ACS nano* **4**, 5731-5736 (2010).

115. H.-q. Chen *et al.*, Graphene oxide as an anaerobic membrane scaffold for the enhancement of B. adolescentis proliferation and antagonistic effects against pathogens E. coli and S. aureus. *Nanotechnology* **25**, 165101 (2014).

116. T. H. Nguyen, M. Lin, A. Mustapha, Toxicity of graphene oxide on intestinal bacteria and Caco-2 cells. *Journal of Food Protection* **78**, 996-1002 (2015).

117. I. Barbolina *et al.*, Purity of graphene oxide determines its antibacterial activity. *2D Materials* **3**, 025025 (2016).

118. J. Campos-Delgado *et al.*, Effect of graphene oxide on bacteria and peripheral blood mononuclear cells. *Journal of Applied Biomaterials & Functional Materials* **14**, 423-430 (2016).

119. L. Hui *et al.*, Availability of the basal planes of graphene oxide determines whether it is antibacterial. *ACS applied materials & interfaces* **6**, 13183-13190 (2014).

120. S. Liu *et al.*, Lateral dimension-dependent antibacterial activity of graphene oxide sheets. *Langmuir* **28**, 12364-12372 (2012).

121. V. Palmieri *et al.*, Bacteria meet graphene: modulation of graphene oxide nanosheet interaction with human pathogens for effective antimicrobial therapy. *ACS Biomaterials Science & Engineering* **3**, 619-627 (2017).

122. L. Wu *et al.*, Aggregation kinetics of graphene oxides in aqueous solutions: experiments, mechanisms, and modeling. *Langmuir* **29**, 15174-15181 (2013).

123. J. Zhao, Z. Wang, J. C. White, B. Xing, Graphene in the aquatic environment: adsorption, dispersion, toxicity and transformation. *Environmental science & technology* **48**, 9995-10009 (2014).

124. Y. Luo *et al.*, Functionalized graphene oxide in microbial engineering: An effective stimulator for bacterial growth. *Carbon* **103**, 172-180 (2016).

125. J. He *et al.*, Killing dental pathogens using antibacterial graphene oxide. *ACS applied materials & interfaces* **7**, 5605-5611 (2015).

126. M. J. Hajipour *et al.*, Antibacterial properties of nanoparticles. *Trends in biotechnology* **30**, 499-511 (2012).

127. S. S. Nanda, S. S. A. An, D. K. Yi, Oxidative stress and antibacterial properties of a graphene oxide-cystamine nanohybrid. *International journal of nanomedicine* **10**, 549 (2015).

128. H. E. Karahan *et al.*, Bacterial physiology is a key modulator of the antibacterial activity of graphene oxide. *Nanoscale* **8**, 17181-17189 (2016).

129. M. Veerapandian, L. Zhang, K. Krishnamoorthy, K. Yun, Surface activation of graphene oxide nanosheets by ultraviolet irradiation for highly efficient anti-bacterials. *Nanotechnology* **24**, 395706 (2013).

130. K. Krishnamoorthy, M. Veerapandian, L.-H. Zhang, K. Yun, S. J. Kim, Antibacterial efficiency of graphene nanosheets against pathogenic bacteria via lipid peroxidation. *The journal of physical chemistry C* **116**, 17280-17287 (2012).

131. W. Hu *et al.*, Graphene-based antibacterial paper. *ACS nano* **4**, 4317-4323 (2010).

132. T. Pulingam *et al.*, Graphene oxide exhibits differential mechanistic action towards Gram-positive and Gram-negative bacteria. *Colloids and Surfaces B: Biointerfaces* **181**, 6-15 (2019).

133. I. E. M. Carpio, C. M. Santos, X. Wei, D. F. Rodrigues, Toxicity of a polymer–graphene oxide composite against bacterial planktonic cells, biofilms, and mammalian cells. *Nanoscale* **4**, 4746-4756 (2012).

134. K. Krishnamoorthy, N. Umasuthan, R. Mohan, J. Lee, S.-J. Kim, Antibacterial activity of graphene oxide nanosheets. *Science of Advanced Materials* **4**, 1111-1117 (2012).

135. O. Akhavan, E. Ghaderi, A. J. T. J. o. P. C. B. Esfandiar, Wrapping bacteria by graphene nanosheets for isolation from environment, reactivation by sonication, and inactivation by near-infrared irradiation. **115**, 6279-6288 (2011).

136. M. Dallavalle, M. Calvaresi, A. Bottoni, M. Melle-Franco, F. Zerbetto, Graphene can wreak havoc with cell membranes. *ACS applied materials & interfaces* **7**, 4406-4414 (2015).

137. Y. Tu *et al.*, Destructive extraction of phospholipids from Escherichia coli membranes by graphene nanosheets. **8**, 594 (2013).

138. C.-H. Yu *et al.*, Understanding the sheet size-antibacterial activity relationship of graphene oxide and the nano-bio interaction-based physical mechanisms. *Colloids and Surfaces B: Biointerfaces* **191**, 111009 (2020).

139. J. Mao, R. Guo, L.-T. Yan, Simulation and analysis of cellular internalization pathways and membrane perturbation for graphene nanosheets. *Biomaterials* **35**, 6069-6077 (2014).

140. X. Liu *et al.*, Antioxidant deactivation on graphenic nanocarbon surfaces. **7**, 2775-2785 (2011).

141. S. Liu *et al.*, Antibacterial activity of graphite, graphite oxide, graphene oxide, and reduced graphene oxide: membrane and oxidative stress. *ACS nano* **5**, 6971-6980 (2011).

142. A. Sharma *et al.*, Structural, electronic structure and antibacterial properties of graphene-oxide nano-sheets. *Chemical Physics Letters* **698**, 85-92 (2018).

143. R. Combarros, S. Collado, M. Díaz, Toxicity of graphene oxide on growth and metabolism of Pseudomonas putida. *Journal of hazardous materials* **310**, 246-252 (2016).

144. A. Yilihamu *et al.*, Interaction between graphene oxide and nitrogen-fixing bacterium Azotobacter chroococcum: Transformation, toxicity and nitrogen fixation. *Carbon* **160**, 5-13 (2020).

145. J. Du, X. Hu, Q. Zhou, Graphene oxide regulates the bacterial community and exhibits property changes in soil. *Rsc Advances* **5**, 27009-27017 (2015).

146. S. Gurunathan, Cytotoxicity of graphene oxide nanoparticles on plant growth promoting rhizobacteria. *Journal of Industrial and Engineering Chemistry* **32**, 282-291 (2015).

147. W.-C. Hou *et al.*, The contribution of indirect photolysis to the degradation of graphene oxide in sunlight. *Carbon* **110**, 426-437 (2016).

148. W.-C. Hou, P.-L. Lee, Y.-C. Chou, Y.-S. Wang, Antibacterial property of graphene oxide: the role of phototransformation. *Environmental Science: Nano* **4**, 647-657 (2017).

149. W.-C. Hou *et al.*, Photochemical transformation of graphene oxide in sunlight. *Environmental science & technology* **49**, 3435-3443 (2015).

150. I. Chowdhury, M. C. Duch, N. D. Mansukhani, M. C. Hersam, D. Bouchard, Colloidal properties and stability of graphene oxide nanomaterials in the aquatic environment. *Environmental science & technology* **47**, 6288-6296 (2013).

151. G. Wang, F. Qian, C. W. Saltikov, Y. Jiao, Y. Li, Microbial reduction of graphene oxide by Shewanella. *Nano Research* **4**, 563-570 (2011).

152. S. Fogden, R. Verdejo, B. Cottam, M. Shaffer, Purification of single walled carbon nanotubes: The problem with oxidation debris. *Chemical Physics Letters* **460**, 162-167 (2008).

153. J. P. Rourke *et al.*, The real graphene oxide revealed: stripping the oxidative debris from the graphene‐like sheets. *Angewandte Chemie* **123**, 3231-3235 (2011).

154. E. Aliyev *et al.*, Structural characterization of graphene oxide: Surface functional groups and fractionated oxidative debris. *Nanomaterials* **9**, 1180 (2019).

155. A. F. Faria, F. o. Perreault, M. Elimelech, Elucidating the Role of Oxidative Debris in the Antimicrobial Properties of Graphene Oxide. *ACS Applied Nano Materials* **1**, 1164-1174 (2018).

156. K. Pulskamp, S. Diabaté, H. F. Krug, Carbon nanotubes show no sign of acute toxicity but induce intracellular reactive oxygen species in dependence on contaminants. *Toxicology letters* **168**, 58-74 (2007).

157. W. Norwood, U. Borgmann, D. Dixon, Chronic toxicity of arsenic, cobalt, chromium and manganese to Hyalella azteca in relation to exposure and bioaccumulation. *Environmental Pollution* **147**, 262-272 (2007).

158. A. Lerf, H. He, M. Forster, J. Klinowski, Structure of graphite oxide revisited. *The Journal of Physical Chemistry B* **102**, 4477-4482 (1998).

159. R. Muzyka, S. Drewniak, T. Pustelny, M. Sajdak, Ł. Drewniak, Characterization of graphite oxide and reduced graphene oxide obtained from different graphite precursors and oxidized by different methods using Raman spectroscopy statistical analysis. *Materials* **14**, 769 (2021).

160. I. Childres, L. A. Jauregui, W. Park, H. Cao, Y. P. Chen, Raman spectroscopy of graphene and related materials. *New developments in photon and materials research* **1**, 1-20 (2013).

161. C. Mattevi *et al.*, Evolution of electrical, chemical, and structural properties of transparent and conducting chemically derived graphene thin films. *Advanced Functional Materials* **19**, 2577-2583 (2009).

162. A. Bagri *et al.*, Structural evolution during the reduction of chemically derived graphene oxide. *Nature chemistry* **2**, 581-587 (2010).

163. A. Kumar, C. K. Dixit, in *Advances in nanomedicine for the delivery of therapeutic nucleic acids*. (Elsevier, 2017), pp. 43-58.

164. A. M. Dimiev, L. B. Alemany, J. M. Tour, Graphene oxide. Origin of acidity, its instability in water, and a new dynamic structural model. *ACS nano* **7**, 576-588 (2013).

165. B. Konkena, S. Vasudevan, Understanding aqueous dispersibility of graphene oxide and reduced graphene oxide through p K a measurements. *The journal of physical chemistry letters* **3**, 867-872 (2012).

166. C.-J. Shih, S. Lin, R. Sharma, M. S. Strano, D. Blankschtein, Understanding the pH-dependent behavior of graphene oxide aqueous solutions: a comparative experimental and molecular dynamics simulation study. *Langmuir* **28**, 235-241 (2012).

167. I. Martin-Gullon, J. M. Pérez, D. Domene, A. J. Salgado-Casanova, L. R. Radovic, New insights into oxygen surface coverage and the resulting two-component structure of graphene oxide. *Carbon* **158**, 406-417 (2020).

168. Q. Bao, D. Zhang, P. Qi, Synthesis and characterization of silver nanoparticle and graphene oxide nanosheet composites as a bactericidal agent for water disinfection. *Journal of colloid and interface science* **360**, 463-470 (2011).

169. I. Chowdhury, N. D. Mansukhani, L. M. Guiney, M. C. Hersam, D. Bouchard, Aggregation and stability of reduced graphene oxide: complex roles of divalent cations, pH, and natural organic matter. *Environmental science & technology* **49**, 10886-10893 (2015).

170. M. A. Buccheri *et al.*, Modification of graphene oxide by laser irradiation: a new route to enhance antibacterial activity. *Nanotechnology* **27**, 245704 (2016).

171. A. Gogoi, T. J. Konch, K. Raidongia, K. A. Reddy, Water and salt dynamics in multilayer graphene oxide (GO) membrane: role of lateral sheet dimensions. *Journal of Membrane Science*, (2018).

172. X. Lin *et al.*, Fabrication of highly-aligned, conductive, and strong graphene papers using ultralarge graphene oxide sheets. *ACS nano* **6**, 10708-10719 (2012).

173. X. Sun *et al.*, Nano-graphene oxide for cellular imaging and drug delivery. *Nano research* **1**, 203-212 (2008).

174. E. Bidram *et al.*, Fractionation of graphene oxide single nano-sheets in water-glycerol solutions using gradient centrifugation. *Carbon* **103**, 363-371 (2016).

175. K. E. Lee *et al.*, Liquid crystal size selection of large-size graphene oxide for size-dependent N-doping and oxygen reduction catalysis. *Acs Nano* **8**, 9073-9080 (2014).

176. H. Geng *et al.*, Size Fractionation of Graphene Oxide Nanosheets via Controlled Directional Freezing. *Journal of the American Chemical Society* **139**, 12517-12523 (2017).

177. X. Wang, H. Bai, G. Shi, Size fractionation of graphene oxide sheets by pH-assisted selective sedimentation. *Journal of the American Chemical Society* **133**, 6338-6342 (2011).

178. W. Zhang *et al.*, Size fractionation of graphene oxide sheets by the polar solvent-selective natural deposition method. *Rsc Advances* **5**, 146-152 (2015).

179. S. Kim, J. Lee, S.-S. Lee, Fractionation of graphene oxides by size-selective adhesion with spherical particles. *Macromolecular Research* **24**, 1098-1104 (2016).

180. J. Chen *et al.*, Synthesis of graphene oxide sheets with controlled sizes from sieved graphite flakes. *Carbon* **110**, 34-40 (2016).

181. F. Lin, X. Tong, Y. Wang, J. Bao, Z. M. Wang, Graphene oxide liquid crystals: synthesis, phase transition, rheological property, and applications in optoelectronics and display. *Nanoscale research letters* **10**, 435 (2015).

182. X. Zhang, Q. Zhou, W. Zou, X. Hu, Molecular mechanisms of developmental toxicity induced by graphene oxide at predicted environmental concentrations. *Environmental science & technology* **51**, 7861-7871 (2017).

183. K. Lim *et al.*, High-Speed AFM reveals molecular dynamics of human influenza A hemagglutinin and its interaction with exosomes. *Nano Letters* **20**, 6320-6328 (2020).

184. Y. Wang *et al.*, Two-dimensional nanomaterials with engineered bandgap: Synthesis, properties, applications. *Nano Today* **37**, 101059 (2021).

185. D. Gupta, V. Chauhan, R. Kumar, A comprehensive review on synthesis and applications of molybdenum disulfide (MoS2) material: Past and recent developments. *Inorg. Chem. Commun* **121**, 108200 (2020).

186. Y. Venkata Subbaiah, K. Saji, A. Tiwari, Atomically thin MoS2: A versatile nongraphene 2D material. *Advanced Functional Materials* **26**, 2046-2069 (2016).

187. W. O. Winer, Molybdenum disulfide as a lubricant: a review of the fundamental knowledge. *Wear* **10**, 422-452 (1967).

188. Z. Wang, B. Mi, Environmental applications of 2D molybdenum disulfide (MoS2) nanosheets. *Environmental science & technology* **51**, 8229-8244 (2017).

189. G. Eda *et al.*, Photoluminescence from chemically exfoliated MoS2. *Nano letters* **11**, 5111-5116 (2011).

190. G. Eda *et al.*, Coherent atomic and electronic heterostructures of single-layer MoS2. *ACS nano* **6**, 7311-7317 (2012).

191. K. Chang *et al.*, Targeted synthesis of 2H‐and 1T‐phase MoS2 monolayers for catalytic hydrogen evolution. *Advanced Materials* **28**, 10033-10041 (2016).

192. S. S. Chou *et al.*, Controlling the metal to semiconductor transition of MoS2 and WS2 in solution. *Journal of the American Chemical Society* **137**, 1742-1745 (2015).

193. D. Voiry *et al.*, Enhanced catalytic activity in strained chemically exfoliated WS 2 nanosheets for hydrogen evolution. *Nature materials* **12**, 850-855 (2013).

194. Y. H. Lee *et al.*, Synthesis of large‐area MoS2 atomic layers with chemical vapor deposition. *Advanced materials* **24**, 2320-2325 (2012).

195. Y. Shi, H. Li, L.-J. Li, Recent advances in controlled synthesis of two-dimensional transition metal dichalcogenides via vapour deposition techniques. *Chemical Society Reviews* **44**, 2744-2756 (2015).

196. J. Xie *et al.*, Defect‐rich MoS2 ultrathin nanosheets with additional active edge sites for enhanced electrocatalytic hydrogen evolution. *Advanced materials* **25**, 5807-5813 (2013).

197. D. Xu *et al.*, Microwave-assisted 1T to 2H phase reversion of MoS2 in solution: a fast route to processable dispersions of 2H-MoS2 nanosheets and nanocomposites. *Nanotechnology* **27**, 385604 (2016).

198. M. Miseljic, S. I. Olsen, Life-cycle assessment of engineered nanomaterials: a literature review of assessment status. *Journal of nanoparticle research* **16**, 1-33 (2014).

199. K. Ai, C. Ruan, M. Shen, L. Lu, MoS2 nanosheets with widened interlayer spacing for high‐efficiency removal of mercury in aquatic systems. *Advanced Functional Materials* **26**, 5542-5549 (2016).

200. H. J. Song, S. You, X. H. Jia, J. Yang, MoS2 nanosheets decorated with magnetic Fe3O4 nanoparticles and their ultrafast adsorption for wastewater treatment. *Ceramics International* **41**, 13896-13902 (2015).

201. X. Wang *et al.*, High supercapacitor and adsorption behaviors of flower-like MoS 2 nanostructures. *Journal of Materials Chemistry A* **2**, 15958-15963 (2014).

202. X. Gao, X. Wang, X. Ouyang, C. Wen, Flexible superhydrophobic and superoleophilic MoS 2 sponge for highly efficient oil-water separation. *Scientific reports* **6**, 1-8 (2016).

203. T. Thurston, J. Wilcoxon, Photooxidation of organic chemicals catalyzed by nanoscale MoS2. *The Journal of Physical Chemistry B* **103**, 11-17 (1999).

204. A. Midya, A. Ghorai, S. Mukherjee, R. Maiti, S. K. Ray, Hydrothermal growth of few layer 2H-MoS 2 for heterojunction photodetector and visible light induced photocatalytic applications. *Journal of Materials Chemistry A* **4**, 4534-4543 (2016).

205. M. R. Hoffmann, S. T. Martin, W. Choi, D. W. Bahnemann, Environmental applications of semiconductor photocatalysis. *Chemical reviews* **95**, 69-96 (1995).

206. W. Li, Y. Yang, J. K. Weber, G. Zhang, R. Zhou, Tunable, strain-controlled nanoporous MoS2 filter for water desalination. *ACS nano* **10**, 1829-1835 (2016).

207. L. Sun, H. Huang, X. Peng, Laminar MoS 2 membranes for molecule separation. *Chemical communications* **49**, 10718-10720 (2013).

208. S. Jiang, R. Cheng, R. Ng, Y. Huang, X. Duan, Highly sensitive detection of mercury (II) ions with few-layer molybdenum disulfide. *Nano Research* **8**, 257-262 (2015).

209. H. Li *et al.*, Fabrication of single‐and multilayer MoS2 film‐based field‐effect transistors for sensing NO at room temperature. *small* **8**, 63-67 (2012).

210. X. Yang *et al.*, Antibacterial activity of two-dimensional MoS 2 sheets. *Nanoscale* **6**, 10126-10133 (2014).

211. S. Pandit, S. Karunakaran, S. K. Boda, B. Basu, M. De, High antibacterial activity of functionalized chemically exfoliated MoS2. *ACS applied materials & interfaces* **8**, 31567-31573 (2016).

212. N. Wu *et al.*, Investigating the influence of MoS2 nanosheets on E. coli from metabolomics level. *PloS one* **11**, e0167245 (2016).

213. G. V. Lowry, K. B. Gregory, S. C. Apte, J. R. Lead. (ACS Publications, 2012).

214. Z. Wang, A. Von Dem Bussche, P. K. Kabadi, A. B. Kane, R. H. Hurt, Biological and environmental transformations of copper-based nanomaterials. *ACS nano* **7**, 8715-8727 (2013).

215. T. Du *et al.*, Photochlorination-induced transformation of graphene oxide: Mechanism and environmental fate. *Water research* **124**, 372-380 (2017).

216. G. S. Simate, S. Ndlovu, Acid mine drainage: Challenges and opportunities. *Journal of Environmental Chemical Engineering* **2**, 1785-1803 (2014).

217. M. Cao *et al.*, Molybdenum derived from nanomaterials incorporates into molybdenum enzymes and affects their activities in vivo. *Nature Nanotechnology* **16**, 708-716 (2021).

218. Z. Wang *et al.*, Chemical dissolution pathways of MoS2 nanosheets in biological and environmental media. *Environmental science & technology* **50**, 7208-7217 (2016).

219. X. Wang *et al.*, Differences in the toxicological potential of 2D versus aggregated molybdenum disulfide in the lung. *Small* **11**, 5079-5087 (2015).

220. M. Bae *et al.*, Nanotoxicity of 2D Molybdenum Disulfide, MoS2, Nanosheets on Beneficial Soil Bacteria, Bacillus cereus and Pseudomonas aeruginosa. *Nanomaterials* **11**, 1453 (2021).

221. W. Z. Teo, E. L. K. Chng, Z. Sofer, M. Pumera, Cytotoxicity of exfoliated transition‐metal dichalcogenides (MoS2, WS2, and WSe2) is lower than that of graphene and its analogues. *Chemistry–A European Journal* **20**, 9627-9632 (2014).

222. C. Moore *et al.*, Industrial grade 2D molybdenum disulphide (MoS2): an in vitro exploration of the impact on cellular uptake, cytotoxicity, and inflammation. *2D Materials* **4**, 025065 (2017).

223. Y. Li, D. Boraschi, Endotoxin contamination: a key element in the interpretation of nanosafety studies. *Nanomedicine* **11**, 269-287 (2016).

224. A. Murali, G. Lokhande, K. A. Deo, A. Brokesh, A. K. Gaharwar, Emerging 2D nanomaterials for biomedical applications. *Materials Today* **50**, 276-302 (2021).

225. J. Zheng *et al.*, Post-graphene 2D materials-based antimicrobial agents: focus on fabrication strategies and biosafety assessments. *Journal of Materials Science* **55**, 7226-7246 (2020).

226. H. Miao, Z. Teng, C. Wang, H. Chong, G. Wang, Recent Progress in Two‐Dimensional Antimicrobial Nanomaterials. *Chemistry–A European Journal* **25**, 929-944 (2019).

227. T. I. Kim, J. Kim, I.-J. Park, K.-O. Cho, S.-Y. Choi, Chemically exfoliated 1T-phase transition metal dichalcogenide nanosheets for transparent antibacterial applications. *2D Materials* **6**, 025025 (2019).

228. T. I. Kim *et al.*, Antibacterial activities of graphene oxide–molybdenum disulfide nanocomposite films. *ACS applied materials & interfaces* **9**, 7908-7917 (2017).

229. R. Wu *et al.*, Membrane destruction and phospholipid extraction by using two-dimensional MoS 2 nanosheets. *Nanoscale* **10**, 20162-20170 (2018).

230. J. Kaur *et al.*, Biological interactions of biocompatible and water-dispersed MoS 2 nanosheets with bacteria and human cells. *Scientific reports* **8**, 1-15 (2018).

231. R. Ye, W. Song, X. Ou, Z. Gu, D. Zhang, Membrane Insertion of MoS2 Nanosheets: Fresh vs. Aged. *Frontiers in chemistry* **9**, 499 (2021).

232. C. E. Taylor, S. D. Garvey, J. E. Pemberton, Carbon contamination at silver surfaces: surface preparation procedures evaluated by Raman spectroscopy and X-ray photoelectron spectroscopy. *Analytical chemistry* **68**, 2401-2408 (1996).

233. U. Krishnan, M. Kaur, K. Singh, M. Kumar, A. Kumar, A synoptic review of MoS2: Synthesis to applications. *Superlattices and Microstructures* **128**, 274-297 (2019).

234. W. Zou, Q. Zhou, X. Zhang, X. Hu, Environmental transformations and algal toxicity of single-layer molybdenum disulfide regulated by humic acid. *Environmental science & technology* **52**, 2638-2648 (2018).

235. D. Voiry *et al.*, Covalent functionalization of monolayered transition metal dichalcogenides by phase engineering. *Nature chemistry* **7**, 45-49 (2015).

236. T.-W. Lee, C.-C. Chen, C. Chen, Chemical stability and transformation of molybdenum disulfide nanosheets in environmental media. *Environmental science & technology* **53**, 6282-6291 (2019).

237. J. Bellenger, T. Wichard, A. Kustka, A. Kraepiel, Uptake of molybdenum and vanadium by a nitrogen-fixing soil bacterium using siderophores. *Nature Geoscience* **1**, 243-246 (2008).

238. Y. Li, Q. Jin, D. Yang, J. Cui, Molybdenum sulfide induce growth enhancement effect of rice (Oryza sativa L.) through regulating the synthesis of chlorophyll and the expression of aquaporin gene. *Journal of agricultural and food chemistry* **66**, 4013-4021 (2018).

239. K. Koenig, J. R. Andreesen, Molybdenum involvement in aerobic degradation of 2-furoic acid by Pseudomonas putida Fu1. *Applied and environmental microbiology* **55**, 1829-1834 (1989).

240. H. Niewerth *et al.*, Complete genome sequence and metabolic potential of the quinaldine-degrading bacterium Arthrobacter sp. Rue61a. *BMC genomics* **13**, 1-19 (2012).

241. W. Peng, H. Li, Y. Liu, S. Song, A review on heavy metal ions adsorption from water by graphene oxide and its composites. *Journal of Molecular Liquids* **230**, 496-504 (2017).

242. X. Liu *et al.*, Graphene oxide-based materials for efficient removal of heavy metal ions from aqueous solution: A review. *Environmental pollution* **252**, 62-73 (2019).

243. C. Greulich *et al.*, The toxic effect of silver ions and silver nanoparticles towards bacteria and human cells occurs in the same concentration range. *RSC advances* **2**, 6981-6987 (2012).

244. C. O. Dimkpa *et al.*, Interaction of silver nanoparticles with an environmentally beneficial bacterium, Pseudomonas chlororaphis. *Journal of hazardous materials* **188**, 428-435 (2011).

245. C. Fajardo, M. Saccà, G. Costa, M. Nande, M. Martin, Impact of Ag and Al2O3 nanoparticles on soil organisms: In vitro and soil experiments. *Science of the total environment* **473**, 254-261 (2014).

246. A. Samarajeewa *et al.*, Effect of silver nano-particles on soil microbial growth, activity and community diversity in a sandy loam soil. *Environmental Pollution* **220**, 504-513 (2017).

247. A. Masrahi, A. R. VandeVoort, Y. Arai, Effects of silver nanoparticle on soil-nitrification processes. *Archives of environmental contamination and toxicology* **66**, 504-513 (2014).

248. V. Shah, D. Collins, V. K. Walker, S. Shah, The impact of engineered cobalt, iron, nickel and silver nanoparticles on soil bacterial diversity under field conditions. *Environmental Research Letters* **9**, 024001 (2014).

249. M. Simonin, A. Richaume, Impact of engineered nanoparticles on the activity, abundance, and diversity of soil microbial communities: a review. *Environmental Science and Pollution Research* **22**, 13710-13723 (2015).

250. Z.-m. Xiu, Q.-b. Zhang, H. L. Puppala, V. L. Colvin, P. J. Alvarez, Negligible particle-specific antibacterial activity of silver nanoparticles. *Nano letters* **12**, 4271-4275 (2012).

251. D. A. Notter, D. M. Mitrano, B. Nowack, Are nanosized or dissolved metals more toxic in the environment? A meta‐analysis. *Environmental toxicology and chemistry* **33**, 2733-2739 (2014).

252. X. Yang *et al.*, Mechanism of silver nanoparticle toxicity is dependent on dissolved silver and surface coating in Caenorhabditis elegans. *Environmental science & technology* **46**, 1119-1127 (2012).

253. D. Cupi, N. B. Hartmann, A. Baun, The influence of natural organic matter and aging on suspension stability in guideline toxicity testing of silver, zinc oxide, and titanium dioxide nanoparticles with Daphnia magna. *Environmental toxicology and chemistry* **34**, 497-506 (2015).

254. Y.-J. Shin, J. I. Kwak, Y.-J. An, Evidence for the inhibitory effects of silver nanoparticles on the activities of soil exoenzymes. *Chemosphere* **88**, 524-529 (2012).

255. T. S. Radniecki, D. P. Stankus, A. Neigh, J. A. Nason, L. Semprini, Influence of liberated silver from silver nanoparticles on nitrification inhibition of Nitrosomonas europaea. *Chemosphere* **85**, 43-49 (2011).

256. R. Combarros, S. Collado, M. Díaz, Toxicity of titanium dioxide nanoparticles on Pseudomonas putida. *Water research* **90**, 378-386 (2016).

257. G. Fu, P. S. Vary, C.-T. Lin, Anatase TiO2 nanocomposites for antimicrobial coatings. *The journal of physical chemistry B* **109**, 8889-8898 (2005).